UNIVERSITY OF CALIFORNIA

Los Angeles

Characteristics of Subduction Zone Ground Motions with an Emphasis on Latin America

A dissertation submitted in partial satisfaction of the requirements for the degree Doctor of Philosophy in Civil Engineering

by

Victor Alejandro Contreras Luarte

2022

ABSTRACT OF THE DISSERTATION

Characteristics of Subduction Zone Ground Motions

with an Emphasis on Latin America

by

Victor Alejandro Contreras Luarte

Doctor of Philosophy in Civil Engineering

University of California, Los Angeles, 2022

Professor Jonathan Paul Stewart, Chair

For engineering design and seismic risk assessments, earthquake ground motions are characterized using intensity measures such as peak acceleration or spectral accelerations. Ground motion models (GMMs) estimate statistical distribution of intensity measures given information about the source, source-site path (distance), and site condition. This research pertains to data resources used to develop GMMs for subduction zone regions and adapts a global GMMs to a target region.

My initial research developed portions of the NGA-Subduction (NGA-Sub) project database. I worked with other experts to characterize seismic sources and source-to-site paths. The database contains data from 1,880 earthquakes in Alaska, Cascadia, Central America and Mexico,

Japan, New Zealand, South America, and Taiwan. Source parameters are related to the earthquake focus and finite fault representations. An important issue was the assignment of event types (intraslab and interface). I developed event type classification procedures that consider hypocenter locations relative to the interface, focal mechanisms, and other factors.

The second phase of research involved collaborating with researchers in Mexico to enhance data resources for that region (relative to NGA-Sub) and to use the information to develop a regionally customized GMM. I selected Mexico because it has high seismic hazard, its available GMMs have deficiencies, and it has substantial data from recent events that were not considered in NGA-Sub.

The database for Mexico is extended by considering small magnitude (**M** < 6) events and three large events (**M** 7.2-8.3) in 2017 and 2018. The latter are particularly important, because they are well recorded over a broad distance range and apply for hazard-critical conditions. These changes increase the size of the database from 593 recordings from 66 events (NGA-Sub) to 1882 recordings from 121 events. These data are examined relative to a global NGA-Sub model, which reveals a number of interesting features including faster anelastic attenuation in backarc than forearc regions and generally similar levels of site response as in the global GMM. A novel model for site response in Mexico City is proposed that is properly centered with respect to GMMs and that accounts for the unique Lake Texcoco geology.

The thesis of Victor Alejandro Contreras Luarte is approved.

Yousef Bozorgnia

Scott J. Brandenberg

Henry Burton

Jonathan P. Stewart, Committee Chair

University of California, Los Angeles

2022

TABLE OF CONTENTS

ABSTRACT OF THE DISSERTATION II

TABLE OF CONTENTS V

LIST OF FIGURES IX

LIST OF TABLES XXI

ACKNOWLEDGMENTS XXIII

VITA XXV

1 INTRODUCTION 1

1.1 SUBDUCTION ZONES 1

1.2 SUBDUCTION ZONE EARTHQUAKES 2

1.3 MODELING SUBDUCTION-ZONE GROUND MOTIONS 6

1.3.1 Introduction 6

1.3.2 NGA-Subduction Project 8

1.4 RESEARCH OBJECTIVES AND SCOPE 14

1.5 OUTLINE OF THE THESIS 17

2 GLOBAL DATABASE OF SUBDUCTION ZONE SOURCE PARAMETERS 21

2.1 INTRODUCTION 21

2.2 OVERVIEW OF EVENTS 23

2.3 GENERAL EARTHQUAKE CATALOG 39

2.3.1 Parameter Definitions 39

2.3.2 Parameter Selection Procedures 40

2.4 FINITE-FAULT SOURCE PARAMETERS FROM PUBLISHED MODELS 56

2.4.1 Finite-Fault Models Collected 56

2.4.2 Selection Criteria 64
2.4.3 Trimming Criteria 68
2.4.4 Multi-rectangle Rupture Models....70
2.5 SIMULATED FINITE-FAULT SOURCE PARAMETERS 74
2.5.1 Empirical Models for Fault Dimensions, Rupture Orientation, and Hypocenter Location....74
2.5.2 Simulation Procedure....83
2.6 EVENTS SUMMARY.... 85
3 SUBDUCTION ZONE EARTHQUAKE SOURCE-TO-SITE PATHS AND QUALITY ASSURANCE PROCEDURES 93
3.1 INTRODUCTION.... 93
3.2 SITE-TO-SOURCE DISTANCE.... 94
3.2.1 Distance Computation....94
3.2.2 Rupture Distance Uncertainty....95
3.3 VOLCANIC ARC FLAGS.... 100
3.4 PATH ATTRIBUTES SUMMARY.... 103
3.5 QUALITY ASSURANCE PROCEDURE 110
4 PRE-NGA-SUB DATABASES AND MODELS FOR SUBDUCTION-ZONE EARTHQUAKES 114
4.1 INTRODUCTION.... 114
4.2 GLOBAL DATABASES AND GMMs.... 114
4.3 LOCAL AND REGIONAL DATABASES AND GMMs 117
4.3.1 Local Databases and GMMs for Mexico....118
4.3.2 Local Databases and GMMs for Chile....126
4.3.3 Local Databases and GMMs for Latin American Countries other than Mexico and Chile....133
4.3.4 Regional Databases and GMMs for Latin America....136

4.3.5 Local Databases for Individual Countries outside Latin America.....142
4.3.6 Consistency and Documentation of Pre-NGA-Sub Local and Regional Databases 143
5 EXTENSION OF NGA-SUB DATABASE FOR CENTRAL AMERICA AND MEXICO 146
5.1 INTRODUCTION..... 146
5.2 ADDITION OF METADATA FOR EVENTS IN THE NGA-SUB DATABASE 148
5.3 POST-NGA-SUB LARGE MAGNITUDE EVENTS..... 154
5.3.1 September 8, 2017 M8.27 Offshore Chiapas Earthquake.....155
5.3.2 September 19, 2017 M7.18 Puebla Earthquake.....166
5.3.3 February 16, 2018 M7.2 Oaxaca Earthquake 170
5.4 GROUND MOTIONS FROM POST-NGA-SUB EVENTS..... 175
5.4.1 Ground Motion Networks and Recordings 175
5.4.2 Data processing.....182
5.4.3 Ground motion attributes 194
5.5 PATH PARAMETERS..... 199
5.5.1 Volcanic Arc Boundary 199
5.5.2 Distance Calculations.....201
5.5.3 Network-specific maximum usable distance 202
5.6 SITE PARAMETERS..... 205
5.6.1 Mexico City Site Conditions.....205
5.6.2 Non-Valley of Mexico Sites 221
6 ADAPTATION OF NGA-SUB GROUND MOTION MODEL FOR MEXICO..... 223
6.1 INTRODUCTION..... 223
6.2 APPROACH 225
6.2.1 Data Selection Criteria.....225
6.2.2 Residuals Analysis Procedures 229

6.3 REGIONAL BIAS AND SOURCE PARAMETER SCALING 232

6.3.1 Initial Analyses 232

6.3.2 Results from Recommended Model.....237

6.4 REGIONAL BIAS AND SOURCE PARAMETER SCALING 239

6.4.1 Initial Analyses 239

6.4.2 Regional Model for Mexico Backarc Anelastic Attenuation.....243

6.5 REGIONAL SITE RESPONSE FOR MEXICO..... 246

6.5.1 Site Response Exclusive of Valley of Mexico Sites.....246

6.5.2 Valley of Mexico Site Response.....249

6.5.3 Discussion.....256

6.6 EPISTEMIC UNCERTAINTY..... 257

7 SUMMARY AND CONCLUSIONS..... 259

7.1 SCOPE OF RESEARCH..... 259

7.2 RESEARCH FINDINGS AND SIGNIFICANCE..... 260

7.3 RECOMMENDATIONS FOR FUTURE RESEARCH..... 262

REFERENCES 265

LIST OF FIGURES

Figure 1.1 Diagram of the geological process of subduction (Schroeder, 2016)..... 1

Figure 1.2 Block diagrams of subduction zones with (a) oceanic-oceanic and (b) oceanic-continental convergent boundaries (USGS, 1996)..... 2

Figure 1.3 Map of the Circum-Pacific region showing the main tectonic plates and their relative movements (white arrows), distribution of the seismicity (black circles), and the position of volcanoes (red triangles). Modified from IRIS (2020). 3

Figure 1.4 Map of world's major subduction zones (thick gray lines) and tectonic plate boundaries (Bird, 2003). Filled circles show locations of known earthquakes of **M** = 7.5 or greater since 1900 (circle radius and grayscaled by magnitude). Open circles are largest known earthquakes from A.D.1700 to 1900 (compiled by Stein and Okal, 2007). Arrows show horizontal velocity of subducting plate relative to overriding plate. Dates are given for all **M**9 quakes (McCaffrey, 2008). 4

Figure 1.5 Map of epicenters of large (**M** ≥ 8.0) earthquakes from 1900 to 2016. Green circles are subduction zone megathrusts ruptures (interface events), and red circles are some important intraslab ruptures (Bilek and Lay, 2018). 5

Figure 1.6 Locations of epicenters in the NGA-Sub database. Regions are indicated by color of the epicenters and labeled as AK (Alaska), CASC (Cascadia), CAM (Central America and Mexico), JP (Japan), NZ (New Zealand), SA (South America), and TW (Taiwan). Bozorgnia et al. (2022)..... 11

Figure 1.7 Distribution in magnitude-rupture distance space of recordings by region from (a) 360 interface events and (b) 383 intraslab events that pass screening criteria described later in Chapter 2. Adapted from Bozorgnia et al. (2022). 12

Figure 2.1 Locations of (a) epicenters and (b) strong motion recording stations in the NGA-Sub database. Regions are indicated by color of the epicenters and stations and labeled as ALK (Alaska), CAS (Cascadia), CAM (Central America and Mexico), JPN (Japan), NZL (New Zealand), SAM (South America), and TWN (Taiwan). 24

Figure 2.2 Epicentral locations of earthquakes with recordings in Alaska..... 25

Figure 2.3 Epicentral locations of earthquakes with recordings in Cascadia. 26

Figure 2.4 Epicentral locations of earthquakes with recordings in Central America and Mexico. 28

Figure 2.5 Epicentral locations of earthquakes with recordings in Japan..... 29

Figure 2.6 Epicentral locations of earthquakes in Northern Japan. 30

Figure 2.7 Epicentral locations of earthquakes in Southern Japan. 31

Figure 2.8 Epicentral locations of earthquakes with recordings in New Zealand. 32

Figure 2.9 Epicentral locations of earthquakes with recordings in South America..... 34

Figure 2.10 Epicentral locations of earthquakes with recordings in Taiwan. The central portion of Taiwan has many shallow crustal earthquakes that are not included in the NGA-Sub database. 36

Figure 2.11 Event locations in CAM and SAM showing locations and magnitudes of classified and unclassified events. 38

Figure 2.12 Schematic representation of the fault rupture plane (Ancheta et al., 2013). Convention of fault strike, dip, and rake follows that described in Aki and Richards (1980). 40

Figure 2.13 M_W-M_L relationships from Bastías and Montalva (2016). Left: Eq. 2.2 for shallow-focus earthquakes ($H \leq 50$ km); Right: Eq. 2.3 for deep-focus earthquakes ($H > 50$ km). A slightly modified form of the relation is used (shifted up 0.033 to reflect M). 46

Figure 2.14 M_S-M_W and M_S-m_b relations from Leyton et al. (2009) Left: Eq. 2.4; Right: Original M_S-m_b relation reported by the authors. A slightly modified form of the M_S-M_W relation is used (shifted up 0.033 to reflect M). 46

Figure 2.15 Event-type classification scheme based on hypocenter location relative to the top of the surface of the subducting plate. Example event is NGAsubEQID 6000485, which is defined as interface..... 52

Figure 2.16 Distribution of hypocentral depths with M for (a) interface and (b) intraslab earthquakes by region. Events with lower confidence in the event-type classifications (negative flags) are not included..... 54

Figure 2.17 Epicentral locations of the earthquakes in (a) Japan and (b) South America with available FFMs from literature in the NGA-Sub database. 64

Figure 2.18 FFMs for the 2010 M8.81 Maule earthquake using a trimming threshold of 50 cm of slip. Locations of the ground-motion stations included in Table 2.6 are shown using yellow triangles for the RENADIC network and red triangles for the C network. The focal plane solution is shown at the epicenter. 65

Figure 2.19 Multi-rectangle rupture models of interface events in the NGA-Sub database in (a) Japan and (b) South America regions. 71

Figure 2.20 Multi-rectangle rupture models of intraslab events in the NGA-Sub database. (a) 1987 M6.53 Off Eastern Chiba, (b) 2001 M6.83 Geiyo, (c) 2008 M6.82 Middle Iwate, and (d) 2012 M7.23 Miyagi-oki earthquakes. 72

Figure 2.21 Examples of multi-rectangle rupture models (a) with continuity of the upper section of the rectangles and (b) variable dip over the fault width (listric faults)..... 73

Figure 2.22 (a) Initial and (b) Updated geometric relations for rupture area for subduction interface earthquakes. Sea16 = Skarlatoudis et al. (2016), MUR13 = Murotani et al. (2013). 75

Figure 2.23 (a) Initial and (b) Updated geometric relations for aspect ratio for subduction interface earthquakes. Sea16 = Skarlatoudis et al. (2016). 76

Figure 2.24 Geometric relations for (a) rupture area and (b) aspect ratio for subduction intraslab earthquakes. Black asterisk represents an event in Japan that was initially considered as intraslab (for regression marked as "Applied") and subsequently reclassified as outer-rise. 77

Figure 2.25 Parameterization of earthquake location on fault (view is normal to fault plane from hanging wall). 78

Figure 2.26 Locations of hypocenters on fault plane for interface events. (a) Results for data analyzed to support project simulations (dated Nov. 2017). (b) Results derived using the data in its current state (dated Dec. 2019). 80

Figure 2.27 Locations of hypocenters on fault plane for intraslab events. (a) Results for data analyzed to support project simulations (dated Nov. 2017). (b) Results derived using the data in its current state (dated Dec. 2019). Black asterisk represents an event in Japan originally considered as intraslab and later reclassified as outer-rise..... 81

Figure 2.28 Distribution of earthquakes with event-type assignments by region..... 86

Figure 2.29 Distribution of (a) earthquakes and (b) recordings by event-type..... 86

Figure 2.30 Magnitude distribution of (a) all earthquakes and (b) earthquakes with event-type assignments. 87

Figure 2.31 (a) Magnitude distribution of the events by type of earthquake. (b) Magnitude distribution of the recordings by type of earthquake. 88

Figure 2.32 Cumulative number of events over time by type of earthquake using (a) linear and (b) logarithmic scales..... 89

Figure 2.33 Distributions of events with FFMs in the NGA-Sub database. 89

Figure 2.34 Magnitude distribution of the events with FFMs in the NGA-Sub database. 90

Figure 2.35 Magnitude distribution of the recordings from events with FFMs in the NGA-Sub database..... 91

Figure 2.36 Rake and dip angles for interface and intraslab events in the NGA-Sub database. . 92

Figure 3.1. Schematics of different site-to-source distance metrics computed in NGA-Sub. (a) R_{rup}, R_{JB}, R_{hyp}, and R_{epi} (modified from Yang et al., 2019); (b) R_x and R_y (Ancheta et al., 2013); U and T parameters from the generalized coordinate system in Spudich and Chiou (2008). Positive directions are shown. 95

Figure 3.2. Example of the rupture rectangles resulting from the simulation procedure (101 realizations) for an interface event in Japan. The epicenter is shown as a red star and the rupture rectangle utilized in NGA-Sub for distance calculations is shown in red. 97

Figure 3.3. R_{rup} distributions for the analyzed sites. 99

Figure 3.4. Cascadia subduction zone geometry, displaying different earthquake sources. Interface earthquakes are labeled as "Subduction zone earthquakes" and intraslab earthquakes are labeled as "Deep earthquakes." After Wells et al. (2000). 100

Figure 3.5. Example of volcanic flag region extents in Alaska/Aleutians subduction zone. The green line between zones 1 and 2 follows the average trend of volcanic peaks. 102

Figure 3.6 Volcanic flag region extents in Japan subduction zone. The green lines between zones 1, 2, and 3 follow the average trend of volcanic peaks. 103

Figure 3.7 2011 M9.12 Tohoku earthquake example. (a) Hypocenter (red star), rupture area (three yellow rectangles with rupture trace marked in red), and sites located in the backarc (yellow triangles) and forearc (orange and red triangles) zones. (b) Distribution of the sites considering the fraction of the path length in the backarc (zone 1). 105

Figure 3.8 Distribution of the recordings considering the fraction of the path length in the backarc zone for interface events in (a, b) Japan and (c, d) South America. The histograms on the right (b, d) are zooming in to the figures on the left (a, c). 106

Figure 3.9 Distribution of the recordings considering the fraction of the path length in the backarc zone for interface events in (a, b) Alaska and (c, d) Central America and Mexico. The histograms on the right (b, d) are zooming in to the figures on the left (a, c). 107

Figure 3.10 Distribution of the recordings considering the fraction of the path length in the backarc zone for intraslab events in (a, b) Japan and (c, d) New Zealand. The histograms on the right (b, d) are zooming in to the figures on the left (a, c). 108

Figure 3.11 Distribution of the recordings considering the fraction of the path length in the backarc zone for intraslab events in (a) Cascadia, (b) South America, (c) Alaska, and (d) Central America and Mexico 109

Figure 3.12 Flowchart illustrating procedure used to resolve issues with prior version of flatfile, ultimately resulting in an updated version of the database. Ovals represent start and finish points of the procedure, blue parallelograms represent data, yellow boxes represent data analyses, and white diamonds represent decision points. 113

Figure 4.1 Magnitude–distance distribution of NGA-Sub database. (a) NGA-Sub versus BCHydro (Abrahamson et al., 2016) datasets. (b) NGA-Sub data distributed by region. Bozorgnia et al. (2022). 117

Figure 4.2 Map of the Pacific region and central Mexico showing epicenters of interface (blue circles) and intraslab (pink squares) earthquakes and recording stations (green triangles) used in the development of the local GMMs by Jaimes and García-Soto (2020, 2021). The Trans-Mexican volcanic belt (TMVB) is indicated and delimited with a shaded area. 125

Figure 4.3 Distribution of (a) magnitude versus distance and (b) focal depth versus distance of the Mexican dataset used in the development of the recent local GMMs by Jaimes and García (2020, 2021). Blue circles correspond to interface events and pink squares correspond to intraslab events. 125

Figure 4.4 Bastías and Montalva (2016) database: magnitude versus distance and magnitude versus focal depth distribution. 128

Figure 4.5 Magnitude versus distance distribution of the datasets used in the development of local GMMs in Chile: (a) Montalva et al. (2017); (b) Idini et al. (2017). 131

Figure 4.6 Distribution of magnitude versus (a) distance and (b) focal depth of the Chilean dataset used in the development of the recent local GMM by Montalva et al. (2021). 132

Figure 4.7 Magnitude-distance distribution of the Central America dataset compiled by Arango et al. (2011a). The distribution of the Chile-Peru dataset in Arango et al. (2011b) is also shown for reference. 138

Figure 4.8 Magnitude-distance distribution of the Chile-Peru dataset compiled by Arango et al. (2011b). 140

Figure 4.9 Magnitude-distance distribution of the SARA project database: (a) interface and (b) intraslab earthquakes. Repi = epicentral distance. Drouet et al. (2017). 140

Figure 5.1. Locations of events in Central America and Mexico showing classified and unclassified earthquakes by event-type. 150

Figure 5.2. Locations of events in Central America and Mexico showing classified and unclassified earthquakes by event-type, after the addition of 59 previously-unclassified events. 151

Figure 5.3. Magnitude-distance distribution of the NGA-Sub database in CAM following updates. 151

Figure 5.4. Magnitude-distance distribution of the NGA-Sub database in CAM including updates and differentiating by event-type. 152

Figure 5.5. Cumulative number of earthquakes over time in CAM including updates and differentiating by event-type. Color dots indicate the total number of events before the updates, which is shown in parenthesis..... 153

Figure 5.6. Cumulative number of recordings over time in CAM for (a) interface and (b) intraslab earthquakes. 153

Figure 5.7. 2017 M8.27 offshore Chiapas, 2017 M7.18 Puebla, and 2018 M7.2 Oaxaca earthquake sequence. SSE=Slow Slip Events; CDMX=Mexico City. (Cruz-Atienza et al., 2021)..... 154

Figure 5.8. Selected FFM modified from Melgar et al. (2018a). The white star is the event hypocenter. (a) Slip distribution. The purple line represents the applied trimming. Green squares are the aftershocks within a distance of 10 km. The orange line labelled TR is the intersection of the fault plane with the projection of the Tehuantepec Ridge. (b) Subvertical fault rupture. Dark blue squares are aftershock locations. Black lines indicate the oceanic and continental crusts. Geotherms are indicated as dashed lines. 157

Figure 5.9. Epicenter location and rupture area of the M8.27 offshore Chiapas earthquake. All ground motion stations from different networks are shown. 158

Figure 5.10. Epicenter location and rupture area of the M8.27 offshore Chiapas earthquake. Ground motion stations from different networks which are relatively close to the event source are shown. 159

Figure 5.11. (a) Relative error $\boldsymbol{\varepsilon}$ (in $\log_{10}$-scale) versus moment magnitude for shallow earthquakes (depth limit 0-70 km) in the Harvard catalog (1982/1/1–1999/12/31). The curves show linear and quadratic fits; the red point is the M8.27 offshore Chiapas event. (b) Dependence of the standard error of $\boldsymbol{\Gamma}$ index ($\boldsymbol{\sigma\Gamma}$) on moment magnitude for shallow earthquakes (depth limit 0-70 km). Linear regression curve ± one standard deviation is shown. Both plots were modified from Kagan (2002). 162

Figure 5.12. Differences in normalized scalar moment between USGS and CMT catalogs for the same earthquakes; modified from Rösler et al. (2021). The red circle marks the 2017 offshore Chiapas earthquake. (a) Differences for all N=5,000 events. The star marks the 2016 Kaikōura earthquake. (b) Differences by magnitude unit bins, for example, 4.5–5.5..... 165

Figure 5.13. Selected FFM modified from Melgar et al. (2018b). The white star is the event hypocenter. (a) Slip distribution. The purple line represents the applied trimming. (b) Cross section showing the fault rupture with respect to the geometry of the subducting slab. Moment tensors from the global CMT database are shown. Slab model is from Ferrari et al. (2012). Oceanic crust thickness and continental Moho are from Pérez-Campos et al. (2008). 168

Figure 5.14. Epicenter location and rupture area of the M7.18 Puebla earthquake. All ground motion stations from different networks are shown. 168

Figure 5.15. Epicenter location and rupture area of the M7.18 Puebla earthquake. Ground motion stations from different networks which are relatively close to the event source are shown..... 169

Figure 5.16. Selected FFM modified from Li et al. (2020). (a) Slip distribution. The red star is the event hypocenter, and the purple line represents the applied trimming. (b) Seismotectonic setting of southern Mexico. Aftershocks of the 2017 M8.27 and the 2018 M7.2 earthquakes are shown with white and gray circles, respectively. White lines represent the slab depth (Hayes et al., 2012). The box in the upper right presents a cross section showing the fault rupture with respect to the geometry of the subducting slab. 172

Figure 5.17. Epicenter location and rupture area of the M7.2 Oaxaca earthquake. All ground motion stations from different networks are shown. 173

Figure 5.18. Epicenter location and rupture area of the M7.2 Oaxaca earthquake. Ground motion stations from different networks which are relatively close to the event source are shown..... 174

Figure 5.19. Location of the ground motion recording stations of the RAII-UNAM network in Mexico. 175

Figure 5.20. Location of the ground motion recording stations (black and blue circles) of the RACM network in Mexico City. The colors denote the microzonation of the city: red = lake zone, yellow = transition zone, light blue = hills zone. 176

Figure 5.21. Location of the ground motion recording stations of the IG network in Mexico. Source: http://www.ssn.unam.mx/acerca-de/estaciones/ 177

Figure 5.22. Location of the ground motion recording stations of the VM network in Mexico City. Source: http://www.ssn.unam.mx/acerca-de/estaciones/ 178

Figure 5.23. Location of the ground motion recording stations of the UV network in Mexico (red triangles). Source: https://www.uv.mx/cienciauv/blog/laredsismicade-veracruz/..... 178

Figure 5.24. Instrument correction of the ground motion recording obtained at the ARIG station during the 2017 M8.27 offshore Chiapas earthquake (Channel HLN, R_{rup} = 627.8 km). The instrument is a Kinemetrics FBA-23 accelerometer with nominal natural frequency of 50 Hz and nominal damping ratio of 70%. Red lines represent the transfer functions of the pre-filtering (first row), the instrument response (second row), and the inverse of the instrument response (third row). The resultant ground motion (third row) has acceleration units (m/s^2). 180

Figure 5.25. Acceleration time series of the recording obtained at LI33 station (Mexico City) during the 2017 M7.18 Puebla earthquake. The vertical segmented lines in red identify the P-waves arrival time that is used to define the pre-event noise window..... 185

Figure 5.26. FAS of one of the horizontal components of the recording obtained at LI33 station (Mexico City) during the 2017 M7.18 Puebla earthquake. The vertical segmented lines are the cutoff frequencies utilized in the filtering of the signal. 186

Figure 5.27. Acceleration, velocity, and displacement time series of one of the horizontal components of the recording obtained at LI33 station (Mexico City) during the 2017 M7.18 Puebla earthquake. Causal filter. 187

Figure 5.28. Acceleration, velocity, and displacement time series of one of the horizontal components of the recording obtained at LI33 station (Mexico City) during the 2017 M7.18 Puebla earthquake. Acausal filter. 188

Figure 5.29. Pseudo-spectral acceleration of one of the horizontal components (Channel N00E) of the recording obtained at LI33 station (Mexico City) during the 2017 M7.18 Puebla earthquake: (a) Results obtained using the MATLAB code developed in this study. (b) Comparison between the results obtained with the code developed in this study and the PEER-NGA code for the acausal filter. The vertical blue lines represent the usable period range (between 0.0425 s and 12.939 s). 189

Figure 5.30. Example of application of a low pass filter to one of the horizontal components (N90E) of the recording obtained at ACAC station during the 2018 M7.2 Oaxaca earthquake: (a) Acceleration time series for the three components. (b) FAS and cutoff frequencies applied. (c) Filtered and baseline corrected acceleration, velocity, and displacement time series. (d) Pseudo-acceleration spectra. The vertical blue lines represent the usable period range (between 0.025 s and 9.412 s)..... 190

Figure 5.31. Example of application of a low pass filter to one of the horizontal components (HLE) of the recording obtained at HLIG station during the 2017 M8.27 offshore Chiapas earthquake: (a) Acceleration time series for the three components. (b) FAS and cutoff frequencies applied. (c) Filtered and baseline corrected acceleration, velocity, and displacement time series. (d) Pseudo-acceleration spectra. The vertical blue lines represent the usable period range (between 0.0329 s and 17.778 s)..... 191

Figure 5.32. Example of application of a high- pass filter to one of the horizontal components (N90W) of the recording obtained at PD42 station during the 2018 **M**7.2 Oaxaca earthquake: **(a)** Acceleration time series for the three components. **(b)** FAS and cutoff frequencies required to meet SNR criteria. **(c)** Filtered and baseline corrected acceleration, velocity, and displacement time series. A high-pass cutoff frequency of f_{min} = 0.55 Hz was required to obtain a reasonable displacement trace. **(d)** Pseudo-acceleration spectra, which is highly modified due to the aggressive filter. The vertical blue line represents the usable period range (T <1.45 s)..... 193

Figure 5.33. Recorded PGA values for the 2017 M8.27 offshore Chiapas earthquake from different networks: (a) RAII-UNAM, (b) IG and UV, (c) RACM, (d) VM. RACM and VM consist of stations in Mexico City only. 194

Figure 5.34. Recorded PGA values for the 2017 M7.18 Puebla earthquake from different networks: (a) RAII-UNAM, (b) IG and UV, (c) RACM, (d) VM. RACM and VM consist of stations in Mexico City only. 195

Figure 5.35. Recorded PGA values for the 2018 M7.2 Oaxaca earthquake from different networks: (a) RAII-UNAM, (b) IG and UV, (c) RACM, (d) VM. RACM and VM consist of stations in Mexico City only. 196

Figure 5.36. Magnitude-distance distribution of the NGA-Sub database in CAM following updates of events with M<6 and the addition of the three large-magnitude earthquakes occurred in 2017 and 2018. 198

Figure 5.37. Magnitude-distance distribution of the NGA-Sub database in CAM including updates (events with M<6 and the new earthquakes in 2017 and 2018) and differentiating by event-type. 198

Figure 5.38. Number of recordings in composite database as function of oscillator period. 199

Figure 5.39. Map showing NGA-Sub (red line) and relocated volcanic front (purple line). Orange symbols are volcanoes with eruptions during the Holocene period and yellow symbols are ground motion stations. 200

Figure 5.40. Map of central Mexico showing adopted volcanic front, ground motion stations considered in this region of Mexico, and hypocenters of the three large events described in Section 5.3. 201

Figure 5.41. $Rmax$ evaluation for the 2017 **M**8.27 offshore Chiapas event. Records from all the networks are plotted with the truncation level evaluated in the text, along with $Rmax$ value. Stations located on the Mexico City (MC) basin are highlighted in red. 203

Figure 5.42. $Rmax$ evaluation for the 2017 **M**7.18 Puebla event. Records from all the networks are plotted with the truncation level evaluated in the text, along with $Rmax$ value. Stations located on the Mexico City (MC) basin are highlighted in red. 204

Figure 5.43. $Rmax$ evaluation for the 2018 **M**7.2 Oaxaca event. Records from all the networks are plotted with the truncation level evaluated in the text, along with $Rmax$ value. Stations located on the Mexico City (MC) basin are highlighted in red. 204

Figure 5.44. Surface geology of Mexico City region (Flores-Estrella et al., 2007). 206

Figure 5.45. Schematic depiction of the hill, transition, and lake zones in Mexico City (Mayoral et al., 2008). 208

Figure 5.46. Zone map of Mexico City showing locations of recording sites used to derive transfer functions relative to the CU site (Reinoso and Ordaz, 1999). 210

Figure 5.47. Zone map for Mexico City in which the lakebed zone is divided into four subzones that are used to predict site period based on location (NTCS, 2003). 211

Figure 5.48. Example of zone-specific **(a)** uniform hazard spectra and **(b)** design response spectra derived using procedure from NTCS (2020). The following site periods were assigned by SASID: Ts = 0.5s, 0.8s, 1.4s, 1.8s, 2.9s, and 4.4s for the sites considered in the example at zones I, II, IIIa, IIIb, IIIc, and IIId, respectively. 212

Figure 5.49. Locations of sites from Table 5.6. Numbers next to sites are the ID numbers from Table 5.6. 217

Figure 5.50. Box and whisker plots of **(a)** V_{S30} and **(b)** site period (T_S) for characterized sites in the Valley of Mexico (using data from Table 5.6)..... 218

Figure 5.51. Correlation between V_{S30} and site period (T_S) for sites in the Valley of Mexico (using data from Table 5.6). The correlation coefficient between log(V_{S30}) and log(T_S) is shown. 219

Figure 6.1. Magnitude-distance distribution of the NGA-Sub database in CAM following updates and addition of large-magnitude Mexico events since 2016. 228

Figure 6.2. Magnitude-distance distribution of the screened NGA-Sub database in CAM..... 228

Figure 6.3. Model bias for peak acceleration, peak velocity, and Sa for a range of periods: (a) interface events, (b) instraslab events. Range indicates 95% confidence interval of the mean bias. 233

Figure 6.4. Trend of event terms for PGA, PGV, 0.3 sec Sa and 3.0 sec Sa with magnitude for interface events. Error bars are 95% confidence intervals..... 234

Figure 6.5. Trend of event terms for PGA, PGV, 0.3 sec Sa and 3.0 sec Sa with magnitude for intraslab events. Error bars are 95% confidence intervals..... 235

Figure 6.6. Trend of event terms for PGA, PGV, 0.3 sec Sa and 3.0 sec Sa with $Zhyp$ for interface events. Error bars are 95% confidence intervals..... 236

Figure 6.7. Trend of event terms for PGA, PGV, 0.3 sec Sa and 3.0 sec Sa with $Zhyp$ for intraslab events. Error bars are 95% confidence intervals..... 236

Figure 6.8. Event-type classification for NGAsubEQID 3000137 based on hypocenter location relative to the top of the surface of the subducting plate. The event is defined as interface. 237

Figure 6.9. Model bias for peak acceleration, peak velocity, and Sa for a range of periods using Pea22 GMM adjusted for backarc attenuation and VM site response effects: (a) interface events, (b) instraslab events. Range indicates 95% confidence interval of the mean bias. 238

Figure 6.10. Trend of event terms for PGA, PGV, 0.3 sec Sa and 3.0 sec Sa with magnitude for interface events using revised Pea22 GMM. Error bars are 95% confidence intervals..... 238

Figure 6.11. Trend of event terms for PGA, PGV, 0.3 sec Sa and 3.0 sec Sa with magnitude for intraslab events using revised Pea22 GMM. Error bars are 95% confidence intervals..... 239

Figure 6.12. Trend of within-event residuals for PGA, PGV, 0.3 sec Sa and 3.0 sec Sa with $Rrup$ for interface events and forearc sites using Pea22 GMM. 241

Figure 6.13. Trend of within-event residuals for PGA, PGV, 0.3 sec Sa and 3.0 sec Sa with $Rrup$ for intraslab events and forearc sites using Pea22 GMM. 241

Figure 6.14. Trend of within-event residuals for PGA, PGV, 0.3 sec Sa and 3.0 sec Sa with $Rrup, b$ for interface events and backarc sites using Pea22 GMM. 242

Figure 6.15. Trend of within-event residuals for PGA, PGV, 0.3 sec Sa and 3.0 sec Sa with $Rrup, b$ for intraslab events and backarc sites using Pea22 GMM. 243

Figure 6.16. Fit of backarc model (Eq. 6.9) to within-event residuals for PGA, PGV, 0.3 sec Sa and 3.0 sec Sa from interface events. 244

Figure 6.17. Fit of backarc model (Eq. 6.9) to within-event residuals for PGA, PGV, 0.3 sec Sa and 3.0 sec Sa from intraslab events. 245

Figure 6.18. Backarc additional anelastic attenuation coefficient $a0b$ for interface and intraslab events. Range indicates ± one standard error of the mean estimate. 245

Figure 6.19. Site response model bias $c1$ for peak acceleration, peak velocity, and Sa for a range of periods. Range indicates ± one standard error of the mean bias. 248

Figure 6.20. Trend of site terms for PGA, PGV, 0.3 sec Sa and 3.0 sec Sa with V_{S30} for Mexico sites exclusive of VM locations. Site terms for Puebla and Oaxaca are highlighted because there are concentrations of stations in these locations and portions of these regions have soft soils where strong site response might be anticipated. 248

Figure 6.21. Locations of six example sites – CUP5 (Zone I), ES57 (Zone II), IB22 (Zone IIIa), SCT2 (Zone IIIb), XP06 (Zone IIIc), and AE02 (Zone IIId). Base map is from Figure 5.47. ... 251

Figure 6.22. Period-dependent site response as derived from non-reference site approach for six sites in Mexico City (locations in Figure 6.21). 252

Figure 6.23. Variation of site amplification with V_{S30} for peak acceleration, peak velocity, Sa(0.3 s), and Sa(3.0 s): **(a)** Data plotted at a scale on y-axis that allows the trends with V_{S30} to be visualized, **(b)** Data plotted at scale that facilitates comparison with the global model of Parker and Stewart (2022). 253

Figure 6.24. Fit of VM model to site amplification data for peak acceleration, peak velocity, Sa(0.3 s), and Sa(3.0 s). Model coefficients are marked in the figure. 255

Figure 6.25. Period-dependence of coefficients for VM-specific site response model in Eq. 6.11: (a) V_{S30}-scaling gradients, (b) reference velocity V_{ref} and corner velocity V_1, and (c) amplification shift parameter f_{VM}. 255

Figure 6.26. Epistemic uncertainty $\sigma\varepsilon$ for Central America and Mexico from Parker et al. (2022) as derived using NGA-Sub database and as found from the present analysis using the expanded

database. The Parker et al. (2022) epistemic uncertainties are identical for intraslab and interface events. 258

LIST OF TABLES

Table 2.1 Example events from NGA-Sub database (highlighted in maps in Figures 2.2-2.10), showing compiled source parameters. 41

Table 2.2 Earthquake catalogs and published studies used to assign seismic moment and hypocenter location. 44

Table 2.3 Fault mechanism based on rake angle (after Ancheta et al., 2013). 49

Table 2.4 Flags in source database that indicate event-type classification. 55

Table 2.5 FFMs selected for use in NGA-Sub database. 58

Table 2.6 Computed distances (R_{rup}) using the seven FFMs for the 2010 Maule earthquake. 66

Table 2.7 Alternate FFMs for 2010 M8.81 Maule earthquake. 68

Table 2.8 Summary of trimming applied to FFMs for NGA-West1 and NGA-West 2 projects. 69

Table 2.9 Hypocenter locations from NGA-Sub data (Contreras et al. 2020) and Mai et al. (2005). NGA-Sub results from full data set and Nov. 2017 subset (in parenthesis); means and standard deviations are for a normal distribution. Mai et al. results are for a normal distribution (all events, along-strike location θ_L), for a Weibull distribution (all events, down-dip location θ_W), and for a Gamma distribution (subduction dip-slip events, down-dip location θ_W). 82

Table 3.1 Description of volcanic arc flags. 102

Table 3.2 Summary of the number of recordings in the forearc zone(s) by region and event-type. 109

Table 3.3 Source review flags. 112

Table 4.1 Summary of pre-2020 global subduction models and databases. 116

Table 4.2 Ground motion datasets and GMMs for subduction earthquakes in Mexico..... 120

Table 4.3 Ground motion datasets and GMMs for subduction earthquakes in Chile. 132

Table 4.4 Ground motion datasets and GMMs for subduction earthquakes in other individual countries in Latin America..... 136

Table 4.5 Ground motion datasets and GMMs for the Central America subduction zone. 138

Table 4.6 Ground motion datasets and GMMs for the South America subduction zone. 141

Table 4.7 Summary of recent local subduction models and databases for individual countries outside Latin America. 142

Table 5.1 Alternate finite-fault models for 2017 **M**8.27 offshore Chiapas earthquake. 156

Table 5.2 Alternate finite-fault models for 2017 **M**7.18 Puebla earthquake. 167

Table 5.3 Alternate finite-fault models for 2018 **M**7.2 Oaxaca earthquake. 171

Table 5.4 Number of ground motion stations and recordings by network. 181

Table 5.5 Number of ground motion recordings by earthquake and network. 181

Table 5.6 Summary of site data from literature for Valley of Mexico stations. 213

Table 5.7 Summary of V_{S30} parameters developed for Valley of Mexico stations without a V_S profile. 220

ACKNOWLEDGMENTS

First, I would like to acknowledge the Chilean National Agency for Research and Development (ANID) for the financial support through the *Becas Chile – Doctorado en el Extranjero* program and for giving me the opportunity to pursue graduate level education at UCLA. I am also grateful to the Civil and Environmental Engineering Department at UCLA, for the financial support they provided during my studies as well. I would also like to thank the following organizations for the financial support of the NGA-Sub research project: FM Global, the US Geological Survey, the California Department of Transportation, and the Pacific Gas & Electric Company.

I would like to thank CSN and RENADIC, both at the University of Chile, for providing the strong motion data from Chile and the information regarding the strong motion stations, especially to Professors Fabián Rojas and Rubén Boroschek for transferring the raw data from RENADIC to UCLA. I am also grateful to FUCHIGE (*Fundación Chilena de Geotecnia*) for providing various geotechnical data and reports for several stations, and to Francisco Ruz for providing numerous unpublished V_S profiles.

I would like to express my gratitude to the following collaborators of the NGA-Subduction project: Yousef Bozorgnia, Jonathan Stewart, Tadahiro Kishida, Robert B Darragh, Brian Chiou, Silvia Mazzoni, Robert Youngs, Nicolas Kuehn, Sean Ahdi, Katie Wooddell, Ruben Boroschek, Fabian Rojas, and Jennyfer Ordenes. I would also like to thank to the following collaborators from UNAM in Mexico: Xyoli Pérez-Campos, Juan Mayoral, and Daniel De La Rosa, who helped me to put together the dataset for Mexico.

A special thank you to my advisor, Jonathan P. Stewart, who has provided much time and guidance throughout my M.S. and Ph.D. work at UCLA, offering suggestions on coursework and research, and advice during the preparation of this thesis. Many thanks for all your support and patience, and for believing in me. I would also like to express my gratitude to the other members serving on my committee: Yousef Bozorgnia, Scott Brandenberg, and Henry Burton for their advice and suggestions during the development of the NGA-Subduction project and for their comments and feedback that helped to improve my research. I would also like to thank all of them for sharing their knowledge and expertise while I was learning from them during their lectures.

I would also like to thank my family for their support, especially to my parents, Erika and Héctor, and my siblings, Camila and Samuel, without whom none of this would have been possible. Finally, I would like to thank Fernanda, for all the sacrifices she has done to help me reach my goals. Thank you so much for all your patience during this process and for all your love and support.

VITA

2021	Hired, Civil Engineering Department, University Diego Portales, Santiago, Chile.
2017	M.S., Civil Engineering, University of California, Los Angeles.
2009 - 2015	Project Engineer, Ruben Boroschek and Associates (RBA), Santiago, Chile.
2009	B.S., Civil Engineering, University of Chile, Santiago, Chile.

SELECTED PUBLICATIONS

Contreras, V, Stewart, JP, Kishida, T, Darragh, RB, Chiou, BSJ, Mazzoni, S, Youngs, RR, Kuehn, NM, Ahdi, SK, Wooddell, K, Boroschek, R, Rojas, F, Ordenes, J (2022). NGA-Sub source and path database. *Earthquake Spectra*, **38** (2): 799–840.

Ahdi, SK, Kwak, DY, Ancheta, TD, **Contreras, V**, Kishida, T, Kwok, AOL, Mazzoni, S, Ruz, F, Stewart, JP (2022). Site parameters applied in NGA-Sub database. *Earthquake Spectra*, **38**(1): 494–520.

Bozorgnia Y, Abrahamson NA, Ahdi SK, Ancheta TD, Al Atik L, Archuleta RJ, Atkinson GM, Boore DM, Campbell KW, Chiou BSJ, **Contreras V**, Darragh RB, Derakhshan S, Donahue JL, Gregor N, Gulerce Z, Idriss IM, Ji C, Kishida T, Kottke AR, Kuehn N, Kwak DY, Kwok AOL, Lin P, Mazzoni S, Midorikawa S, Muin S, Parker GA, Rezaeian S, Si H, Silva WJ, Stewart JP, Walling M, Wooddell K, Youngs RR (2022). NGA-Subduction research program, *Earthquake Spectra*, **38**(2): 783–798.

Mazzoni S, Kishida T, Stewart JP, **Contreras V**, Darragh RB, Ancheta TD, Chiou BS-J, Silva WJ and Bozorgnia Y (2022). Relational database used for ground-motion model development in the NGA-Sub project. *Earthquake Spectra*, **38**(2): 1529–1548.

Sean Kamran Ahdi, Silvia Mazzoni, Tadahiro Kishida, Pengfei Wang, Chukwuebuka C. Nweke, Nicolas M. Kuehn, **Victor Contreras**, Badie Rowshandel, Jonathan P. Stewart, Yousef Bozorgnia (2020). Engineering Characteristics of Ground Motions Recorded in the 2019 Ridgecrest Earthquake Sequence. *Bulletin of the Seismological Society of America* ; **110** (4): 1474–1494.

Contreras V., Ruz F., Ahdi S.K., Stewart J.P. (2018). "VS profile database and proxy-based models for VS30 prediction in Chile for NGA-Subduction*", Eleventh U.S. National Conference on Earthquake Engineering (11NCEE)*. June 25-29, Los Angeles, California.

Contreras V., Stewart J.P., Darragh R.B., Kishida T., Youngs R.R. (2018). "Earthquake Source Parameters for Chilean Events for use in the NGA-Subduction Project", *Eleventh U.S. National Conference on Earthquake Engineering (11NCEE)*. June 25-29, Los Angeles, California.

1 INTRODUCTION

1.1 SUBDUCTION ZONES

A subduction zone is a region dominated by a convergent plate boundary where usually two tectonic plates come together, one subducting (diving) beneath the other and sinking into the Earth's mantle due to gravitational potential energy, as indicated schematically in Figure 1.1. Subduction zones around the world comprise a total length above 50,000 km with a mean rate of convergence of approximately 6 cm/yr (Bird, 2003). Rates of subduction vary between regions (e.g., 6 to 9 cm/year in Japan, 6 to 8 cm/yr in South America, and 3 to 4 cm/yr in Cascadia). As the subducting plate bends and begins to descend beneath the overriding plate, it generates a large topographic depression of the sea floor called an oceanic trench. These trenches are the deepest parts of the Earth's surface, extending typically 3 to 4 km below the level of the surrounding oceanic floor. The Mariana Trench is the deepest, reaching 11 km below sea level.

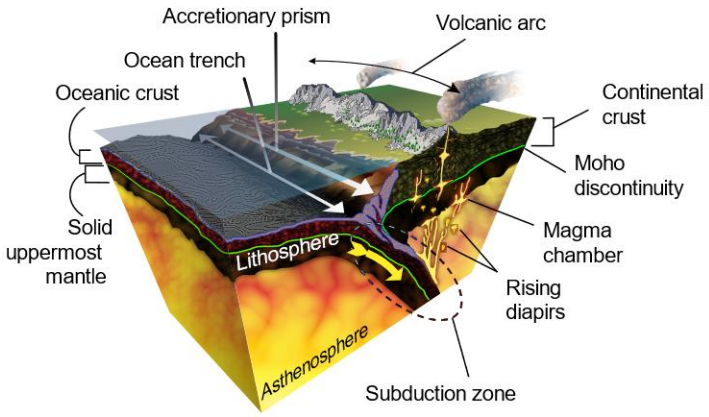

Figure 1.1 Diagram of the geological process of subduction (Schroeder, 2016).

Subduction zones are regions with a high seismic activity and volcanism. The subducting plate (slab) generates earthquakes at the interface with the overriding plate (interface events) and earthquakes associated with the tensile deformation in the upper portion of the slab (intraslab events). Volcanic activity is caused by high temperatures at the frictional interface between the subducting and overriding slab, which melts portions of the lithosphere. The heated, softened material has lower density than surrounding rock, and migrates toward the surface. This can produce a linear belt of volcanoes parallel to the oceanic trench. This chain of volcanos is called an island arc when caused by an oceanic-oceanic convergent boundary, as shown in Figure 1.2a (e.g., the Aleutian Island chain). On the other hand, this belt is called a volcanic arc when caused by an oceanic-continental convergent boundary as shown in Figure 1.2b, examples of which include the Andes volcanic arc of South America and the Cascade volcanic arc of the Pacific Northwest in the U.S.

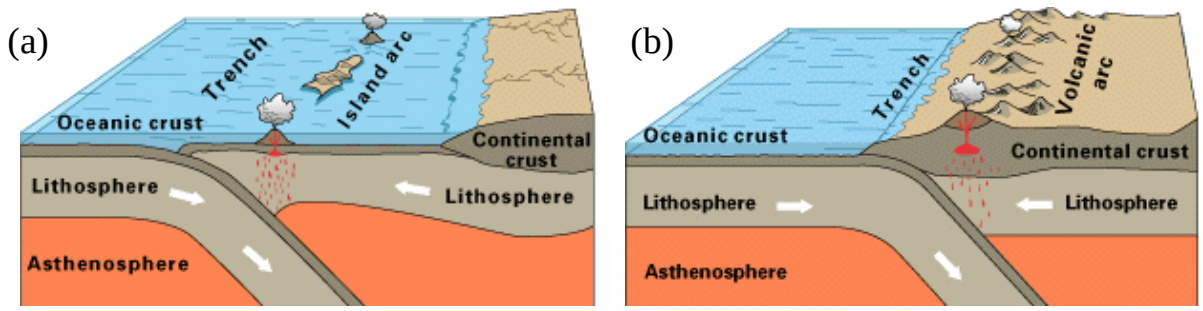

Figure 1.2 Block diagrams of subduction zones with (a) oceanic-oceanic and (b) oceanic-continental convergent boundaries (USGS, 1996).

1.2 SUBDUCTION ZONE EARTHQUAKES

The Circum-Pacific region, which is responsible for approximately 80% of earthquakes worldwide, contains many subduction zone plate boundaries. In addition to the high seismicity,

the Circum-Pacific subduction zones are also home to over 400 active volcanoes as shown in Figure 1.3 (IRIS, 2020). These subduction zones have produced Earth's largest earthquakes, along with multitudes of smaller events directly or indirectly related to the subduction process. Interface earthquakes occur at hypocentral depths typically smaller than 60 km. Intraslab earthquakes have deeper hypocenters, reaching depths above 500 km in certain regions. Interface events are associated with larger rupture areas than intraslab events, and have higher maximum observed magnitudes (~**M**9 for interface and ~**M**8 for intraslab). Interface earthquakes have a reverse faulting mechanism while intraslab earthquakes present different types of faulting, although the predominant mechanism is normal faulting.

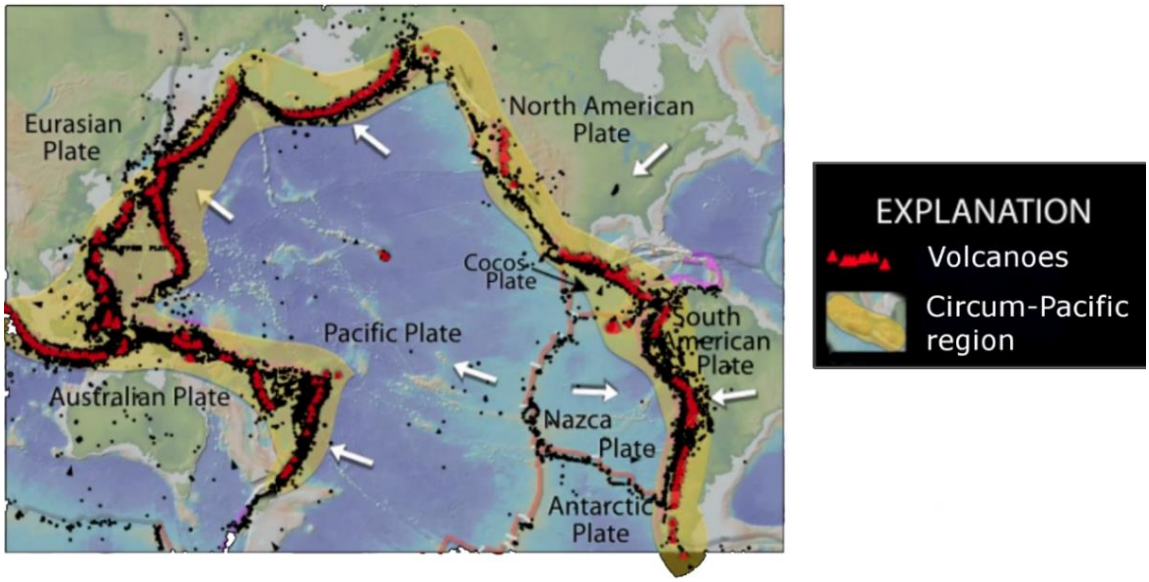

Figure 1.3 Map of the Circum-Pacific region showing the main tectonic plates and their relative movements (white arrows), distribution of the seismicity (black circles), and the position of volcanoes (red triangles). Modified from IRIS (2020).

A substantial number of large magnitude earthquakes worldwide have occurred in the Circum-Pacific region subduction zones. Figure 1.4 presents a map showing the epicenters of

major known subduction zone earthquakes (**M** ≥ 7.5) that occurred between 1700 and 2006. The South America subduction zone is the source of the largest earthquake ever recorded, the 1960 **M**9.5 Valdivia (Chile) megathrust earthquake. Examples of large historic events in other regions include the 1700 **M**9.1 Cascadia earthquake, the 1707 **M**8.8 Nankai (Japan) earthquake, the 1833 **M**9.2 South Sumatra earthquake, the 1932 **M**8.1 Jalisco (Mexico) earthquake, and the 1964 **M**9.3 Alaska earthquake.

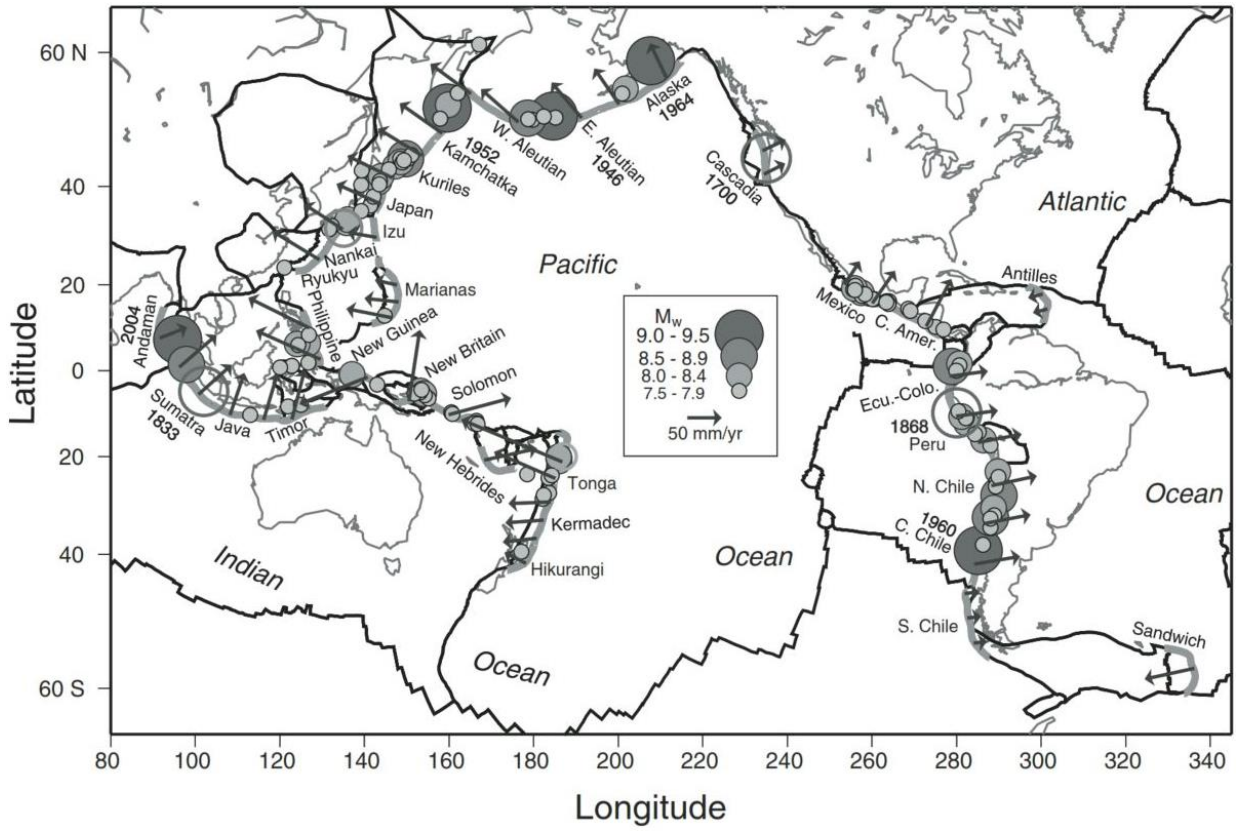

Figure 1.4 Map of world's major subduction zones (thick gray lines) and tectonic plate boundaries (Bird, 2003). Filled circles show locations of known earthquakes of **M** = 7.5 or greater since 1900 (circle radius and grayscaled by magnitude). Open circles are largest known earthquakes from A.D.1700 to 1900 (compiled by Stein and Okal, 2007). Arrows show horizontal velocity of subducting plate relative to overriding plate. Dates are given for all **M**9 quakes (McCaffrey, 2008).

Figure 1.5 shows a map of the epicenters of large (**M** ≥ 8.0) subduction zone earthquakes from 1900 to 2016. Most of these events are interface earthquakes, although some important intraslab ruptures are also included. The largest recent event is the 2011 **M**9.12 Tohoku (Japan) earthquake which is the largest event with available recorded ground motions (about 2,000 recordings). Other major recent events are the 2004 **M**9.3 Sumatra earthquake, the 2010 **M**8.81 Maule (Chile) earthquake, the 2001 **M**8.41 southern Peru earthquake, the 2013 **M**8.36 Okhotsk Sea (Russia) earthquake, the 2006 **M**8.33 Kuril Islands earthquake, the 2015 **M**8.31 Illapel (Chile) earthquake, the 2003 **M**8.29 Tokachi-oki (Japan) earthquake, the 2014 **M**8.15 Iquique (Chile) earthquake, and the 2007 **M**8 Pisco (Peru) earthquake.

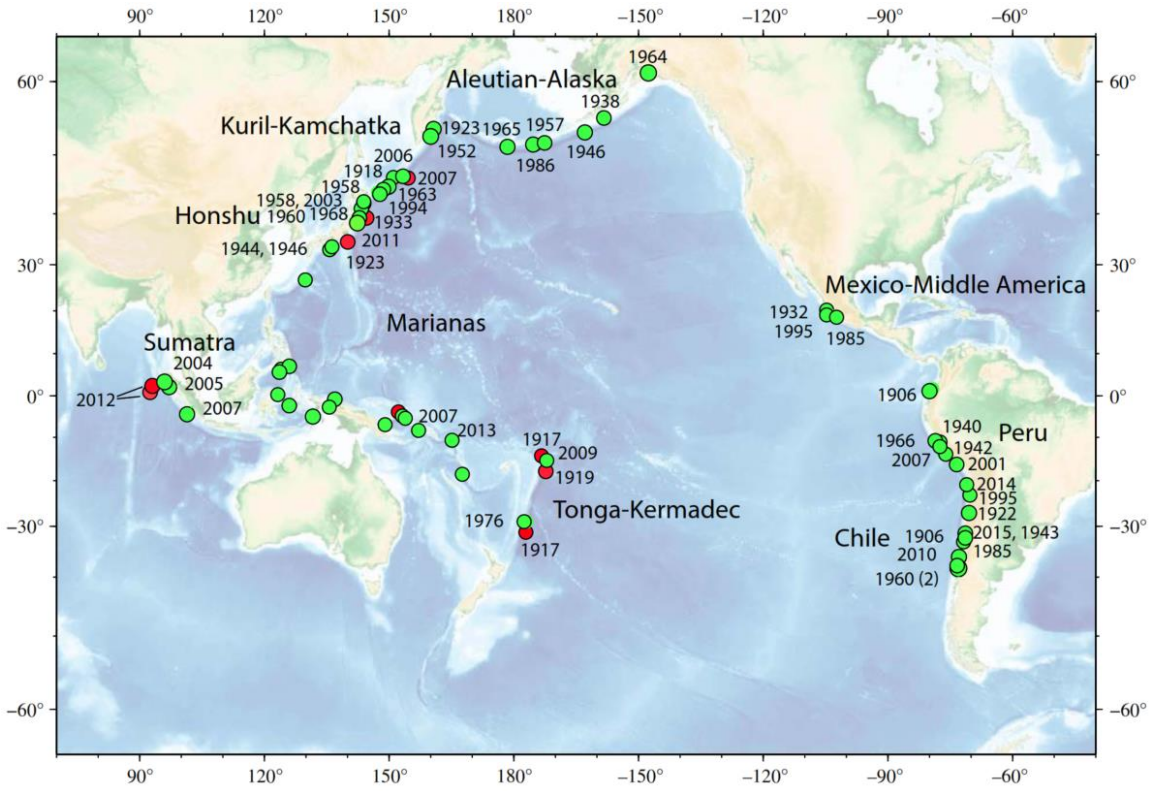

Figure 1.5 Map of epicenters of large (**M** ≥ 8.0) earthquakes from 1900 to 2016. Green circles are subduction zone megathrusts ruptures (interface events), and red circles are some important intraslab ruptures (Bilek and Lay, 2018).

1.3 MODELING SUBDUCTION-ZONE GROUND MOTIONS

1.3.1 Introduction

Based on the information presented in the previous sections, it is evident that subduction zones are dominant sources of seismic hazard in many regions globally, which include areas of Alaska, the Pacific North West region of North America, Mexico, Central America, South America, Japan, Taiwan, New Zealand, and Sumatra, among others. The quantification of seismic hazard in these regions is needed to assess risk from, and mitigate the threats posed by, ground shaking from this type of earthquakes.

Ground motion characterization is a critical component of any seismic hazard assessment and subsequent risk analysis for a particular site or region of interest. As engineers, we would like to have a direct method to reliably predict the levels of shaking produced by a specific earthquake for applications that require seismic demand estimates, such as seismic design of structures and non-structural components, seismic protection, seismic code provisions, assessments of the potential for other hazards triggered by ground shaking (e.g., liquefaction, landslides), loss estimation, urban planning, and so on. However, due to the inherent randomness of the earthquake's occurrence and the lack of understanding of many of the physical processes involved, such a direct method is not currently attainable. Instead, we rely on probabilistic models called Ground Motion Models (GMMs) – also known as Ground Motion Prediction Equations (GMPEs) and previously simply called "attenuation relations" – that estimate the mean and dispersion of parameters that quantify ground motion intensity.

GMMs are mathematical expressions that estimate ground shaking levels in terms of intensity measures (IM) that are useful for engineering applications, such as peak ground acceleration (PGA), peak ground velocity (PGV), pseudo spectral acceleration (PSa) at various oscillator periods and for a reference level of damping (typically 5%), Arias Intensity (I_A), and significant duration. These models probabilistically relate different relevant parameters – associated with earthquakes characteristics, seismic waves traveling, and site conditions – with the IMs of interest. Thus, the GMMs formulation typically considers three sets of parameters as an input for ground motion estimation: source, path, and site characteristics. In general terms, these models have the functional form shown in Equation 1.1:

$$\ln(Y) = \mu_{lnY} + \varepsilon\sigma_{lnY} \tag{1.1}$$

where Y is the observed IM of interest (measured data), μ_{lnY} is the natural log median prediction of the model conditioned on various independent variables, ε is the standard normal variate (zero mean, standard deviation of 1), and σ_{lnY} is the standard deviation in natural log units.

As shown in Equation 1.2, the median prediction (μ_{lnY}) can be broadly expressed using three terms: a source term (f_E) associated with the earthquake source parameters, a path term (f_P) related to the variation of ground motion with distance, and a site term (f_S) that assesses the effect of site parameters on the model prediction. The source term is typically a function of moment magnitude (**M**), earthquake depth (focal depth H or alternatively the depth to the top of the rupture Z_{TOR}), and event type (interface or intraslab in a subduction environment); the path term depends on source-to-site distance (usually the closest distance to the source rupture plane R_{rup} or

alternatively for small events the hypocentral distance R_{hyp}) and the geographic region (as the properties of the Earth's crust vary from one region to another); the site term is generally characterized through site parameters like V_{S30} (the time-averaged shear wave velocity in the upper 30 m of a site), f_0^{HVSR} (the fundamental site frequency estimated using horizontal-to-vertical Fourier amplitude spectral ratios), or Z_x (the distance from the ground surface to the first crossing of a specific shear wave velocity isosurface; typically $Z_{1.0}$ and $Z_{2.5}$ for depths to the 1.0 km/s and 2.5 km/s isosurfaces). Additional source, path, and site parameters may be considered in the development of GMMs, although for simplicity only the most important variables are explicitly included in Equation 1.2.

$$\mu_{lnY} = f_E(\mathbf{M}, H, Z_{TOR}, \text{event type}, \text{region}) + f_P\big(R_{rup}, R_{hyp}, \text{region}\big) + f_S(V_{S30}, f_0^{HVSR}, Z_x, region) \quad (1.2)$$

1.3.2 NGA-Subduction Project

In 2003, the Pacific Earthquake Engineering Research Center (PEER) initiated a large research program to develop next generation ground-motion models (GMMs) for shallow crustal earthquakes in active tectonic regions (Power et al., 2008). This project, initially named Next Generation Attenuation (NGA) project and now referred to as NGA-West1, made a strong impact in the engineering and seismological community in three main respects:

1. It changed the research culture related to the database and GMM development, bringing leading experts together to collaborate on database development who routinely shared thoughts and best practices during model development. This improved model thoroughness and quality.

2. The GMMs were of high quality for the time, combining scaling from first principals (and informed by simulations) with data analyses to provide models that operated over the ranges required for many practical applications.
3. The database was shared by all GMM developer teams and then publicly disseminated via a PEER website, which ultimately supported many subsequent research projects and practical applications related to time-series selection.

The impact of the NGA-West1 project created demand for subsequent projects that were structured similarly. In total, three separate NGA projects have been coordinated by PEER:

a) NGA-West1 (Power et al., 2008) and NGA-West2 (Bozorgnia et al., 2014), for shallow crustal earthquakes in active tectonic regimes such as California, Japan, Turkey, Taiwan, and Italy, among other regions. NGA-West2 significantly expanded the database and certain GMPE attributes with respect to NGA-West1. More information about the NGA-West1 and NGA-West2 projects is available at http://peer.berkeley.edu/ngawest and http://ngawest2.berkeley.edu, respectively.

b) NGA-East (Goulet et al., 2014), for stable continental regions, particularly central and eastern North America, along with an important portion of Europe, South Africa, and other regions. NGA-East made more extensive use of simulations than other regions due to data paucity for the magnitudes and distances of typical engineering interest. More information about the NGA-East project is available at http://peer.berkeley.edu/ngaeast.

c) NGA-Subduction (NGA-Sub) applied the NGA framework to subduction-zone earthquakes in active tectonic regimes like the Pacific Northwest (PNW) region of North America, northern California and Alaska in the United States, Japan, Taiwan, Mexico, and South America, among other areas (Bozorgnia et al., 2022). The database for this project is recently published (Mazzoni et al., 2022; Ahdi et al., 2022; Contreras et al., 2022; and this thesis) and several ground motion models have been completed (Abrahamson and Gülerce, 2020; Kuehn et al., 2020; Si et al., 2022; Parker et al., 2022).

All NGA projects provide uniformly-processed ground motion data from earthquakes recorded in different tectonic settings and regions, including time series and intensity measure values, such as peak ground acceleration (PGA), peak ground velocity (PGV), pseudo spectral acceleration (PSa), Arias Intensity (I_A), and significant duration. As explained previously, the databases and the corresponding documentation that result from these efforts are public and available on the internet, freely allowing researchers and practitioners to access and use these resources.

NGA-Sub is a major multi-year international project in engineering seismology utilizing a multidisciplinary approach to develop database resources and ground motion models (GMMs) for subduction-zone earthquakes. NGA-Sub involves highly collaborative research with extensive technical interaction and cooperation among many organizations and participants from different countries around the world.

The NGA-Sub project database is described in Mazzoni et al. (2022). Source and path parameters are described in Contreras et al. (2022) and site parameters are described in Ahdi et al. (2022). Figure 1.6 shows the hypocenters of earthquakes included in the database. The magnitude-distance distributions of the recordings associated with interface and intraslab earthquakes are presented in Figure 1.7, with differentiation by region. The ground motion database includes the processed recordings and supporting source, path, and site metadata from the regions of Alaska, Cascadia, Central America and Mexico, Japan, New Zealand, South America, and Taiwan.

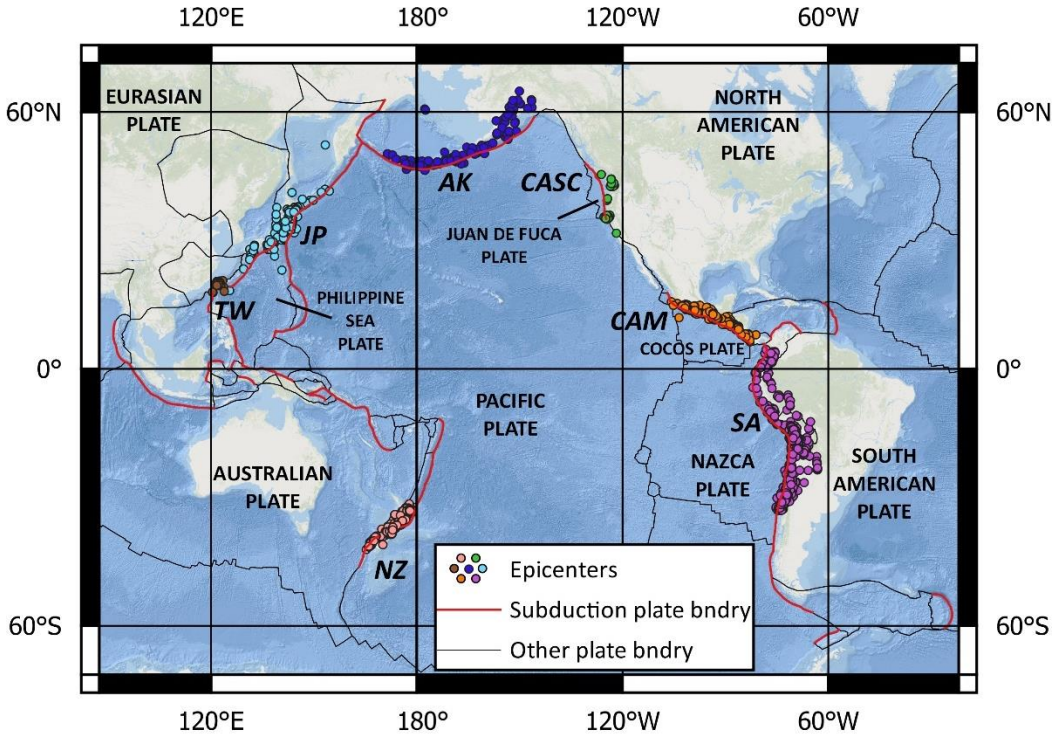

Figure 1.6 Locations of epicenters in the NGA-Sub database. Regions are indicated by color of the epicenters and labeled as AK (Alaska), CASC (Cascadia), CAM (Central America and Mexico), JP (Japan), NZ (New Zealand), SA (South America), and TW (Taiwan). Bozorgnia et al. (2022).

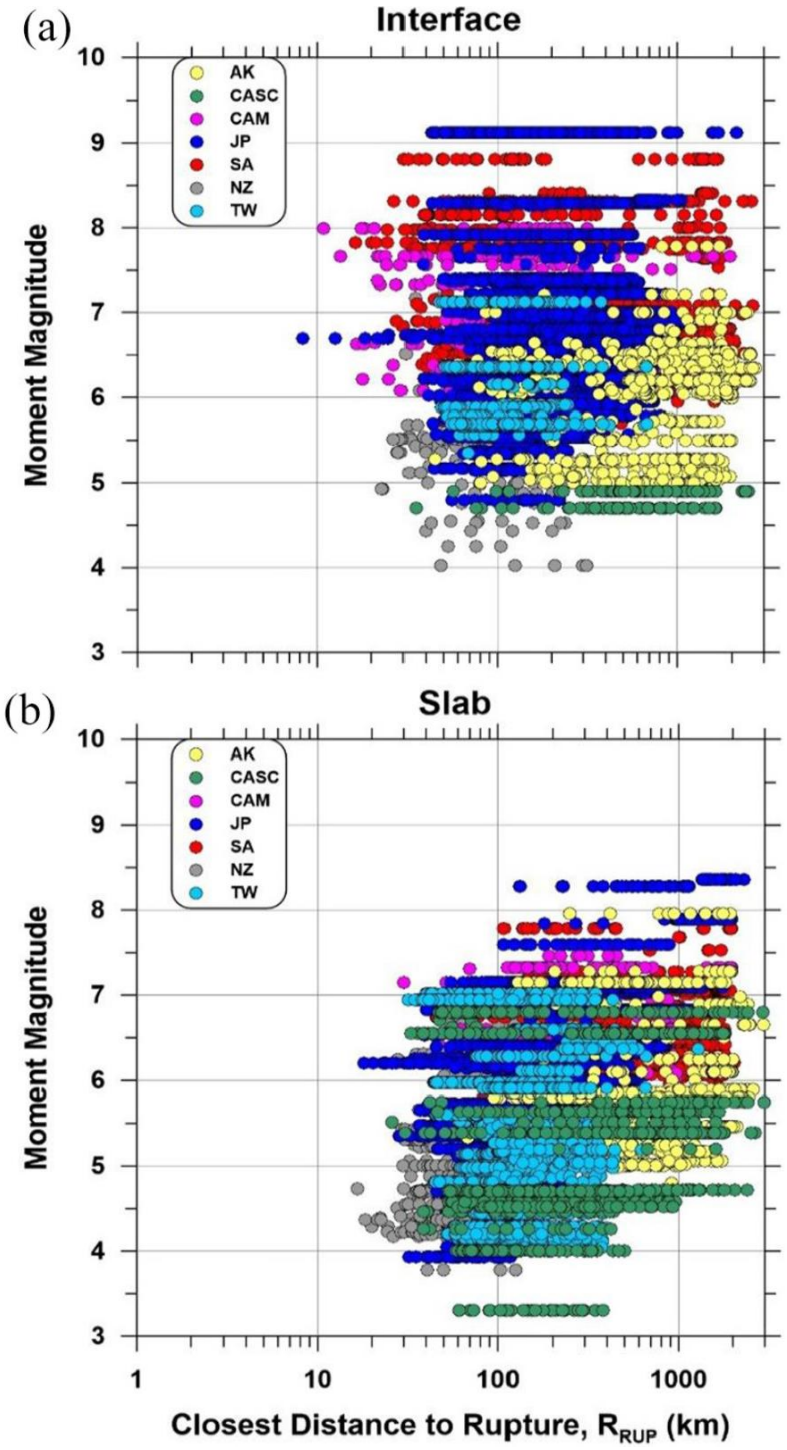

Figure 1.7 Distribution in magnitude-rupture distance space of recordings by region from (a) 360 interface events and (b) 383 intraslab events that pass screening criteria described later in Chapter 2. Adapted from Bozorgnia et al. (2022).

The subduction ground motion database developed during the NGA-Sub project is the most comprehensive database assembled for subduction zones worldwide. Many other regions are known to have subduction zone earthquakes, but are not represented in this database (e.g., Indonesia, Greece, Calabria/Italy). These omissions were not accidental (the NGA-Sub team was aware of the significance of subduction earthquake hazards). However, data from these additional regions was not incorporated into the database either because the NGA-Sub team anticipated not having ready access to sufficient data to benefit the project or they anticipated that the necessary data simply were not available.

The ground motion modeling work undertaken in NGA-Sub improved upon prior work in the following respects:

1. The underlying NGA-Sub models, against which regional effects are to be evaluated, are based on a much larger database than all prior regional studies (approximately 71,000 recordings from 2000 events).
2. The underlying models consider "deterministic" features related to slab geometry (Ji and Archuleta, 2018; Campbell, 2020), which impact the scaling of ground motions with magnitude.
3. Regional adjustments are applied to these relatively robust global models (when the amount of data allows it), which operates more effectively over a broad parameter space. For instance, global NGA-Sub GMMs have been customized for specific regions (e.g., Japan, Taiwan).

In the case of the Central America and Mexico region, NGA-Sub GMMs have not been regionalized because of the limited amount of data at the time of producing the models, i.e., these are pure global models. This highlights the need that exists in this region to regionalize these models and improve their performance.

1.4 RESEARCH OBJECTIVES AND SCOPE

The research presented in this dissertation is broadly related to database development and ground motion characterization for subduction zone earthquakes. Initially, a considerable part of my work was focused on the characterization of the source and path parameters for subduction zone earthquakes around the world, as part of the NGA-Sub project database development. As mentioned previously, NGA-Sub involved the collaboration of a large number of investigators and truly represents a group effort. However, the aspects of the project that are presented here represent work that I was mainly responsible for performing under the direction of my advisor, with review and comments from many other members of the broader NGA-Sub team. My work for NGA-Sub also examined site parameters and ground motion recording sites for specific regions in South America (Chile). In summary, I had a critical role in developing the source and path database for NGA-Sub, which is reflected by my first-authorship of the related chapter in the data report (Contreras et al., 2020) and the subsequent journal paper describing source and path metadata (Contreras et al., 2022). Moreover, I undertook work to assign site parameters for ground motion recording sites in Chile. The initial work on this topic (Contreras et al., 2018), which used a limited dataset of V_S profiles in Chile, is incorporated into the NGA-Sub site table (Ahdi et al. 2022). In this dissertation that database is expanded and improved models for predicting site parameters are provided.

The subsequent stage of my Ph.D. work has focused on ground motion characterization of subduction zones with an emphasis on Central America and Mexico (CAM). This work builds upon the NGA-Subduction database and GMMs to investigate regional source, path, site, and ground motion dispersion effects in CAM.

There is a need to validate NGA-Sub GMMs relative to "new data" (i.e., data not used in the GMM development) and test if they work appropriately when applied in different regions. Using data from the CAM region, I have investigated trends of NGA-Sub GMMs residuals with respect to different variables, including: source parameters (e.g. magnitude scaling), path effects (e.g. distance attenuation, backarc regions), and site effects (e.g. V_{S30} scaling, basin effects, site predominant period). Regional adjustments to the NGA-Sub GMMs for the studied CAM region are proposed, when supported by the data. Additionally, the variability of the computed residuals has also been analyzed.

The first task undertaken for the CAM-focused research was to extend the NGA-Sub database in two ways: (1) adding new ground motion data and developing associated source, path, and site metadata from three large magnitude events that occurred in Mexico in 2017 and 2018, (2) developing source, path, and site metadata for ground motions already included in NGA-Sub database, which significantly increased the amount of data for this region. The enhancement of NGA-Sub database for Mexico to support ground motion research in Latin America has been carried out in collaboration with the research group of Prof. Juan Mayoral at the Institute of Engineering of the National Autonomous University of Mexico (UNAM) and Prof. Xyoli Perez-Campos at the Institute of Geophysics at UNAM. Dr. Perez-Campos also serves as the head of the

National Seismological Service (SSN) in Mexico from 2014 to 2021. This collaboration has greatly facilitated the access to and interpretation of ground motion data and associated source, path, and site metadata.

Second, the performance of a CAM-regionalized global NGA-Sub GMM (Parker et al., 2022; Pea22) has been analyzed. For the CAM region, Pea22 regionalize the model constant term (c_0) and anelastic attenuation term (a_0). The V_{S30}-scaling term (s_2), which is regionalized for many other regions worldwide, was not regionalized for CAM due to limited ground motion data and relatively low quality V_{S30} estimates at ground motion sites.

For the source and path models (which are regionalized), I have evaluated the performance of the existing model with the aim of seeing whether adjustments to the regional parameters are needed. In the case of anelastic attenuation, regional variations are commonly observed due to variable crustal properties that lead to different rates of anelastic attenuation of high-frequency components of ground motion in different regions, both in forearc and backarc areas. Differences between forearc and backarc attenuation have been observed elsewhere (mainly in Japan: Ghofrani and Atkinson, 2011; Skarlatoudis and Papazachos, 2012; and Cramer and Jambo, 2020), but were not examined in Mexico by Pea22. As part of the present work, I have evaluated whether different anelastic attenuation parameters are justified by the Mexico data.

Another regional effect is related to site response. These regional effects manifest in two forms: (1) variable scaling relationships between ground motion amplitude and V_{S30} (i.e., s_2 parameter in Pea22); and (2) variable levels of site-to-site variability in ground motions. In addition to these regional effects, local site response effects have been studied. One example of a local site

response effect is basin structure, which was investigated in the NGA-Sub project for specific basins in Japan and Cascadia (Pacific Northwest). In this research, I consider basin effects in Mexico City, which is a well-known case because of the large site amplification observed due to its unique geologic and geotechnical characteristics.

The broad objective of this dissertation research is to better understand regional effects in the Latin America region and to produce regional adjustments to NGA-Sub GMMs to account for these effects. These adjusted GMMs will significantly improve upon current local models which rely on much more limited data sets. The approach taken in Central America and Mexico could be repeated for other regions in Latin America (Chile), once new ground motion data and associated metadata are developed.

1.5 OUTLINE OF THE THESIS

Chapter 2 of this dissertation describes the characterization of source metadata for the NGA-Sub database. This chapter is part of Chapter 4 of a report on the NGA-Sub database (Contreras et al., 2020), subsequently modified for a journal paper (Contreras et al., 2022). Section 2.5 has been extended with respect to the published material to include additional information regarding earthquakes with finite-fault models in NGA-Sub.

Chapter 3 of this dissertation describes path parameters characterization for use in NGA-Sub project along with the quality assurance procedures carried out to check accuracy and consistency of the database. This chapter is part of Chapter 4 of a report on the NGA-Sub database (Contreras et al., 2020), subsequently modified for a journal paper (Contreras et al., 2022). Section 3.2 has been extended with respect to the published material to include a brief discussion regarding

site-to-source distances uncertainty. Additionally, Section 3.4 includes now a summary of the path attributes in terms of percentage of path in the forearc and backarc regions.

Chapter 4 summarizes the main efforts to develop global databases and GMMs previous to the NGA-Sub project (Section 4.2). Additionally, considering the emphasis of this dissertation on subduction zones in Latin America, Section 4.3 focuses on summarizing local and regional databases, along with associated GMMs, for subduction zones in Central America and Mexico (CAM) and South America (SAM). This includes local databases and GMMs for specific countries in Latin America (Mexico, Chile, and others), along with regional databases and GMMs for Central America and South America. Local models for individual countries outside Latin America (e.g., Japan, Taiwan) are also presented for reference.

Chapter 5 describes an expansion of the NGA-Subduction (NGA-Sub) database for the Central America and Mexico (CAM) region. The first area of improvement was to develop source, path, and site metadata for events already included in the NGA-Sub database but for which critical event type classifications (interface, intraslab, shallow crustal, or outer-rise) were not made. Absent those classifications, these events were not used for model-building in NGA-Sub. This applies to events with magnitudes below **M**6 in the Central America and Mexico region. The second area of improvement was to add data for new events that were not available at the time ground motion recordings were compiled for NGA-Sub or from events that occurred too late to be considered. This task involves ground motion data processing and development of source, path, and site metadata. This applies mainly to the two large-magnitude intraslab events that occurred in Mexico in September 2017 and one interface earthquake that occurred in February 2018. Most

of the work presented in this chapter is focused on the new data from Mexico, considering their importance in terms of earthquake magnitude and the availability of information through our UNAM collaborators.

Chapter 6 describes the residual analyses carried out to investigate the performance of an NGA-Sub GMM in the Central America and Mexico region, with an emphasis on Mexico. This chapter presents the following:

- Computation of residuals relative to one available NGA-Sub model (Parker et al., 2022), using processed ground motion data and applicable metadata.

- Partitioning of residuals using mixed effects regression techniques, to separate systematic effects of source and site from other effects.

- Investigation of observed trends in source terms (event terms) with source parameters (magnitude, hypocentral depth) to evaluate whether adjustments to the regional constant term is needed or other adjustments should be considered.

- Investigation of observed trends in within-event residuals with distance to evaluate whether adjustments to the regional anelastic term is need and whether back-arc effects are present.

- Investigation of observed trends in site terms with V_{S30} using data outside of Mexico City to evaluate whether a CAM-specific V_{S30}-scaling parameter is needed.

- Using the data in the Valley of Mexico, evaluate three options for characterizing the variations of site response across the region: (1) based on V_{S30} alone; (2) based on currently

established zones having different site conditions; and (3) based on basin depth and HVSR-based site period, potentially in combination with V_{S30}. Identify the preferred model for application.

- Analysis of dispersion properties of residuals to study path-to-path and site-to-site variabilities and their potential differences from global models (Pea22).

Chapter 7 summarizes future research related to ground motion data analysis for subduction zones in Latin America, that were not fully considered in this dissertation. In particular: (1) Replicate the approach taken for Mexico utilizing new ground motion data obtained in Chile, (2) Investigate basin effects in Chile (Concepcion, Viña del Mar-Valparaiso, Santiago), (3) investigate source uncertainty and associated distance uncertainty and its impact on GMMs.

2 GLOBAL DATABASE OF SUBDUCTION ZONE SOURCE PARAMETERS

The main contents of this chapter and Chapter 3 are taken from a part of Chapter 4 of a report on the NGA-Sub database (Contreras et al., 2020), subsequently modified for a journal paper (Contreras et al., 2022). In this chapter, I describe the source parameters characterization for use in NGA-Sub project. The NGA-Sub project involved many people and truly represents a group effort. However, the portions of Contreras et al. (2020, 2022) that are reproduced here represent work that the author was mainly responsible for performing, with review and comments from others. Portions of the aforementioned documents that other NGA-Sub researchers led are not reproduced here. The organization, formatting, and numbering of the different sections were adjusted for this document. Section 2.5 has been extended to include additional information regarding earthquakes with finite-fault models in NGA-Sub.

2.1 INTRODUCTION

The Next Generation of Ground-Motion Attenuation for Subduction zones (NGA-Sub) project relational database (Mazzoni et al., 2022) contains ground-motion time series, intensity measures, and supporting metadata on source, path, and site parameters that are used in the development of ground-motion models (GMMs). The relational database contains 20 tables, nine of which are related to source parameters and two of which are related to path parameters; the development of the former nine tables is the focus of this chapter. The nine tables not directly related to source and

path parameters are described in Mazzoni et al. (2022) (ground motions) and Ahdi et al. (2022) (site and station metadata). Source parameters that are directly used in GMM development are moment magnitude (**M**), event type (interface, intraslab, shallow-crustal, outer-rise, etc.), event classification (i.e., mainshock/aftershock designations in the form of Class 1 or 2), hypocentral depth, depth to top-of-rupture, and event location in forearc or backarc regions. Path parameters that are used are rupture distance (R_{rup}), the maximum rupture distance that should be considered for a given data provider and event to avoid sampling bias (R_{max}), and the portion of the source-to-site path in forearc and backarc regions (as applicable). Other distance metrics not directly used in NGA-Sub GMMs are also provided (described in Section 3.2).

The procedures developed and applied to populate the nine source tables are described here. This information is compiled for events with ground-motion recordings obtained in seven regions affected by subduction-zone earthquakes world-wide (Figure 2.1): the Pacific Northwest region of North America (referred to here as Cascadia; CAS), Alaska (ALK), Japan (JPN), Taiwan (TWN), New Zealand (NZL), South America (SAM), and Central America and Mexico (CAM).

Following this introduction, the general locations and characteristics of events in the database are presented for all regions. The earthquake catalog for NGA-Sub is described, including compiled source parameters, procedures used to select moment tensor-related parameters (hypocenter location, seismic moment, strike, dip, and rake angle), and the development of rupture surface parameters (along-strike length, down-dip width, and depth to top-of-rupture) for events with and without published rupture surface models. This chapter concludes by presenting a statistical summary of the database with respect to event attributes.

2.2 OVERVIEW OF EVENTS

As described in the *Introduction*, NGA-Sub sources are organized in seven major regions that are illustrated in Figure 2.1: CAS, ALK, JPN, TWN, NZL, SAM, and CAM. Figure 2.1 also shows the main tectonic plates and plate boundaries as defined in a digital model (Bird 2003); red lines mainly indicate classical oceanic-beneath-continental subduction boundaries whereas black lines indicate other plate boundaries. The distribution of data among these regions is non-uniform, with some regions being especially data-rich in events (JPN, SAM) or recordings (JPN), and others being data-sparse (CAS).

A key aspect of the source parameters is the classification of each earthquake into one of four types: interface, intraslab, shallow crustal, or outer-rise. While the NGA-Sub project focuses on subduction-zone events (i.e., interface and intraslab), there is an important number of shallow crustal events and a small number of outer-rise events. The presence of these events in the database is a byproduct of the manner in which the database was developed; ground motion recordings were collected in the seven study regions in Figure 2.1 without establishing *a priori* earthquake type. Once the data had been collected and processed, instead of discarding data from non-subduction sources, it was retained and flagged based on the event-type.

Figure 2.2 presents earthquake locations from the NGA-Sub database in the Alaska region differentiated by magnitude and event type. Earthquakes are generated by subduction of the north-west dipping Pacific Plate beneath the North American Plate. As shown in Figure 2.2, the plate boundary is immediately south of the Aleutian Island chain and about 330 km south of mainland Alaska in the vicinity of Anchorage.

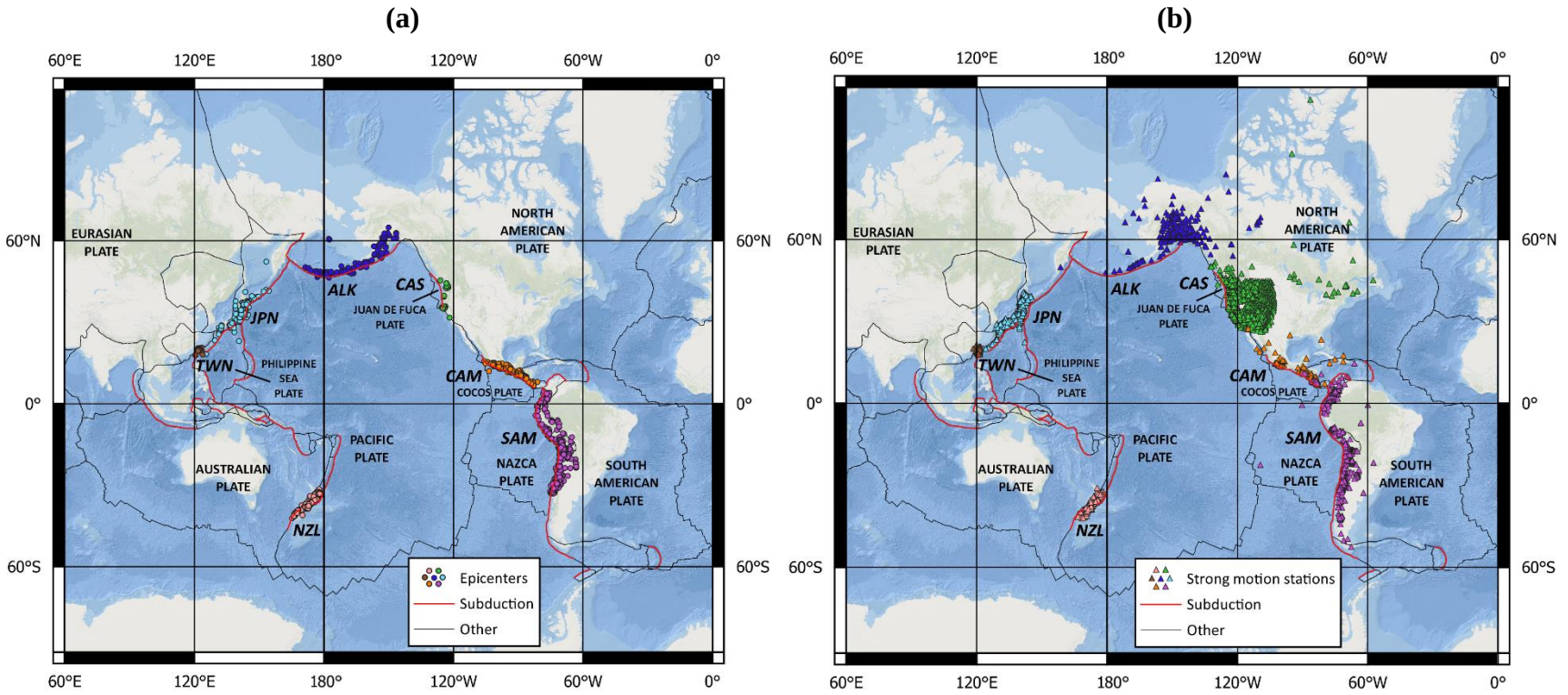

Figure 2.1 Locations of (a) epicenters and (b) strong motion recording stations in the NGA-Sub database. Regions are indicated by color of the epicenters and stations and labeled as ALK (Alaska), CAS (Cascadia), CAM (Central America and Mexico), JPN (Japan), NZL (New Zealand), SAM (South America), and TWN (Taiwan).

Along the Aleutian Island chain, a mixture of event types occurs, but most events are interface, whereas further to the east the available events are predominantly intraslab. The largest interface event is the 2003 **M**7.78 Rat Islands earthquake, and the largest intraslab event in the eastern region is the 2016 **M**7.15 Iniskin earthquake. The 2018 **M**7.1 Anchorage earthquake, while not included in the NGA-Sub database (because it occurred after the 2016 cutoff applied in the project, as described further below), is also in the eastern part of the subduction zone.

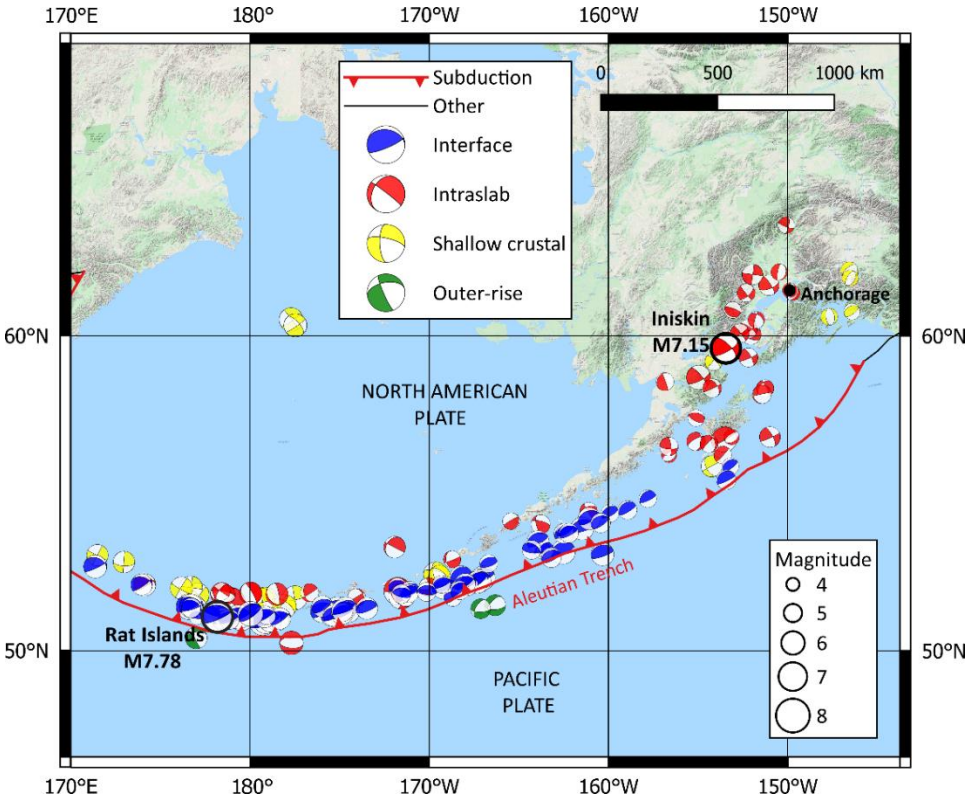

Figure 2.2 Epicentral locations of earthquakes with recordings in Alaska.

Figure 2.3 presents the earthquake locations from the NGA-Sub database in Cascadia. Earthquakes are generated by subduction of the east-dipping Juan de Fuca Plate beneath the North American Plate. As shown in Figure 2.3, the plate boundary is approximately 60-140 km west of

the coastline in Oregon and Washington. There are three event clusters. Starting from the south near Eureka, California, the database contains a series of shallow crustal and intraslab earthquakes with a magnitude range of 4.26-7.22. There are few events between the Eureka region in the south and the Seattle and Vancouver areas to the north, with only two interface events in the database west of Eugene with magnitudes of 4.7 and 4.9. Events in the Seattle-Vancouver regions are intraslab, with magnitudes ranging from 3.3-6.8. The largest event in the NGA-Sub database for Cascadia is the 2001 **M**6.8 Nisqually (Washington) intraslab earthquake.

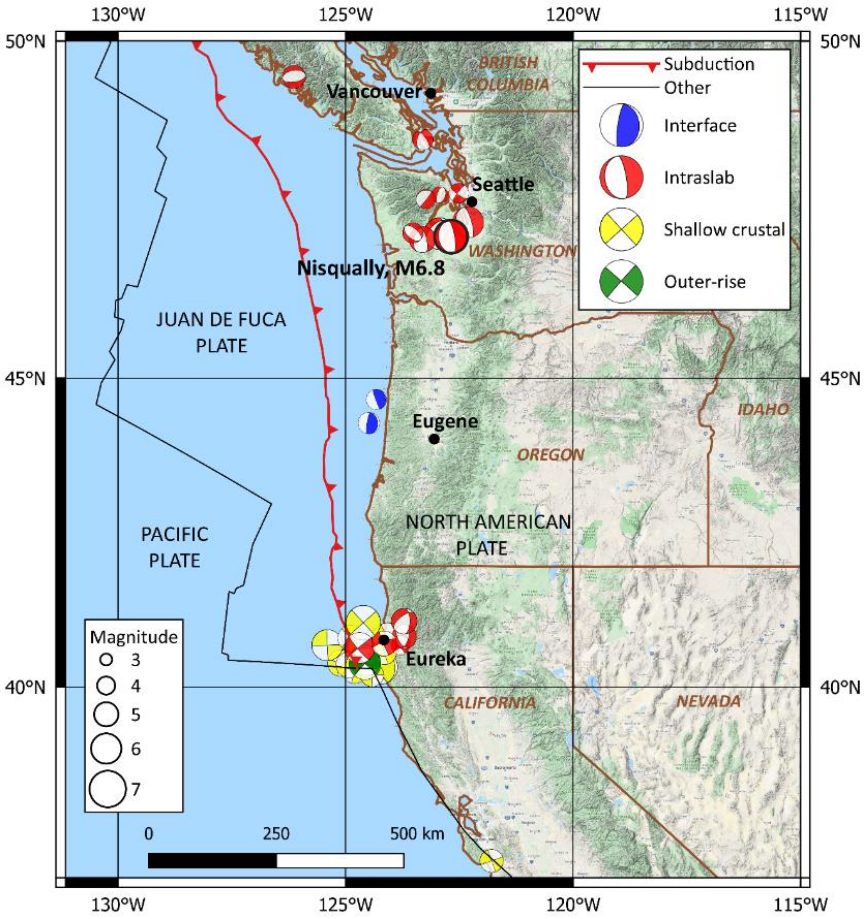

Figure 2.3 Epicentral locations of earthquakes with recordings in Cascadia.

Figure 2.4 presents the locations of earthquakes included in the NGA-Sub database in the Central America and Mexico region. Subduction earthquakes are generated in Central America and Mexico by subduction of the north-east-dipping Cocos Plate beneath the North American Plate, the Caribbean Plate, and the Panama Plate. The small Rivera Plate, north of Cocos, also subducts beneath the North American Plate. As shown in Figure 2.4, the plate boundary is approximately 30-170 km southwest of the coastline. Significant numbers of interface and intraslab events occur throughout this region. However, the largest interface events are clustered in the northwest sector, including the 1985 **M**7.99 Michoacan (Mexico) earthquake. The largest intraslab event in the NGA-Sub database is the 1999 **M**7.46 Oaxaca (Mexico) earthquake. Two relatively recent large events occurred in Mexico in September 2017: the September 8, 2017 **M**8.27 offshore Chiapas earthquake and the September 19, 2017 **M**7.18 Puebla earthquake. These earthquakes are not currently part of the NGA-Sub database. Each produced substantial numbers of recordings and will be included in future updates. Chapter 4 describes one such update for Central America and Mexico.

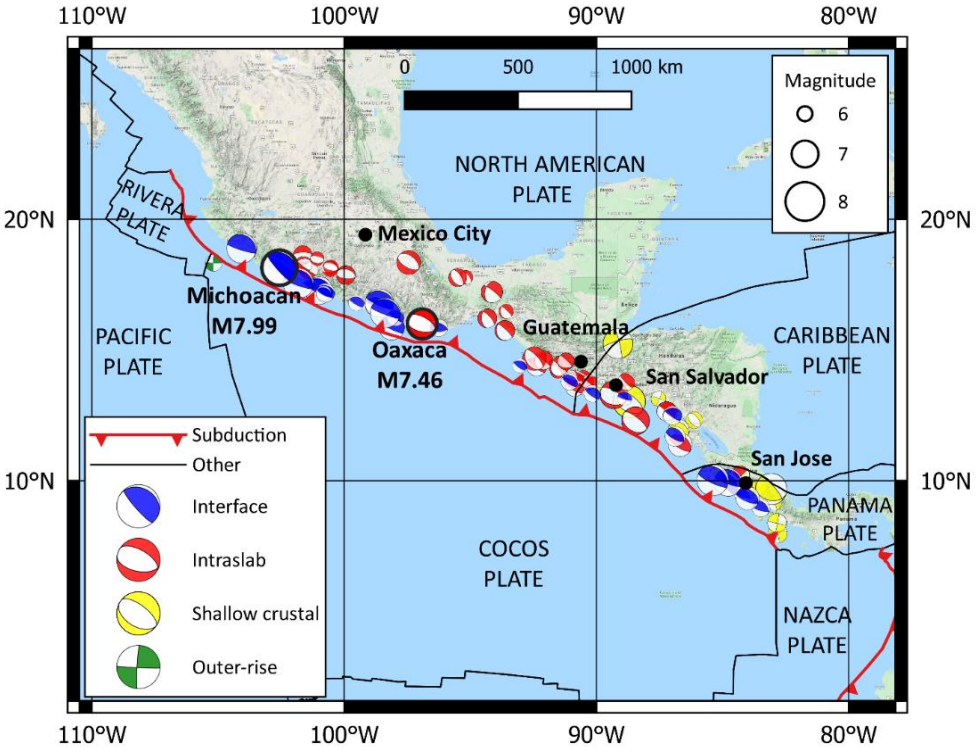

Figure 2.4 Epicentral locations of earthquakes with recordings in Central America and Mexico.

Figure 2.5 presents earthquake locations from the NGA-Sub database in Japan. Because of the large number of earthquakes in Japan and the complexity of the tectonics, Figure 2.6 and Figure 2.7 show more detailed views of the northern and southern sectors, respectively. In the north, the northwest-dipping Pacific Plate subducts beneath the Okhotsk Plate (an extension of the North American Plate) at the Japan Trench. To the west, in the Sea of Japan, a convergent plate boundary occurs between the Okhotsk Plate to the east and the Amur plate to the west. Near the middle of the main island (Honshu), the Pacific Plate's western boundary bends south and east, and the Philippine Sea Plate subducts beneath Japan at the Nankai Trough.

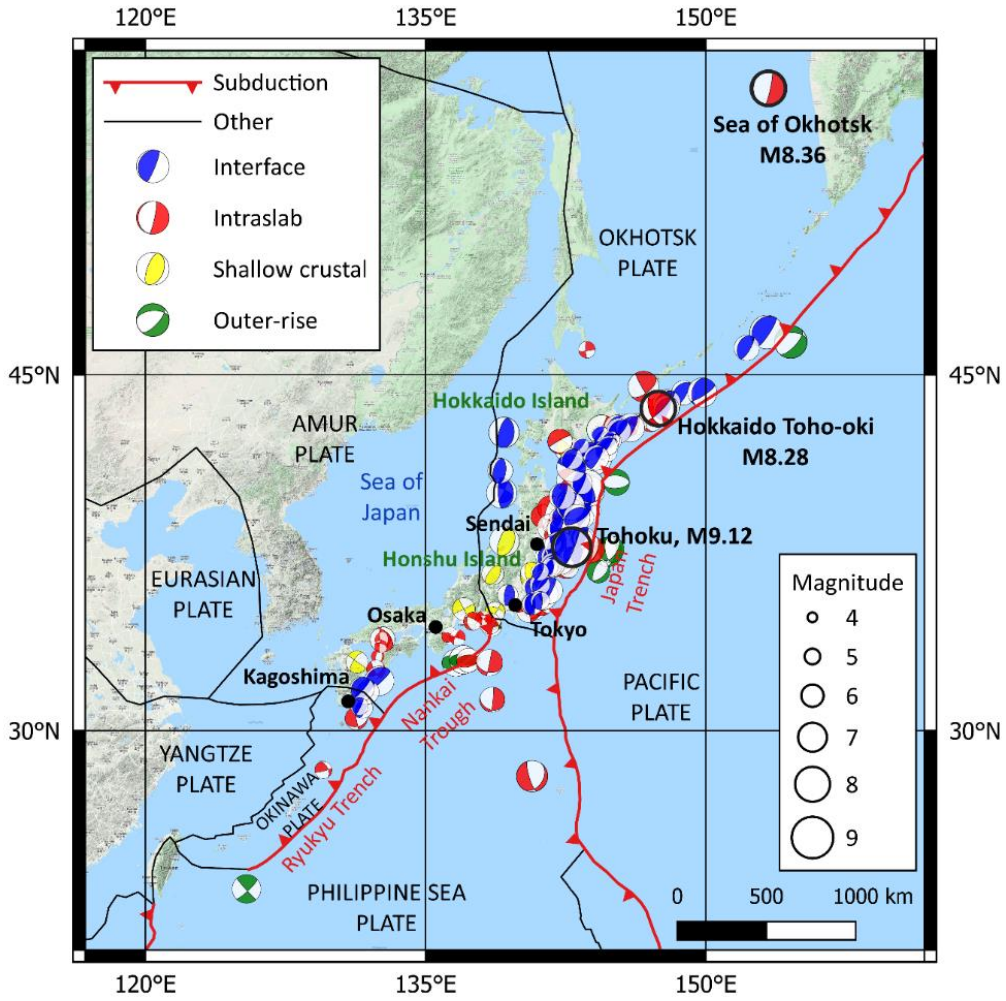

Figure 2.5 Epicentral locations of earthquakes with recordings in Japan.

The northern sector has many interface and intraslab events in the vicinity (and inboard of) the Japan trench, including the 2011 **M**9.12 Tohoku earthquake (an interface event). The largest intraslab earthquake in this region and proximate to Japanese islands is the 1994 **M**8.28 Hokkaido Toho-oki earthquake. As shown in Figure 2.6, interface earthquakes also occur west of the island at the convergent boundary in the Sea of Japan. As shown in Figure 2.7, the southern sector has

fewer events, with the region east of Osaka having primarily intraslab events, while the southern terminus of Honshu (near Kagoshima) has a series of interface and intraslab events.

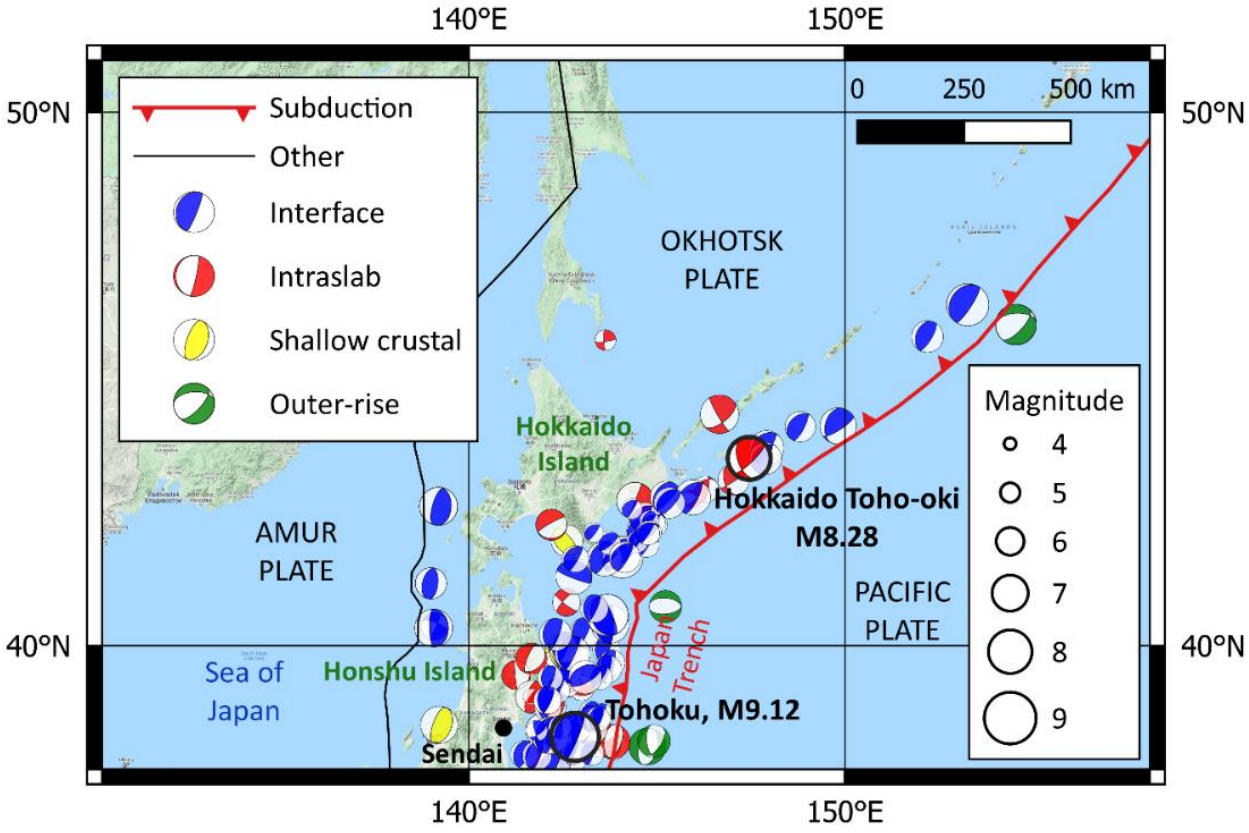

Figure 2.6 Epicentral locations of earthquakes in Northern Japan.

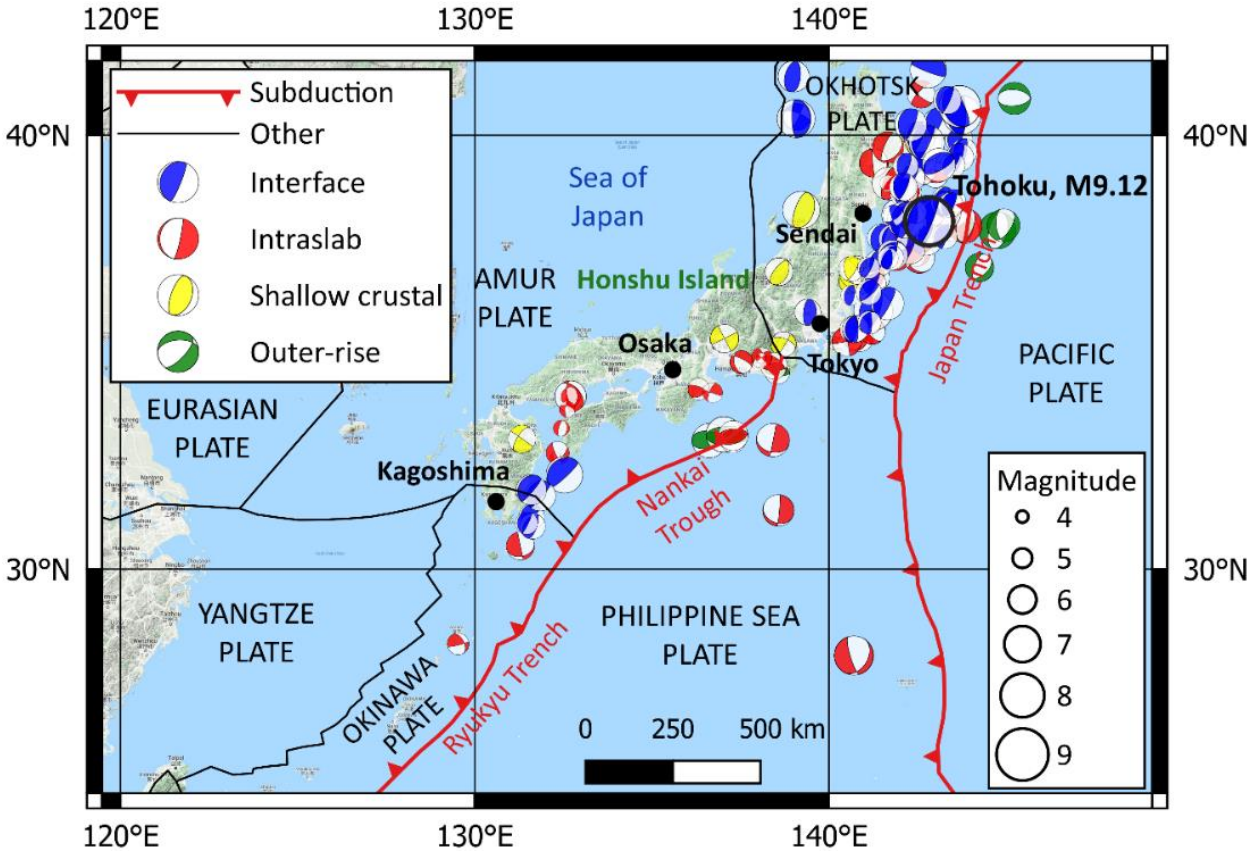

Figure 2.7 Epicentral locations of earthquakes in Southern Japan.

Figure 2.8 presents the locations of earthquakes included in the NGA-Sub database in the New Zealand region. The occurrence of subduction earthquakes in New Zealand is associated with its position across the boundary between the Pacific Plate to the southeast and the Australian Plate to the northwest, with the transform Alpine fault passing across the South Island. To the east of the North Island is the Kermadec Trench. The subducting Pacific Plate has produced many intraslab earthquakes in this northern sector. To the west of the southwest end of the South Island is the Puysegur Trench, where the Australian Plate subducts beneath the Pacific Plate. This Fiordland region has primarily produced a series of interface events. The largest interface and

intraslab events are the 2009 **M**7.81 Fiordland earthquake and the 1988 **M**6.69 Te Anau earthquake, respectively; both located in the South Island of New Zealand.

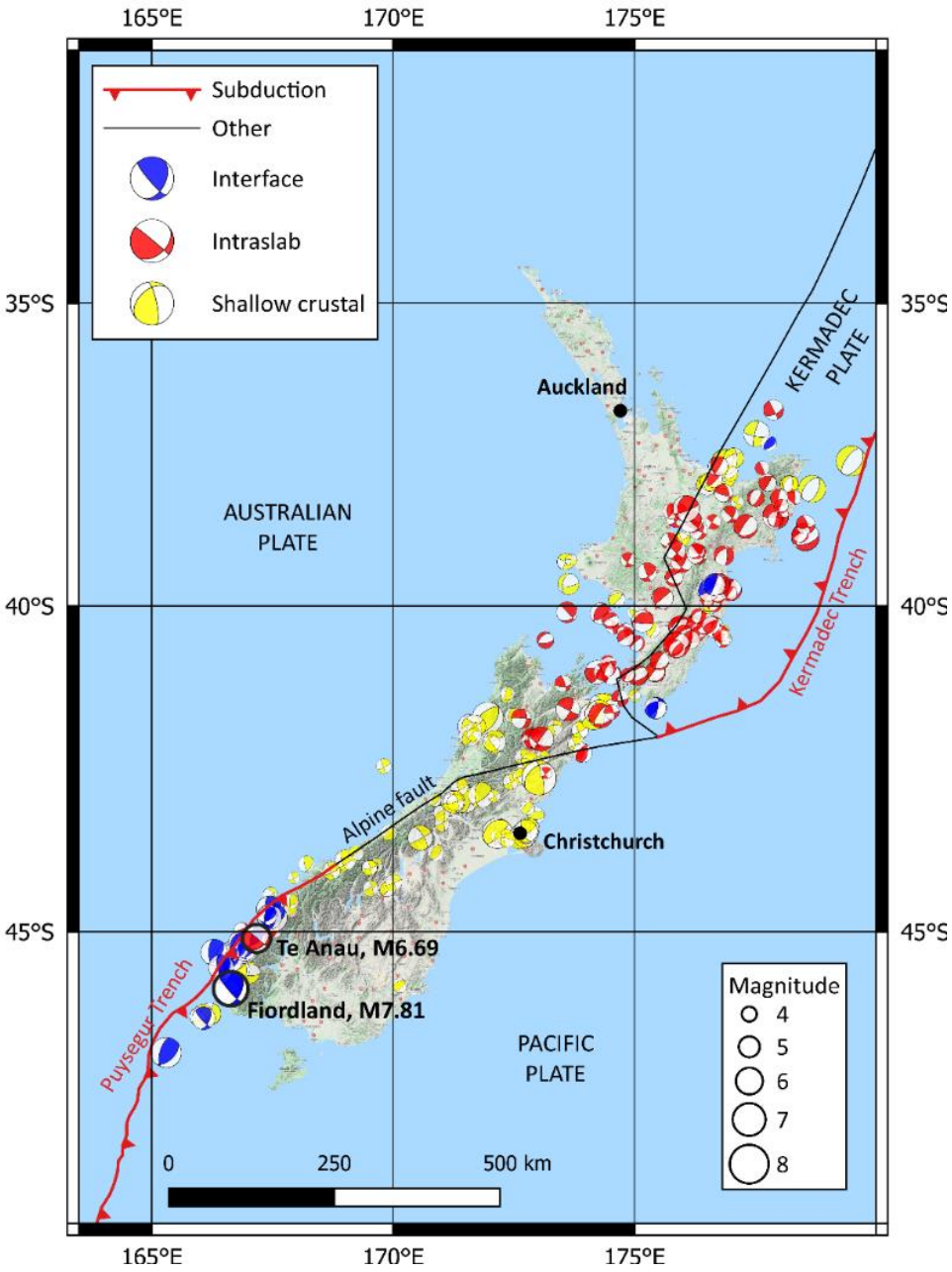

Figure 2.8 Epicentral locations of earthquakes with recordings in New Zealand.

Figure 2.9 presents earthquake locations from the NGA-Sub database in South America. Earthquakes are generated by subduction of the east-dipping Nazca Plate beneath the South American Plate at the Peru-Chile Trench, also called the Atacama Trench. The database contains many interface events located near the trench, as well as intraslab events located further east beneath the South American Plate. The interface events are most concentrated off the coast of Chile, and include the 1985 **M**7.98 Valparaiso and 2010 **M**8.81 Maule (Chile) earthquakes. There is a particular concentration of intraslab earthquakes near Antofagasta, including the 2005 **M**7.78 Tarapaca earthquake. Event concentrations are relatively sparse further north in Peru, Ecuador, and Colombia.

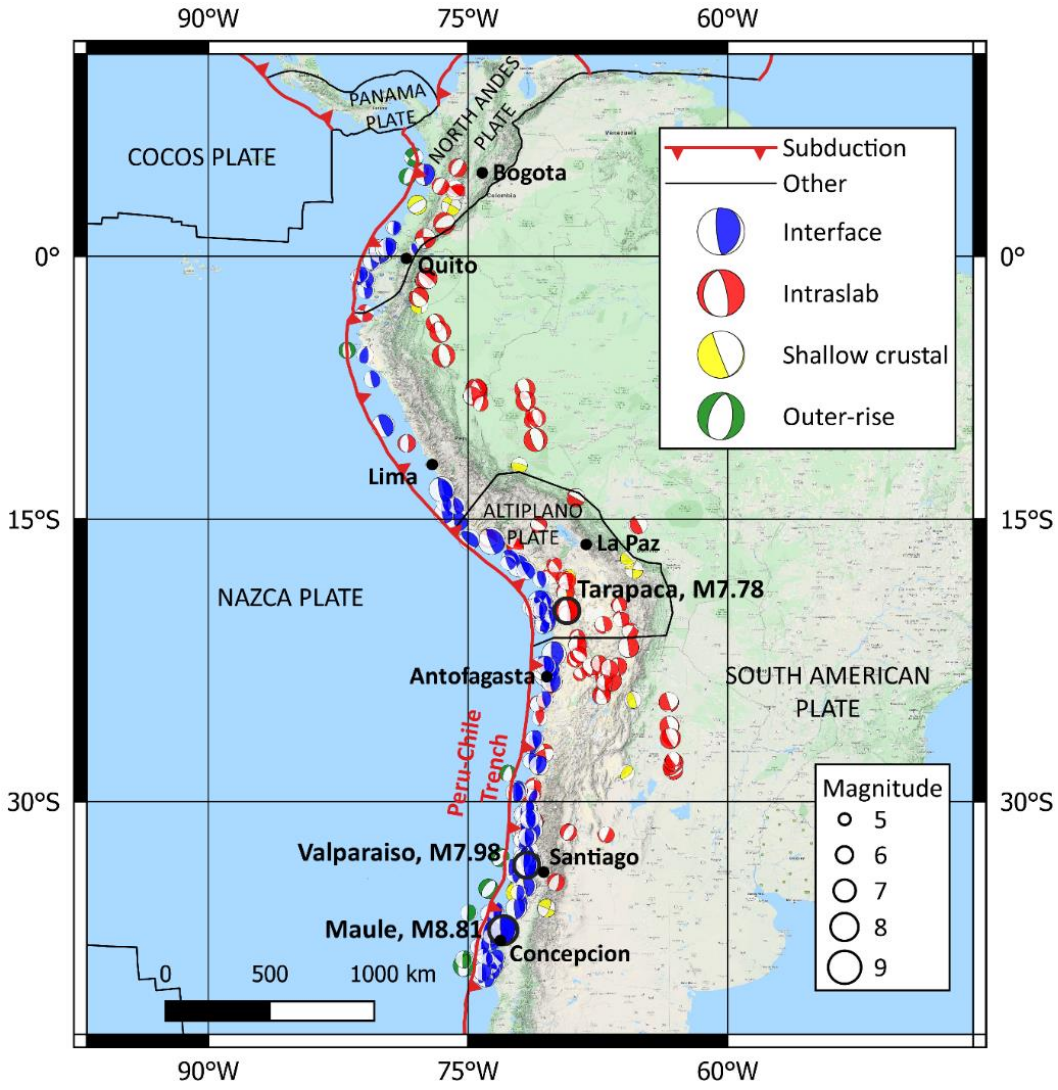

Figure 2.9 Epicentral locations of earthquakes with recordings in South America.

Figure 2.10 presents the locations of earthquakes included in the NGA-Sub database in the Taiwan region, with differentiation by magnitude and type of earthquake. Taiwan occupies a position amidst a complex series of plate boundaries, which give rise to a couple of atypical subduction zones. Because of this complexity, region specific studies were used to define some of the boundaries shown in Figure 2.10, which do not match the digital global model assembled by Bird (2003). The predominant boundary is convergent between the northwest-displacing Philippine Sea Plate to the southeast and the Yangtze Plate to the northwest, however, this

boundary has not produced earthquakes in the NGA-Sub database (shallow crustal earthquakes have occurred in this region that are in the NGA-West2 database). Rather the events are clustered near other plate boundaries northeast and south of the island.

Well northeast of Taiwan, the Philippine Sea Plate subducts beneath the Okinawa Plate at the Ryukyu Trench. As that boundary approaches Taiwan from the east, it transitions to a convergent boundary, but the subduction persists. This subduction terminates near the northeastern portion of Taiwan (Wu et al., 2009). As shown in Figure 2.10, interface subduction events occur immediately north of the convergent boundary, and intraslab events occur beneath much of the southwestern portion of the Okinawa Plate. The largest interface event in Taiwan, the 2002 **M**7.12 Offshore Hualien (Taiwan) earthquake, occurred in this region. The largest intraslab event in this region is the 2004 **M**6.59 earthquake with event ID 7000045.

In the south, the east-dipping Sunda Plate subducts beneath the Philippine Sea Plate. That boundary evolves into a convergent boundary from south to north but the subduction continues in the transition between southern Taiwan and north of the Sunda Plate (Malavielle et al., 2002). The database does not contain interface events in this region, but does include two intraslab events east of the boundary, including the 2006 **M**7.02 Offshore Pingtung (Taiwan) earthquake.

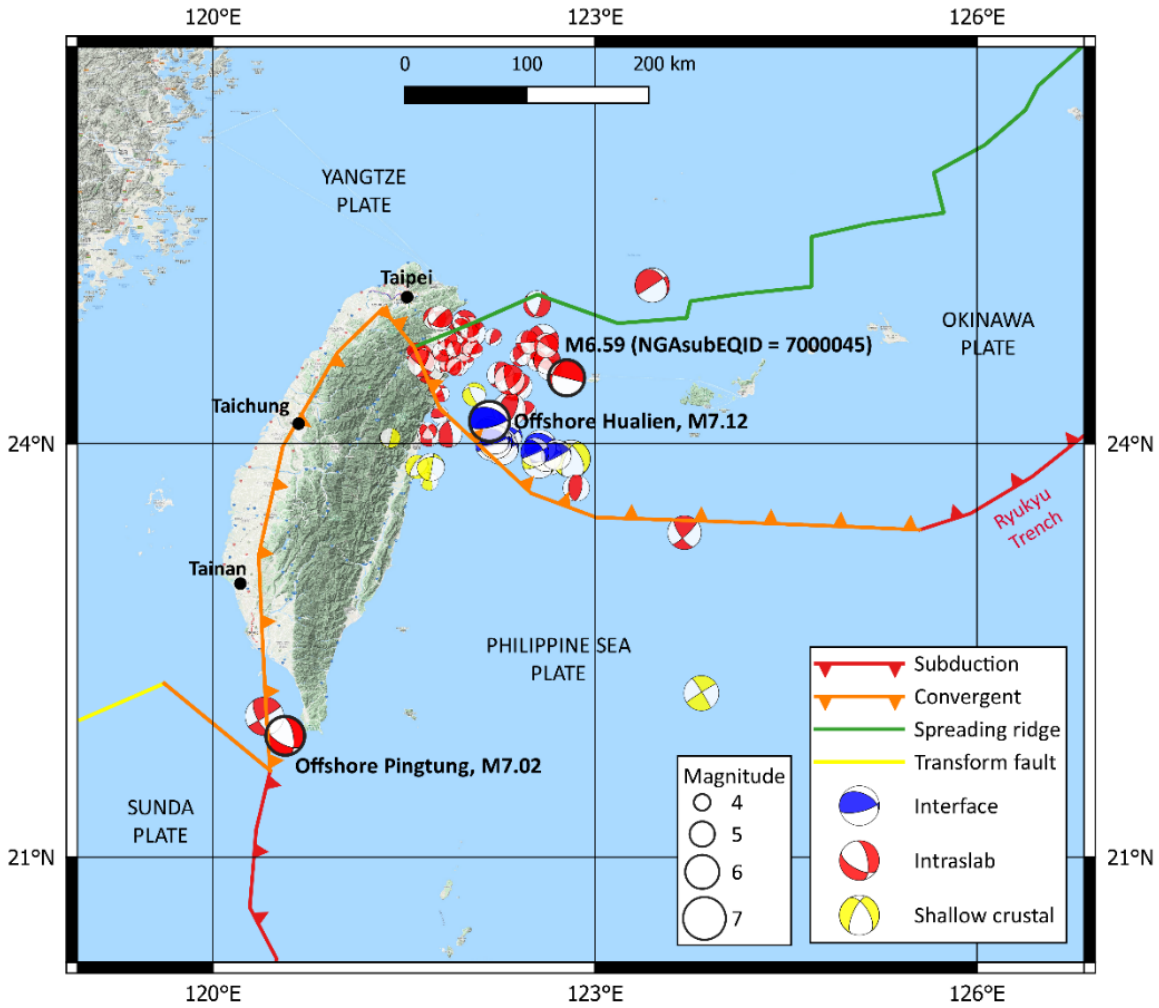

Figure 2.10 Epicentral locations of earthquakes with recordings in Taiwan. The central portion of Taiwan has many shallow crustal earthquakes that are not included in the NGA-Sub database.

It should be noted that there are a significant number of earthquakes included in the NGA-Sub database for which classification according to event-type (interface, intraslab, shallow crustal, or outer-rise) was not performed as part of the NGA-Sub project. As a results of these missing classifications, these events did not go through the quality assurance (QA) procedures described subsequently (Section 3.5), and therefore their source parameters may be less reliable and certain information may be missing.

Figure 2.11 shows the regions of South America and Central America and Mexico, with locations of both classified and unclassified events (most of the unclassified events are in these regions). As shown in Figure 2.11, the unclassified events have small magnitudes (**M**<6) and are in the same general locations as larger events that are included in the NGA-Sub database. The unclassified earthquakes by region are:

- 594 events with magnitudes **M**<6 in South America. Most of these earthquakes (61%) have only one or two recordings.
- 181 events with magnitudes **M**<6 in Central America and Mexico. 41% of these earthquakes have only one or two recordings.
- Three events with magnitudes **M**<5.2 in New Zealand.

The lack of event classification and application of QA procedures for these events was a simple matter of allocating limited resources elsewhere during the data compilation and refinement phases of the NGA-Sub project. Since publication of the NGA source parameters database (Contreras et al., 2020; Contreras et al., 2022), about 60 previously unclassified events that occurred in Central America and Mexico have been assigned an event-type, as described in Section 5.2. This subset of events was selected considering that each of these earthquakes produced at least five recordings at different ground-motion stations.

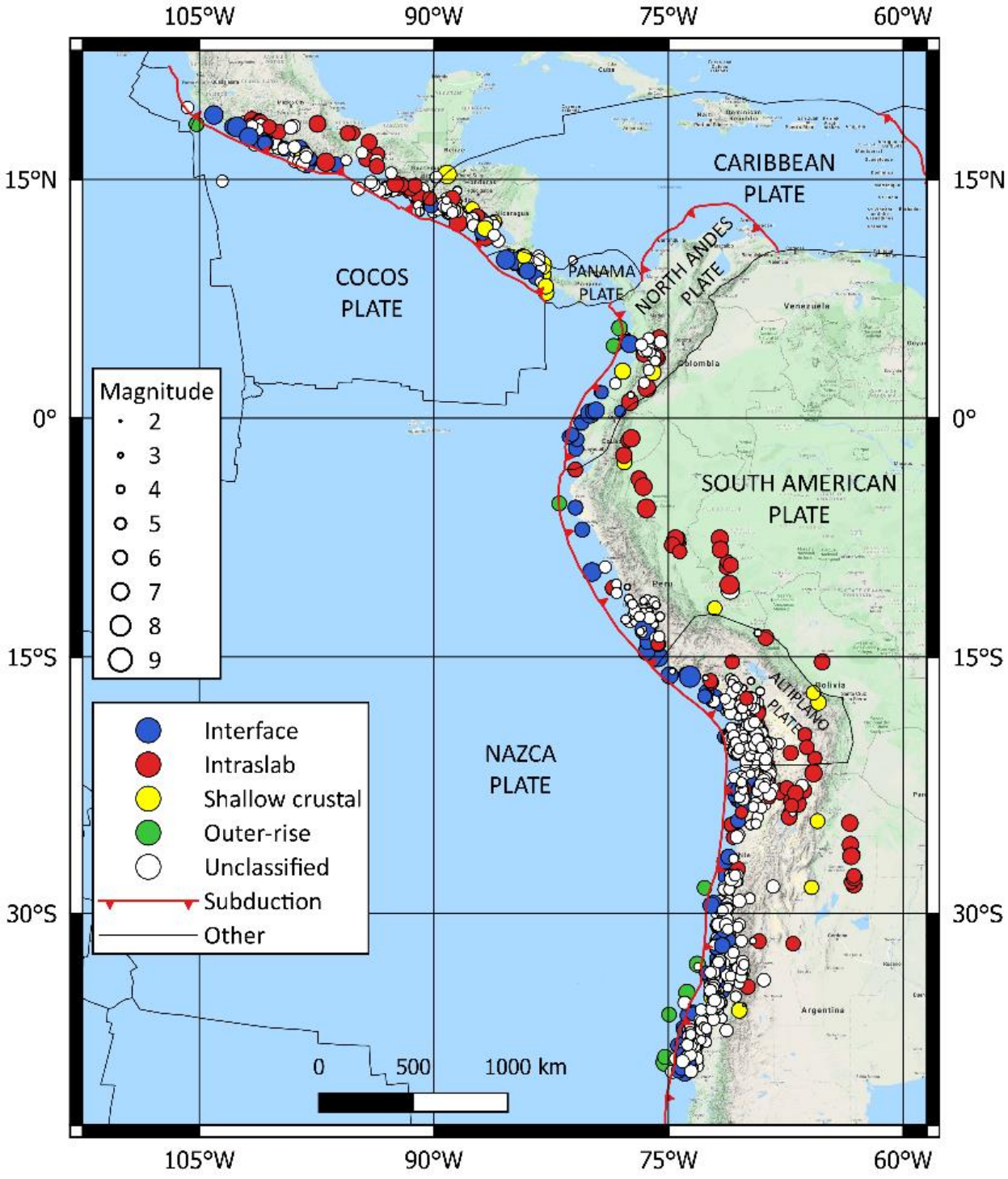

Figure 2.11 Event locations in CAM and SAM showing locations and magnitudes of classified and unclassified events.

2.3 GENERAL EARTHQUAKE CATALOG

2.3.1 Parameter Definitions

Earthquake information and source-related parameters that were collected from different sources or derived for the NGA-Sub database are origin date and time, seismic moment, moment magnitude (**M**), hypocenter location (latitude, longitude, and focal depth), and the following features illustrated in Figure 2.12:

- Location of the fault rupture plane (upper left corner when viewed from hanging wall) and number of rectangles used to model the rupture surface.
- Fault rupture plane dimensions: length (L), width (W), and area (A).
- Strike (ϕ), dip (δ), and rake (λ) angles of nodal planes.
- Depth to top of the fault rupture plane (Z_{TOR}).
- Fault type as either strike-slip, normal, reverse, reverse-oblique, or normal-oblique, as inferred from rake angle.
- Earthquake type as either interface, intraslab, shallow-crustal, or outer-rise.

The geometric parameters in the first four bullets define a rectangular rupture surface, which is sufficient to define the geometry of the ruptured fault in most cases. The development of finite-fault parameters is presented in subsequent sections. Whenever possible, the geometric and slip-direction parameters listed above are taken from published finite-fault models (FFMs), as

described in Section 2.4. When FFMs are not available, which is the case for most events, simulation procedures described in Section 2.5 are used to approximate finite-fault geometric parameters and associated computations of closest distance for ground-motion stations. Table 2.1 lists source parameters for 18 significant events, some of which are highlighted in Figures 2.2-2.10. The remainder of this section focuses on non-finite-fault source parameters.

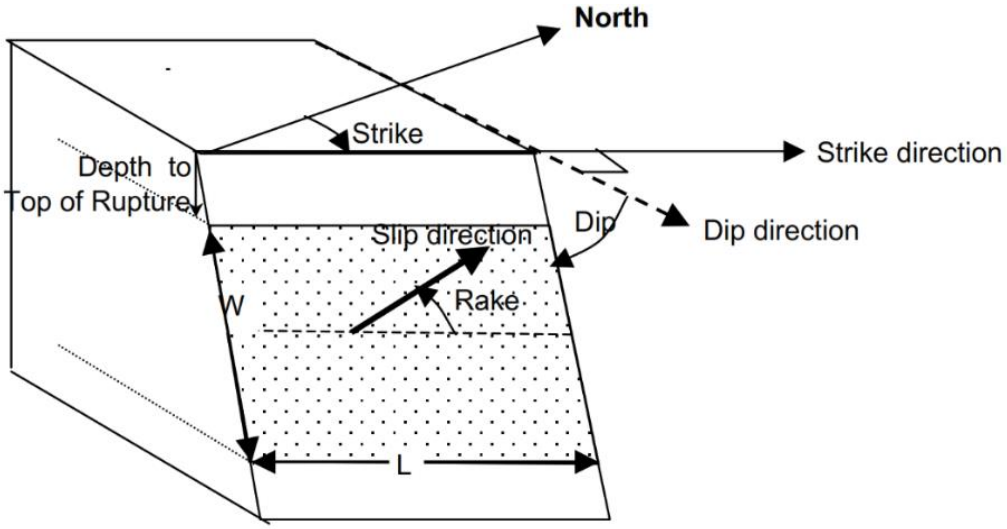

Figure 2.12 Schematic representation of the fault rupture plane (Ancheta et al., 2013). Convention of fault strike, dip, and rake follows that described in Aki and Richards (1980).

2.3.2 Parameter Selection Procedures

The procedures used to define magnitude, hypocenter location, fault type, and event type are described here. Within the relational database, these parameters appear in the *EventHypo* and *EventType* tables (Mazzoni et al., 2022), and are provided in electronic supplement Table ES-1 in Contreras et al., 2022.

Table 2.1 Example events from NGA-Sub database (highlighted in maps in Figures 2.2-2.10), showing compiled source parameters.

Region	NGAsub EQID	Earthquake name, Country/State	Date	M	Hypocenter location			Event-Type Flag (1)	FFM flag (2)	Number of rectangles	L (km)	W (km)	Ztor (km)	Strike (deg)	Dip (deg)	Rake (deg)	Source review flag (3)	# recs.
					Latitude (deg)	Longitude (deg)	Depth (km)											
ALK	1000002	Rat Islands, Alaska	2003/11/17	7.78	51.1965	178.1844	29.7262	0	1	1	120	140.4	5.61	280.4	18.8	121.9	0	6
	1000142	Iniskin, Alaska	2016/1/24	7.15	59.6531	-153.4457	129.4159	1	1	1	30	28	108.62	60	66	33	0	191
CAS	2000004	Nisqually, Washington	2001/2/28	6.8	47.1574	-122.6801	53.1749	1	1	1	24	21	46.13	350	70	-91	0	147
	2000009	1815881, Oregon	2004/7/12	4.9	44.2977	-124.4869	12.82	0	0	1	3.6	3.6	12.279	353	16	75	0	92
	2000011	1852721, Oregon	2004/8/19	4.7	44.6677	-124.3201	18.09	0	0	1	2.7	2.8	17.908	349	7	99	0	76
CAM	3000271	Michoacan, Mexico	1985/9/19	7.99	18.1814	-102.5691	16.2637	0	1	1	150	139	6	300	14	72	0	26
	3000201	Oaxaca, Mexico	1999/9/30	7.46	16.054	-96.907	40	1	0	1	69.9	32.3	32.582	300	49	-78	0	8
JPN	4000001	Tohoku, Japan	2011/3/11	9.12	38.1165	142.823	17.4965	0	1	3	482	186	8.65	200	12	88	0	1293
	4000219	Sea of Okhotsk, Russia	2013/5/24	8.36	54.8172	153.3558	608.1717	1	1	1	195	70	601	184	10	-98	0	48
	4000093	Hokkaido Tohu-oki, Japan	1994/10/4	8.28	43.711	147.457	27.459	1	1	1	60	70	18.1	160	40	30	0	30
NZL	5000179	Fiordland, New Zealand	2009/7/15	7.81	-45.8339	166.6363	20.9	0	1	1	100.23	100.23	8.76	27	33	154	0	27
	5000013	Te Anau, New Zealand	1988/6/3	6.69	-45.1	167.17	60	1	0	1	25	55	32.57	310	86	118	0	3
SAM	6000149	Maule, Chile	2010/2/27	8.81	-36.2089	-72.9587	30.4055	0	1	1	480	160	0.74	15	18	109.3	2	49
	6000323	Valparaiso, Chile	1985/3/3	7.98	-33.125	-71.61	40	0	1	2	222	135	6.4	5	20.4	97.2	0	27
	6000061	Tarapaca, Chile	2005/6/13	7.78	-20.03	-69.28	110	1	1	1	47.5	45	101.21	187	23	-73	0	30
TWN	7000044	Offshore Hualien, Taiwan	2002/3/31	7.12	24.1602	122.172	33	0	1	1	33	32	21.34	292	32	121	0	426
	7000048	Offshore Pingtung, Taiwan	2006/12/26	7.02	21.88703	120.56844	44.1	1	1	1	89.9	35	24.13	349	53	-54	0	458
	7000045	7418598, Taiwan	2004/10/15	6.59	24.470833	122.777833	88.02	1	0	1	18.7	23.5	84.756	200	17	6	0	439

(1) 'Event-type flag' is defined in Table 2.4 and refers to the event-type classification as interface, intraslab, shallow crustal, or outer-rise.

(2) 'FFM flag' indicates if the event has an available finite-fault model in the database (0 = event without model, 1 = event with model).

(3) 'Source review flag' is defined in Table 3.3 and refers to the Quality Assurance procedure applied to review the source parameters of each event.

(a) Magnitude

Moment magnitude is the magnitude scale used in NGA projects, including NGA-Sub. Whenever possible, moment magnitude is computed from seismic moment, M_0 (Hanks and Kanamori, 1977) as:

$$\boldsymbol{M} = \frac{2}{3} log\, M_0 - 10.7 \qquad (2.1)$$

Seismic moment (M_0) and/or hypocenter location was collected from:

- The Global Centroid Moment Tensor, CMT (Ekström et al., 2012),
- The National Earthquake Information Center (NEIC) at the United States Geological Survey (USGS),
- The Lamont-Doherty Cooperative Seismographic Network (LD) at Columbia University,
- The International Seismological Centre (ISC, 2019): A groomed version of the ISC catalogue was produced by Engdahl et al. (1998) and is referred to as the EHB catalogue. That catalogue was later expanded and improved by Engdahl et al. (2020) and is referred to as the ISC-EHB catalogue,
- The Duputel et al. W phase catalog, DUPUTEL (Duputel et al., 2012) at the University of Strasbourg,
- The International Data Centre (IDC) at the Headquarters of the Comprehensive Nuclear-Test-Ban Treaty Organization (CTBTO) in Vienna,
- In Alaska, the Alaska Earthquake Center (AEC), housed at the University of Alaska Fairbanks,

- In Cascadia, the Pacific Northwest Seismic Network (PNSN), housed at the University of Washington, and Natural Resources Canada (NRCAN),
- The Northern California Earthquake Data Center (NCEDC), housed at UC Berkeley,
- In Chile, the Chilean National Seismological Center (CSN), also referred as GUC (Department of Geophysics at the University of Chile),
- In Taiwan, the National Center for Research on Earthquake Engineering (NCREE) and the Broadband Array in Taiwan for Seismology (BATS),
- In Japan, the National Research Institute for Earth Science and Disaster Resilience (NIED) and the Japan Meteorological Agency (JMA).

Seismic moments from the CMT catalog were preferred because (1) they are derived from global recordings that sample more of the focal sphere and average out variations in radiation pattern, and (2) it provides between-region consistency. Global CMT was available for most events. Other catalogs were used when CMT estimates of M_0 were not available; Table 2.2 lists the catalogs considered by region in order of preference for the selected M_0. For eight earthquakes in Japan and ten in Cascadia with finite-fault models, the seismic moment was taken from the literature. For New Zealand, magnitudes were adopted directly from Van Houtte et al. (2017).

Seismic moment is not available for some older events (pre-1976 when the CMT catalog began) and events of small magnitude. In the NGA-Sub source database, 96% of **M**>6 events and 79% of **M**<6 events are based on seismic moment (considering only earthquakes with an event-type classification). For those events without a reported M_0 value, **M** was estimated from alternate magnitude scales. For such cases, the alternate scale (most often local or surface wave magnitudes,

M_L or M_S) is indicated along with the reported magnitude in the *EventHypo* table.

Table 2.2 Earthquake catalogs and published studies used to assign seismic moment and hypocenter location.

Region	Preferred Catalog (M_0)	No. events	Preferred Catalog (location)	No. events
Alaska	CMT	128	EHB / ISC-EHB	99
	ISC	2	ISC	33
			NEIC	2
			IDC	1
			Other studies: USGS (2003), USGS (2014), USGS (2016)	3
Cascadia	Adopted from NGA-West2	13	Adopted from NGA-West2	13
	NEIC	6	ISC	12
	CMT	3	Oppenheimer et al. (1993)	3
	Ichinose et al. (2006b)	3	Williams et al. (2011)	2
	Oppenheimer et al. (1993)	3	NRCAN	2
	NRCAN	2	PNSN	1
	Williams et al. (2011)	2	Ichinose et al. (2004)	1
	PNSN	1	Ichinose et al. (2006a)	1
	Ichinose et al. (2004)	1		
	Ichinose et al. (2006a)	1		
Central America and Mexico	CMT	79	EHB / ISC-EHB	56
	NEIC	1	ISC	23
			CMT	1
			Mendoza and Hartzell (1989)	1
			Mendoza (1993)	1
Japan	CMT	142	JMA	115
	NIED	10	JMA / Bai et al. (2014)*	16
	LD	1	NEIC	5
	Abe (1975)	1	ISC	2
	Hatanaka & Takeo (1989)	1	CMT	2
	Kanamori (1971)	1	SEVO (1996)	2
	Kikuchi & Fukao (1987)	1	NIED	1
	Shiba & Uetake (2011)	1	Other studies: Abe (1975), Atkinson and Macias (2009), Fukuyama and Irikura (1986), JMA (2012a), JMA (2012b), JMA / EIC (2003), JMA / HERP (2006), Koketsu et al. (2004), Nagai et al. (2001), Nakayama and Takeo (1997), Namegaya and Tsuji (2005), Shiba and Uetake (2011), Takeo and Mikami (1990), Takiguchi et al. (2011), Tanioka et al. (1995), Tsuchida et al. (1983), Yagi (2004), Yagi et al. (1998), Yamanaka (2005), Yamanaka and Kikuchi (2004)	21
	Takeo & Mikami (1990)	1		
	Yagi et al. (1998)	1		
	Yoshioka & Abe (1976)	1		
South America	CMT	210	CSN	107
	NEIC	3	EHB / ISC-EHB	69
			ISC	31
			NEIC	3
			Other studies: Delouis et al. (2010), Hayes (2016), Kuge et al. (2010), Lay et al. (2010), Lay et al. (2014), Melgar et al. (2016), Mendoza et al. (1994), Salichon et al. (2003), Schurr et al. (2012), Shao and Ji (n.d), Sladen (2007)	12
Taiwan	CMT	34	NCREE (2019)	75

Region	Preferred Catalog (M_0)	No. events	Preferred Catalog (location)	No. events
	NIED/BATS	15		
	BATS	8		
	DUPUTEL	4		
	NEIC	3		
	LD	1		

* For aftershocks of the 2011 Tohoku earthquake.

The converted moment magnitude is also provided using region-specific conversion relations. For Taiwan, Wu et al. (2016) relations were utilized. For Chilean earthquakes, alternate magnitude scales were obtained from the CSN. An adjusted version of the relations developed by Bastías and Montalva (2016) for M_L and by Leyton et al. (2009) for M_S and m_b were applied. These relations, shown in the following equations and presented in Figure 2.13 and Figure 2.14, were developed using only information from Chilean earthquakes. These correlations were developed for M_W whereas NGA-Sub uses **M**; accordingly, the intercept terms are increased by 0.033.

Modified from Bastías and Montalva (2016)

Z_{hyp} < 50 km: $\mathbf{M} = 0.915M_L + 0.524 \quad (\sigma = 0.26)$ (2.2)

Z_{hyp} > 50 km: $\mathbf{M} = 0.847M_L + 0.727 \quad (\sigma = 0.25)$ (2.3)

Modified from Leyton et al. (2009)

$$\mathbf{M} = 0.887M_S + 1.095 \quad (2.4)$$

$$\mathbf{M} = 1.173m_b - 0.634 \quad (2.5)$$

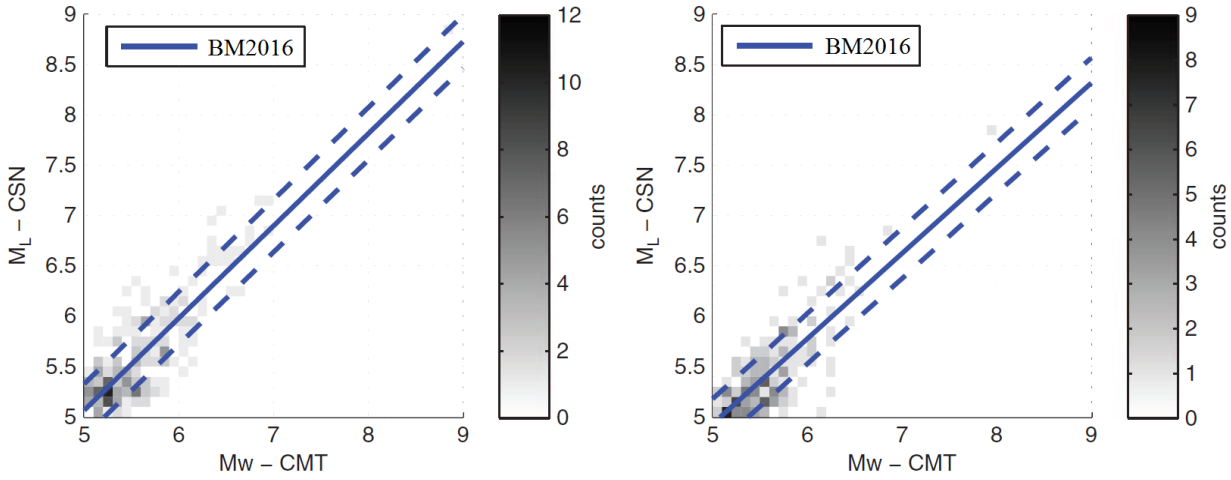

Figure 2.13 M_W-M_L relationships from Bastías and Montalva (2016). Left: Eq. 2.2 for shallow-focus earthquakes (H ≤ 50 km); Right: Eq. 2.3 for deep-focus earthquakes (H > 50 km). A slightly modified form of the relation is used (shifted up 0.033 to reflect **M**).

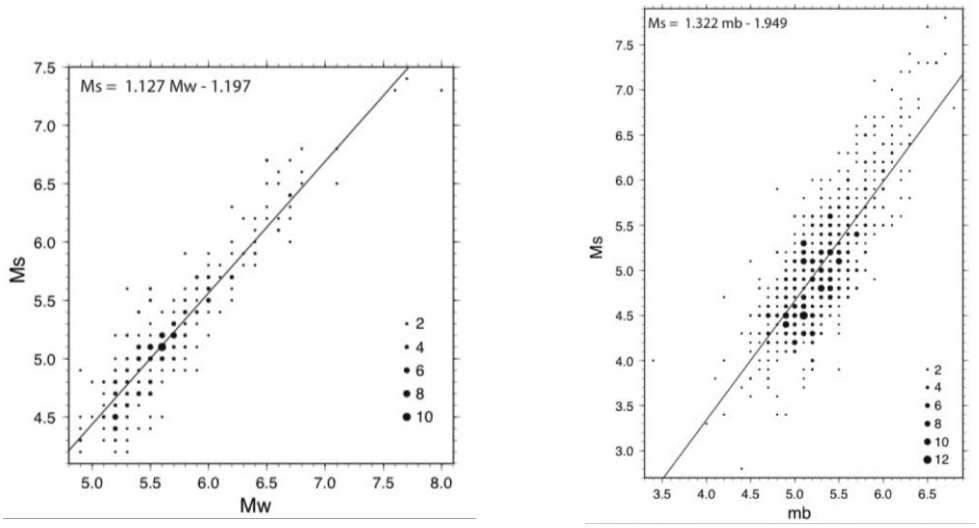

Figure 2.14 M_S-M_W and M_S-m_b relations from Leyton et al. (2009) Left: Eq. 2.4; Right: Original M_S-m_b relation reported by the authors. A slightly modified form of the M_S-M_W relation is used (shifted up 0.033 to reflect **M**).

For New Zealand events source tables from Van Houtte et al. (2017) were adopted. These tables include seismic moment, so conversions from other magnitude scales are not required. For other regions, the following procedures were applied to estimate moment magnitudes:

- **M** is derived from other type of magnitudes taken as-is or using relationships between **M** and other magnitude scales. The selection criteria use, in order of preference, M_S, then M_L, then m_b. These preferences are intended to minimize the potential for saturation bias (i.e., to use the scale that tracks **M** over the widest possible range). M_S has the least saturation because it is derived from 20-sec period surface waves. M_L is derived from the peak of horizontal displacements from broadband sensors (which are controlled by lower periods). m_b is based on 1-sec P-waves, and generally are measured from the vertical component.
- Alaska: Eight events that occurred in 2001, 2002, 2003, and 2014 lack seismic moments. These events collectively have only 14 recordings. For these events, **M** is taken as M_S, m_b, and M_L for 6, 1, and 1 event, respectively.
- Cascadia: No events lack seismic moment.
- Central America and Mexico: Two events lack seismic moment; **M** is taken as M_w from NEIC for one event and **M** is taken as M_S for the other event.
- Japan: A group of 25 earthquakes prior to 1974 lack seismic moment. Due to various problems with the recordings from these events, the source database does not include information for these events. In addition, two aftershocks of the 2003 Tokachi-oki earthquake (events 4000199 and 4000200) lack seismic moment because they occurred just

after the large magnitude event; for event 4000199 **M** is taken as M_L and for event 4000200 **M** is taken as M_S.

- South America: Ten events lack seismic moment. **M** is taken as M_w from CSN for four events, **M**-M_L relations (Eqs. 2.2 and 2.3) are applied to four events, and the **M**-M_S relation (Eq. 2.4) is applied to two events.
- Taiwan: 10 events prior to 2000 lack seismic moments, mostly because in this period the Broadband Array in Taiwan for Seismology (BATS) did not routinely compute M_0 for events with magnitudes < 6.2. These events have produced 928 records. For these events, **M** is obtained using the methodology described in Wu et al. (2016).

(b) Hypocenter location

Hypocenter locations incorporated into selected finite-fault models were used when available, and in most cases, the hypocenter is on the ruptured fault plane. In some cases, the hypocenter documented in the paper is not on the fault plane. In these cases, the hypocenter was projected on to the fault rupture plane (the projection was made in the direction orthogonal to the plane).

When finite-fault models were not available, which is the case for most events, hypocenter locations were obtained from the catalogues in Table 2.2. Global CMT is not preferred for hypocenter location because this solution provides the location of the center of the earthquake moment distribution in time and space (Ekström et al. 2012). This central location may not correspond well with the location of the initial slip, as required for the hypocenter. For this reason, hypocenter locations from local agencies are preferred over global CMT where available. These

different preferences are reflected in Table 2.2. For New Zealand, hypocenter locations were adopted directly from Van Houtte et al. (2017).

(c) Fault type

Style of faulting was defined based on rake angle as shown in Table 2.3. Rake angle is compiled for all events with moment-tensor solutions from earthquake catalogs (Table 2.2). When a rake angle is provided with a finite-fault model, it is preferred to values from catalogs.

Table 2.3 Fault mechanism based on rake angle (after Ancheta et al., 2013).

Fault Mechanism	Flag	Range of rake angle (°)
Strike-Slip	0	$-180 < \lambda < -150$ $-30 < \lambda < 30$ $150 < \lambda < 180$
Normal	1	$-120 < \lambda < -60$
Reverse	2	$60 < \lambda < 120$
Reverse – Oblique	3	$30 < \lambda < 60$ $120 < \lambda < 150$
Normal – Oblique	4	$-150 < \lambda < -120$ $-60 < \lambda < -30$
Unknown	-999	Unknown

(d) Event-type

Where event-type (interface, intraslab, shallow crustal, and outer-rise) is defined in literature (typically the same documents that have finite-fault models), the recommended event-types are adopted. Otherwise, event-type is estimated using an automated process (modified from Poblete 2008 and Contreras 2009) that considers the hypocenter location relative to the depth of the surface of the subducting (typically oceanic) plate as defined by Hayes et al. (2012) (later updated by Hayes et al. (2018), which did not change the event-type assignments) and the event focal mechanism. Exceptions to the use of these automated procedures are Cascadia, Taiwan, and New

Zealand: in Cascadia, event-type classifications were adopted from the literature or from NGA-West2; in Taiwan, event-type classifications from NCREE (2019) were used; for New Zealand, event-type classifications from Van Houtte et al. (2017) were used.

The procedure for classifying event-type is illustrated through the example shown in Figure 2.15 (September 16, 2015, **M**7.13 event in central Chile; NGAsubEQID = 6000485). This is the largest aftershock of the 2015 **M**8.31 Illapel, Chile earthquake. The blue solid line is the geometry of the top surface of the subducting Nazca plate as provided by the Hayes et al. (2018) model and the blue dashed lines represent the estimated error (±10 km) (based mainly on seismicity-model comparisons from South America, which were assumed to apply globally). Red circles are the hypocenters of the earthquakes between 1964 and 2017 with magnitude ≥ 4 taken from the ISC-EHB catalog. To apply the automated procedure, three horizontally-oriented zones (i.e., on the surface of the earth) are defined based on interface depth, as follows:

i. Zone A: depth to top of subducting plate, using the mean representation, is < 10 km
ii. Zone B: 10 km ≤ depth to top of subducting plate ≤ Z_{BC}
iii. Zone C: depth to top of subducting plate > Z_{BC}

Depth Z_{BC} is the depth to the top of subducting slab at the maximum depth of interface earthquakes, and is region-dependent. In the regions for which this procedure was applied, Z_{BC} was taken from literature as 50 km in ALK and CAM, and 55 km in JPN and SAM (Hayes et al. 2012, Tichelaar and Ruff, 1993). Depth Z_{BC} defines the boundary between Zones B and C.

Horizontal zones A-C and the plate boundary are used to make initial event-type classifications as follows:

1. *Shallow Crustal (green region in Figure 2.15):* Earthquakes shallower than the shallowest interpretation of the subducting plate depth (mean – standard deviation depth), or 20 km in Interval B, or 30 km in Interval C, whichever is shallower. Any focal mechanism is allowed.
2. *Interface (light blue region in Figure 2.15)*: Earthquakes within Zone B, deeper than the shallowest interpretation of the subducting plate depth or 20 km, whichever is shallower, and shallower than 60 km (this threshold, which is larger than Z_{BC}, is applied based on expert opinion that 60 km is an effective upper limit on depth of interface events for screening purposes). The interface flag is not assigned for depths > 60 km.
3. *Intraslab (orange region in Figure 2.15)*: Earthquakes within Zone C, deeper than the shallowest interpretation of the subducting plate depth or in Zones A-B at depths > 60 km.
4. *Outer-rise (yellow region in Figure 2.15)*: Earthquakes within Zone A at depths < 60 km.
5. *Undetermined (gray region in Figure 2.15)*: Earthquakes within Zone C, below 30 km and above the shallowest interpretation of the subducting plate depth.

Event 6000485 in Figure 2.15 is in the second region (*light blue region*) and the event-type is classified as interface. Table 2.4 lists event-type flags, including flags applied when the available information produces low confidence.

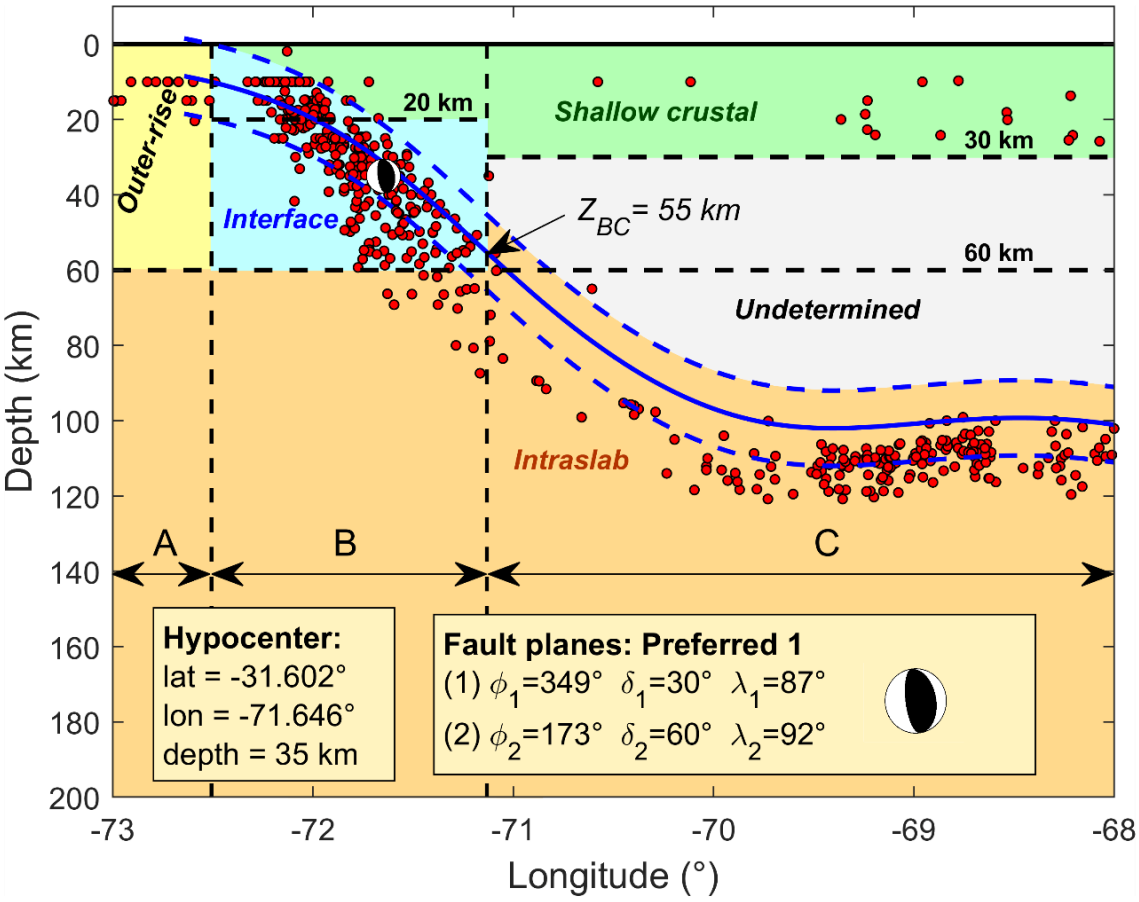

Figure 2.15 Event-type classification scheme based on hypocenter location relative to the top of the surface of the subducting plate. Example event is NGAsubEQID 6000485, which is defined as interface.

Following these initial classifications, event-types were checked based on human interpretation. One check is based on moment-tensor solutions. Interface earthquakes should have reverse mechanisms. If an event near the interface is not reverse, a shallow crustal designation is assigned. Intraslab earthquakes are typically normal or strike slip, but all event types (including reverse slip) are allowed within this category. The second check examines the event location relative to the interface (similar to Figure 2.15). In some cases, the results of the initial classifications were overruled, for example, when a reverse event occurs on the interface at depths

slightly greater than Z_{BC} (e.g, NGAsubEQID = 3000123 in Central America has a hypocentral depth of 77.3 km > Z_{BC} and was classified as intraslab by the automated procedure. However, the event was re-classified as interface (event-type flag = 0) due to its reverse mechanism and the proximity of the hypocenter to the interface between the subducting and overriding plates.

Event-type is reported in the source database using flags as defined in Table 2.4. Low confidence flags (-444, -666, -777, -888) are assigned when (1) nodal planes are not available to check event-type assignments, (2) event locations are near the boundaries between regions, or (3) moment tensors are incompatible with the region (e.g., normal faulting in interface region). Events assigned with an event-type flag=5 are intraslab earthquakes that have occurred in areas of subduction zones where the Wadati–Benioff zone corresponds to two well-defined parallel surfaces of seismicity, separated by tens of kilometers, particularly when those events are located at the lower plane of the double seismic zone. The database has three such events, each located in Japan.

Figure 2.16 shows the distribution of hypocentral depths with **M** for interface and intraslab earthquakes for which event-type classifications have high confidences (flags of 0 or 1). Interface events have hypocentral depths generally smaller than 55 km. Five events have deeper hypocenters ($Z_{HYP} > Z_{BC}$); these events were manually assigned as interface because they are located close to the interface and have reverse mechanisms (as in the example of NGAsubEQID = 3000123). Approximately 65% of the intraslab events have $Z_{HYP} > 55$ km. Shallower intraslab events received this classification because the hypocenter was located beneath the interface and the mechanism was not reverse. Our understanding is that similar criteria were applied for the event-type

classifications made externally to NGA-Sub and adopted here for Cascadia, Taiwan, and New Zealand (NCREE, 2019 for Taiwan; Van Houtte et al., 2017 for New Zealand). Of the 35% of intraslab events with Z_{HYP} < 55 km, 57% are from those regions, so both the event assignments here and from prior work produce cases of relatively shallow intraslab events.

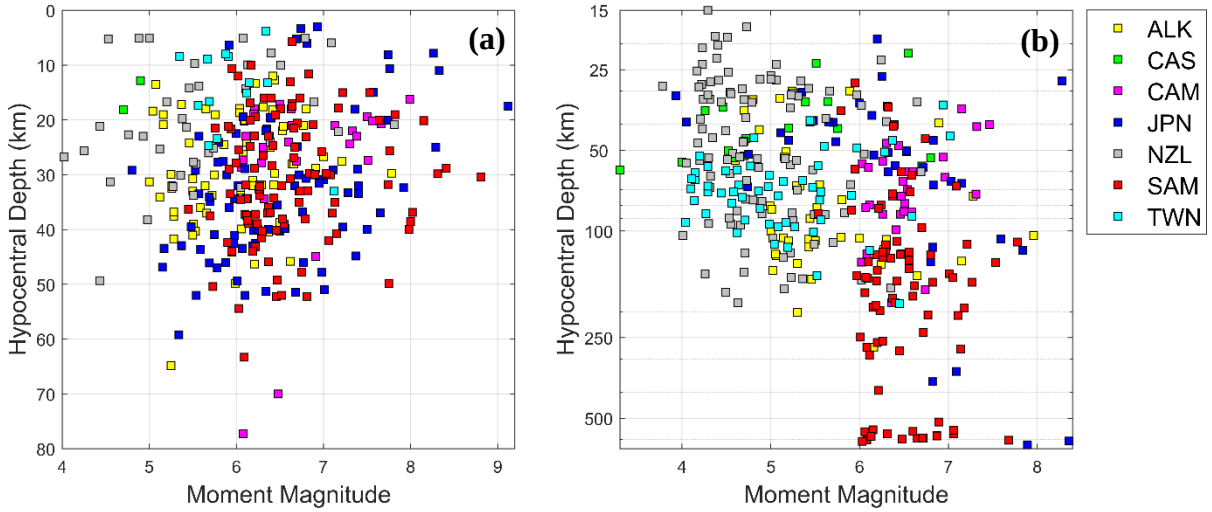

Figure 2.16 Distribution of hypocentral depths with **M** for (a) interface and (b) intraslab earthquakes by region. Events with lower confidence in the event-type classifications (negative flags) are not included.

Flag -999 is applied when event-type is not assigned. Such events did not go through the quality assurance (QA) procedures described subsequently in Section 3.5, and therefore their source parameters may be less reliable and certain information may be missing. These events have small magnitudes (**M**<6) and are mainly located in the CAM and SAM regions. The lack of event classification and application of quality assurance procedures for these events was the consequence of limited resources, not any inherent problem with the data from these events. Table 2.4 also presents the number of events, and the number of recordings associated with those events, for each

event-type flag. Considering the earthquakes with known event-type classifications (flag ≠ -999), most of subduction events (interface and intraslab only) have event-type classifications with a high level of confidence (about 91% of interface earthquakes and about 96% of intraslab earthquakes). More importantly, most of the data in terms of recordings are from earthquakes with an assigned event-type flag (about 92% of the ground-motion recordings).

Table 2.4 Flags in source database that indicate event-type classification.

Event-Type Classification	Flag	Number of events	Number of recordings
Interface	0	330	21326
Intraslab	1	363	23129
Shallow crustal / overriding intraplate	2	212	8763
Outer-rise	4	21	2589
Intraslab, specially lower double seismic zone	5	3	1364
Outer-rise event with lower confidence	-444	5	2040
Shallow crustal / overriding events with lower confidence	-666	9	816
Intraslab events with lower confidence	-777	17	3100
Interface events with lower confidence	-888	31	2241
Unknown / Unassigned	-999	889	5972

The procedures for event-type assignments developed in NGA-Sub have practical significance, because separate GMMs are provided for interface and intraslab events (Kuehn et al., 2020; Parker et al., 2022). Although a review of seismic source characterization models used in global subduction regions is beyond the scope of the present work, it would be appropriate for such models to define event types in a similar manner to that used here for compatibility with the

GMMs. Ongoing and future work will likely extend and improve the source and path tables by (1) adding information for major events in Alaska, Mexico, and South America since 2016; (2) adding event types for the 889 events for which such classifications were not made in NGA-Sub; and (3) considering finite fault uncertainties, whether from published models or simulations, which would produce distance uncertainties that are currently not provided.

2.4 FINITE-FAULT SOURCE PARAMETERS FROM PUBLISHED MODELS

Parameters that describe the location and dimensions of the fault rupture surface are needed for the calculation of source-to-site distances, including rupture distance R_{rup} (closest distance to the fault surface), which is the only distance metric used in the NGA-Sub GMMs. The rupture surface is represented as one or more rectangles characterized by its upper-left corner as viewed from the hanging wall (geodetic coordinates and depth), strike and dip angles, and along-strike and down-dip dimensions. This section describes how models of rupture surfaces from the literature (denoted finite-fault models) were identified and (in most cases) modified for application in NGA-Sub.

Information derived from finite-fault models is contained in the *FFmodel* table in the NGA-Sub database. When the model is described by more than one rectangle, information on the rectangles is contained in the *FFmodelmultiseg* table. For those events, the finite-fault parameters in the *FFmodel* table are for a single planar representation of the full model (needed for when single values of *L* and *W* are required for modeling purposes, e.g., for studies of directivity).

2.4.1 Finite-Fault Models Collected

FFMs were identified mainly by reviewing compilations of past studies at the following websites:

a) SRCMOD website (Mai and Thingbaijam, 2014), available at http://equake-rc.info/SRCMOD/ (last accessed Nov 2019).

b) Source Models of Large Earthquakes, Caltech Tectonic Observatory, available at http://www.tectonics.caltech.edu/slip_history/index.html (last accessed Nov 2019).

c) Rupture processes of global large earthquakes (**M** > 7), UC Santa Barbara, available at http://www.geol.ucsb.edu/faculty/ji/big_earthquakes/home.html (last accessed Nov 2019).

d) Association for the Development of Earthquake Prediction website (last accessed Nov. 2020) with (1) Catalog of non-uniform fault parameters in Japan (1980-1995) and (2) Catalog of non-uniform fault parameters in Japan (1994-2003).

Independent literature searches were performed for the largest magnitude events (2010 **M**8.81 Maule, Chile and 2011 **M**9.12 Tohoku, Japan) and other recent, large events, some of which occurred contemporaneously with the data compilation for NGA-Sub (e.g., the 2001 **M**8.41 Arequipa earthquake in Southern Peru and the 2007 **M**7.75 Tocopilla, 2014 **M**8.15 Iquique, and 2015 **M**8.31 Illapel earthquakes in Chile).

Table 2.5 lists finite-fault models for 88 earthquakes used in NGA-Sub for regions other than New Zealand. Twelve New Zealand events are not included because their source parameters were adopted directly from Van Houtte et al. (2017) without further review. For some earthquakes, more than one model is available; the *Selection Criteria* section below describes how a preferred model was selected in these cases. In many cases, the fault dimensions from models in the literature were trimmed to develop the values shown in Table 2.5; the *Trimming Criteria* section describes how this trimming was performed. *Multiple-Rectangle Rupture Models* section discusses special considerations related to multi-rectangle rupture surface models.

Table 2.5 FFMs selected for use in NGA-Sub database.

NGA sub EQID	Date	Earthquake name, Country/State	M	FFM reference	Hypocenter location [1]			Nodal plane [2]			Slip [3] (cm)		Rupture dimensions		Upper-left corner			Event Class. flag [4]
					Lat. (°)	Lon. (°)	Depth (km)	ϕ (°)	δ (°)	λ (°)	M	T	L (km)	W (km)	Lat. (°)	Lon. (°)	Z_{TOR} (km)	
Japan (JPN) – 63 events																		
4000001	3/11/2011	Tohoku, Japan	9.12	Yokota et al. (2011)	38.1165	142.823	17.4965	200	5	88	3500	NO	482	63	39.5163	144.4071	8.65	0
									12				482	62	39.7144	143.7911	13.9	
									20				482	61	39.9103	143.1683	26.4	
4000219	5/24/2013	Okhotsk, Russia	8.36	Ye et al. (2013)	54.8172	153.3558	608.1717	184	10	-98	990	220	195	70	55.4265	154.0676	601	1
4000222	11/15/2006	Kuril Doublet1	8.33	Ammon et al. (2008)	46.592	153.266	11	215	15	92	700	NO	310	130	48.1243	155.5177	0	0
4000068	9/25/2003	Tokachi-oki	8.29	Koketsu et al. (2004)	41.7796	144.0786	25.0101	230	20	90	706	NO	120	100	42.1796	144.8114	23.3	0
4000093	10/4/1994	Hokkaido Toho-oki	8.28	Tanioka et al. (1995)	43.711	147.457	27.459	160	40	30	1680	NO	60	70	43.8256	147.5468	18.1	1
4000095	5/16/1968	Tokachi-oki	8.26	Nagai et al. (2001)	40.6184	143.6866	7.851	156	20	90	929	NO	200	80	41.6671	143.1441	5.58	0
4000223	1/13/2007	Kuril Doublet2	8.13	Ammon et al. (2008)	46.229	154.5457	20.6325	43	59	-115	1400	200	235	55	45.6304	153.5358	0	4
4000010	3/11/2011	IbarakiOff	7.92	JMA (2011a)	36.1037	141.2473	32.3653	200	29	90	488	NO	90	90	36.2174	141.8235	7.8	0
4000220	5/30/2015	Chichi-shima	7.89	JMA (2015)	27.8713	140.7021	627.5655	32	25	-44	656	98	36	40	27.8226	140.3958	617	1
4000094	12/28/1994	Sanriku-ho	7.76	Nakayama & Takeo (1997)	40.4365	143.7558	10.6174	180	6	90	495	74	100	80	40.9315	144.05	8	0
									16				90	10	40.9315	143.1	16.36	
									30				90	80	40.9315	142.9734	19.45	
4000091	7/12/1993	Hokkaido_sw	7.74	Mendoza & Fukuyama (1996)	42.7814	139.2002	20.015	20	29.8	100	436	NO	110	70	42.355	138.6511	5	0
								340		50			80	70	41.4618	138.9642	2	
4000097	5/26/1983	Middle.Japan.Sea	7.74	Fukuyama & Irikura (1986)	40.3583	139.0708	8.0782	15	20	90	758	NO	30	30	40.2998	138.9469	5	0
								350					60	30	40.5607	139.0387	5	
4000096	6/12/1978	Miyagi-oki	7.65	Yamanaka & Kikuchi (2004)	38.1496	142.1672	36.9798	200	20	95	211	NO	80	70	38.6003	142.4336	35.28	0

Table 2.5 FFMs selected for use in NGA-Sub database.

NGA sub EQID	Date	Earthquake name, Country/State	M	FFM reference	Hypocenter location [1]			Nodal plane [2]			Slip [3] (cm)		Rupture dimensions		Upper-left corner			Event Class. flag [4]
					Lat. (°)	Lon. (°)	Depth (km)	ϕ (°)	δ (°)	λ (°)	M	T	L (km)	W (km)	Lat. (°)	Lon. (°)	Z_{TOR} (km)	
4000173	6/16/1964	Niigata	7.65	Shiba & Uetake (2011)	38.3672	139.2182	24.7595	200	60	90	880	NO	84	24	38.6882	139.5023	5.7	2
4000092	1/15/1993	Kushiro-oki	7.59	Ide & Takeo (1996) Nozu (2007)	42.8903	144.4208	107.1658	256	0.5	-36	800	NO	60	40	42.748	144.6072	107	1
4000108	4/1/1968	Hyuganada	7.57	Yagi et al. (1998)	32.2798	132.5302	14.9961	227	12	90	403	60	63	63	32.2729	132.8647	10.32	0
4000074	9/5/2004	Ki_se	7.41	Yagi (2004)	33.235	137.0304	12.6998	85	40	90	390	110	108	21.3	33.242	136.3208	7.1	-444
4000009	3/11/2011	Iwate_off	7.40	JMA (2011b)	39.8339	142.6992	32.0373	187	10	74	346	NO	45	50	40.0155	142.9985	28	0
4000132	6/17/1973	Nemuro-oki	7.40	Namegaya & Tsuji (2005)	42.9571	145.9611	33.4149	230	27	111	120	NO	90	100	42.8375	146.9804	1	0
4000069	9/25/2003	Tokachiokiaft	7.37	Atkinson & Macias (2009)	41.7534	143.6114	44.8185	208	18	86	N/A	N/A	60	24	41.9021	143.7943	43	0
4000002	3/9/2011	Tohoku foreshock	7.36	JMA (2011c)	38.301	143.221	18.0334	187	11	75	222	78	70	70	38.7201	143.5146	14.2	0
4000102	10/9/1994	Hokkaido.Eastoff.as	7.28	Ye et al. (2016)	43.9124	147.9175	33.2881	227	19	104.6	270	50	50	50	43.936	148.3136	26.5	0
4000054	12/7/2012	Miyagi-oki	7.23	JMA (2012a)	38.0216	143.8381	21.0373	174	61	82	908	136	24	24	37.9492	144.1553	41	-777
								188	44	-100			75	40	38.2722	144.0363	8.2	
4000073	9/5/2004	Ki_se	7.23	Yagi (2004)	33.0904	136.619	18.4711	280	42	105	510	150	54	30	32.9064	136.9093	4.6	-444
4000078	8/16/2005	Miyagi-Eq	7.22	Yamanaka (2005)	38.1438	142.2324	39.5357	198	25	76	90	30	25	20	38.2335	142.3349	37	0
4000035	4/7/2011	Miyagi_Pre.Off	7.15	JMA (2011d)	38.253	141.9645	66.4296	24	37	87	250	51	45	35	38.1898	141.6554	50	1
4000111	6/12/1968	Iwate-oki	7.11	Yoshioka & Abe (1976)	39.3549	143.0977	29.0773	241	30	90	N/A	N/A	80	30	39.4374	143.8059	16.7	0
4000167	8/9/2009	TokaidoSouth	7.09	ERI (2009)	33.1017	138.4143	334.2059	105	25	-176	140	40	50	30	33.2104	138.0448	332.9	1
4000042	7/10/2011	Sanrikuoki	7.03	JMA (2011e)	38.0338	143.51	34.3521	67	74	7	117	NO	100	30	37.9547	143.1135	14.8	-777
4000067	5/26/2003	SouthSanriku	7.03	Okada & Hasegawa (2003)	38.9471	141.6793	65.2354	198	60	92	300	60	24	20	38.9436	141.7217	59	1
4000146	7/23/1982	Ibaraki-oki	7.03	Takiguchi et al. (2011)	36.2699	141.65	29.9684	203	14	86	660	NO	11.4	11.4	36.2958	141.7642	27.9	0
4000077	11/28/2004	Kushirooki	7.01	HERP (2006)	42.9533	145.2529	51.0142	211	24	81	400	150	25	25	42.9775	145.4365	45.93	0

Table 2.5 FFMs selected for use in NGA-Sub database.

NGA sub EQID	Date	Earthquake name, Country/State	M	FFM reference	Hypocenter location [1]			Nodal plane [2]			Slip [3] (cm)		Rupture dimensions		Upper-left corner			Event Class. flag [4]
					Lat. (°)	Lon. (°)	Depth (km)	ϕ (°)	δ (°)	λ (°)	M	T	L (km)	W (km)	Lat. (°)	Lon. (°)	Z_{TOR} (km)	
4000162	11/14/2005	Sanriku	7.01	JMA (2005)	38.0255	144.927	8.0399	173	49	-118	140	NO	56	22	38.3626	144.9447	1	4
4000072	10/31/2003	Fukushima-oki	7.00	EIC (2003)	37.7175	142.7453	30.8572	204	14	92	60	20	80	76	38.0882	143.4563	20.8	0
4000050	3/14/2012	Sanrikuoki	6.98	JMA (2012b)	40.7922	145.2319	15.2067	276	42	-81	367	NO	31	24.5	40.7016	145.2839	6.6	4
4000145	3/21/1982	S.Urakawa	6.91	Tsuchida et al. (1983)	42.1079	142.6131	12.5433	320	65	90	60	NO	30	40	42.0466	142.5898	0	-666
4000059	1/28/2000	NemuroSE	6.83	Takahashi & Hirata(2003)	43.2973	147.0443	67.4	160	35	15	N/A	N/A	30	15	43.4429	147.0521	63.1	1
4000063	3/24/2001	Geiyo	6.83	Kakehi (2004)	34.1298	132.7025	45.8808	170	60	110	240	NO	15	18	34.1744	132.7258	40	1
								177	63				3	18	34.0375	132.7511	40	
								183	67				3	18	34.0075	132.7489	40	
								190	70				9	18	33.9779	132.7385	40	
4000049	1/1/2012	Torishima	6.82	JMA (2012c)	31.4268	138.5691	364.9843	5	84	-73	103	NO	31	25	31.3563	138.5537	357.6	1
4000224	7/23/2008	Middle Iwate	6.82	Suzuki et al. (2009)	39.739	141.6665	114.8789	179	71	-93	240	50	14	35	39.6856	141.7613	94.2	5
								223	65	-107			16	35	39.872	141.7623	93.3	
4000225	9/11/2008	Toakchi-oki	6.80	JMA (2008)	41.7792	144.1493	30.6548	228	21	108	160	NO	36	31	41.8064	144.4086	26	0
4000161	12/6/2004	KushiroAs	6.77	HERP (2006)	42.8463	145.3371	45.9837	222	26	90	200	50	20	20	42.859	145.5011	41.6	0
4000041	6/22/2011	Iwateoff	6.76	JMA (2011f)	39.9678	142.5565	36.7789	185	17	74	86	17	18.25	12	40.0639	142.5974	36	0
4000165	10/19/1996	Hyuganada	6.74	Yagi et al. (1999)	31.7808	131.8515	3.3449	210	12	80	290	NO	32.12	29.2	31.9065	132.0591	1.22	0
4000048	9/16/2011	Iwate-oki	6.70	JMA (2011g)	40.2604	143.0867	24.8842	172	17	57	94	NO	36	37	40.4121	143.3957	16.23	0
4000036	4/11/2011	Hamadori	6.69	Anderson et al. (2013)	36.9597	140.726	4.2147	342	66	-75	172	NO	23	20	36.9492	140.7081	0	2
								308					15	15	36.9864	140.829	0	
4000166	12/2/1996	Hyuganada2	6.69	Yagi et al. (1999)	31.9197	131.5977	5.1662	210	12	80	140	NO	29.2	29.2	31.9159	131.8221	1.22	0

Table 2.5 FFMs selected for use in NGA-Sub database.

NGA sub EQID	Date	Earthquake name, Country/State	M	FFM reference	Hypocenter location [1]			Nodal plane [2]			Slip [3] (cm)		Rupture dimensions		Upper-left corner			Event Class. flag [4]
					Lat. (°)	Lon. (°)	Depth (km)	ϕ (°)	δ (°)	λ (°)	M	T	L (km)	W (km)	Lat. (°)	Lon. (°)	Z_{TOR} (km)	
4000100	12/17/1987	ChibaEastoff	6.53	Fukuyama (1991)	35.4012	140.5014	50.4243	349	85	180	N/A	NO	16	24	35.3556	140.4907	28.5	1
								79	90	0	N/A	NO	6.4	8	35.3483	140.4069	45	
4000070	9/29/2003	Tokachias	6.47	Atkinson & Macias (2009)	42.3041	144.579	35.5	244	17	114	N/A	N/A	19	10	42.3029	144.7082	34	0
4000119	9/9/1969	Gifu	6.43	Takeo & Mikami (1990)	35.47	137.05	2	333	89.9	180	170	NO	20	11.2	35.3899	137.1001	0.6	2
4000045	7/30/2011	Fukushimaoki	6.40	JMA (2011h)	36.852	141.3085	56.9556	21	39	93	205	31	14	18	36.8429	141.1918	49.4	1
4000043	7/23/2011	Miyagi-oki	6.37	JMA (2011i)	38.8743	142.0966	39.9204	173	26	62	53	8	15	15	38.9722	142.1837	35.62	0
4000044	7/24/2011	Fukushimaoki	6.34	JMA (2011j)	37.7479	141.4771	51.2429	200	22	88	51	8	24	24	37.7474	141.6788	44.5	0
4000014	3/11/2011	NorthNagano	6.33	Nagumo (2012)	36.9883	138.5921	9.3111	26	32	80	100	NO	12	10	37.0028	138.5025	4.4	2
4000047	8/19/2011	Fukushima-oki	6.32	JMA (2011k)	37.6415	141.7811	50.96	190	53	92	117	NO	14	15	37.7	141.8146	48.6	1
4000038	4/11/2011	ChibaEastoff	6.25	HERP (2011)	35.4786	140.8657	26.4153	299	75	162	78	N/A	20	10	35.3986	141.0067	20.5	1
4000082	8/10/2009	Suruga-bay	6.20	GSI (2009)	34.8406	138.4434	19.2	309	38	122	77	N/A	16.7	5.6	34.7779	138.4993	17.5	1
4000218	11/24/2011	UrakawaOff	6.19	JMA (2011l)	41.7457	142.8422	43.0034	223	16	103	132	17	16	14	41.7644	142.9922	40.8	0
4000112	7/1/1968	Saitama	6.10	Abe (1975)	36.072	139.3972	52	6	30	90	N/A	N/A	6	10	36.0534	139.2979	47	0
4000022	3/15/2011	ShizuokaEast	6.00	JMA (2011m)	35.3354	138.7148	14.1	31	80	42	110	NO	12	7	35.2915	138.6758	11.1	2
4000046	8/1/2011	Surugawan	5.98	JMA (2011n)	34.7054	138.5393	21.3002	284	31	99	150	33	10	8	34.6431	138.6105	18.21	-444
4000037	4/12/2011	Nakadori	5.97	JMA (2011o)	37.0497	140.6217	18.3625	170	40	58	248	NO	12	6	37.0904	140.6522	15.47	2
4000024	3/19/2011	NorthIbaraki	5.86	JMA (2011p)	36.7729	140.6166	3.5106	150	45	-81	28	7	14	8.4	36.8353	140.5938	1.8	2
South America (SAM) – 13 events																		
6000149	2/27/2010	Maule, Chile	8.81	Delouis et al. (2010)	-36.2089	-72.9587	30.4055	15	18	109.3	2129	319	480	160	-37.8975	-74.5879	0.74	0
6000057	6/23/2001	Arequipa, Peru	8.41	Lay et al. (2010)	-16.2081	-73.6217	28.7746	310	18	62	N/A	N/A	264	145	-18.1423	-72.4881	0.24	0
6000338	9/16/2015	Illapel, Chile	8.31	Melgar et al. (2016)	-31.5571	-71.6617	29.81	3.7	10.5	109	1070	161	240	50	-32.1337	-72.6568	7.4	0

Table 2.5 FFMs selected for use in NGA-Sub database.

NGA sub EQID	Date	Earthquake name, Country/State	M	FFM reference	Hypocenter location [1]			Nodal plane [2]			Slip [3] (cm)		Rupture dimensions		Upper-left corner			Event Class. flag [4]
					Lat. (°)	Lon. (°)	Depth (km)	ϕ (°)	δ (°)	λ (°)	M	T	L (km)	W (km)	Lat. (°)	Lon. (°)	Z_{TOR} (km)	
									17.0				140	38	-31.6236	-72.0986	16.51	
									23.5				130	55	-31.9598	-71.7436	27.62	
6000079	4/1/2014	Iquique, Chile	8.15	Lay et al. (2014)	-19.6420	-70.8173	20.1125	357	18	106	670	101	157.5	105	-20.3526	-71.0105	12.20	0
6000081	7/30/1995	Antofagasta, Chile	8.02	Shao and Ji (n.d.)	-23.4317	-70.4542	36.86	4	18	97	387	58	180	91	-24.9529	-71.4113	9.10	0
													150	52	-24.3340	-70.5128	37.21	
6000272	8/15/2007	Pisco, Peru	8.00	Sladen (2007)	-13.3247	-76.5154	38.55	318	6	59.5	986	148	144	20	-14.5955	-76.5687	5.53	0
									20				144	70	-14.4809	-76.4289	7.25	
									30				144	90	-14.0844	-75.9724	31.05	
6000323	3/3/1985	Valparaiso, Chile	7.98	Mendoza et al. (1994)	-33.125	-71.610	40.0	5	15	90	329	49	255	75	-34.6044	-72.8109	6.4	0
									30	110			180	60	-34.1236	-71.9781	25.81	
6000339	4/16/2016	Coastal Ecuador, Ecuador	7.82	Hayes (2016)	0.2988	-79.9979	19.0058	29	15	114	397	60	168	155	-0.0722	-80.9329	0.00	0
6000061	6/13/2005	Tarapaca, Chile	7.78	Kuge et al. (2010)	-20.03	-69.28	110.0	187	23	-73	>1000	200	47.5	45	-19.8048	-69.0515	101.21	1
6000080	4/3/2014	Iquique afs., Chile	7.76	Lay et al. (2014)	-20.5165	-70.4689	25.6509	357	18	113.6	279	42	90	90	-20.9471	-70.8842	10.8	0
6000095	11/14/2007	Tocopilla, Chile	7.75	Schurr et al. (2012)	-22.3421	-70.0235	49.844	3	20	98	258	39	180	60	-23.2348	-70.5310	32.78	0
6000050	11/12/1996	Nazca, Peru	7.74	Salichon et al. (2003)	-15.0056	-75.6422	31.7612	307	30	47	437	66	180	120	-16.1123	-74.7536	8.00	0
6000055	7/7/2001	Arequipa afs., Peru	7.64	Kikuchi & Yamada (2001)	-17.543	-72.077	20.0	315	16	64	450	68	80	80	-18.0399	-72.0691	9.00	0
Cascadia (CAS) – 4 events																		
2000004	2/18/2001	Nisqually, Washington	6.80	Ichinose et al. (2004)	47.1574	-122.6801	53.1749	350	70	-91	200	30	24	21	47.0337	-122.6825	46.13	1
2000001	4/13/1949	Olympia, Washington	6.70	Ichinose et al. (2006a)	47.2028	-122.9315	57.1527	0	66	-111	166	25	34	28	47.0371	-122.9907	47.1	1
2000002	4/29/1965	Olympia, Washington	6.62	Ichinose et al. (2004)	47.3714	-122.3060	59.9797	344	70	-90	200	30	20	18	47.2876	-122.3037	53.4	1
2000014	1/10/2010	Ferndale, California	6.55	Pitarka et al. (2013)	40.6548	-124.6933	21.6881	230	86	11	120	N/A	25	14	40.7259	-124.5766	18	1
Alaska (ALK) – 3 events																		
1000001	6/23/2014	Aleutian_Isl-Alaska	7.96	USGS (2014)	51.6928	178.8871	103.7969	206	25	-13	789	NO	80	130	51.8207	179.8826	77.92	1

Table 2.5 FFMs selected for use in NGA-Sub database.

NGA sub EQID	Date	Earthquake name, Country/State	M	FFM reference	Hypocenter location [1]			Nodal plane [2]			Slip [3] (cm)		Rupture dimensions		Upper-left corner			Event Class. flag [4]
					Lat. (°)	Lon. (°)	Depth (km)	ϕ (°)	δ (°)	λ (°)	M	T	L (km)	W (km)	Lat. (°)	Lon. (°)	Z_{TOR} (km)	
1000002	11/17/2003	Rat_Islands-Alaska	7.78	USGS (2003)	51.1965	178.1844	29.7262	280.4	18.8	121.9	184	28	120	140.4	50.4649	178.8753	5.61	0
1000142	1/24/2016	Iniskin	7.15	USGS (2016)	59.6531	-153.4457	129.4159	60	66	33	302	45	30	28	59.6912	-153.644	108.62	1
Taiwan (TWN) – 3 events																		
7000044	3/31/2002	2944860	7.12	Lee (2019)	24.16020	122.17200	33.0	292	32	121	462.4	<100	33	32	23.9104	122.3585	21.34	0
7000048	12/26/2006	Pingtung.Doublet1	7.02	Lee et al. (2008)	21.88703	120.56844	44.1	349	53	-54	319	48	89.9	35	21.376	120.527	24.13	1
7000049	12/26/2006	Pingtung.Doublet2	6.94	Lee et al. (2008)	22.02975	120.40508	33.8	151	55	4	260	39	84.9	35	22.29	120.313	25.61	1
Central America and Mexico (CAM) – 2 events																		
3000271	9/19/1985	Michoacan, Mexico	7.99	Mendoza and Hartzell (1989)	18.1814	-102.5691	16.2637	300	14	72	749	112.4	150	139	17.2996	-101.7377	6.0	0
3000272	9/21/1985	Zihuatanejo, Mexico	7.56	Mendoza (1993)	17.5977	-101.8192	20.1586	300	14	100	209	31.4	67.5	67.5	17.1640	-101.6485	12.0	0

(1) Hypocenter location is not necessarily exactly the same as in the FFM. Many times, it was adjusted to make it consistent with the trimmed FFM.

(2) ϕ = strike, δ = dip, λ = rake.

(3) M = maximum, T = trimmed. N/A = Slip values are not reported (only relative distribution). The model is already trimmed using approx. 15-20% of maximum slip as limit. NO = no trimming was applied.

(4) Event classification defined in Table 2.4.

Most of the earthquakes with FFMs listed in Table 2.5 are for events in Japan (63) and South America (13); Figure 2.17 shows the locations of these earthquakes. The magnitude range of events with FFM is 5.86 to 9.12. Interface and intraslab events account for 53% and 31% of events, with the balance (16%) being shallow crustal and outer-rise earthquakes. Out of the 100 events with published finite-fault models considered in NGA-Sub, 68 occurred since 2000.

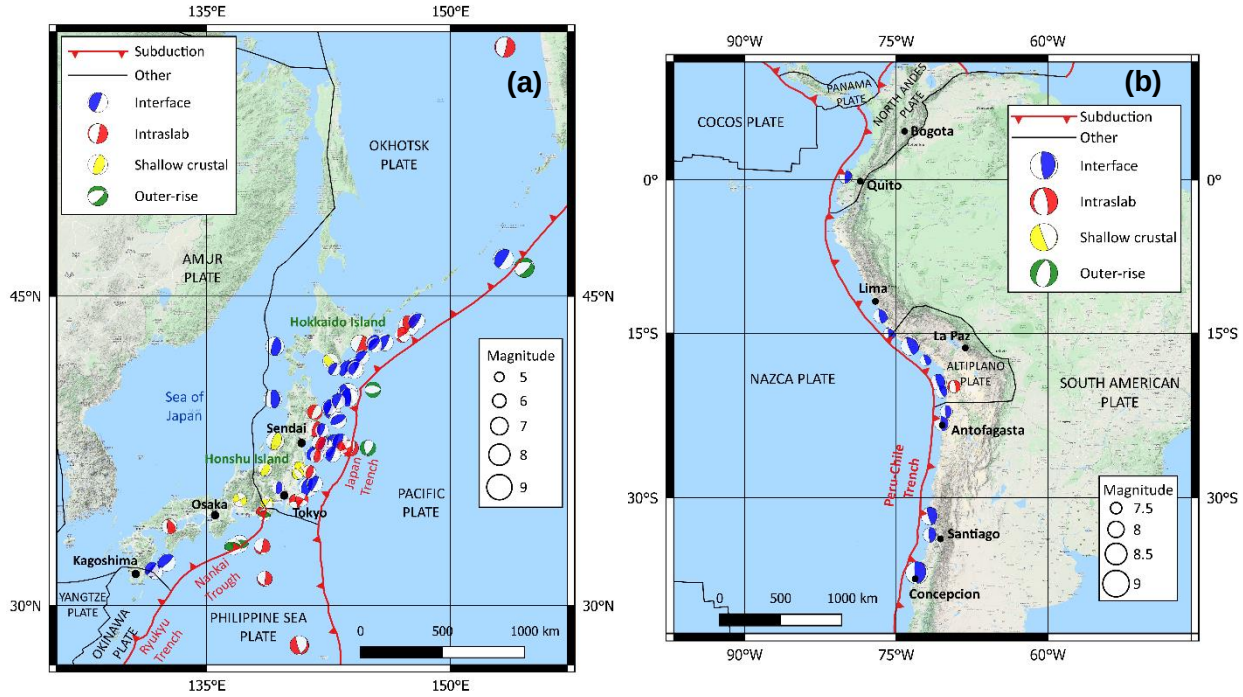

Figure 2.17 Epicentral locations of the earthquakes in (a) Japan and (b) South America with available FFMs from literature in the NGA-Sub database.

2.4.2 Selection Criteria

The compiled FFMs were reviewed to select the single most appropriate model for each earthquake (this provides one distance for each event-recording site pair). The 2010 **M**8.81 Maule, Chile earthquake is utilized as an example to illustrate the approach. For this event, seven different FFMs were considered. Following some trimming (details in Section 2.4.3), the outlines of these seven models are shown in Figure 2.18 along with the locations of strong motion stations in the near-

fault region. The selection of a model among the seven candidates in Figure 2.18 is a topic of practical importance because they produce different source-to-site distances.

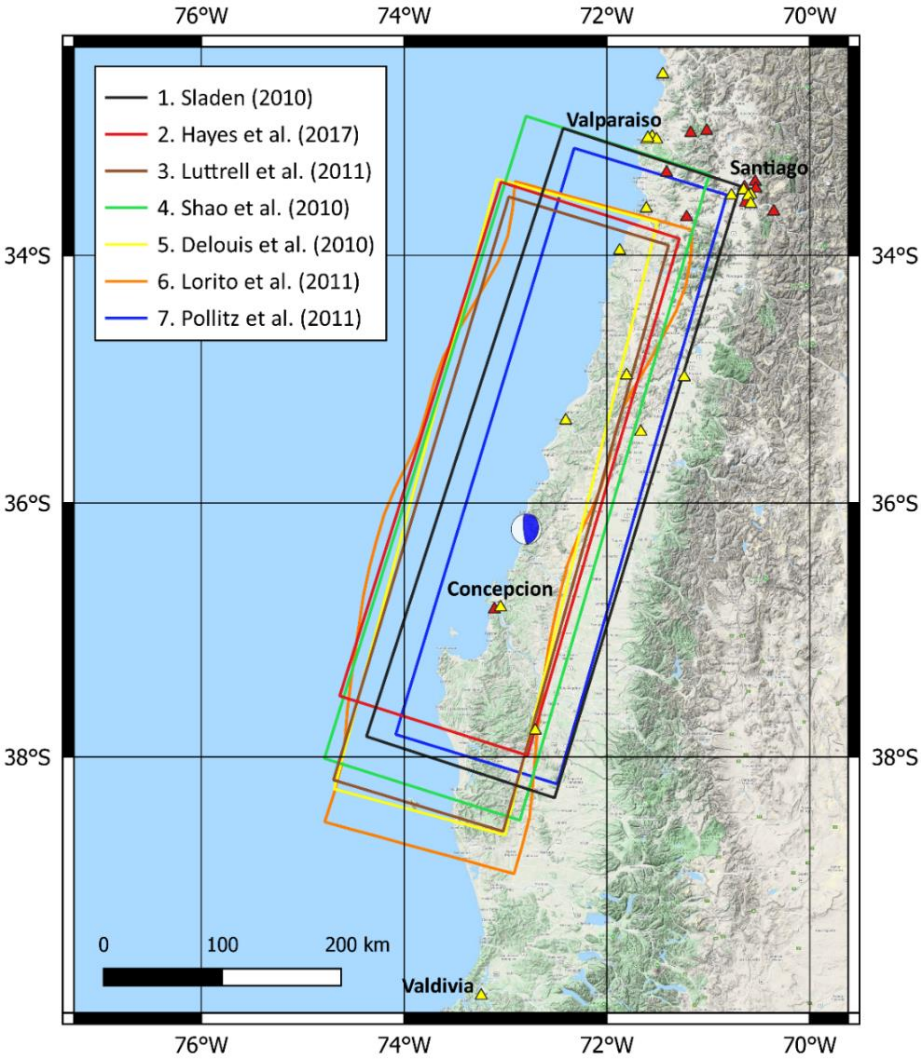

Figure 2.18 FFMs for the 2010 **M**8.81 Maule earthquake using a trimming threshold of 50 cm of slip. Locations of the ground-motion stations included in Table 2.6 are shown using yellow triangles for the RENADIC network and red triangles for the C network. The focal plane solution is shown at the epicenter.

Table 2.6 presents rupture distances (R_{rup}) for the 29 stations in the NGA-Sub database that recorded this event with rupture distances (from any of the alternate models) less than 500 km. Rupture distances are shown for all of the FFMs. The results show considerable differences in some cases – the sites with the largest ranges of distances are highlighted.

Table 2.6 Computed distances (R_{rup}) using the seven FFMs for the 2010 Maule earthquake.

Recorded Strong Motion			Closest distance to the fault rupture plane, R_{rup} (km)								
No	NGAsub RSN	Network	FFM 1	FFM 2	FFM 3	FFM 4	FFM 5	FFM 6	FFM 7	Range (min - max)	
1	6001819	RENADIC	82	142	150	82	137	135	86	**82**	**150**
2	6001829	RENADIC	39	88	94	41	83	80	36	**36**	**94**
3	6001810	RENADIC	39	88	93	42	83	80	36	**36**	**93**
4	6001827	RENADIC	36	84	90	38	80	76	32	**32**	**90**
5	6001828	RENADIC	37	86	92	39	81	78	33	**33**	**92**
6	6001817	RENADIC	39	43	40	42	43	41	30	30	43
7	6001824	RENADIC	63	88	91	66	93	83	54	54	93
8	6001821	RENADIC	60	80	81	63	83	75	51	51	83
9	6001822	RENADIC	65	91	94	70	97	86	56	56	97
10	6001811	RENADIC	65	89	91	69	95	84	56	56	95
11	6001823	RENADIC	66	87	90	71	95	83	57	57	95
12	6001818	RENADIC	36	36	28	38	38	34	26	26	38
13	6001815	RENADIC	64	66	60	66	74	68	54	54	74
14	6001816	RENADIC	48	49	38	51	49	51	38	38	51
15	6001825	RENADIC	57	57	46	59	58	63	47	46	63
16	6001813	RENADIC	36	36	27	38	36	40	26	26	40
17	6001809	RENADIC	35	35	25	37	32	38	24	24	38
18	6001812	RENADIC	54	54	41	56	50	53	43	41	56
19	6001826	RENADIC	189	215	146	163	146	120	197	**120**	**215**
20	6001799	C	34	33	24	35	30	36	22	22	36
21	6001807	C	50	55	50	53	54	52	41	41	55
22	6001805	C	66	99	103	70	104	93	58	58	104
23	6001802	C	73	101	105	84	113	96	66	66	113
24	6001803	C	63	90	93	66	95	85	54	54	95
25	6001804	C	65	84	86	68	92	80	55	55	92
26	6001800	C	66	96	100	71	103	91	57	57	103
27	6001801	C	61	112	116	63	106	104	59	**59**	**116**
28	6001806	C	41	68	71	44	64	61	32	32	71
29	6001808	C	54	105	109	56	99	97	52	**52**	**109**

The three major considerations in the selection process are (1) model is generated using default (automated) procedures vs. an inversion process managed and interpreted by experts; (2)

the data sources considered in the inversion; and (3) peer-review, or lack thereof, of the model and the process by which it was derived. Data sources used in FFM development can include:

- Permanent crustal displacement caused by the earthquake, typically measured from GPS sensors, InSAR, or measurements of on-land elevation change (typically in coastal areas);
- Teleseismic waveforms from global network;
- Local seismic data in reasonably close proximity to the source;
- Tsunami-related data (run up heights, wave heights as measured by ocean buoys).
- Spatial distribution of aftershocks, typically within 24 to 60 hours of the mainshock.

FFMs that have been reviewed/developed by experts (not preliminary or automatic solutions), have been developed using multiple data sources (inclusive of ground-motion data, preferably from proximate stations), and have appeared in peer-reviewed documents, were preferred.

In the case of the Maule earthquake, the seven considered models have the attributes shown in Table 2.7. Three are automatically generated models. Five consider only a single data source (teleseismic or ground displacement only). The model by Delouis et al. (2010) was ultimately identified as the preferred model because it considered multiple data sources, is not from an automated procedure, and appears in a peer-reviewed journal. Lorito et al. (2011) has similar attributes, but the considered data sources do not include ground motions, which causes us to prefer Delouis et al. (2010). The hypocenter of the Maule earthquake from the preferred FFM is shown in Figure 2.18, and is located essentially on the fault plane (no projection required).

Table 2.7 Alternate FFMs for 2010 **M**8.81 Maule earthquake.

Model	Automated (Y/N)	Data Sources	Peer-review document (Y/N)
Sladen (2010)	Y	Teleseismic	N
Hayes (2010, 2017)	Y (2010), N (2017a)	Teleseismic	N
Luttrell et al. (2011)	N	Crustal displacement	Y
Shao et al. (2010)	Y	Teleseismic	N
Delouis et al. (2010)	N	Teleseismic; crustal displacement	Y
Lorito et al. (2011)	N	Crustal displacement; tsunami	Y
Pollitz et al. (2011)	N	Crustal displacement	Y

2.4.3 Trimming Criteria

Once a FFM model is selected, it is typically necessary to trim the rupture dimensions. This is important because faults are often set as large geometric objects at the outset of the inversion to define the area of potential rupture. As a result, the inverted fault may contain broad regions with relatively little slip, in addition to concentrated areas of high slip. This need for trimming is not unique to NGA-Sub, and was addressed earlier in the NGA-West1 project (Power et al., 2008) by selecting event-specific slip thresholds; i.e., portions of the fault having slip below the threshold were trimmed (excluded) in the development of representative rupture dimensions. At that time, on average, a threshold of 50 cm of slip was generally applied. Similar procedures were subsequently used in NGA-West2 (Ancheta et al., 2013).

Because the amounts of slip on subduction sources can be very large relative to the crustal sources considered in NGA-West1 and NGA-West2, a point of concern was that the 50 cm threshold may not provide a reliable basis for fault trimming in all cases. Accordingly, the process by which slip thresholds are selected was re-examined for NGA-Sub, with the aim of developing uniform criteria that can be applied over a wide range of magnitudes and peak fault slips. First, a

fresh look was taken at the source models used to develop slip thresholds in previous NGA projects. The trimmed models for ten crustal events in California, Idaho, and northern Mexico are summarized in Table 2.8, three of which were trimmed by the FFM authors, five were trimmed in NGA-West1, and two were judged to not require trimming. Table 2.8 shows the maximum slip for each event, the maximum slip in the trimmed portions of the rupture, and the ratio of those two slip quantities. These events had maximum slips in the approximate range of 45 to 790 cm, threshold slips of 0 to 180 cm (average of 50 cm), and threshold slip ratios of 0 to 35% (average of 15%).

Table 2.8 Summary of trimming applied to FFMs for NGA-West1 and NGA-West 2 projects.

EQ ID	Earthquake name	Magnitude M	Maximum slip (cm)	Maximum slip in the trimmed areas (cm)	Percentage of maximum trimmed slip to maximum slip
48	Coyote Lake	5.9	120	0	0%
87	Borah Peak	6.8	128	9	7%
101	North Palm Springs	6.2	45	9-11	22%
113*	Whittier Narrows	5.9	90	No trim (< 58 cm)	No trim (<64)
125	Landers	7.3	790	60	8%
127*	Northridge	6.7	319	No trim (< 140 cm)	No trim (<46)
118*	Loma Prieta	6.9	513	0 (< 105 cm)	0 (< 20 cm)
280	El Mayor-Cucupah	7.2	700	180	26%
177	San Simeon	6.5	300	70	23%
179	2004 Parkfield	6.0	52	18	35%
		Average**	**305 cm**	**50 cm**	**~15%**

* Events 113 (Whittier Narrows), 127 (Northridge), and 118 (Loma Prieta) applied models as published, because trimming appears to have been done by the FFM authors.

**Average is computed without the pre-trimmed events.

Based on this re-analysis, it was next considered the use of a 15% slip threshold criterion for several large subduction events with finite-fault models, including the 2010 Maule, 2015

Illapel, 2014 Iquique, and 1985 Valparaíso. The resulting trimmed regions of the rupture surfaces were judged to be reasonable and preferred to those obtained by alternative criteria using slip thresholds based on a fixed displacement. Accordingly, the finite-fault models were trimmed by applying a threshold of 15% of the maximum slip and then drawing one or more rectangles around the high-slip areas. Exceptions to the 15% criterion were made in cases where trimming was not required. Table 2.5 presents rupture dimensions and slip thresholds applied for each event with a finite-fault model.

2.4.4 Multi-rectangle Rupture Models

Some rupture surfaces are modelled with multiple rectangles. Figure 2.19 presents all eight interface events in the NGA-Sub database having multiple-rectangle models. Four are in Japan, including the 2011 **M**9.12 Tohoku earthquake (Figure 2.19a), and four are in South America, including the 2016 **M**8.31 Illapel, Chile earthquake (Figure 2.19b). Both the Tohoku and Illapel earthquakes are modeled with three rectangles. Four intraslab events are modelled with multiple rectangles as shown in Figure 2.20. All are located in Japan, including the 2001 **M**6.83 Geiyo earthquake (Figure 2.20b), which is the event with the most rectangles (4) in the NGA-Sub database.

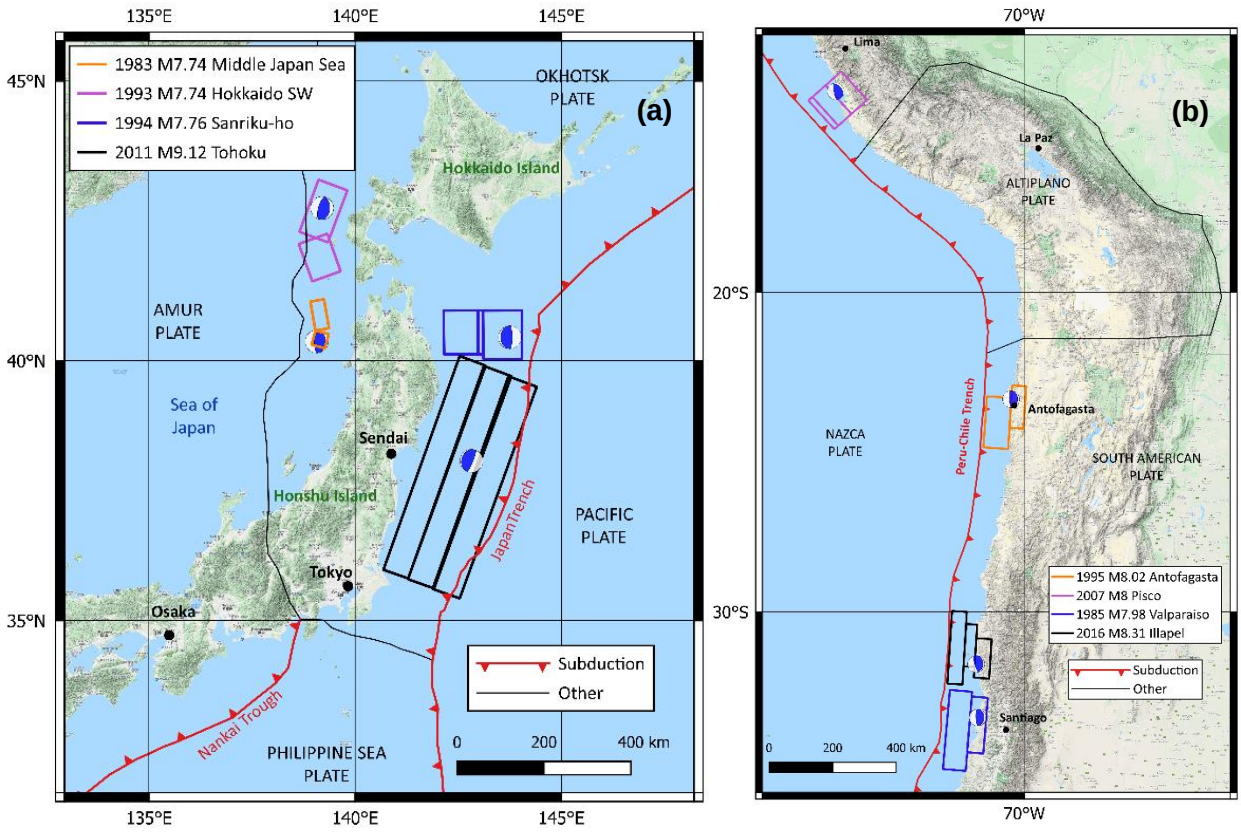

Figure 2.19 Multi-rectangle rupture models of interface events in the NGA-Sub database in (a) Japan and (b) South America regions.

Multiple-rectangle rupture models introduce some issues related to distance calculation and representation of the fault with a single rectangle, as required for the *FFmodel* table. To describe the manner in which multi-rectangle faults are managed for distance calculation, the required configuration of fault geometry for the distance computation code (P4CF; Section 3.2) should be understood. While most earthquakes are represented by a single rectangle, this code can take as input a series of rectangles provided they share a continuous line at the top (shallowest portion) of the fault (e.g., Figure 2.21a, which shows continuous (at the top) rupture rectangles for the 1983 Middle Japan Sea earthquake). In this case, the various rectangles are provided to the code, closest distance parameters are computed for each internally within the code, and the rectangle producing the smallest values is used. For multi-rectangle ruptures that are discontinuous at the top (e.g.,

Figure 2.20a and Figure 2.20d), or that are listric (dip varies across fault width; Figure 2.21b), each rectangle must be entered separately for distance calculation, and the smallest value selected by the analyst at the end. Listric-fault events included in the NGA-Sub database are the 1994 **M**7.76 Sanriku-ho and the 2011 **M**9.12 Tohoku earthquakes in Japan (Figure 2.19a), and the 2007 **M**8 Pisco (Peru), the 1985 **M**7.98 Valparaiso (Chile), and the 2016 **M**8.31 Illapel (Chile) earthquakes in South America (Figure 2.19b).

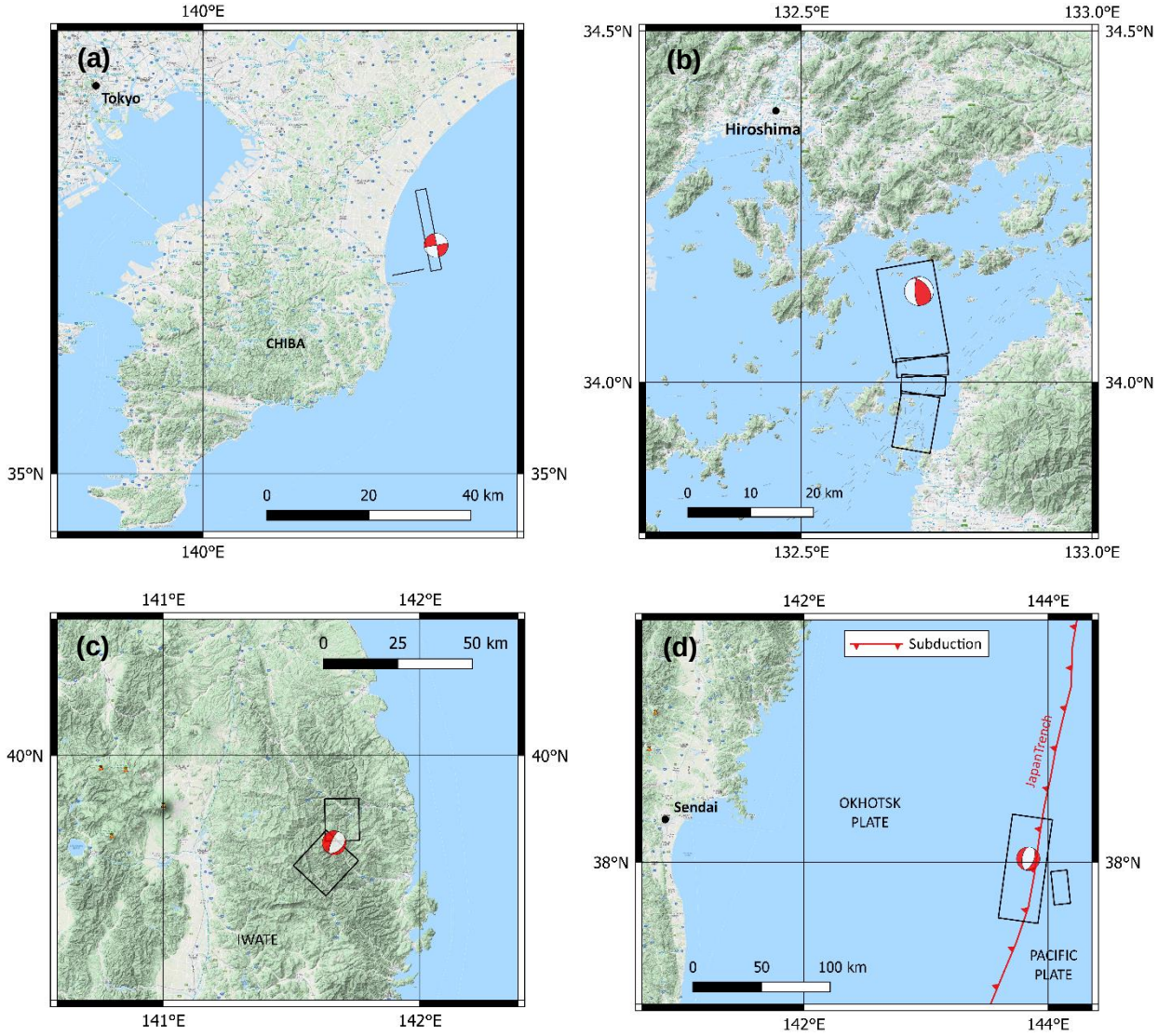

Figure 2.20 Multi-rectangle rupture models of intraslab events in the NGA-Sub database. (a) 1987 **M**6.53 Off Eastern Chiba, (b) 2001 **M**6.83 Geiyo, (c) 2008 **M**6.82 Middle Iwate, and (d) 2012 **M**7.23 Miyagi-oki earthquakes.

As a separate exercise from distance calculation, multi-rectangle faults were represented as a single rectangle for inclusion on the *FFmodel* table. This was done to support potential future work related to rupture directivity. In the case of multiple rectangles having the same strike but different widths and dips (e.g., Figure 2.21b showing the trimmed area of the 1985 **M**7.98 Valparaiso, Chile earthquake), the width of the rectangle is taken as the sum of the rectangle widths and a weighted average length and dip are computed. The weights are proportional to the widths of each rectangle. In the case of multiple segments having different strikes, widths and dips, a width is computed as the ratio of total fault rupture area divided by the sum of rectangle lengths. The length in this case is taken as the cumulative lengths of the multiple rectangles. The strike and dip are taken as a weighted average by area. In some cases involving discontinuous rectangles and significantly different rectangle areas (e.g., intraslab events in Figure 2.20a and Figure 2.20d), only the rectangle with the largest area is considered, whereas the smaller rectangle is ignored.

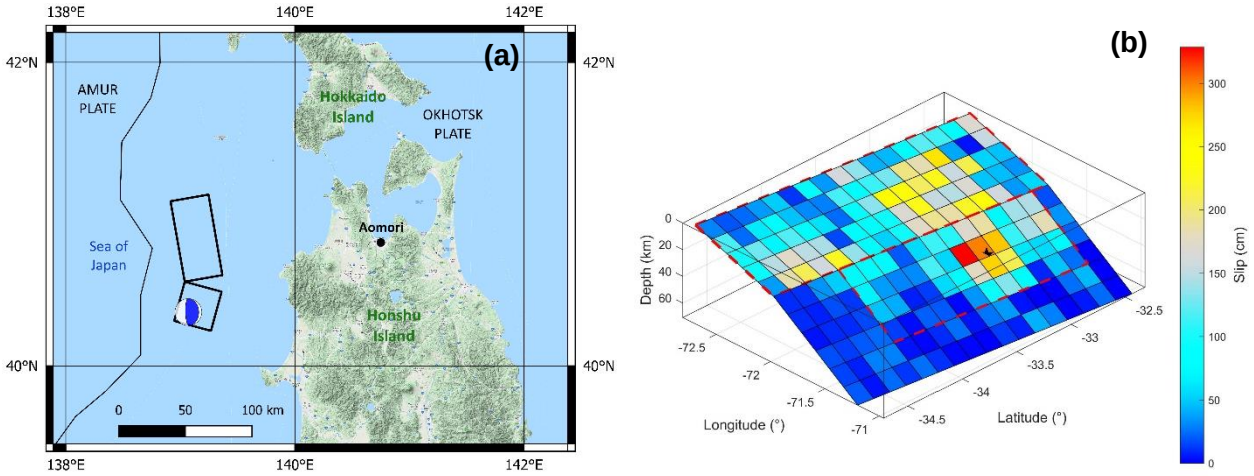

Figure 2.21 Examples of multi-rectangle rupture models (a) with continuity of the upper section of the rectangles and (b) variable dip over the fault width (listric faults).

The properties of multi-rectangle rupture models are provided in the *FFmodelmultiseg* and *FFmodel* tables. The number of rectangles in the model (Norect) is provided in *FFmodel*. When

Norect > 1, table *FFmodelmultiseg* provides the geometric parameters for each rectangle. Table *FFmodel* provides a single-rectangle representation of multi-rectangle ruptures to support potential future work related to rupture directivity.

2.5 SIMULATED FINITE-FAULT SOURCE PARAMETERS

Most earthquakes with event-types in the NGA-Sub database do not have available finite-fault models in literature (891 out of 991). Because there is need for a representation of rupture geometry for each earthquake, a simulation procedure was applied for events without published models. This section describes empirical models for fault dimensions of subduction earthquakes (Section 2.5.1) and the simulation procedure that is applied to estimate the rupture geometry (Section 2.5.2).

2.5.1 Empirical Models for Fault Dimensions, Rupture Orientation, and Hypocenter Location

Models for the rectangular dimensions of finite faults (along-strike length L and down-dip width W), the orientation of the rectangles (strike ϕ and dip δ), and hypocenter location within the rectangle, are required. Models for these parameters are derived using finite-fault models for NGA-Sub events (as given in Table 2.5) in combination with data and models from prior studies. Murotani et al. (2013) and Skarlatoudis et al. (2016) provide models for fault area (A) for interface subduction events. A model for hypocenter location is provided by Mai et al. (2005).

Figure 2.22 shows fault rupture areas and Figure 2.23 shows aspect ratios for 47 interface events with FFMs in the NGA-Sub database. Also shown are rupture-area data from Skarlatoudis et al. (2016) and regression fits. Rupture-area data (Figure 2.22) are fit with the linear expression:

$$lnA = a_1 + a_2\mathbf{M} + \varepsilon_{n1}\sigma_A \quad (2.6)$$

where A is rupture area in km^2, a_1 is a regression coefficient, a_2 is fixed based on self-similarity, ε_{n1} is the standard normal variate (zero mean, standard deviation of 1) and σ_A is the standard deviation. Regressions were performed at two stages in the NGA-Sub project. The first regression was performed using data from 29 earthquakes (subset of data from Table 2.5) available at that time (approximately Nov 2017) along with data from Skarlatoudis et al. (2016); the 29 events used at that time are depicted in Figure 2.22a and the resulting coefficients are indicated in the figure (marked as "Initial"). The next regression was performed using all 47 events and Skarlatoudis et al. (2016) data for non-redundant events with the results shown in Figure 2.22b (marked as "Updated").

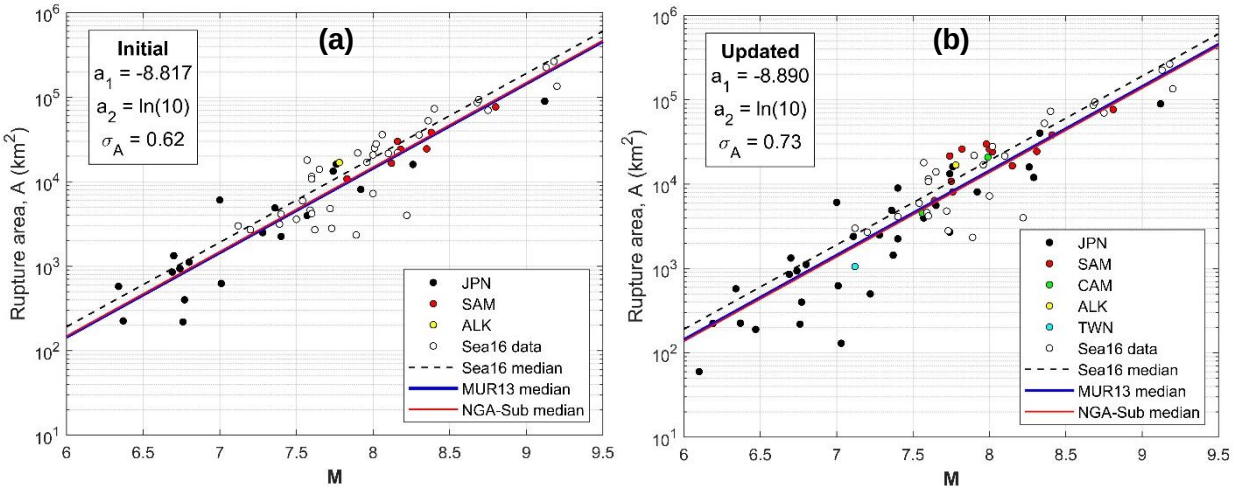

Figure 2.22 (a) Initial and (b) Updated geometric relations for rupture area for subduction interface earthquakes. Sea16 = Skarlatoudis et al. (2016), MUR13 = Murotani et al. (2013).

Self-similarity is assumed, which is typical in models of this sort, meaning that a_2 is unity for the $\log_{10}$ of area (equivalent to $a_2 = ln(10)$). The regression coefficients and standard deviations from the two models in literature and the present model are provided in Figure 2.22. There is no appreciable difference between the "Initial" and "Updated" versions of the mean model, although dispersion increases in the update. The fits derived in the present study are similar

to those derived by Murotani et al. (2013) and are lower than those provided by Skarlatoudis et al. (2016).

For the aspect ratio relation, the following expression was used to fit the available data:

$$ln(L/W) = \begin{cases} \mathbf{M} \geq \mathbf{M_1}\text{: } a_3(\mathbf{M} - \mathbf{M_1}) + \varepsilon_{n2}\sigma_{L/W} \\ \mathbf{M} < \mathbf{M_1}\text{: } \varepsilon_{n2}\sigma_{L/W} \end{cases} \quad (2.7)$$

where L/W is aspect ratio and a_3 and $\mathbf{M_1}$ are model coefficients. Results are shown in Figure 2.23 for the first regression ("Initial"; Figure 2.23a) and the subsequent regression ("Updated"; Figure 2.23b), with similar results. The mean aspect ratio does not extend below unity, which is guided by the data trends in Figure 2.23. Figure 2.23 shows data both from the literature (Skarlatoudis et al. 2016) and the present study. No prior models for the aspect ratio L/W of subduction events are available from the literature, so only the fit from Eq. (2.7) is shown.

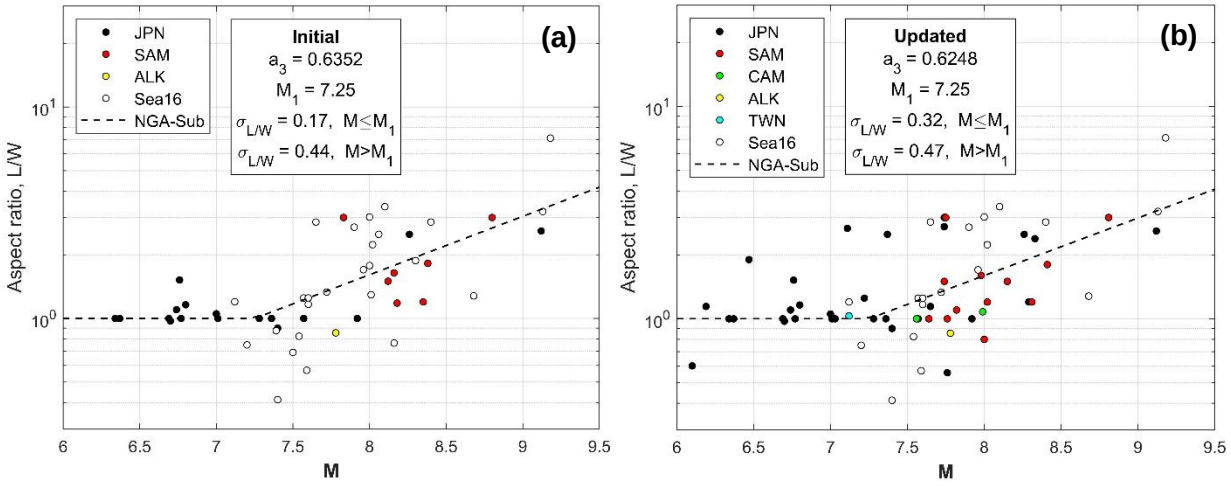

Figure 2.23 (a) Initial and (b) Updated geometric relations for aspect ratio for subduction interface earthquakes. Sea16 = Skarlatoudis et al. (2016).

Figure 2.24 shows fault rupture areas and aspect ratios for 27 intraslab events with FFMs. A rupture-area model with the same form as Eq. 2.6 by Strasser et al. (2010) is shown. This model was found to be unbiased with respect to the NGA-Sub data and hence was applied. A model for

L/W was not found in literature for intraslab events. The Nov 2017 data set was fit using Eq. 2.7 with the result shown in Figure 2.24(b) and marked as "Applied". That data set included 16 earthquakes in Table 2.5 along with one event in Japan (marked with a black asterisk) that was initially considered as intraslab and subsequently reclassified as outer-rise; those events are depicted in Figure 2.24(b) using filled symbols. The open symbols represent ten events in Japan and one event in Cascadia that were not used in the regression but are now part of the NGA-Sub database. The addition of the new data suggests that the dependency of the aspect ratio on magnitude for intraslab events is not as strong as it was initially considered. The mean of all the data (excluding the outer-rise event) is also shown in Figure 2.24(b) for reference.

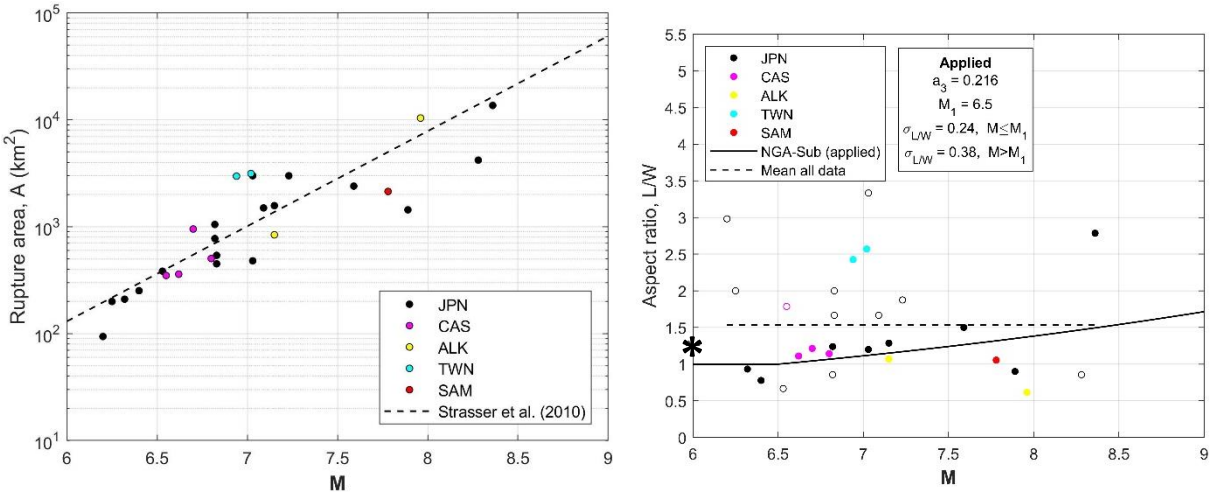

Figure 2.24 Geometric relations for (a) rupture area and (b) aspect ratio for subduction intraslab earthquakes. Black asterisk represents an event in Japan that was initially considered as intraslab (for regression marked as "Applied") and subsequently reclassified as outer-rise**.**

The orientation of the rectangle representing the rupture surface is given by strike angle ϕ and dip angle δ (Figure 2.12). Most earthquakes without FFMs have moment tensor solutions that provide two estimates of these angles. One is often preferred based on physical considerations (i.e., alignment of dip angle with slab orientation) and is used in the simulations. Where a particular

nodal plane is not preferred, both are considered in the simulation procedure. For events without a moment tensor, the mean strike ($\bar{\phi}$) is estimated as parallel to the nearest portion of the subducting plate (for all event-types). Mean dip ($\bar{\delta}$) is similarly taken from the dip of the subducting plate for interface events, whereas for intraslab events, the mean dip is taken as an average of nearby events with available moment tensor solutions. A specific set of angles used in simulations is given as:

$$\phi = \bar{\phi} + \varepsilon_{\phi} \tag{2.8}$$

$$\delta = \bar{\delta} + \varepsilon_{\delta} \tag{2.9}$$

where ε_{ϕ} and ε_{δ} are uniform distributions centered on the means with ranges of ± 30 degrees and 10 degrees, respectively.

Figure 2.25 shows the parameterization of hypocenter location on the rupture plane, with θ_L and θ_W representing normalized location relative to the upper left corner (as viewed from the hanging wall). A model for these locations was presented by Mai et al. (2005). The mean location along strike is at the midpoint ($\bar{\theta}_L = 0.5$) and slightly deeper than the mid-point in the down-dip direction ($\bar{\theta}_W = 0.57$; Mai et al. 2005).

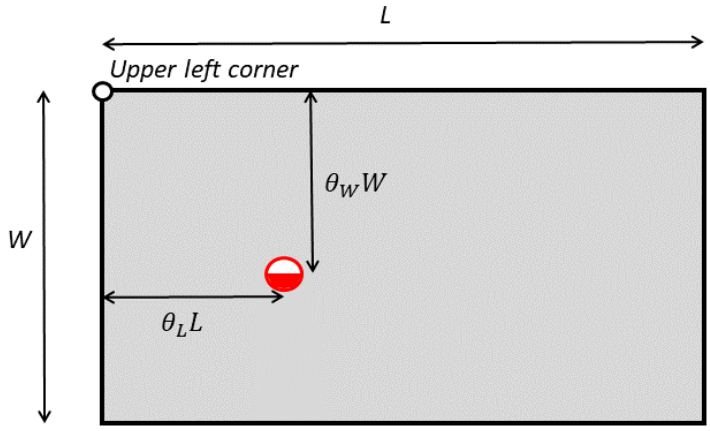

Figure 2.25 Parameterization of earthquake location on fault (view is normal to fault plane from hanging wall).

Figure 2.26 shows hypocenter locations using the data from Table 2.5 for interface events. An earlier analysis (Nov 2017) used to derive parameters used in simulations was based on a subset of 27 events, mainly from Japan and South America, which are shown in Figure 2.26(a). The results confirm an along-strike mean close to the mid-point ($\bar{\theta}_L = 0.535$) whereas the down-dip mean varies by region ($\bar{\theta}_W = 0.451$ for events in Japan and $\bar{\theta}_W = 0.624$ for events in South America). Figure 2.26(b) presents updated results derived using data in its current state, which include 18 additional interface events. Results are congruent with previous observations, though the difference observed in the down-dip direction by region is less evident in the light of the new data.

Similarly, Figure 2.27 shows hypocenter locations using the data from Table 2.5 for intraslab events. A subset of 15 events was used to perform the analysis shown in Figure 2.27(a). The results indicate that both along-strike and down-dip means are close to the mid-point ($\bar{\theta}_L = 0.424$ and $\bar{\theta}_W = 0.511$) independent of region. Updated results derived after adding nine events since Nov 2017 are presented in Figure 2.27(b). These new observations do not differ significantly from the previous results.

For modeling purposes, a specific hypocenter location is expressed as:

$$\theta_L = \bar{\theta}_L + \varepsilon_{n3}\sigma_{\theta_L} \tag{2.10}$$

$$\theta_W = \bar{\theta}_W + \varepsilon_{n4}\sigma_{\theta_W} \tag{2.11}$$

where ε_{n3} and ε_{n4} are standard normal variates. The distributions are truncated at the limits of the rectangle (i.e., both θ_L and θ_W have a range of 0 to 1.0).

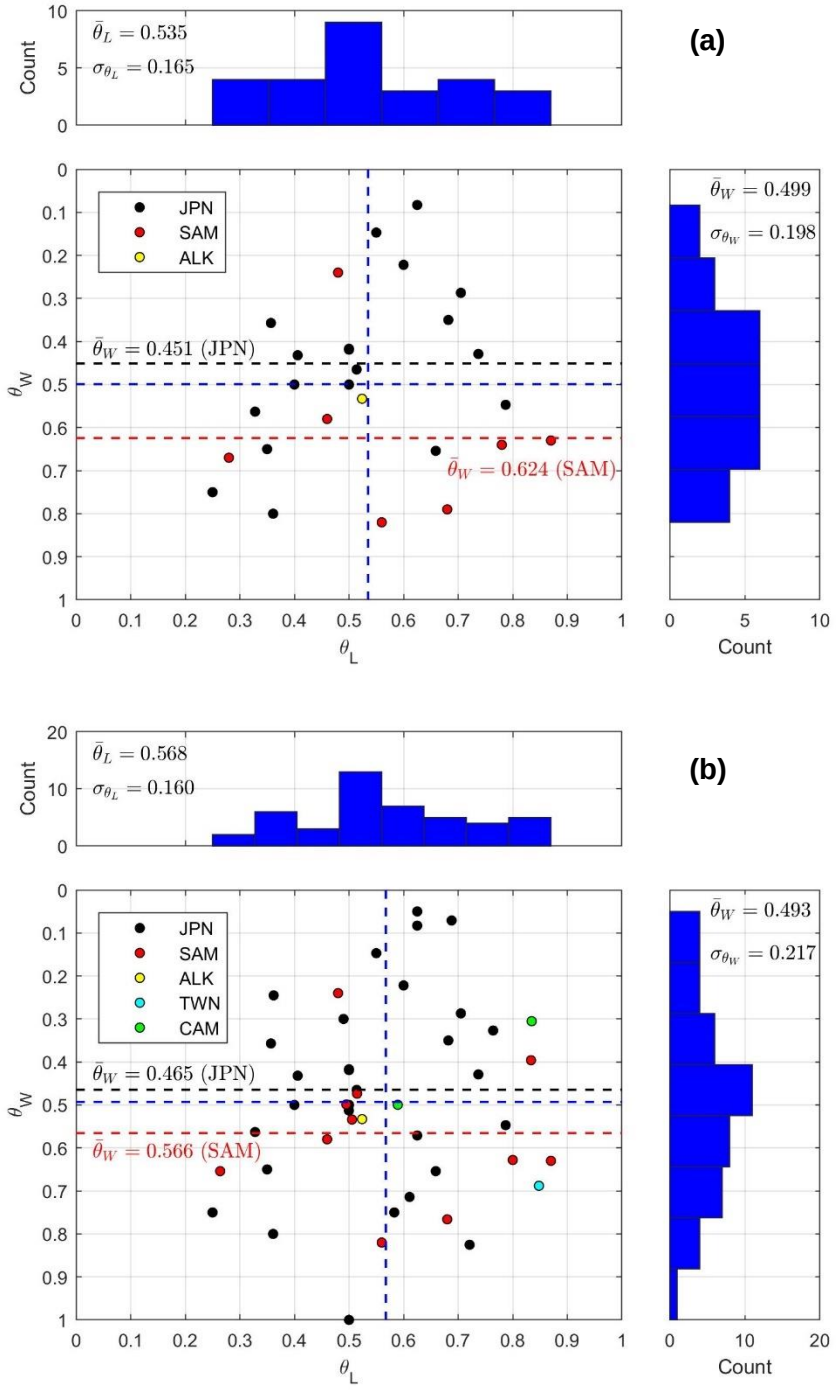

Figure 2.26 Locations of hypocenters on fault plane for interface events. (a) Results for data analyzed to support project simulations (dated Nov. 2017). (b) Results derived using the data in its current state (dated Dec. 2019).

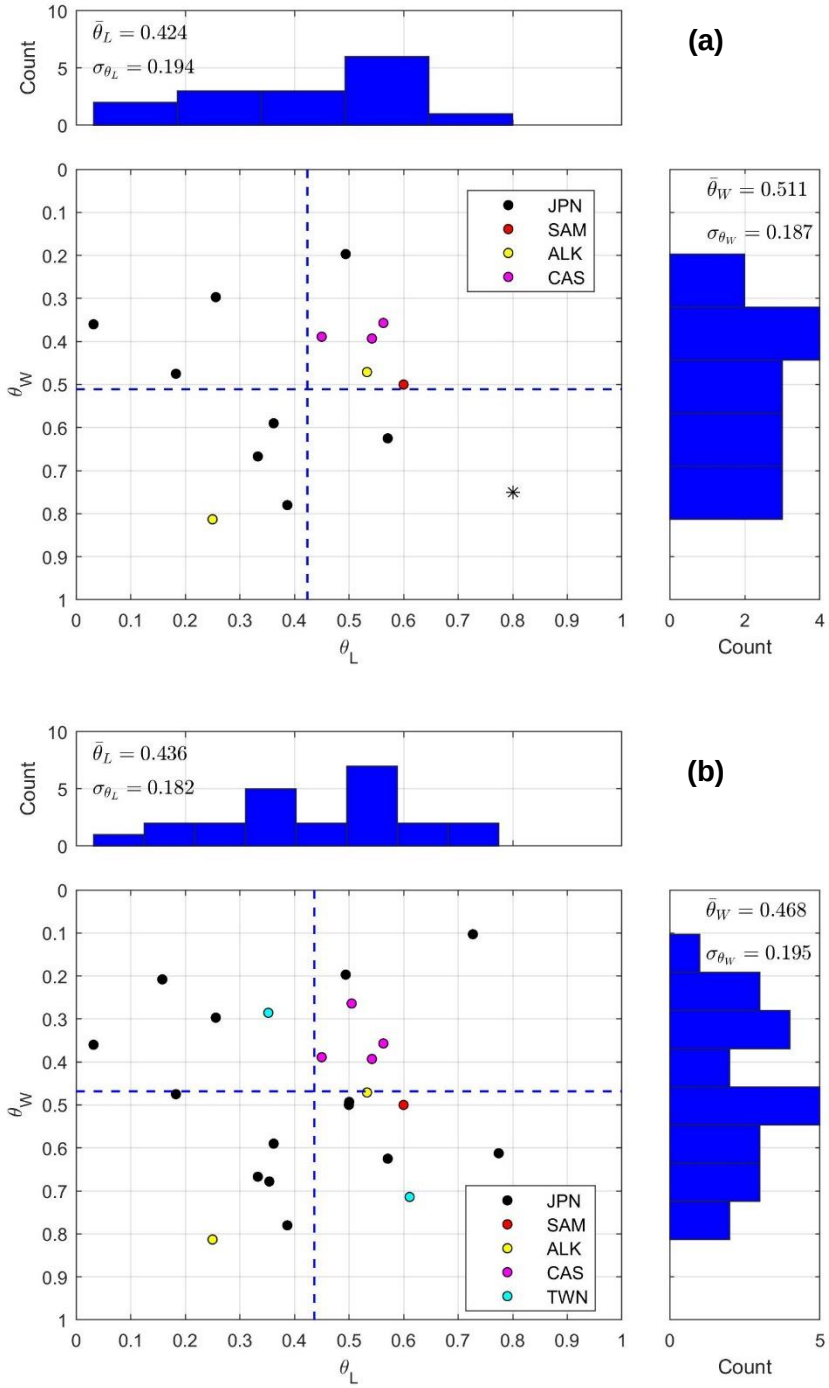

Figure 2.27 Locations of hypocenters on fault plane for intraslab events. (a) Results for data analyzed to support project simulations (dated Nov. 2017). (b) Results derived using the data in its current state (dated Dec. 2019). Black asterisk represents an event in Japan originally considered as intraslab and later reclassified as outer-rise.

Based on the results of earlier analyses performed to support project simulations (dated Nov. 2017) and shown in Figure 2.26(a) and Figure 2.27(a), the along-strike mean was taken at the mid-point ($\bar{\theta}_L = 0.5$) for both interface and intraslab earthquakes. Down-dip means were taken using the regionally variable values in Figure 2.26(a) for interface events and at mid-depth ($\bar{\theta}_W = 0.5$) regardless of region for intraslab. The utilized standard deviation values as derived from data are indicated in Figure 2.26(a) for interface events and in Figure 2.27(a) for intraslab events.

Table 2.9 summarizes the resulting means ($\bar{\theta}_L$, $\bar{\theta}_W$) and standard deviations (σ_{θ_L}, σ_{θ_W}) of the locations of the hypocenters along-strike and down-dip that were investigated using NGA-Sub data by region and event type. Results provided by Mai et al. (2005), also shown in Table 2.9, are similar to the present findings. The utilized means and standard deviations are as given in Table 2.9.

Table 2.9 Hypocenter locations from NGA-Sub data (Contreras et al. 2020) and Mai et al. (2005). NGA-Sub results from full data set and Nov. 2017 subset (in parenthesis); means and standard deviations are for a normal distribution. Mai et al. results are for a normal distribution (all events, along-strike location θ_L), for a Weibull distribution (all events, down-dip location θ_W), and for a Gamma distribution (subduction dip-slip events, down-dip location θ_W).

Case	$\bar{\theta}_L$	σ_{θ_L}	$\bar{\theta}_W$	σ_{θ_W}
JPN interface	0.543 (0.516)	0.145 (0.156)	0.465 (0.451)	0.238 (0.190)
JPN slab	0.402 (0.327)	0.210 (0.171)	0.470 (0.499)	0.207 (0.201)
SAM interface	0.588 (0.587)	0.187 (0.204)	0.566 (0.624)	0.164 (0.191)
SAM slab	0.6 (0.6)	Only one event	0.5 (0.5)	Only one event
All regions interface	0.568 (0.535)	0.160 (0.165)	0.493 (0.499)	0.217 (0.198)
All regions slab	0.436 (0.424)	0.182 (0.194)	0.468 (0.511)	0.195 (0.187)
Mai et al. (2005); all events	0.5	0.23	0.549	0.181
Mai et al. (2005); subduction dip-slip events	N.A.	N.A.	0.430	0.121

2.5.2 Simulation Procedure

A simulation procedure is used to generate approximate fault dimensions conditional on the magnitude of the earthquake (**M**), the earthquake type, the hypocenter location (latitude, longitude, and focal depth), and orientation of one or two nodal planes (strike and dip). This procedure is modified from a previous version presented by Chiou and Youngs (2008) and has the following steps:

1. Identify source-specific information that comprises the input to the simulation procedure – hypocenter location, **M**, nodal plane strikes and dips (if available). The procedure allows for one preferred nodal plane from a moment tensor, two equally likely nodal planes from a moment tensor, or variable plane strike/dip angles when no moment tensor is available (per Eqs. 2.8-2.9).

2. Compute mean values of along-strike length as $\overline{lnL} = 0.5\left(\overline{lnA} + \overline{lnL/W}\right)$ and down-dip width as $\overline{lnW} = 0.5\left(\overline{lnA} - \overline{lnL/W}\right)$, with mean area and aspect ratio taken from Eqs. 2.6-2.7, respectively (with "Initial" coefficients and ε_n terms set to zero). The "Initial" coefficients were used in simulations before the "Updated" model was available; due to the lack of appreciable differences in the mean model, the simulations were not repeated with the "Updated" model (despite the increased dispersion).

3. Using independent random number generators, select a realization of variates ε_{n1} to ε_{n4}.

4. Define the fault dimensions *L* and *W* for the realization in (3) as:

$$lnL = 0.5\left(\overline{lnA} + \varepsilon_{n1}\sigma_A + \overline{lnL/W} + \varepsilon_{n2}\sigma_{L/W}\right) \tag{2.12}$$

$$lnW = 0.5\left(\overline{lnA} + \varepsilon_{n3}\sigma_A - \overline{lnL/W} - \varepsilon_{n4}\sigma_{L/W}\right) \quad (2.13)$$

5. Define the specific rupture location aligned with the strike and dip of the nodal plane using Eqs. 2.8-2.9 with the means and standard deviations of normalized locations from NGA-Sub data in Table 2.9 . Note that the absolute location of the hypocenter in space is fixed and does not change.

6. Sample across random variables as follows:

    a. If a preferred moment-tensor nodal plane is defined for the event, use N = 101 realizations across variates ε_{n1} to ε_{n4}.

    b. If two alternative nodal planes are to be considered, repeat the process in (4a) for both nodal planes. For this case, N = 101 realizations was used across both variates ε_{n1} to ε_{n4} and across both nodal planes (approximately 50 realizations of the variates for each plane).

    c. For events without a moment tensor in which strike and dip are estimated, N = 101 realizations are applied for variates ε_{n1} to ε_{n4}, ε_{ϕ}, and ε_{δ}.

7. For all 101 realizations of rupture rectangles from (3)-(6), compute distances to a grid of points on the ground surface. The grid is defined as an array in polar coordinates (ρ, θ). The radius (ρ) extends to 300 km from the epicenter, with variable spacing between grid points ranging from 2 km near the epicenter ($\rho \leq 20$ km) to 25 km in the outermost region (125 km $\leq \rho \leq$ 300 km). The angular coordinate (θ) varies from 0 to 345 degrees in 15 degree increments.

8. For each grid point, compute the median distance among realizations. Identify the single fault plane among the 101 realizations that minimizes the misfit (sum of square of residuals) to the set of medians for all grid points.

   This procedure is coded in Fortran (CCLD5).

2.6 EVENTS SUMMARY

The total number of events in the source database with an assigned earthquake identification number (NGAsubEQID) is 1,880. QA procedures (Section 3.5) eliminated 98 events, mostly because of missing magnitudes or hypocenter locations, decreasing the number of potentially usable earthquakes to 1,782. Screening to remove events without an assigned event-type reduced the number of events to 991. Table ES-1 in Contreras et al., 2022 contains hypocenter and moment-tensor information for these 991 events, along with event-type assignments.

Figure 2.28 shows the regional distribution of the 991 events with event-type classifications, including both subduction earthquakes (interface and intraslab) and other earthquake types (shallow crustal and outer-rise). South America contributes the most subduction earthquakes, followed by Japan and New Zealand, which have similar number of subduction events. For most regions, subduction events are dominant; New Zealand is an exception, with 135 shallow crustal and 139 subduction earthquakes.

Figure 2.29(a) shows the event-type distribution combining events with flags indicating high - and low - confidence. The dataset is dominated by interface and intraslab earthquakes which are nearly evenly distributed. A significant number (221) of shallow crustal earthquakes are present in the database, mostly from New Zealand. While not directly useful for NGA-Sub

modeling, these data were retained in the database. The contribution of outer-rise earthquakes is small. Figure 2.29(b) shows the distribution of recordings by event-type, which generally mirrors the event distribution. If unclassified events were included in Figure 2.29, they would comprise more than 40% of the events, but only 5% of the recordings.

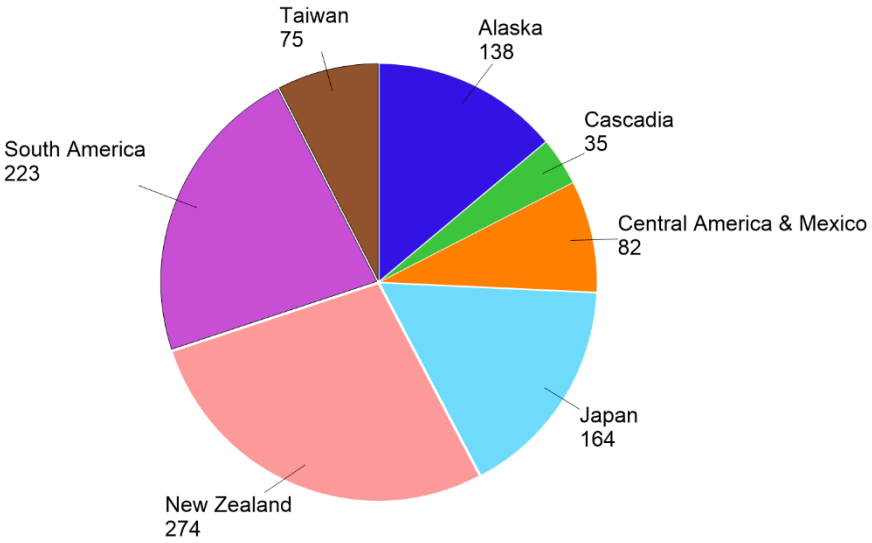

Figure 2.28 Distribution of earthquakes with event-type assignments by region.

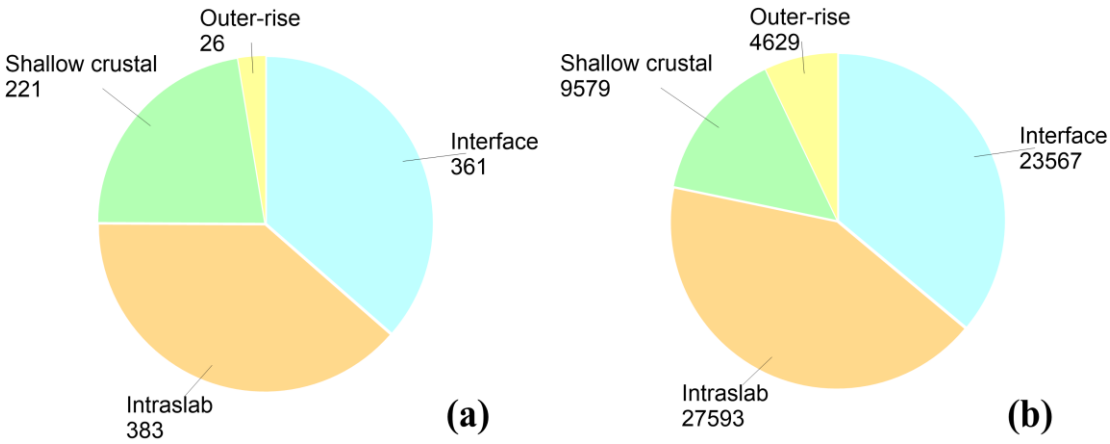

Figure 2.29 Distribution of (a) earthquakes and (b) recordings by event-type.

Figure 2.30(a) shows the magnitude distribution of all earthquakes included in the NGA-Sub database, including those without event-type classifications. Approximately 73% of the events have magnitudes **M** ≥ 5.0 and the dataset is dominated by mid-size earthquakes with **M** = 4.5 to 7.0. There are 13 large events with **M** ≥ 8; six of these occurred in South America while seven occurred in Japan. Ten of the **M** ≥ 8 events are interface, two are intraslab, and one is outer-rise. The majority of the earthquakes with magnitudes **M** < 5 are from South America (~40%) and New Zealand (~30%). Figure 2.30(b) shows the magnitude distribution of earthquakes with event-type classifications. The subset of events with subduction event-types (interface or intraslab) are also identified in Figure 2.30(b); subduction events dominate for **M** > 5.5 and all events with **M** ≥ 8.15 are subduction.

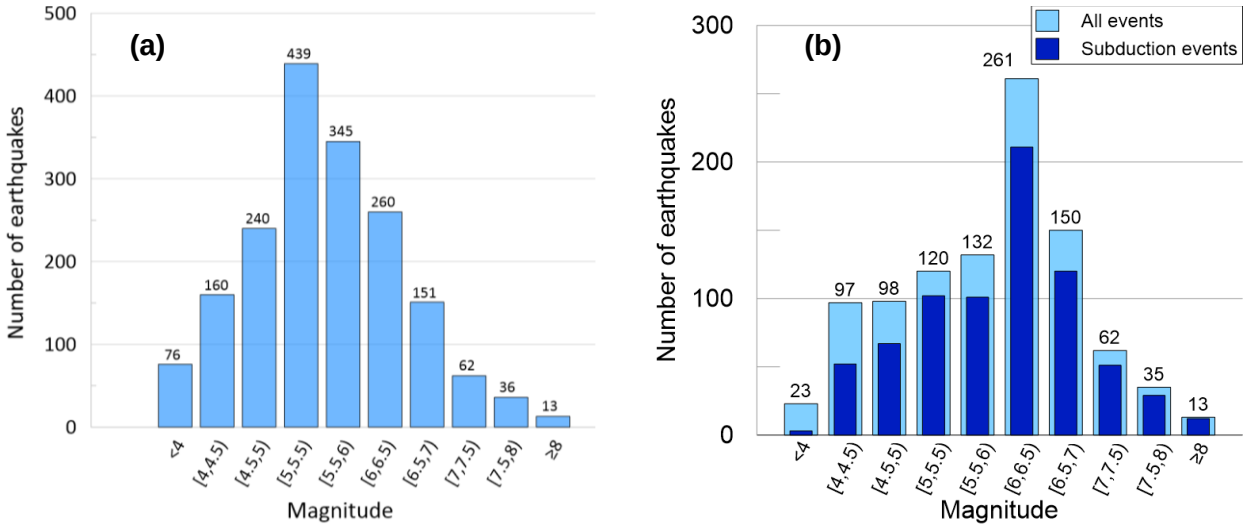

Figure 2.30 Magnitude distribution of (a) all earthquakes and (b) earthquakes with event-type assignments.

Figure 2.31(a) shows the magnitude distribution of earthquakes differentiated by event-type, and Figure 2.31(b) similarly shows the magnitude distribution of recordings. Unclassified events are a significant fraction of the database for **M** < 6, intraslab and interface events contribute

roughly equally for magnitudes between 4.5 and 7, and interface events dominate at larger magnitudes.

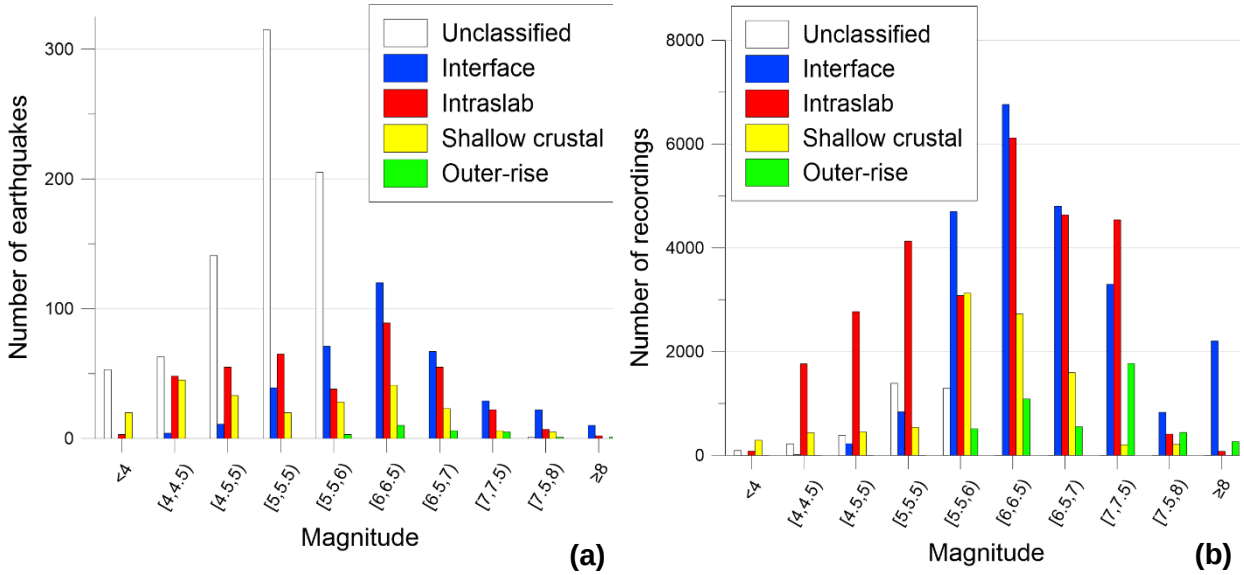

Figure 2.31 (a) Magnitude distribution of the events by type of earthquake. (b) Magnitude distribution of the recordings by type of earthquake.

The time period covered by the 991 events in the source database extends from 1937 to 2016. It was necessary to apply a cutoff date as part of NGA-Sub, which was 2016; data for significant events since 2016 are being added in post-NGA-Sub projects. Figure 2.32 presents the cumulative number of earthquakes over time with differentiation by type of earthquake, in linear and logarithmic scales. More than 80% of the events in the database occurred after 2000, including the 2010 **M**8.81 Maule (Chile) earthquake and the 2011 **M**9.12 Tohoku (Japan) earthquake. Relatively recent large earthquakes include the 2014 **M**8.15 Iquique (Chile), 2015 **M**7.89 Chichi-shima (Japan), the 2015 **M**8.31 Illapel (Chile), the 2016 **M**7.82 Ecuador, and the 2016 **M**7.85 Kaikoura (New Zealand) earthquakes.

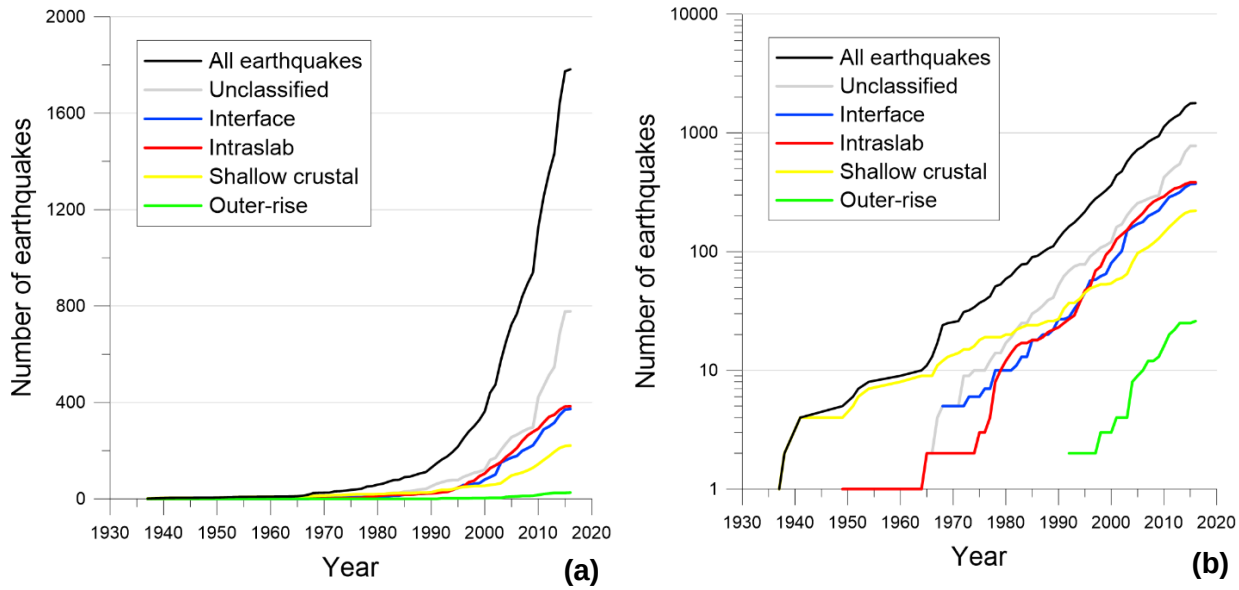

Figure 2.32 Cumulative number of events over time by type of earthquake using (a) linear and (b) logarithmic scales.

There are 100 NGA-Sub events with published finite-fault models incorporated into the database. While only 5% of the events, they contribute 35% of the ground-motion recordings. Figure 2.33 summarizes the distribution of FFMs by event-type; more than 80% of these events are subduction (47 interface and 35 intraslab earthquakes).

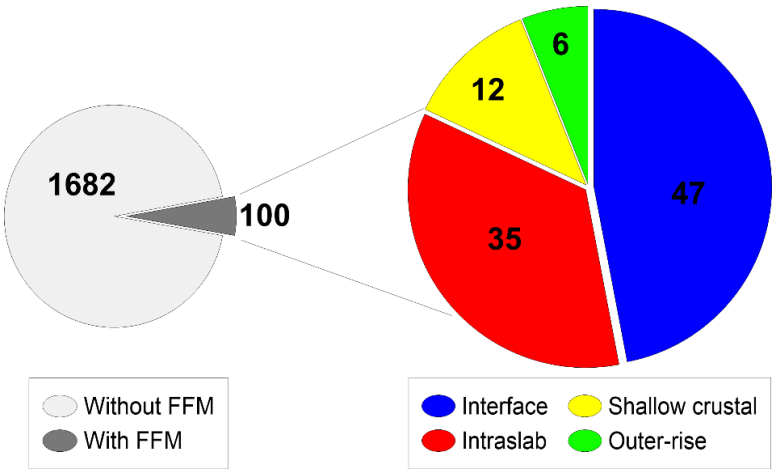

Figure 2.33 Distributions of events with FFMs in the NGA-Sub database.

Figure 2.34 shows the magnitude distribution of the 100 events with FFMs in the NGA-Sub database (shaded in blue). Most of the earthquakes (90 events) have magnitudes ranging from **M** = 6 to 8.5. Earthquakes located in Japan (63 events, shaded in red) contribute disproportionately to the total number of events with FFMs.

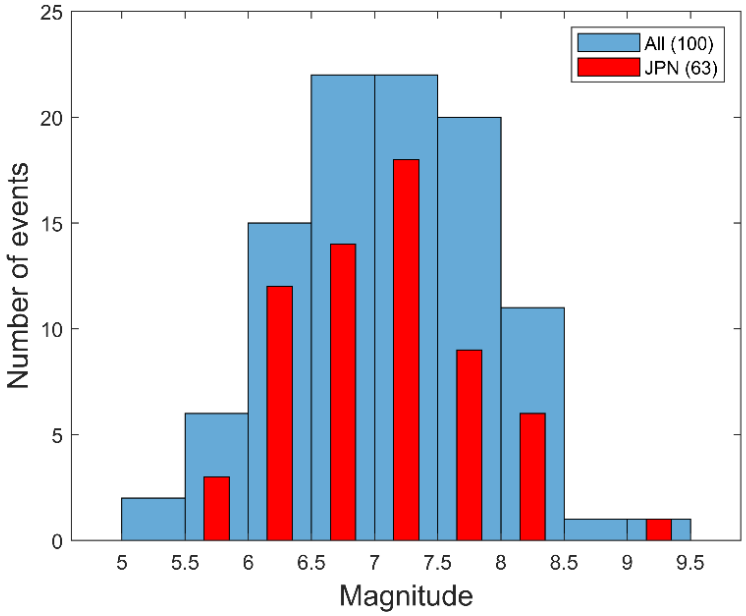

Figure 2.34 Magnitude distribution of the events with FFMs in the NGA-Sub database.

Figure 2.35 shows the magnitude distribution of the recordings from the 100 events with FFMs in the NGA-Sub database (shaded in blue). Approximately 83% of the recordings are from earthquakes with magnitudes ranging from **M** = 6 to 7.5. Most of the recordings (87%, shaded in red) are from earthquakes located in Japan, including the 1293 recordings contributed by the 2011 **M**9.11 Tohoku earthquake.

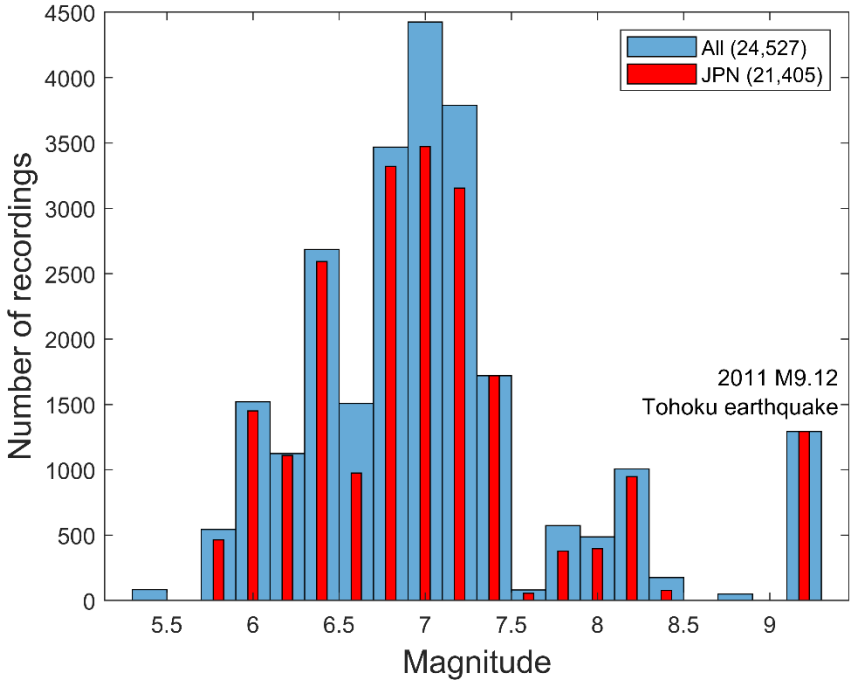

Figure 2.35 Magnitude distribution of the recordings from events with FFMs in the NGA-Sub database.

Parameters descriptive of style-of-faulting (or fault type) are compiled independently of event-type. For example, intraslab earthquakes can commonly have normal or strike slip fault types. In NGA-Sub, fault type is defined based on rake angle, as described in Section 2.3.2c. Figure 2.36 shows the distribution of NGA-Sub events with respect to rake and dip angles. Interface events (blue squares) are mostly associated with reverse faulting (60°<rake<120°) and with reverse-oblique faulting (30°<rake<60° and 120°<rake<150°), whereas intraslab events (red circles) have different faulting styles. Furthermore, most of interface events have dip angles lower than 30 degrees, which is consistent with the geometry of the subducting plates; whereas intraslab events dip in different directions. There are a two apparently misclassified events that are assigned low confidence (Section 2.3.2d), one with dip of 79° and rake -152° (Event 4000017), the other with dip of 33° and rake of 5° (Event 4000013).

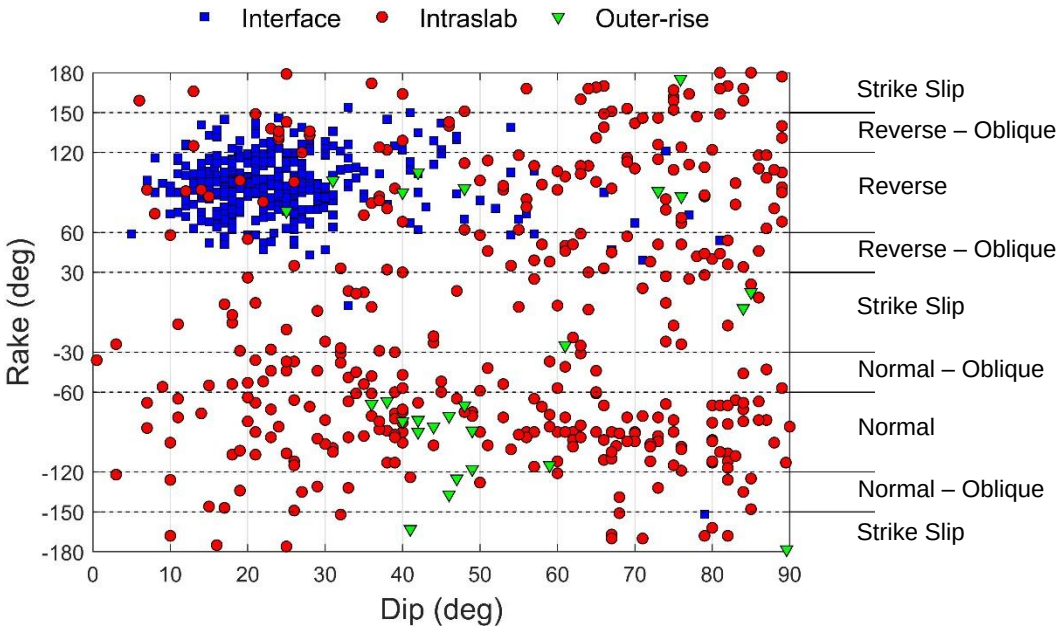

Figure 2.36 Rake and dip angles for interface and intraslab events in the NGA-Sub database.

3 SUBDUCTION ZONE EARTHQUAKE SOURCE-TO-SITE PATHS AND QUALITY ASSURANCE PROCEDURES

The main contents of Chapter 2 and this chapter are taken from a part of Chapter 4 of a report on the NGA-Sub database (Contreras et al., 2020), subsequently modified for a journal paper (Contreras et al., 2022). In this chapter, I describe the path parameters characterization for use in NGA-Sub project along with the quality assurance procedures carried out to check accuracy and consistency of the database. The NGA-Sub project involved many people and truly represents a group effort. However, the portions of Contreras et al. (2020, 2022) that are reproduced here represent work that the author was mainly responsible for performing, with review and comments from others. Portions of the aforementioned documents that other NGA-Sub researchers led are not reproduced here. The organization, formatting, and numbering of the different sections were adjusted for this document. Section 3.2 has been extended to include a brief discussion regarding site-to-source distances uncertainty. Section 3.4 has been added to include a summary of the path attributes in terms of percentage of path in the forearc and backarc regions.

3.1 INTRODUCTION

As mentioned in Chapter 2, the NGA-Sub relational database contains 20 tables, nine of which are related to source parameters and two of which are related to path parameters; the development of the latter two tables is the focus of this chapter. Path parameters that are used in NGA-Sub GMMs are rupture distance (R_{rup}), the maximum rupture distance that should be considered for a given data provider and event to avoid sampling bias (R_{max}), and the portion of the source-to-site path in

forearc and backarc regions (as applicable). Other distance metrics not directly used in NGA-Sub GMMs are also provided. The development of R_{max} criteria is not described here, because the author had a minor role in this work (information available from Contreras et al. 2020, 2022).

3.2 SITE-TO-SOURCE DISTANCE

3.2.1 Distance Computation

Site-to-source distance computations were performed using a code (P4CF) that takes as input the geodetic coordinates of instruments that recorded the event and the three-dimensional representation of the ruptured fault. The fault is represented by one or more rectangles, as described in Chapter 2. Where more than one rectangle is used to represent a rupture surface, distances are computed to each, and the closest distance is used. The distances are calculated using the preferred rupture rectangle(s) for each event as described above. Alternate realizations of rupture rectangles to investigate distance uncertainties have not been considered.

The output of P4CF for a given site is rupture distance R_{rup} (closest distance from site to any point on the rupture surface), Joyner-Boore distance R_{JB} (closest distance from site to any point on the surface projection of the rupture surface), R_x (distance measured perpendicular to the fault strike from the surface projection of the up-dip edge of the rupture surface), R_y (distance measured parallel to the fault strike from the midpoint of the surface projection of the rupture surface), R_{y0} (distance measured parallel to the fault strike from the end of the surface projection of the rupture surface), R_{hyp} (hypocentral distance), R_{epi} (epicentral distance), R_{rms} (root-mean-square distance), the location on the fault surface from which the closest distance was measured (geodetic coordinates and depth), and a series of parameters related to rupture directivity modeling that were not used in NGA-Sub. These outputs are saved to the *Path* table in the relational database.

Mean rupture distance (Thompson and Baltay, 2018) is a promising distance metric, although it was not computed for the NGA-Sub database.

Schematics showing the definition of different site-to-source distances computed in NGA-Sub are provided in Figure 3.1. Another path-related table, derived using procedures described in Section 3.3, lists percentages of the path through zones with different volcanic arc flags (*EventVolArc* table).

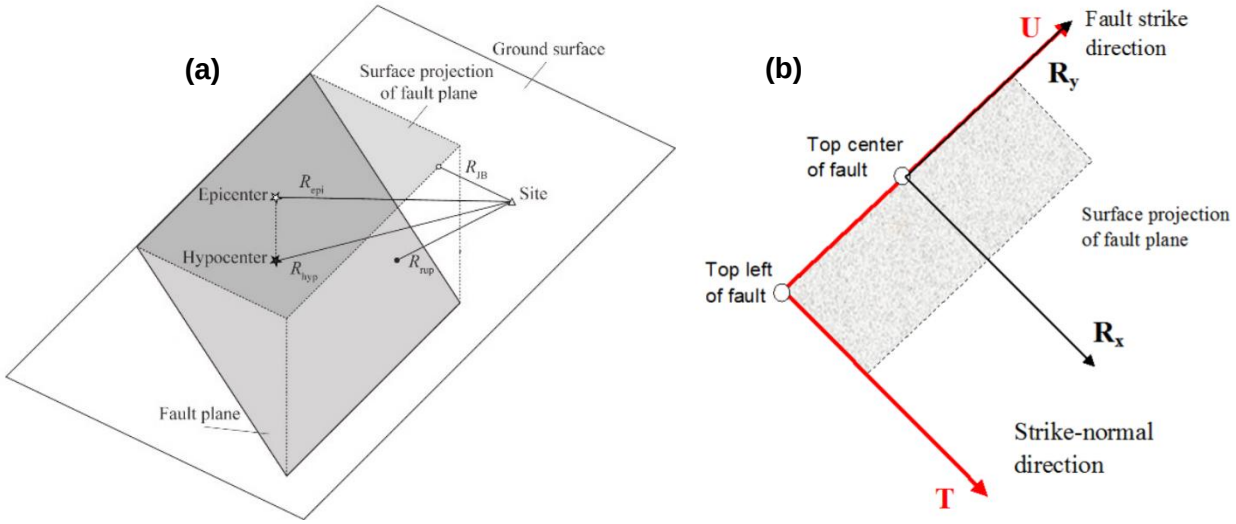

Figure 3.1. Schematics of different site-to-source distance metrics computed in NGA-Sub. (a) R_{rup}, R_{JB}, R_{hyp}, and R_{epi} (modified from Yang et al., 2019); (b) R_x and R_y (Ancheta et al., 2013); U and T parameters from the generalized coordinate system in Spudich and Chiou (2008). Positive directions are shown.

3.2.2 Rupture Distance Uncertainty

Rupture distance uncertainty due to variability of the rupture surface geometry for the same earthquake was not investigated in NGA-Sub. Instead, distance metrics were computed considering a single rupture geometry, by means of selecting and trimming a preferred FFM or from the result of the simulation procedure (described in Section 2.5.2), which provides a single

rupture rectangle out of the 101 realizations performed. Rupture distance uncertainty is conceptualized as follows:

- When published FFMs are available, the uncertainty could be derived from a single model if the study provides uncertain fault dimensions associated with the inversion. Alternatively, if multiple studies using preferred data sources were available, variations among the resulting models could be viewed as contributing to rupture distance uncertainty. When multiple models are available for a single event, but only one of the models uses preferred data sources, the resulting model-to-model variations may not lead to reasonable rupture distance uncertainties.

- When FFMs are not available, the uncertainty would be derived from the alternate realizations from the simulation procedure in Section 2.5.2.

In Section 2.4.2, variations of rupture distance associated with different FFMs was explored for the 2010 **M**8.81 Maule, Chile earthquake. The R_{rup} demonstrated considerable differences for some stations located near the rupture when computed using different FFMs. Since some of these models do not use preferred data sources, the variations described may overestimate rupture distance uncertainties.

I investigate here R_{rup} uncertainty for the case of an event without a published FFM. An earthquake in Japan (NGAsubEQID = 4000040, **M** = 6.22, event-type = interface, and hypocentral depth = 42.5 km) has been considered to analyze the distribution of R_{rup} resulting from all the 101 simulated fault planes. Figure 3.2 shows all the rupture rectangles simulated for this event, including the rectangle utilized in NGA-Sub for distance calculations (shown in red). All these

realizations have the same hypocenter (red star), strike, and dip angles (which is the typical procedure adopted for interface events with an available moment-tensor solution) but the rupture dimensions (length L, width W, and aspect ratio L/W) and the location of the hypocenter along the strike and dip directions are randomized, as explained in Section 2.5.2. There are seven sites with $R_{rup} \leq 50$ km in the NGA-Sub database that recorded this event (identified by their names in Figure 3.2). Using P4CF, R_{rup} distances were computed for these seven sites, considering now all 101 simulated rupture rectangles besides the single rectangle utilized in NGA-Sub.

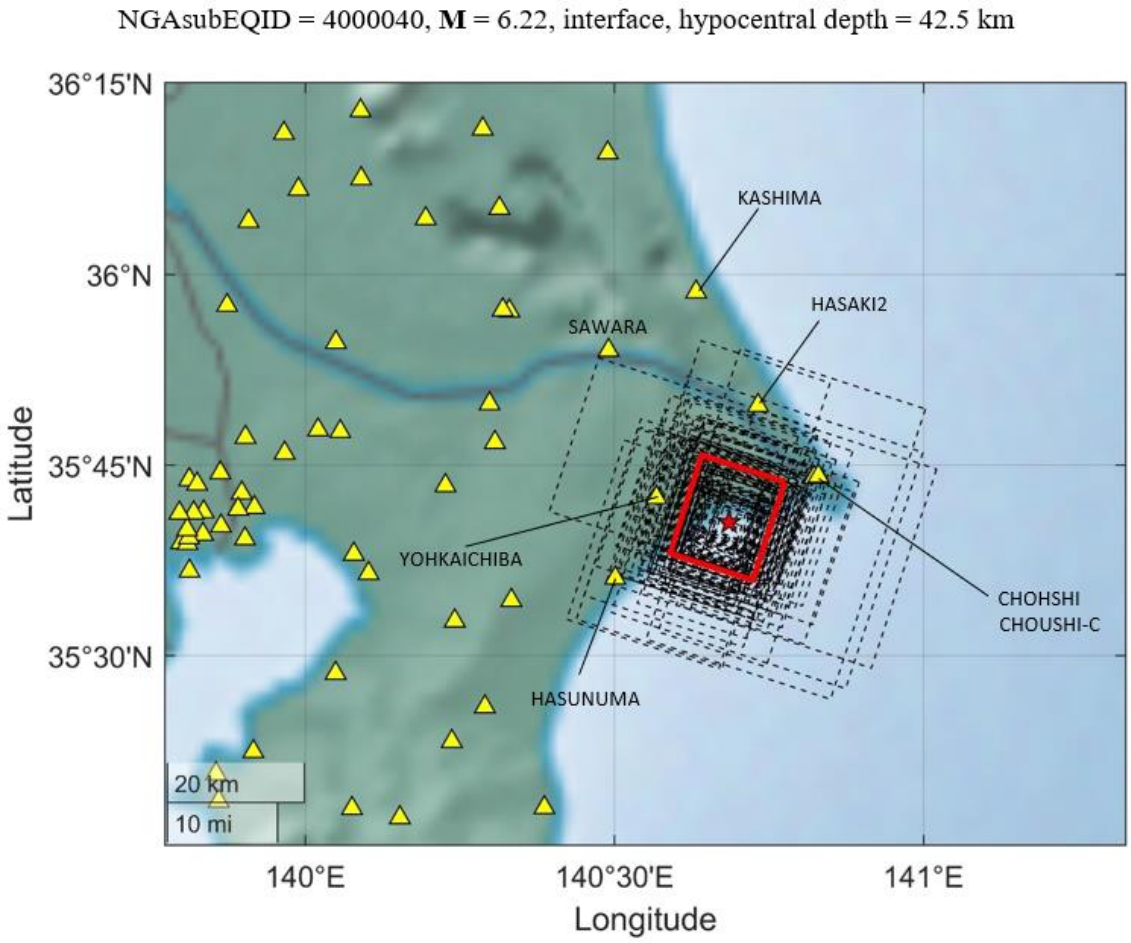

Figure 3.2. Example of the rupture rectangles resulting from the simulation procedure (101 realizations) for an interface event in Japan. The epicenter is shown as a red star and the rupture rectangle utilized in NGA-Sub for distance calculations is shown in red.

Figure 3.3 shows the R_{rup} distributions for the six recording sites identified in Figure 3.2, along with the median R_{rup} value (black dashed lines), and the R_{rup} value used in NGA-Sub (red lines); CHOHSHI and CHOHSHI-C are located very close to each other and the distance distributions are practically the same; only CHOHSHI is shown in Figure 3.3. The median R_{rup} and the R_{rup} value utilized in NGA-Sub are different because the simulation procedure (CCLD5 code) uses a grid of pseudo-stations to find the realization that minimizes the difference between R_{rup} and the median R_{rup} across all the pseudo-stations. Figure 3.3 shows that the range of R_{rup} distributions varies depending on the location of the sites with respect to the rupture realizations. For sites located northeast of the area where the simulated ruptures concentrate (CHOHSHI, HASAKI2, and KASHIMA), the distance range is approximately 10 km, which seems not neglectable for short distances. For the other sites considered in the analysis, the distance range is approximately 1-3 km, which is not very significative.

The studied example is for a **M**6.22 interface earthquake with hypocentral depth of 42.5 km, which generates relatively narrow distance distributions. A higher impact on R_{rup} distributions is anticipated for larger and shallower interface events because of the larger associated rupture area and its proximity to the ground surface. Another factor that probably introduces higher uncertainty is when the strike and dip angles are randomized instead of being fixed. A more systematic investigation including more subduction events with different characteristics would provide additional insights.

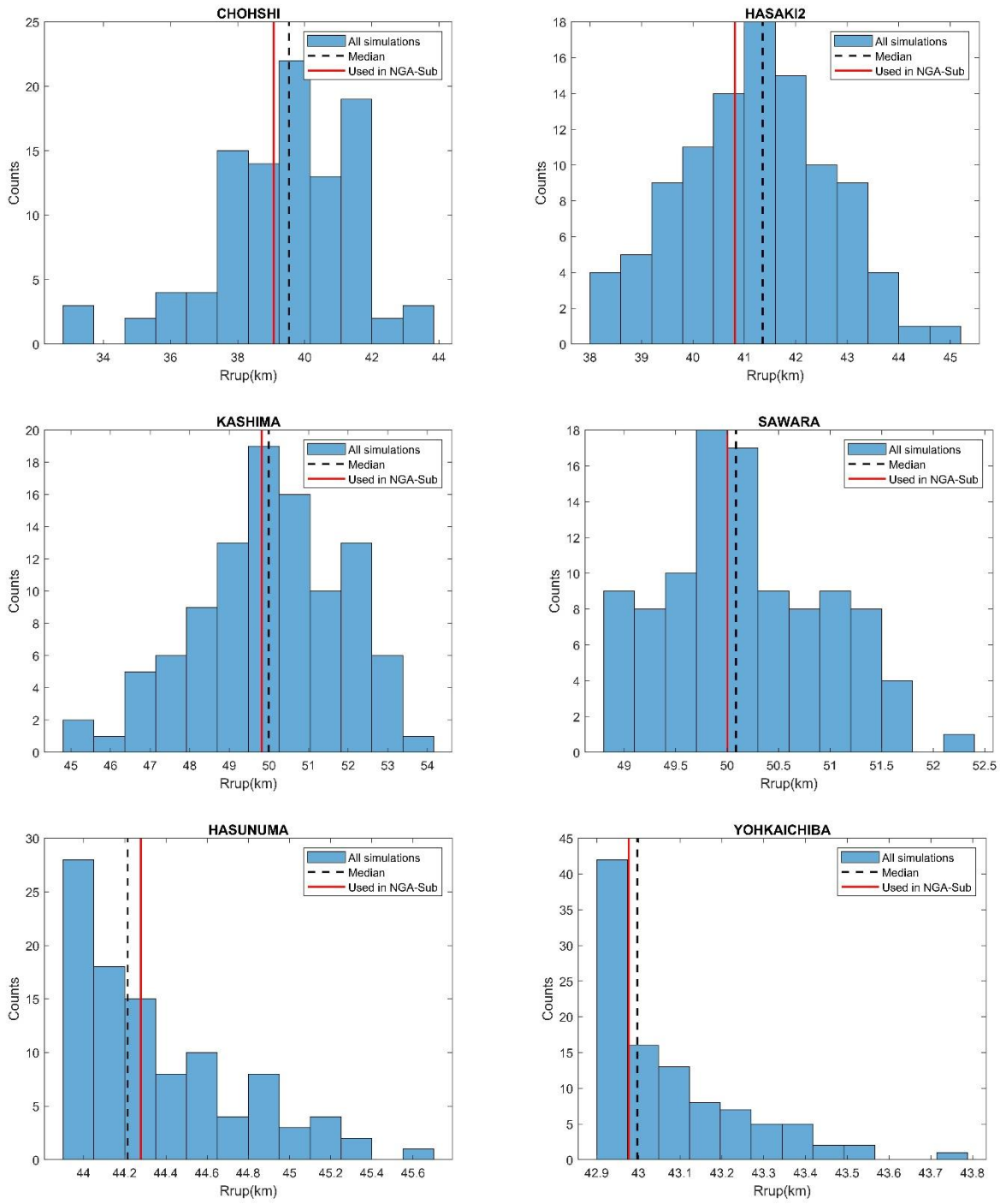

Figure 3.3. *Rrup* distributions for the analyzed sites.

3.3 VOLCANIC ARC FLAGS

Subduction zone plate boundaries produce geologic structures in the crust and upper mantle that affect seismic wave propagation. Many subduction zones are associated with a volcanic arc, where the down-going oceanic slab begins to melt, and plumes of magma rise to form volcanoes on the surface of the overriding slabs. For NGA-Sub, volcanic arc locations were used to categorize the forearc (trench-side) and backarc of each subduction zone region.

The delineation of the volcanic arc allows both epicentral locations and strong motion sites to be classified as forearc or backarc. Most subduction zone events occur either at the interface or within the subducting slab. Interface events are generally in the forearc. Intraslab events are also mostly in the forearc, but some can occur in the backarc when located in the slab at great depth (e.g., Figure 3.4).

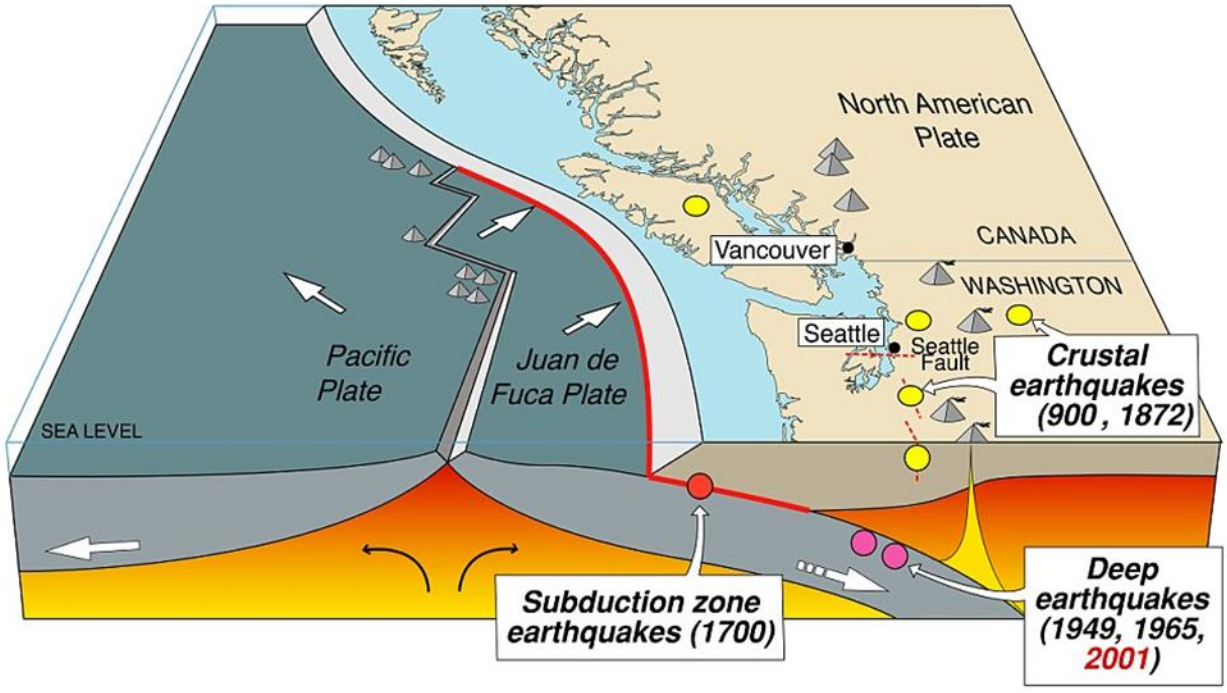

Figure 3.4. Cascadia subduction zone geometry, displaying different earthquake sources. Interface earthquakes are labeled as "Subduction zone earthquakes" and intraslab earthquakes are labeled as "Deep earthquakes." After Wells et al. (2000).

Volcanic arcs were determined for each of the seven regions in the NGA-Sub database by drawing a line by eye through the average trend of volcanic peaks. The locations of volcanic peaks, based on volcanoes with eruptions during the Holocene period (approximately the last 10,000 years), were obtained from the Smithsonian Institute's Global Volcanism Program (2013). Judgment was used to draw a smooth line for the volcanic arc, rather than to represent the arc as a jagged piecewise line connecting individual volcanic peaks. Figure 3.5 shows Alaska volcano locations (orange symbols) and the volcanic arc passing through them (green line between zones 1 and 2). This was repeated for all of the NGA-Sub regions except Taiwan, for which all sites are assigned as forearc because the island largely consists of forearc accretionary sediments (Ho 1986, Chemenda et al. 1997, Lundberg et al. 1997).

All events and ground-motion recording sites were assigned one of the volcanic arc flags listed in Table 3.1. Volcanic arc flags are provided for each event in the *EventVolArc* table within the source database and for each site in the *SiteVolArc* table (Tables 3-4 in Mazzoni et al. 2022). Most back-arcs correspond to Flag 1 and most forearcs to Flag 2. Japan's complex tectonic geometry required it to be separated into multiple forearc and backarc regions. There are two forearcs, relating to subduction of both the Pacific and Philippine Sea plates under Japan (Figure 3.6). The forearc region associated with the subduction of the Pacific plate at the Japan Trench is designated the generic Flag 2. The Philippine Sea plate subducts beneath the southern portion of Japan at the Nankai Trough and beneath the Okinawa plate at the Ryukyu Trench; the associated forearc is designated Flag 3 (Table 3.1).

Table 3.1 Description of volcanic arc flags.

Flag	Event Count	Site Count	Description
0	168	561	Outside of volcanic arc zone
1	175	1927	Backarc
2	1408	3169	Forearc, including Japan Trench in the Japan region
3	31	708	Forearc, Ryukyu Trench and Nankai Trough in the Japan region

The lateral limits of the volcanic arc correspond to the limits of the subducting slab. In general, the edges of the subducting slab were defined by the limits of slab depth contours as defined by the USGS's Slab1.0 model (Hayes et al., 2012). Figure 3.5 shows how the edges of the slab, as well as the edges of the forearc and backarc zones, were defined for the example of the Alaska subduction zone. Areas deemed to be outside of the subduction zone (east of the edge in Figure 3.5) are assigned Flag 0. Similarly, Figure 3.6 shows how the boundaries for the forearc and backarc zones were defined for the Japan subduction zone.

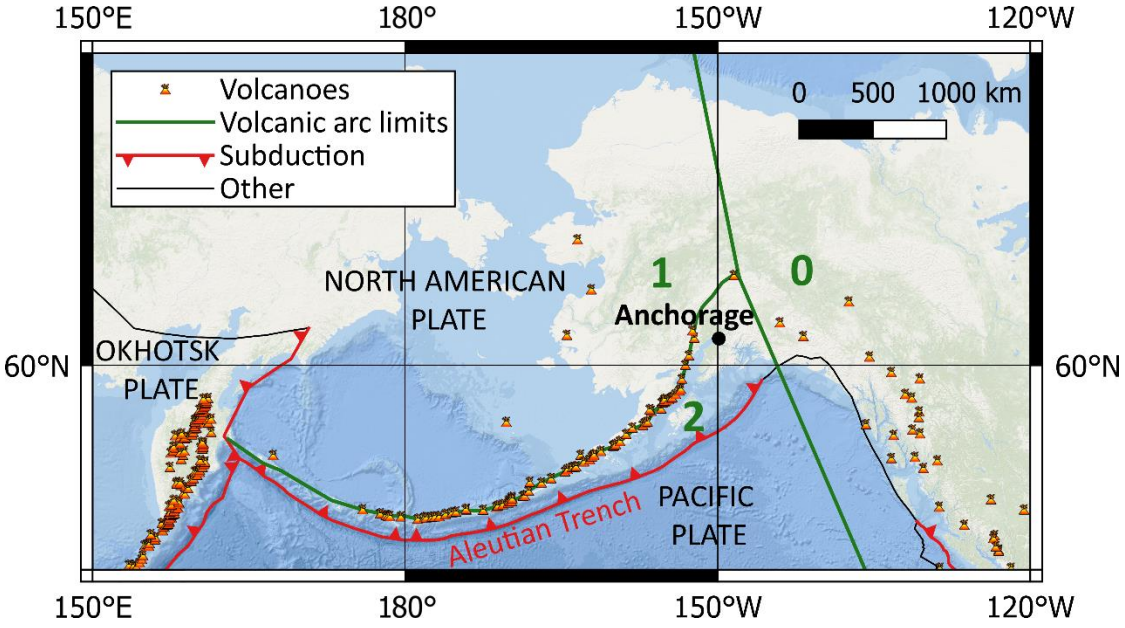

Figure 3.5. Example of volcanic flag region extents in Alaska/Aleutians subduction zone. The green line between zones 1 and 2 follows the average trend of volcanic peaks.

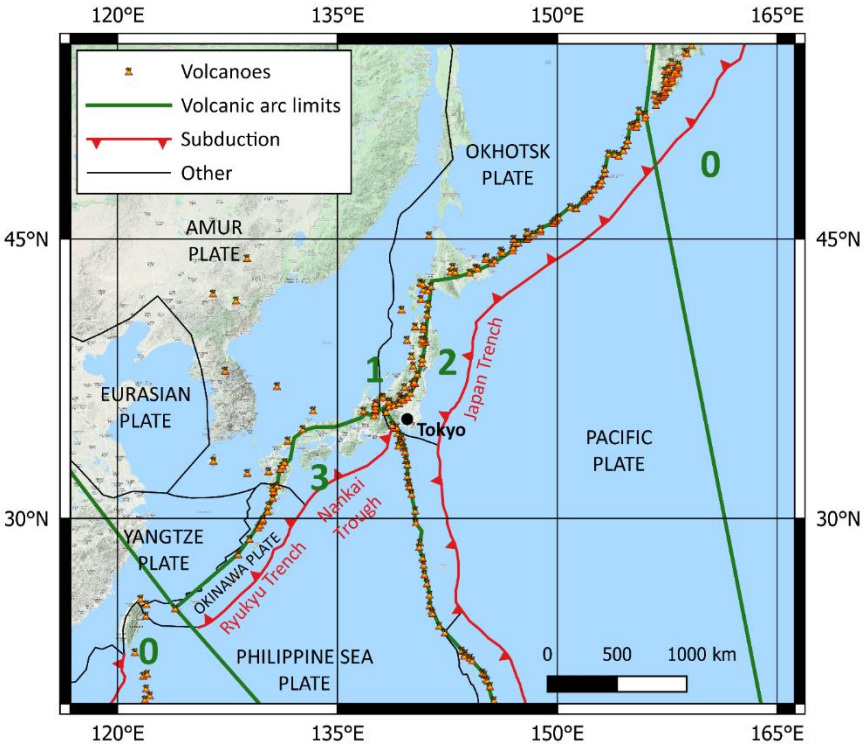

Figure 3.6 Volcanic flag region extents in Japan subduction zone. The green lines between zones 1, 2, and 3 follow the average trend of volcanic peaks.

The volcanic arc regions described in this section were used to compute portions of path lengths within each zone for use in GMM development. Path length is computed from the point on the fault from which the closest distance is measured (an output of the P4CF code; Section 3.2) to the site on a straight line, and the fractions are evaluated based on the portion of this line in zones with different flags, as applicable. Zone percentages for a given path are listed in the *PathVolArc* table.

3.4 PATH ATTRIBUTES SUMMARY

This section briefly summarizes the path attributes for different NGA-Sub regions considering the fraction of the path in the forearc and backarc zones, as defined in the previous section. For this analysis, subduction events (interface and intraslab only) with the epicenter located within the

forearc zone(s) are considered, i.e., events that are usable in GMM development for subduction zones.

Figure 3.7 shows an example to illustrate the analysis using the 1293 sites that recorded the 2011 **M**9.12 Tohoku, Japan earthquake. Figure 3.7(a) shows the hypocenter (red star located in the forearc zone 2), the rupture area (three yellow rectangles with the fault trace marked in red), the sites located in the backarc (yellow triangles in zone 1), and the sites located in the forearc (orange triangles in zone 2 and red triangles in zone 3). The fractions of the path length in different zones (1, 2, and 3 in Figure 3.7(a)) are provided in the NGA-Sub database. Figure 3.7(b) presents the distribution of the fractions of the path lengths in the backarc zone (zone 1). Most of the sites are in the forearc (zones 2 and 3) and therefore the fraction of the path in the backarc is zero for these sites, as revealed in the large number of sites (>800) on the left of the histogram. Among the sites that have some fraction of their path in the backarc, the relative frequency is nearly uniform from about 0.05 to 0.45, and gradually decreases for fractions > 0.45.

Figure 3.8 and Figure 3.9 show histograms formulated in a similar manner but now aggregating all the interface events and differentiating by region. In this case, the distribution is on the number of recordings instead of unique sites. In Japan, approximately 61% of the recordings do not have a fraction of the path length in the backarc zone, i.e., they have pure forearc paths. This percentage is approximately 78% in South America, 28% in Alaska, and 74% in Central America and Mexico. Path likelihoods decrease with increasing backarc fraction for Japan and Central America and Mexico, are roughly constant for South America, and increase for Alaska. Cascadia and New Zealand are not considered because of the small number of recordings from interface events. In the case of Taiwan, all the sites are assigned as forearc. A high percentage of

forearc recordings (or low percentage of backarc) is encountered when the size of the backarc is limited by the regional geography (Japan and Central America/Mexico) or if the backarc region is a different political domain from which data could not be obtained in significant numbers in the NGA-Sub project (South America; e.g., data from Argentina, which is east of Chile, was not available). Conversely, where the backarc region is large and data is available, the backarc fractions are relatively high (Alaska).

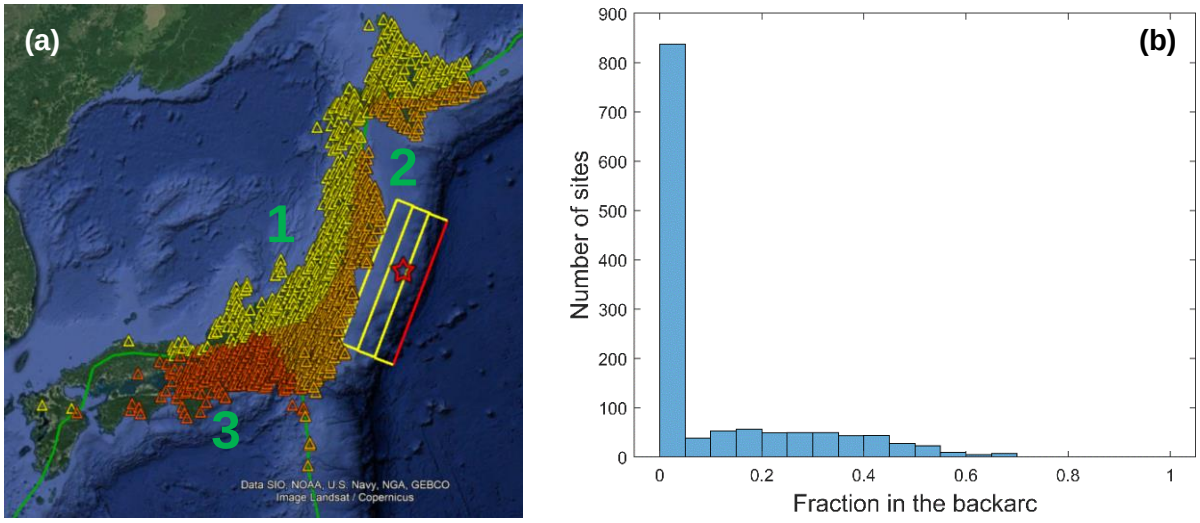

Figure 3.7 2011 **M**9.12 Tohoku earthquake example. (a) Hypocenter (red star), rupture area (three yellow rectangles with rupture trace marked in red), and sites located in the backarc (yellow triangles) and forearc (orange and red triangles) zones. (b) Distribution of the sites considering the fraction of the path length in the backarc (zone 1).

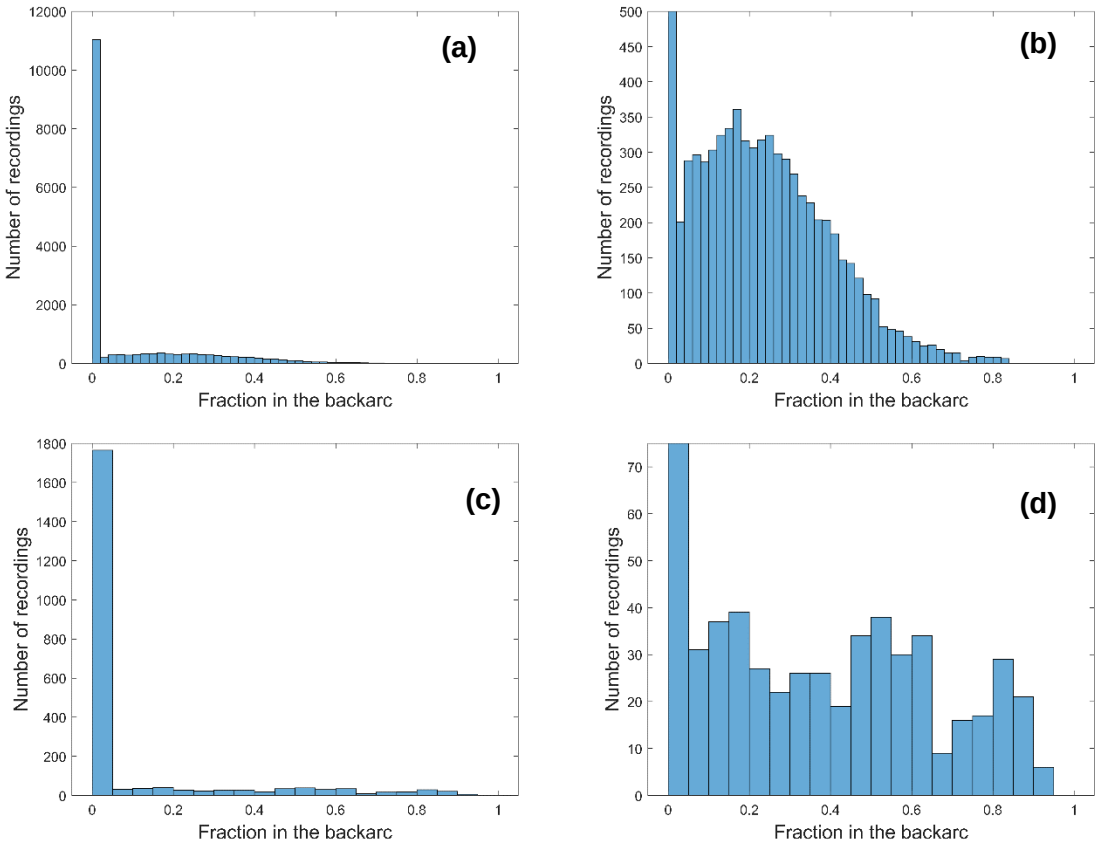

Figure 3.8 Distribution of the recordings considering the fraction of the path length in the backarc zone for interface events in (a, b) Japan and (c, d) South America. The histograms on the right (b, d) are zooming in to the figures on the left (a, c).

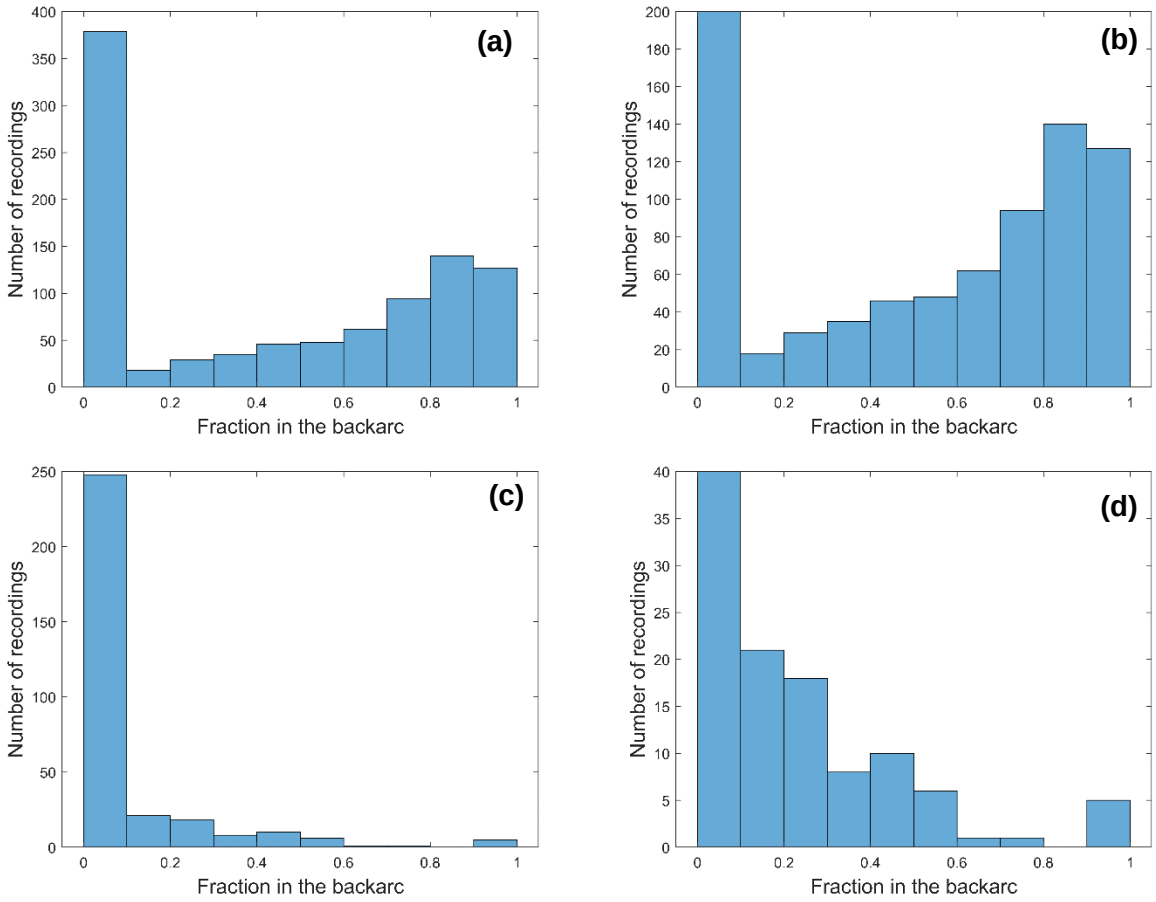

Figure 3.9 Distribution of the recordings considering the fraction of the path length in the backarc zone for interface events in (a, b) Alaska and (c, d) Central America and Mexico. The histograms on the right (b, d) are zooming in to the figures on the left (a, c).

Figure 3.10 and Figure 3.11 show histograms of the fractions of the path lengths in the backarc zone, aggregating now all the intraslab events and differentiating by region. In Japan, approximately 69% of the recordings have pure forearc paths. This percentage is approximately 51% in Alaska, 58% in Cascadia, 62% in Central America and Mexico, 94% in New Zealand, and 69% in South America. Path likelihoods decrease with increasing backarc fraction for Japan, New Zealand, and Central America and Mexico, are roughly

constant for South America, and increase for Cascadia and Alaska. In the case of Taiwan, all the sites are assigned as forearc.

Table 3.2 shows a summary of the number of recordings in the forearc zone by region and event-type. Only earthquakes with the epicenter located within the forearc zone(s) were considered. The explanations for the trends shown in Figures 3.10-3.11 and Table 2 mirrors that for interface events—the main difference with the intraslab data is that large fractions of backarc data are apparent for Cascadia (the backarc is a large region without data restrictions).

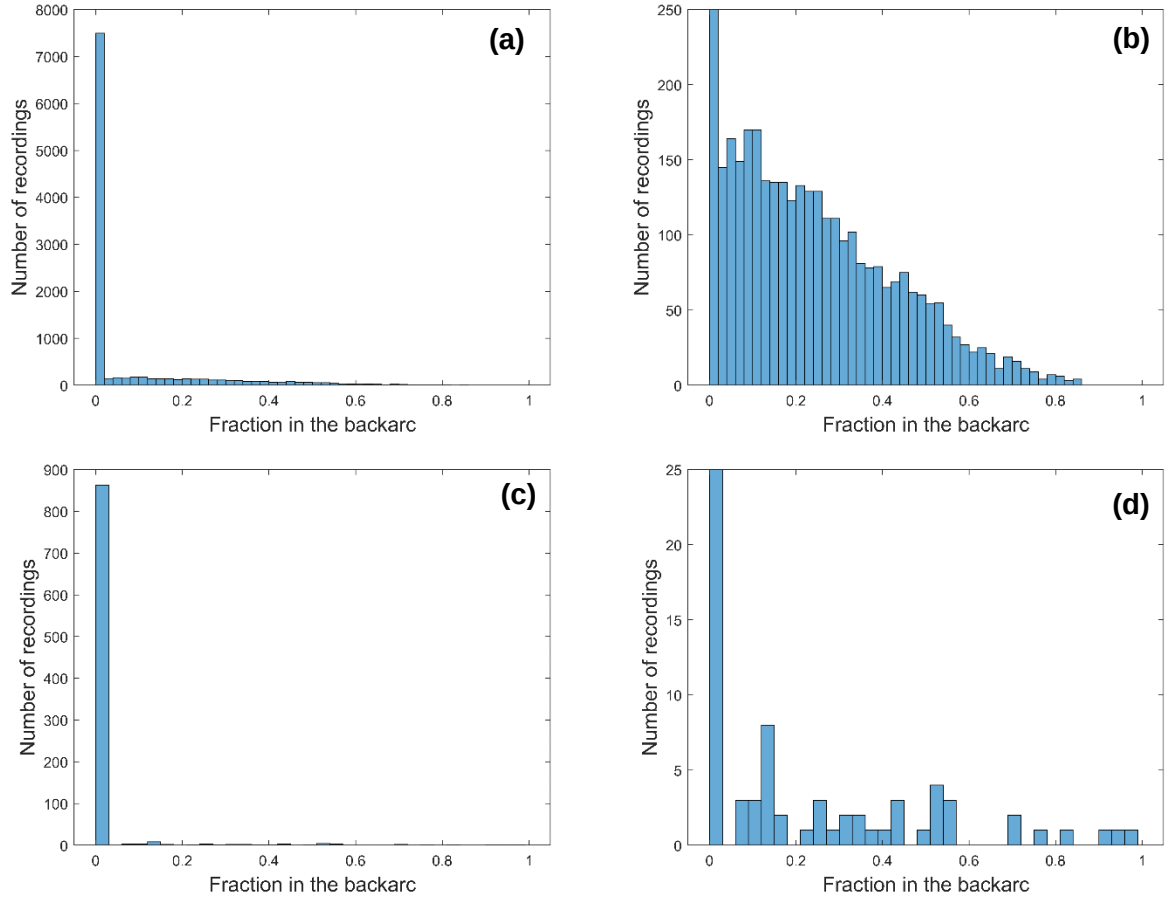

Figure 3.10 Distribution of the recordings considering the fraction of the path length in the backarc zone for intraslab events in (a, b) Japan and (c, d) New Zealand. The histograms on the right (b, d) are zooming in to the figures on the left (a, c).

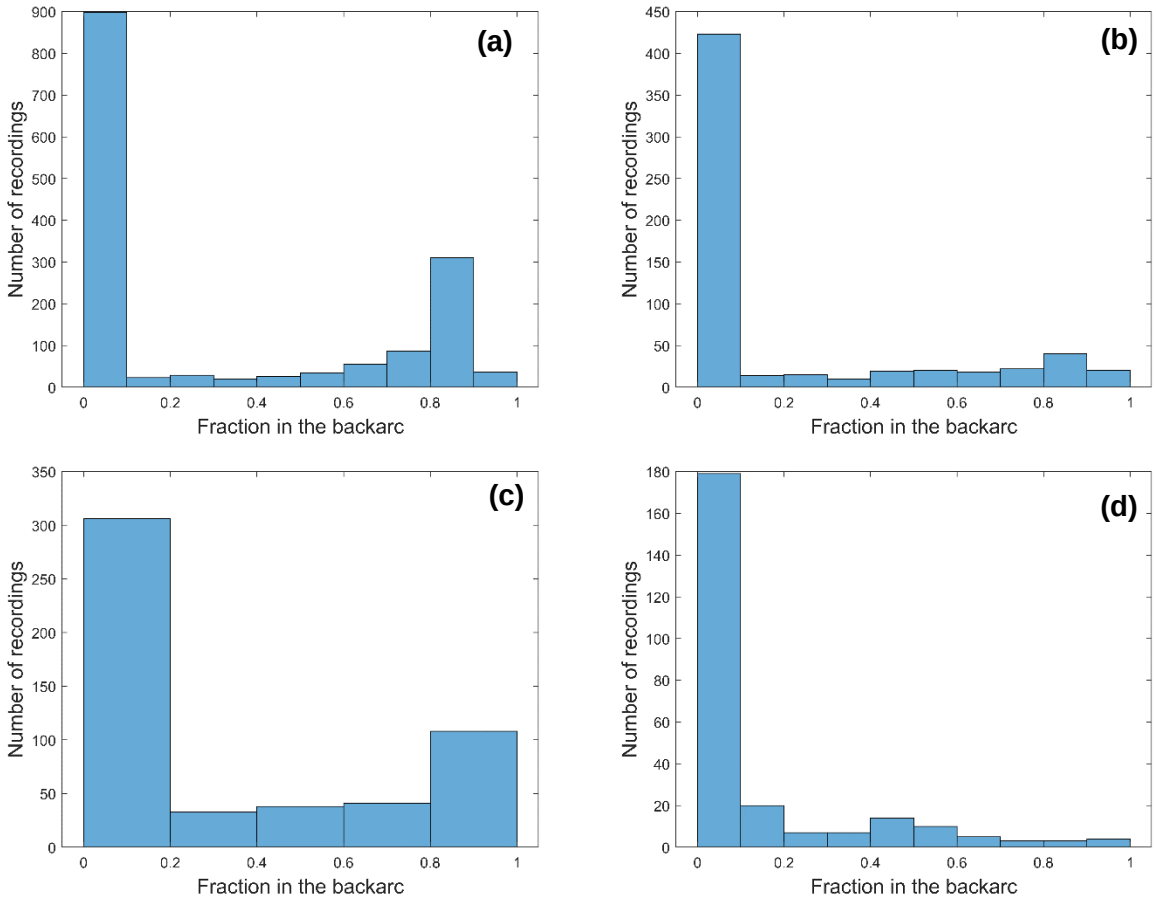

Figure 3.11 Distribution of the recordings considering the fraction of the path length in the backarc zone for intraslab events in (a) Cascadia, (b) South America, (c) Alaska, and (d) Central America and Mexico.

Table 3.2 Summary of the number of recordings in the forearc zone(s) by region and event-type.

Region	Recordings from interface events			Recordings from intraslab events		
	No. total	No. in forearc	% in forearc	No. total	No. in forearc	% in forearc
Alaska	978	270	28%	526	267	51%
Cascadia	126	80	63%	1518	874	58%
Central America and Mexico	318	235	74%	252	155	62%
Japan	17569	10743	61%	10566	7325	69%
New Zealand	21	19	90%	908	851	94%
South America	2226	1735	78%	601	413	69%
Taiwan	1674	1669	100%	8994	8982	100%
All regions	**22912**	**14751**	**64%**	**23365**	**18867**	**81%**

3.5 QUALITY ASSURANCE PROCEDURE

The process of assembling the NGA-Sub database included iterative procedures for checking information for accuracy and consistency. These quality assurance (QA) procedures operate on a "current" version of the database for which some issues are to be checked. Those issues often involve seismic source details as described in Chapter 2 and this chapter (e.g., missing source parameters, protocol errors in parameter assignments, duplicate events, and inconsistencies in hypocentral locations, event-type classifications, or distance metrics). This is depicted with the white oval on the left side of Figure 3.12 (*NGA-Sub flatfile (ver i) issues*). Figure 3.12 refers to a *flatfile*, which is a large table extracted from the full relational database (Mazzoni et al., 2022). Most database users interact with the database through flatfiles. Changes to the database are made at the relational database level through edits to component tables. Once the database is updated, a new flatfile is generated.

The QA procedure in Figure 3.12 begins by comparing entries in the "current" flatfile with information from regional flatfiles, which preceded the relational database. These regional flatfiles consist of source, site, and ground-motion tables developed in early stages of the NGA-Sub project, when the main emphasis was data collection from diverse sources. Regional flatfiles were assembled for Alaska, Cascadia, Central America and Mexico, Japan, New Zealand, South America, and Taiwan. The *Data Comparison* depicted in Figure 3.12 is to check for consistency between the content of the relational database and the regional flatfiles. Differences could occur due to logistical errors in copying material from one set of tables to another, or from technical updates made following completion of the regional flatfiles.

If an inconsistency is found (in Figure 3.12, *Consistent?* → No), regional source information is next checked (i.e., the information used to assemble the regional flatfiles). This occurs in the *Analyze Issues* box in Figure 3.12. This might include, for example, re-examining the regional earthquake catalogs used to assign seismic moments and hypocenter locations (e.g., Table 2.2). These comparisons check for data entry errors or protocol errors (e.g., not using the preferred earthquake catalog for a given region). Various iterations of these checks have impacted event locations (and therefore site-to-source distances), magnitudes, event-types (interface, intraslab, shallow crustal, outer-rise), and fault types (focal mechanisms). On the basis of this review, a source review flag is assigned, as shown in Table 3.3. In many cases, events with negative source review flags are not considered in model development (Kuehn et al., 2020; Parker et al., 2022). Other aspects of the data that might be evaluated in the *Analyze Issues* box include data derived from recordings (Kishida et al., 2022) and site data (Ahdi et al., 2022).

Moving to the right in Figure 3.12, if issues cannot be resolved through the checks of source documents (*Resolved?* diamond), the data in question is marked with a flag (Table 3.3 for the case of issues with source parameters; Table 7 of Mazzoni et al. 2022 for ground motions). Apart from the unclassified earthquakes for which event-type was not assigned (Table 2.4), there are 70 events with unresolved issues related to source parameters (source review flag = -2). If the issues are resolved, the data enter the protocol for distance metrics calculation. This phase is also reached when the consistency check between regional databases and the current flatfile does not identify problems.

Table 3.3 Source review flags.

Source review flag	Description
-999	Earthquake review is pending. Avoid using the recordings from these events.
-888	NGA-West 2 event. Source parameters were not reviewed in NGA-Sub project.
-2	Earthquake was not reviewed because of limited information or missing moment tensor solution
-1	Earthquake was reviewed but there are important inconsistencies
0	Earthquake was reviewed based on the existing information. All the required parameters were available or estimated
1	Rake angle is defined based on the event-type flag (not from finite-fault model or moment-tensor solution)
2	Hypocentral coordinates were slightly modified to be consistent with the finite-fault models.
3	Moment Magnitude **M** is estimated from other magnitude scales (M_S, M_L, or m_b)
4	Strike, dip, and rake angles are based on the event-type flag and/or simulations (not from finite-fault model or moment-tensor solution)

Moving forward in Figure 3.12, in order to compute distance metrics different paths are followed depending on the availability of a FFM from literature (*Available FFM?* diamond). For events with a published model, the fault plane is used in P4CF to compute distances (*Distance calculation (P4CF)*). In the absence of a model, source geometry simulations are performed using CCLD5 (*Fault plane simulation (CCLD5)*), which produce a fault plane that is then used in P4CF. Distance revisions, along with any updates to source and other parameters, including the source review flag, are then applied to component tables in the relational database (*Update Relational Database*). A new flatfile is then generated, which completes an iteration of the review-and-update process.

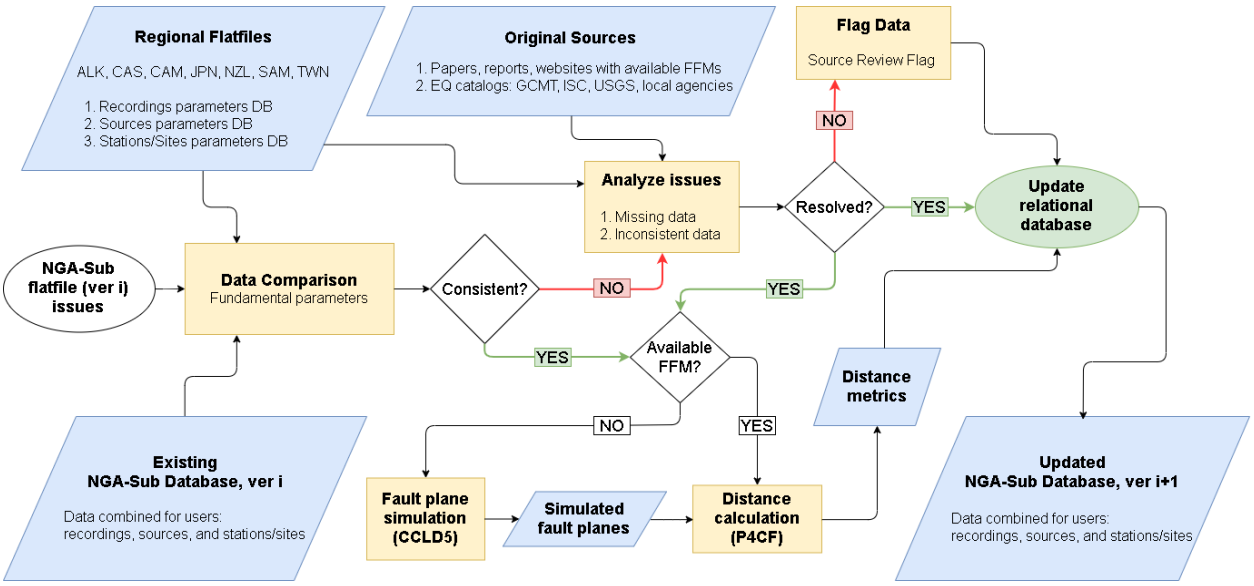

Figure 3.12 Flowchart illustrating procedure used to resolve issues with prior version of flatfile, ultimately resulting in an updated version of the database. Ovals represent start and finish points of the procedure, blue parallelograms represent data, yellow boxes represent data analyses, and white diamonds represent decision points.

4 PRE-NGA-SUB DATABASES AND MODELS FOR SUBDUCTION-ZONE EARTHQUAKES

4.1 INTRODUCTION

Section 1.3 briefly described how GMMs are usually formulated to characterize source, path, and site response effects on ground motions. That section also introduced the NGA-Sub project. The purpose of this chapter is to describe the ground motion data compilations and GMMs that were undertaken previous to, or contemporaneously with, the NGA-Sub project. The aim is to highlight differences between the global NGA-Sub project, prior global databases and models (Section 4.2), and a series of relatively local modeling efforts with an emphasis on subduction zones in Latin America (Section 4.3). In Section 4.3, I distinguish between local and regional databases/GMMs. "Local" databases and GMMs apply to specific countries and are presented for Mexico, Chile, other Latin American countries, and other individual countries outside of Latin America. "Regional" databases apply for broader geographic areas and are presented for CAM and SAM in Subsection 4.3.4.

4.2 GLOBAL DATABASES AND GMMs

GMMs can be developed using ground motions (acceleration or velocity records) obtained from different geographic regions that have a similar tectonic environment (e.g., subduction zone earthquakes). This approach produces *global models*, developed from associated global databases, that are applicable to any region where the tectonic environment and the type of earthquakes are similar in nature to the events considered in model development. Compared to local or regional

models (Section 4.3), the compiled global datasets contain more ground motion records from more events spanning a wider range of parameters of interest (e.g., magnitudes, distances, and site conditions). For instance, a very important component of ground motion models is the magnitude-scaling term (part of the source term f_E introduced previously), which describe how ground motion IMs change (scale) with magnitude. In order to obtain a robust magnitude-scaling term, data from a wide range of magnitudes are needed, which is possible in most cases (especially at the upper limit of the magnitude range for a give region) only by combining the available data from different regions.

Data development efforts to compile subduction zone records from different regions, along with the associated metadata (i.e., source, path, and site parameters), were pioneered by Crouse et al. (1988) and Youngs et al. (1988). Both studies included records obtained in the subduction zones of Alaska, Chile, Peru, Japan, and Mexico. The former authors also utilized data from New Britain/Bougainville, whereas the latter study incorporated records from the Solomon Islands. Table 4.1 summarizes some key attributes of pre-2020 subduction databases. Most of the data in the Crouse et al. (1988), Youngs et al. (1988), and Youngs et al. (1997) databases are from sparsely-recorded events (often one recording). This gradually improved over time, with the Atkinson and Boore (2003) and Abrahamson et al. (2016) models having substantially more data, with some events being well recorded. Atkinson and Boore (2003) combined data of Crouse (1991) and Youngs et al. (1997) with additional data from Cascadia (strong-motion and broadband seismographic records), Japan (Kyoshin Network data), Mexico (Guerrero array data), and El Salvador. Abrahamson et al. (2016) expanded the Atkinson and Boore (2003) dataset adding data from Japan, Taiwan, South America, Central America, and Mexico.

Table 4.1 Summary of pre-2020 global subduction models and databases.

Reference	M range	R_{rup} or R_{hyp} range (km)	# events	# recs	Event-types distinguished?
Crouse et al. (1988) [1]	5.1-8.2	28-470	84	129	No
Youngs et al. (1988) [2]	5.0-8.1	15-450	60	197	Yes: interface, intraslab
Youngs et al. (1997)	5.0-8.2	8.5-550	160	474	Yes: interface, intraslab
Atkinson and Boore (2003)	5.5-8.3	10-400	77	1148	Yes: interface, intraslab
Abrahamson et al. (2016)	5.0-8.4	13-300	292	9946	Yes: interface, intraslab

[1] The database from Crouse et al. (1988) was subsequently updated for the development of a GMPE by Crouse (1991), but event details for the latter were not presented and hence are not shown in Table 1.1. The expanded Crouse (1991) database was used subsequently by Youngs et al. (1997).

[2] This study also utilized 389 additional recordings from non-subduction events to constrain the model features.

None of the pre-2020 global subduction databases listed in Table 4.1 included the large-magnitude events from Tohoku Japan in 2011 (**M**9.12) and Maule Chile in 2010 (**M**8.81). These and many other events, such as the 2018 **M**7.1 Anchorage, Alaska, earthquake and the large-magnitude intraslab events from Mexico in 2019 (**M**8.27 and **M**7.71), have significantly expanded the number of usable records. Figure 4.1 (Bozorgnia et al., 2022) presents the magnitude-distance distribution of the NGA-Sub database, compared to the dataset utilized by Abrahamson et al., 2016 (Figure 4.1a) and distributed over the seven regions considered in the project (Figure 4.1b). The NGA-Sub database is 6.5 times larger (in terms of recordings) and 3.3 times larger (in terms of events) than the Abrahamson et al. (2016) dataset. Moreover, the magnitude-distance distribution of NGA-Sub data is more exhaustive, including more recordings from large-magnitude earthquakes, along with more recordings from small to mid-size events.

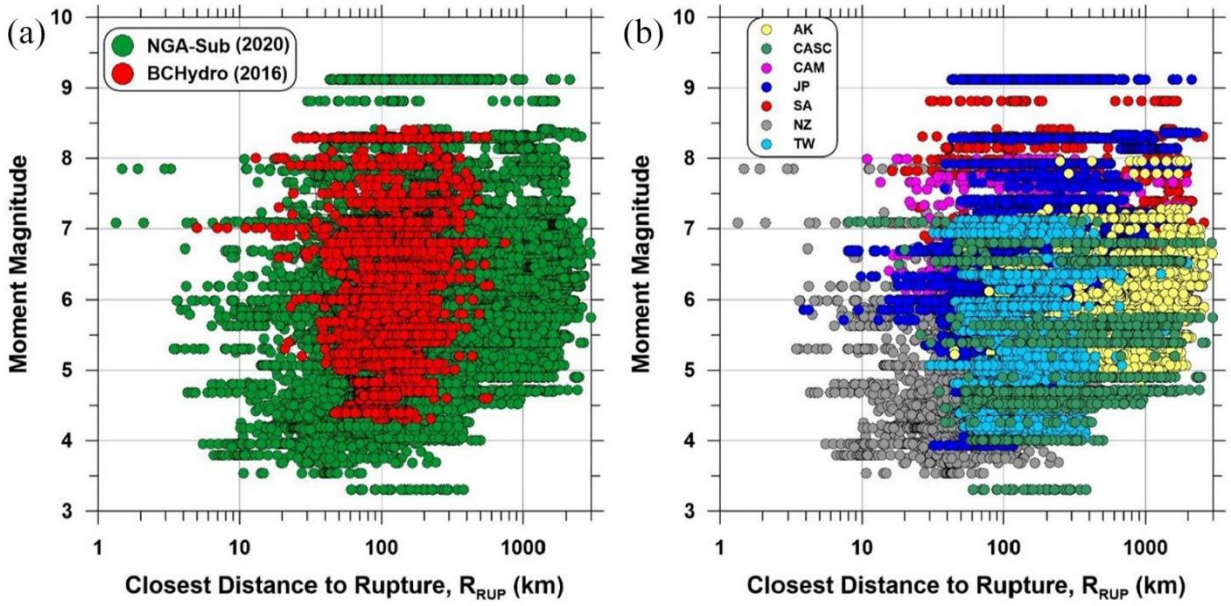

Figure 4.1 Magnitude–distance distribution of NGA-Sub database. (a) NGA-Sub versus BCHydro (Abrahamson et al., 2016) datasets. (b) NGA-Sub data distributed by region. Bozorgnia et al. (2022).

4.3 LOCAL AND REGIONAL DATABASES AND GMMs

As explained in the previous section, the use of global datasets and GMMs has advantages, such as a more exhaustive range of the parameters of interest and more statistically robust estimates of regressed model parameters, than is possible with more limited local or regional datasets. The downside of the global approach is that certain features may not be captured properly for a specific region that has distinct features relative to global trends. For instance, the geometry of the subducting slab significantly varies from one subduction region to another (or even within a subduction zone). This affects the magnitude break parameter that divides the magnitude scaling function into two segments with different slopes. The attenuation of ground motion with distance (path effect) and site response are also region-dependent, due to distinctive crustal properties and near-surface geologic conditions (such as the gradient of shear wave velocity with depth and the depth to the 1.0 km/s shear wave velocity isosurface, $Z_{1.0}$).

To account for local effects, GMMs are often developed using records obtained from a specific region. This approach produces *local models*, developed from associated local databases, that are only applicable in the region from which the ground motion data were collected. Local GMMs are in principle more suitable than global GMMs in regions where the available data are sufficient to produce relatively exhaustive datasets and robust models. A disadvantage of local models is that they are typically poorly constrained for the large-magnitude conditions that typically govern seismic hazard estimates for engineering applications.

Many previous studies have collected ground motion data for specific geographic regions with the goal of developing associated GMMs. Besides data availability, these regions are defined based on considerations regarding tectonic environment (e.g., a specific subducting plate), geographic features (e.g., an island or a continent), and/or political boundaries (e.g., a specific country).

The sub-sections below describe local and regional databases, along with the associate GMMs. Emphasis is placed on Latin American subduction zones, specifically the Central America and Mexico subduction zone and for the South America subduction zone. Other regions are more briefly summarized (Section 4.3.5).

4.3.1 Local Databases and GMMs for Mexico

In Mexico, the installation of a strong motion network started in the early 1960s, following the 1957 Mw 7.6 Guerrero earthquake. In 1962, three accelerographs were deployed in Mexico City, two at the city center (in the Central Alameda Park and in the Latin American Tower) and one at a hill zone site (Ciudad Universitaria, CU). Since 1964, the CU station has recorded several events and has become a reference site to study earthquake ground motions in the Mexico City Valley

(Jaimes et al., 2006). Starting in the 1980s, the National Autonomous University of Mexico (UNAM) in cooperation with the University of California, San Diego (UCSD), significantly increased the number of instruments by the deployment of the Guerrero Accelerograph Network. This network is not in operation at present; however, some recording stations were absorbed into the networks installed by the Institute of Engineering at UNAM. Following the 1985 **M**7.99 Michoacan earthquake, several institutions installed and operated networks. Currently, the main strong motion data operators in Mexico are the Institute of Engineering at UNAM (IINGEN), the National Seismological Service of Mexico (SSN) at the Geophysical Institute of UNAM, the Instrumentation and Seismic Recording Center (CIRES) in Mexico City, the Seismic Network of CICESE (Center of Scientific Research and Higher Education of Ensenada, Baja California), and the Federal Electricity Commission. There are additional smaller networks maintained by other operators in different states of Mexico.

Table 4.2 presents a summary of different ground motion datasets and GMMs for Mexico that were developed utilizing recordings from subduction earthquakes. In Mexico, earthquake ground motion recordings and modeling have often focused on the seismic response of the Valley of Mexico (which is located in the volcanic belt), under the occurrence of subduction zone interface events (e.g., Singh et al., 1987; Castro et al., 1988; Rosenblueth et al., 1989; Ordaz et al., 1994). The emphasis on this location is a consequence of the large population of Mexico City (8.9M), and the extensive damage and the numerous casualties caused by the 1985 **M**7.99 Michoacan (Mexico) earthquake. Mexico City has unique geotechnical conditions, consisting of lakebed deposits, that produce strong site effects. On the contrary, less attention was initially given to the areas outside the valley of Mexico. For the forearc region, a few GMMs for PGA and Modified Mercalli Intensity (MMI) were developed in the late 1980s and 1990s (e.g., Anderson and Quaas,

1988; Ordaz et al., 1989; Anderson and Lei, 1994; Anderson 1997), which are mainly valid for the state of Guerrero. Perea and Sordo (1998) produced a local GMM for the urban area of Puebla City and Reyes (1998) used data from one station in Mexico City (Ciudad Universitaria, CU), a relatively firm site located in the hill zone. None of these GMMs distinguished event type and are not listed in Table 4.2.

Table 4.2 Ground motion datasets and GMMs for subduction earthquakes in Mexico.

Author	**Region**	**Time frame**	**# Events**	**# Recordings**	**Mag. range**	R_{rup} **or** R_{hyp} **range**
García et al. (2005)	Central Mexico	1994-2004	16 intraslab	277	5.2 – 7.4	4 – 400 km
Jaimes et al. (2006) [1]	Mexico City	1965-2004	21 interface	21 (CU site)	6.0 – 8.1	280 – 530 km
García et al. (2009)	Mexico	1985-2004	46 interface	469	5.0 – 8.0	20 – 400 km
Hong et al. (2009)	Mexico	1985-2004	40 interface 16 intraslab	418 277	5.0 – 8.0 5.2 – 7.4	Unspecified
Arroyo et al. (2010)	Mexico (Pacific coast)	1985-2004	40 interface	418	5.0 – 8.0	20 – 400 km
Rodríguez-Pérez (2014) [2]	Central & southern Mexico	1995-2011	8 interface 25 intraslab	75 121	5.1 – 8.0 5.0 – 7.2	50 - 580 km 70 - 540 km
Jaimes et al. (2015) [3]	Mexico City	1964-2013	22 intraslab	22 (CU site) 15 (SCT site) 13 (CDAO site)	5.2 – 7.4	103 - 464 km
García-Soto and Jaimes (2017)	Mexico (Pacific coast)	1985-2004	40 interface	418	5.0 – 8.0	17 - 400 km
Jaimes and García-Soto (2020)	Mexico	1994-2017	23 intraslab	366	5.2 – 8.2	22 - 400 km
Jaimes and García-Soto (2021)	Mexico	1985-2017	40 interface 23 intraslab	418 366	5.0 – 8.0 5.2 – 8.2	17 - 400 km 22 - 400 km

Table 4.2 Ground motion datasets and GMMs for subduction earthquakes in Mexico.

Author	Region	Time frame	# Events	# Recordings	Mag. range	R_{rup} or R_{hyp} range
Lermo-Samaniego et al. (2020)	Southern east Mexico	1995-2017	86 subduction & others	261	5.0 – 8.2	52 - 618 km

[1] CU = Ciudad Universitaria station located in the hill zone in Mexico City.

[2] Near-trench thrust interface earthquakes only.

[3] SCT = Secretaría de Comunicaciones y Transportes station located in the lake-bed zone in Mexico City. CDAO = Central de Abastos Oficinas station located in the lake-bed zone in Mexico City.

More recently, many local GMMs for portions of Mexico, mainly outside of Mexico City, have been produced, including the following models listed in Table 4.2:

- García et al. (2005) developed a local GMM for intraslab earthquakes in Central Mexico, based on 277 recordings from 16 intraslab normal-faulting events. All the ground motion data were obtained at 51 sites classified as firm to hard rock (NEHRP, National Earthquake Hazard Reduction Program, class B sites). All stations located in the Valley of Mexico were omitted. This model estimates PGA, PGV, and PSa at periods between 0.04 and 5 seconds.
- Jaimes et al. (2006) utilized ground motions recorded at a single station located in the hill zone in Mexico City (Ciudad Universitaria, CU) to produce a local GMM for interface earthquakes using Bayesian regression. The dataset consisted of 21 events. This model predicts Fourier Amplitude Spectra (FAS) and, using random vibration theory, approximate the response spectra (PSa values) for at periods between 0.2 and 6 seconds.
- García et al. (2009) compiled a local dataset of 469 recordings from 46 interface earthquakes in Mexico, to investigate path effects in coastal and inland Mexico for FAS at different frequencies. They proposed that site or source effects would not be the cause of

the difference observed between the attenuation rates along the Pacific coast and inland area, but rather that the geometry and structure of the subduction zone would be responsible (path effects). This analysis only included sites located in the forearc region and, therefore, differences between forearc and backarc were not assessed.

- Hong et al. (2009) produced a local GMM for both interface and intraslab earthquakes in Mexico, utilizing the ground motion dataset compiled in the studies by García et al. (2005) and García (2006), which consisted of 695 recordings from 56 earthquakes, divided into 418 recordings from 40 interface events and 277 recordings from 16 intraslab events. All the recordings are from NEHRP B sites. This model estimates PGA and PSa values at periods between 0.1 and 3 seconds, considering different definitions of the intensity measures (maximum, geometric mean, and quadratic mean of the two horizontal components).
- Arroyo et al. (2010) developed a local GMM for interface earthquakes in Mexico, utilizing a subset of the database compiled by García et al. (2009). This subset consisted of 418 recordings from 40 events, obtained at 56 free-field stations classified as NEHRP B sites. Sites with known significant site amplifications and those located in the volcanic belt were excluded. This model estimates PGA and PSa values at periods between 0.04 and 5 seconds, using Bayesian regression.
- Rodríguez-Pérez (2014) developed a local GMM for Mexico utilizing ground motion data from "near-trench" interface and normal intraslab earthquakes for PGA, PGV, and PSa values at periods between 0.04 and 5 seconds ("near-trench" was defined as interface earthquakes that produce predominantly low frequency ground motions at a particular firm site in Mexico City, Ciudad Universitaria; Shapiro et al., 1998). This dataset consisted of

196 recordings from 33 earthquakes, divided into 75 recordings from 8 near-trench interface events and 121 recordings from 25 normal intraslab events. All the recordings were obtained at free-field rock sites (limestone, basalt, diorite, or quartz monzonite), 25 of them located in central Mexico and about 15 in southern Mexico. Soil sites were excluded, particularly those recorded in the Mexico City Valley, at which high amplifications have been observed.

- Jaimes et al. (2015) produced a local GMM utilizing ground motions from normal intraslab earthquakes recorded at three stations located in Mexico City: Ciudad Universitaria site (CU) is located in the hill zone of Mexico City, whereas Secretaría de Comunicaciones y Transportes (SCT) and Central de Abastos Oficinas (CDAO) sites are located in the lake-bed zone of Mexico City. The dataset consisted of 22, 15, and 13 recordings from CU, SCT, and CDAO sites, respectively, recording during 22 intraslab events. This model estimates PGA, PGV, and PSa values at periods between 0.2 and 5 seconds. Bayesian regression was used because of the limited amount of data. For the lake-bed sites (SCT and CDAO), 1D analytical transfer functions derived from soil profiles were used to estimate the intensity measures, following the methodology presented in Jaimes et al. (2006).
- García-Soto and Jaimes (2017) developed a local GMM for interface earthquakes in Mexico, utilizing the same dataset used by Arroyo et al. (2010), i.e., 418 recordings from 40 interface events, obtained at 56 NEHRP B sites. This model estimates PGA, PGV, and PSa values at periods between 0.01 and 5 seconds. Additionally, it estimates vertical spectral accelerations and vertical-to-horizontal spectral acceleration ratios.
- Jaimes and García-Soto (2020) improved the ground motion database utilized by García et al. (2005) for intraslab earthquakes in Mexico (originally 277 recordings from 16 intraslab

normal-faulting events), which resulted in an extended database of 366 recordings from 23 intraslab events, recorded at 69 stations. All sites are NEHRP class B, as in the studies by García et al. (2005) and García (2006). The extended database included the relatively recent large earthquakes that occurred in Mexico in September 2017: the September 8, 2017 **M**8.27 offshore Chiapas event and the September 19, 2017 **M**7.18 Puebla event. This model estimates PGA, PGV, and spectral acceleration for the horizontal and the vertical components (including V/H ratios), at periods between 0.01 and 5 seconds. Jaimes and García-Soto (2021) combined the dataset of 418 recordings from 40 interface events utilized by García-Soto and Jaimes (2017) with the extended dataset for intraslab earthquakes presented in Jaimes and García (2020), to propose a local GMM for significant duration of subduction zone earthquakes for Mexico, which is based on 5%–75%, 5%–95%, and 2.5%–97.5% of Arias intensity. Figure 4.2 shows a map with the location of the earthquakes and stations used in the studies by Jaimes and García (2020, 2021). Figure 4.3 presents magnitude and focal depth versus distance distributions for these datasets.

- Lermo-Samaniego et al. (2020) developed a local GMM for southeastern Mexico utilizing 261 recordings from 86 earthquakes of various focal mechanisms, including subduction zone events and other types of earthquakes. The ground motions were obtained at nine stations and the dataset included recordings from the September 8, 2017 **M**8.27 offshore Chiapas earthquake. Average horizontal-to-vertical spectral ratios obtained from the recordings are utilized to remove site effects and thus the GMM is considered to be representative of firm ground sites. This model estimates PGA, PGV, and PSa values at periods between 0.01 and 10 seconds.

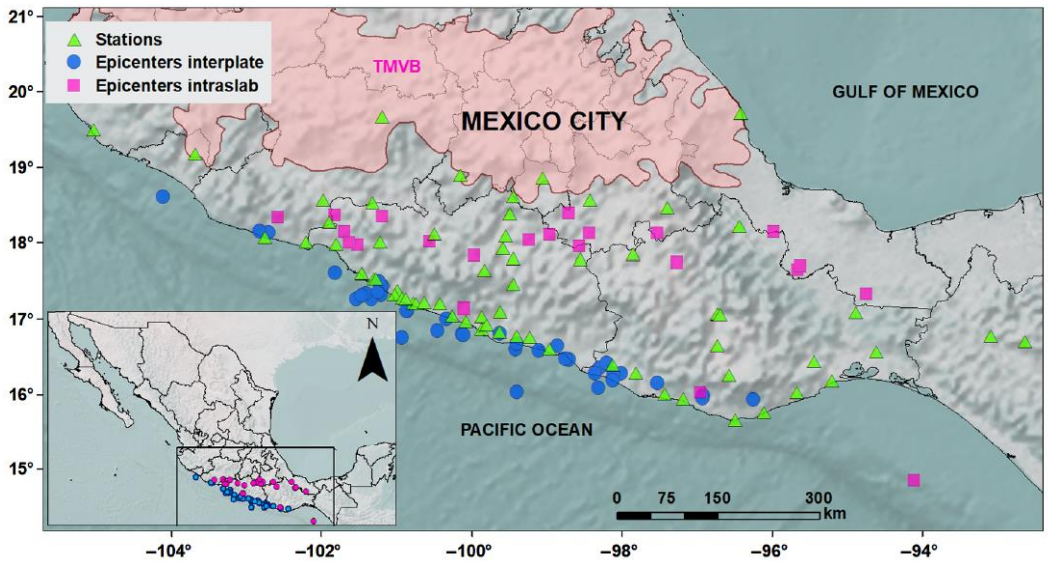

Figure 4.2 Map of the Pacific region and central Mexico showing epicenters of interface (blue circles) and intraslab (pink squares) earthquakes and recording stations (green triangles) used in the development of the local GMMs by Jaimes and García-Soto (2020, 2021). The Trans-Mexican volcanic belt (TMVB) is indicated and delimited with a shaded area.

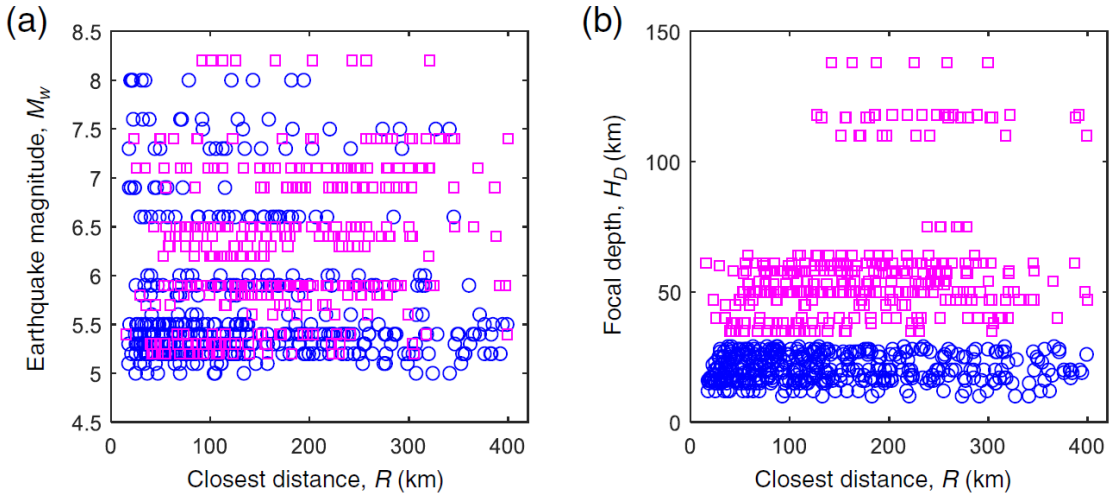

Figure 4.3 Distribution of (a) magnitude versus distance and (b) focal depth versus distance of the Mexican dataset used in the development of the recent local GMMs by Jaimes and García (2020, 2021). Blue circles correspond to interface events and pink squares correspond to intraslab events.

4.3.2 Local Databases and GMMs for Chile

In this subsection, previous efforts to compile local strong motion datasets for Chile, along with prior ground motion modeling efforts for this country, are described. In Chile, the first accelerograph was installed in 1944 at the School of Engineering of the University of Chile, and the first earthquake ever recorded was the 1945 M_S 7.1 event that occurred near Santiago. Other recordings were obtained later, which produced a small dataset (Boroschek et al., 2017). Since 1968, the University of Chile has operated and maintained strong motion arrays, when the Department of Geophysics, Seismology, and Geodesy began the installation of a network of instruments that could register future earthquakes (Husid, 1973). This first effort initiated the Central Chile Accelerograph Network that was operated later by the Department of Geophysics and Geodesy (DGG) and the Department of Civil Engineering (DIC) at the University of Chile. The data from the DGG network are relevant mainly because of the accelerograms recorded at 26 sites during the interface **M**7.98 Valparaiso earthquake that occurred on March 3, 1985. That earthquake was one of the first major subduction-zone events that was well recorded and studied, thanks to data acquired in locations with various geological conditions and at relatively close distances to the fault rupture plane, ranging from approximately 25 to 220 km. Currently, strong motion networks in Chile are mainly operated by the DIC (RENADIC network) and the Chilean National Seismological Center (CSN) managed by the Department of Geophysics at the University of Chile, which distributes data from different networks (C, C1, CX, and others). The stations from these data operators have recorded several large magnitude events including the intraslab 2005 **M**7.78 Tarapaca earthquake and the interface 2010 Maule (**M**8.8), 2014 Iquique (**M**8.15), and 2015 Illapel (**M**8.31) earthquakes.

Ruiz and Saragoni (2005) assembled one of the first ground motion datasets of recordings obtained in Chilean territory. This dataset differentiated interface and intraslab events and characterized the strong motion recording stations based on shear wave velocity (V_S) values. It consisted of approximately 90 recordings from eight interface earthquakes and nine intraslab events that occurred between 1945 and 2005, with surface-wave magnitudes (M_S) ranging from 5.6 to 7.9. The distance range of the recordings was approximately 35-350 km according to the measure used by the authors (hypocentral distance, R_{hyp}). Afterward, Contreras and Boroschek (2012, 2015) developed a Chilean strong motion dataset including 285 recordings from interface earthquakes and 246 recordings from intraslab events (more than 530 recordings in total) obtained between 1985 and 2010, including the ground motion recordings of the **M**8.8 2010 Maule event. The distances ranged from 25 to 700 km utilizing the closest distance to the fault rupture plane (R_{rup}), whereas the magnitude range was **M**5.0-8.8 for interface earthquakes and **M**5.0-7.8 for intraslab earthquakes.

Bastías and Montalva (2016) developed a ground motion dataset for Chilean events containing 3572 recordings from 477 earthquakes recorded between 1985 and 2015, including the mega-thrust 2010 Maule (**M**8.81), 2014 Iquique (**M**8.15) and 2015 Illapel (**M**8.31) events. Figure 4.4 shows the magnitude versus distance and magnitude versus focal depth distributions. The magnitude range is **M**4.6-8.8, whereas the distance range is R_{rup} 20-650 km. The recordings were obtained at 181 strong motion recording stations characterized with V_{S30} values ranging from 110 to 1951 m/s. The reported intensity measures are PGA, PGV, I_A, and PSa values for periods from 0.01 to 10 s. Similarly, Idini et al. (2017) compiled a dataset for Chile of 1207 ground motion recordings obtained at 154 different strong motion recording stations from 184 earthquakes recorded between 1985 and 2015. These authors only considered events with moment magnitudes

(**M**) ranging from 5.5 to 8.8 for interface earthquakes and from 5.0 to 7.8 for intraslab earthquakes, including the large events previously mentioned (2010, 2014 and 2015 interface earthquakes). The reported intensity measures for this model are PGA and PSa values for periods from 0.01 to 10 s. The flat file of the dataset compiled by Bastías and Montalva (2016) is available at https://datacenterhub.org/resources/chilean_motion. In the case of Idini et al. (2017), a flat file with a subset of the full database (used for GMM development as explained further below) is available as supplemental material. Ground motion time series are not publicly available for any of these studies.

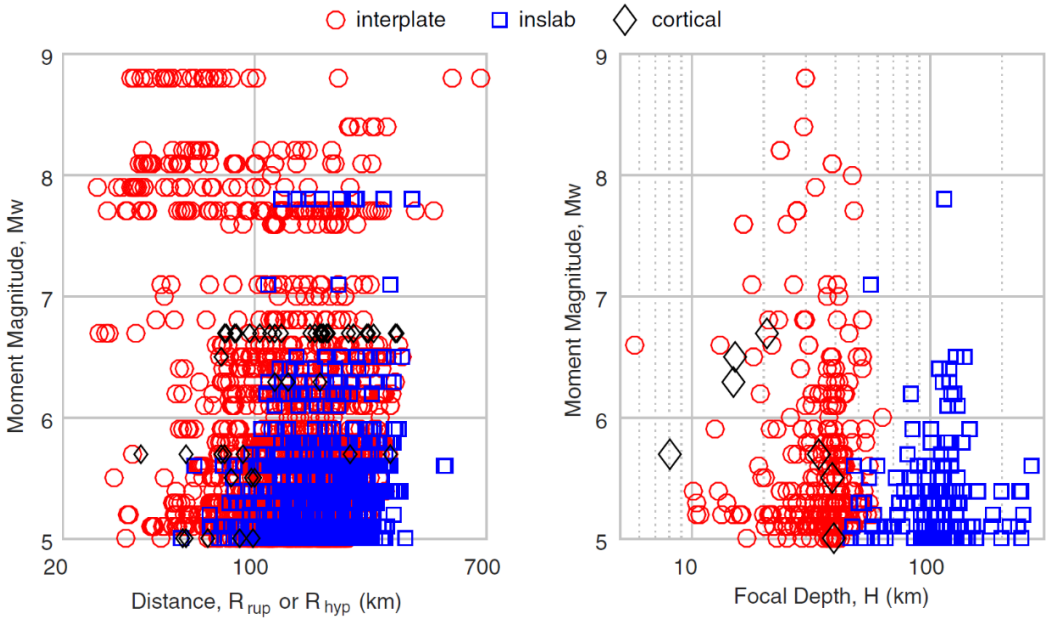

Figure 4.4 Bastías and Montalva (2016) database: magnitude versus distance and magnitude versus focal depth distribution.

Regarding local GMMs, several studies that estimate PGA values were developed in Chile between 1976 and 1998 utilizing limited data available at the time (Ruiz and Saragoni, 2005). Those GMMs typically did not distinguish earthquake mechanism, treated site response effects as

linear, and had relatively rudimentary path models (lack of anelastic attenuation, lack of magnitude-dependent geometric spreading, etc.).

The first GMM for the Chilean subduction zone that separated the effects of interface and intraslab seismic sources was proposed by Ruiz and Saragoni (2005, RS2005) based on the dataset described previously in this subsection, which contained approximately 90 recordings. This GMM only estimates PGA values and uses M_S as the magnitude measure and R_{hyp} as the distance measure. Additionally, the model utilizes two broad site categories named "hard rock" and "rock and stiff soil", defined by means of a broad shear wave velocity range used as representative of each site class (V_S > 1500 m/s for hard rock; 1500 m/s > V_S > 360 m/s for rock and stiff soil). Subsequently, Contreras and Boroscheck (2012, 2015; CB2015) produced the first GMM that estimates both PGA and PSa values up to periods of 3 seconds for Chile, based on the dataset compiled by these authors which consists of 531 recordings, including the ground motion recordings of the **M**8.8 Maule event. The GMM evaluated both interface and intraslab earthquakes and considered two site categories: generic rock, which is taken as $V_{S30} \geq$ 900m/s and generic soil, which is taken as V_{S30} < 900m/s. In this case, the local GMM does not include data from the numerous Maule earthquake aftershocks or the subsequent large events in 2014 (**M**8.15) and 2015 (**M**8.31).

Haendel et al. (2015) derived a local GMM for Northern Chile (PGA and PSa) utilizing a dataset that included 1094 recordings from 138 earthquakes, divided into 374 recordings from 48 interface events and 720 recordings from 90 intraslab events, including the 2014 **M**8.15 Iquique earthquake. This model used mainly accelerograms recorded within the Integrated Plate Boundary Observatory Chile (IPOC) project, which maintains more than 20 permanent ground motion recording stations installed throughout Northern Chile. Haendel et al. (2015) presented a new

mixture model that combined eight existing GMMs for subduction earthquakes (five local and three global) based on their predictive performance of observed local data at different spectral periods. The authors indicated that the mixture model performed better than any of its component GMMs and that it produced similar results to what would be obtained by developing a local GMM by regression.

Two relatively recent local GMMs for Chile were published by Montalva et al. (2017, MEA2017) and Idini et al. (2017, IEA2017) for the Chilean subduction zone. The magnitude versus distance distributions of the recordings utilized in the development of these GMMs are shown in Figure 4.5 for each case. The data used by MEA2017 is an updated version of the Bastías and Montalva (2016) dataset and include 3774 recordings from 473 earthquakes, divided into 2461 recordings from 281 interface events and 1313 recordings from 192 intraslab events. These ground motion recordings were obtained at 235 strong motion recording stations characterized with V_{S30} values ranging from 108 to 1951 m/s. On the other hand, IEA2017 utilized a new subset of 483 recordings (out of the initial 1207 recordings) for the GMM derivation, consisting of 114 strong motion recordings from 38 intraslab earthquakes and 369 strong motion recordings from 65 interface events. The subset is defined after applying two specific selection criteria to remove bias caused by the trigger threshold of accelerometers and to avoid using recordings that had lost high frequency content after the processing methodology.

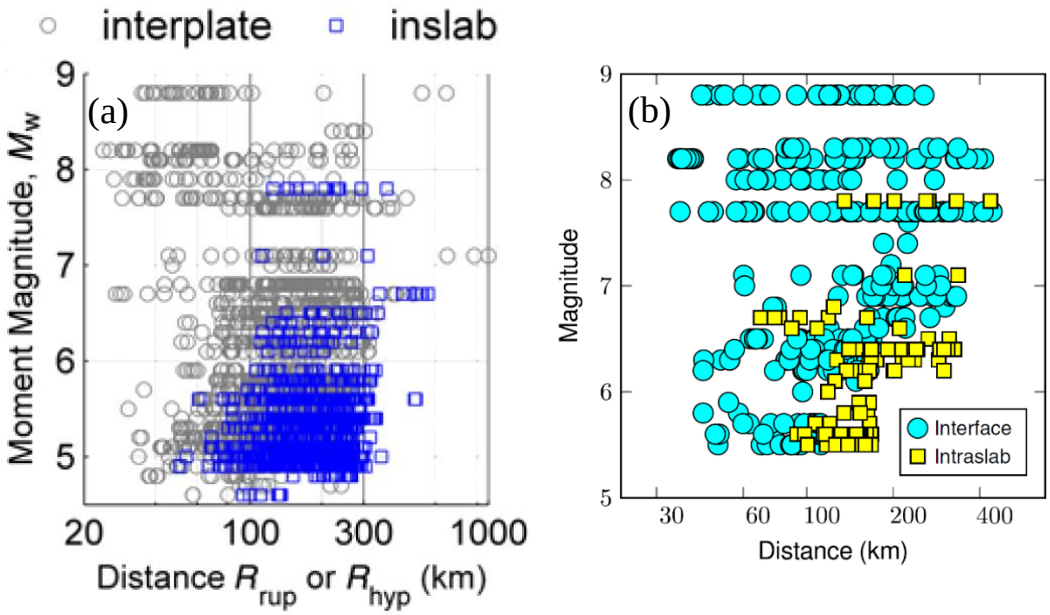

Figure 4.5 Magnitude versus distance distribution of the datasets used in the development of local GMMs in Chile: (a) Montalva et al. (2017); (b) Idini et al. (2017).

Montalva et al. (2021) recently presented an updated ground motion dataset for Chile, along with a local GMM (MEA2021) for PGV and spectral velocity (Sv) at periods between 0.06 and 10 seconds for the Chilean subduction zone. This database is an updated version of the Bastías and Montalva (2016) dataset and include 19,437 recordings from 3560 earthquakes, divided into 9690 recordings from 2032 interface events and 9747 recordings from 1528 intraslab events. These ground motion recordings were obtained at 361 strong motion recording stations, from which 208 have measured V_{S30} values. In addition to V_{S30} as a site characterization parameter, the MEA2021 model utilizes the site's fundamental frequency (f_0) as an explanatory variable for the site term. Figure 4.6 shows the magnitude versus distance distribution of this dataset, along with magnitude versus focal depth. The magnitude range is **M**4.0-8.8, whereas the distance range is R_{rup} 24-725 km.

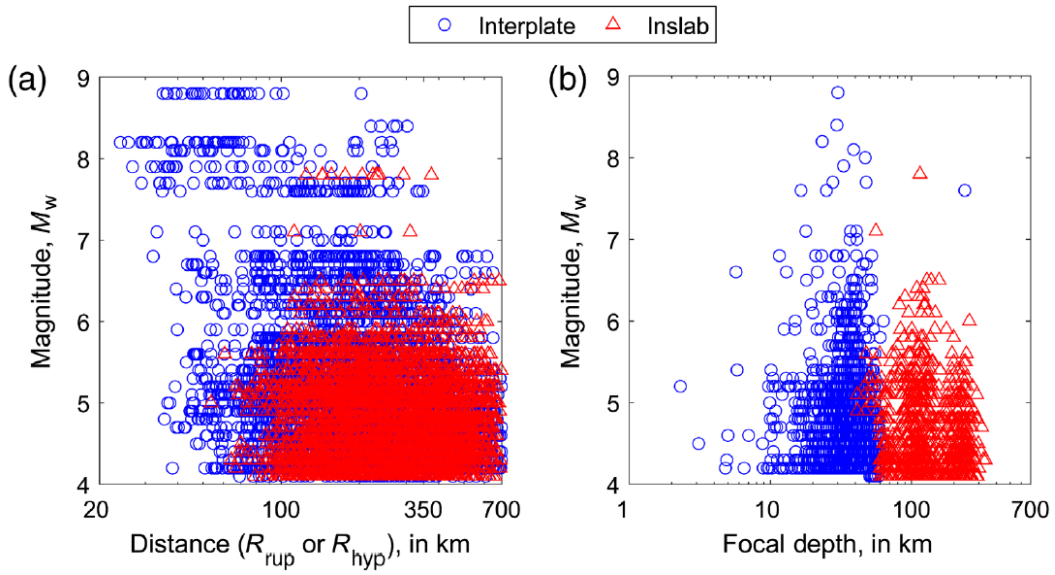

Figure 4.6 Distribution of magnitude versus (a) distance and (b) focal depth of the Chilean dataset used in the development of the recent local GMM by Montalva et al. (2021).

Table 4.3 presents a summary of different ground motion datasets that include recordings from subduction events obtained in Chile, along with the GMMs that have been produced using these databases.

Table 4.3 Ground motion datasets and GMMs for subduction earthquakes in Chile.

Author	**Region**	**Time frame**	**# Events**	**# Recordings**	**M range**	***R_{rup}* or *R_{hyp}* range**	**GMM**
Ruiz and Saragoni (2005) [1]	Chile	1945-2005	8 interface 9 intraslab	49 41	6.4 - 7.8 5.6 - 7.9	35 - 315 km 62 - 350 km	RS2005
Contreras and Boroschek (2015)	Chile	1985-2010	200 interface & intraslab	285 246	5.0 – 8.8 5.0 – 7.8	25 – 700 km	CB2015
Haendel et al. (2015)	Northern Chile	1966-2012	48 interface 90 intraslab	374 720	5.0 – 8.1 5.0 – 7.8	40 – 300 km	HEA2015
Bastías and Montalva (2016)	Chile	1985-2015	279 interface 191 intraslab 7 crustal	2229 1300 43	4.6 – 8.8 4.6 – 7.8 4.9 – 6.7	20 – 650 km	MEA2017
Idini et al. (2017)	Chile	1985-2015	184 interface & intraslab	1207	5.5 – 8.8 5.0 – 7.8	Unspecified	IEA2017

Table 4.3 Ground motion datasets and GMMs for subduction earthquakes in Chile.

Author	Region	Time frame	# Events	# Recordings	M range	R_{rup} or R_{hyp} range	GMM
Montalva et al. (2021)	Chile	1985-2020	2032 interface 1528 intraslab	9690 9747	4.0 – 8.8 4.0 – 7.8	24 – 725 km	MEA2021

[1] Ruiz and Saragoni (2005) utilized surface-wave magnitude (M_S) and R_{hyp} (instead of **M** and R_{rup}).

4.3.3 Local Databases and GMMs for Latin American Countries other than Mexico and Chile

In this subsection, previous efforts to compile strong motion datasets and develop GMMs for individual countries in Latin America, other than Mexico and Chile, are described. In Central America, strong motion networks are currently operating in Costa Rica, El Salvador, Guatemala, Nicaragua, and Panama. A brief synopsis of deployed strong motion networks and available ground motion recordings in each of these countries is presented here, based on the information provided by Arango et al. (2011a), Boroschek et al. (2017), and data retrieved from public available resources as part of the present work.

In Costa Rica, the first accelerograph was installed in the early 1940s at the University of Costa Rica, which recorded the first strong motion in San Jose during the 1945 M_S 7.0 earthquake. In 1984, the deployment of a strong motion network of accelerographs began at the University of Costa Rica, as part of an instrumentation program launched at that time. This network was subsequently operated by the Earthquake Engineering Laboratory of the University of Costa Rica (LIS-UCR), which was established in 1989. Currently, there are mainly two strong motion data operators in Costa Rica: LIS-UCR and the Costa Rican Institute of Electricity (ICE). The most important earthquakes recorded are the 1990 Mw 6.0 Piedras Negras event, the 1991 Mw 7.1

Limon event, the 2004 Mw 6.2 Parrita event, the 2009 Mw 6.2 Chinchona event, and the 2012 Mw 7.6 Samara event.

In El Salvador, the first accelerograph was installed by the National Seismological Observatory in 1964, followed by the deployment in 1966 of three additional instruments after the 1965 M_S 6.0 San Salvador earthquake. The first strong motion recordings were obtained in 1967. Currently, three institutions operate strong motion networks: the Ministry of Environment and Natural Resources (MARN), the UCA University, and the Rio Lempa Hydroelectrical Commission. The most important earthquakes recorded are the 1985 Mw 5.7 event and the 2001 Mw 7.7 event.

In Guatemala, after the 1976 Mw 7.5 earthquake, which affected Puerto Santo Tomas, Zacapa, Chichicastenango, and Guatemala City, four accelerographs were deployed as temporary ground motion recording stations, to record some of the aftershocks related to this event. Prior to this earthquake, only one accelerograph was in operation in Guatemala City at the Observatorio Nacional. In 2001, the National Commission for Disaster Reduction (CONRED) installed a local network of accelerographs located in the Guatemala City area. Currently, the National Institute of Seismology, Volcanology, and Meteorology (INSIVUMEH) maintains a national network with 15 broadband stations and five strong motion stations located across the country.

In Nicaragua, the first accelerographs were deployed in 1966. This initial installation was funded by the Central Bank of Nicaragua and the National University. Other instruments were installed with the support of Esso Standard Oil in 1967 and 1968 (Knudson, 1978). The first significant earthquake recorded by this network was the 1972 Mw 6.2 Managua event. In 1975, the Seismic Research Institute of Nicaragua (IIS) installed a new network of accelerographs, which

were in operation until 1982. There is currently one national strong motion network operated by the Nicaraguan Institute of Territorial Studies (INETER), which was created in 1991. In 1999, the INETER network was expanded in Managua and other major cities. Currently, the INETER network operates in the main cities of Nicaragua: Managua, Masaya, Granada, Jinotega, Matagalpa, and Juigalpa.

In Panama, the first accelerograph was installed in 1934 in the Balboa Heights Administration Building in Panama City, being the first strong motion recording instrument installed in Latin American countries (Knudson, 1978). At this location, the Seismological Observatory of Balboa Heights Panama (BHP) operated until 1977. In 1979, the strong motion recording instruments were transferred to the Geosciences Institute (IGC) at the University of Panama. Since 1983, the IGC has been monitoring the seismic activity at a national level.

Turning next to Central America GMMs, in Costa Rica and El Salvador ground motion datasets and local GMMs have been produced. For instance, Algermissen et al. (1988), Alfaro et al. (1990), and Singh et al. (1993) presented PGA attenuation models for El Salvador. The latter was utilized to estimate the seismic hazard for the 1994 Salvadorian seismic code. Table 4.4 presents a summary with two local databases and GMMs. For Costa Rica, Schmidt et al. (1997) developed a local GMM for PGA and spectral ordinates, based on a dataset consisting of 200 recordings from 57 earthquakes (subduction and shallow crustal events), 67 of which are from subduction events and 133 of which are from shallow crustal events. This model utilized three soil categories (rock, hard soil, soft soil) and considered separate regressions for subduction versus shallow crustal events, although it did not account for differences between interface and intraslab earthquakes. Cepeda et al. (2004) produced a local GMM for subduction intraslab earthquakes for

El Salvador to predict PGA and PSa values at periods between 0.3 and 1 seconds. This GMM was developed by adjusting the magnitude scaling term of the Atkinson and Boore (2003) intraslab model, utilizing the data from the 2001 Mw 7.7 El Salvador earthquake and its aftershocks. The subduction dataset consisted of 254 recordings from 61 intraslab events.

Table 4.4 Ground motion datasets and GMMs for subduction earthquakes in other individual countries in Latin America.

Author	Region	Time frame	# Events	# Recordings	M range	R_{rup} or R_{hyp} range
Schmidt et al. (1997) [1]	Costa Rica	Unavailable	57 subduction & shallow crustal	67 (subduction) 133 (other)	3.3 – 7.6	6 – 182 km
Cepeda et al. (2004)	El Salvador	2001	61 intraslab 127 shall. crustal	254 (subduct.) 225 (other)	2.8 – 7.7 2.4 – 6.6	58 – 190 km 0 – 103 km

[1] This model does not account for the differences between interface and intraslab earthquakes.

4.3.4 Regional Databases and GMMs for Latin America

In this subsection, previous efforts to compile regional strong motion datasets and develop regional GMMs for the Central America and the South America subduction zones, are described. Unlike in NGA-Sub, Mexico has been typically excluded from regional compilations in Central America, although early work that combined subduction and shallow crustal events included data from Mexico (e.g., Climent et al., 1994; Dahle et al., 1995).

(a) Regional Databases and GMMs in Central America

The Norway Cooperation Agency (NORAD) and the Coordination Center for the Prevention of Natural Disasters in Central America (CEPREDENAC) undertook the RESIS I project, which produced a regional strong motion database for Central America (Taylor et al., 1992) and spectral attenuation models (Climent et al., 1994; Dahle et al., 1995; Schmidt et al.,

1997). Climent et al. (1994) performed a regression analysis on 280 recordings from 72 earthquakes from Costa Rica, Mexico, Nicaragua, and El Salvador. This was slightly modified by Dahle et al. (1995). In both models, data from shallow events and subduction events were mixed, without differentiation in the model development.

Table 4.5 presents two regional ground motion datasets and GMMs that include recordings obtained in the Central America subduction zone. Bommer et al. (1996) produced a GMM for subduction earthquakes that estimates both PGA and spectral ordinates for periods between 0.1 and 2 seconds, based on a database of 36 recordings from 20 subduction events from El Salvador and Nicaragua. This model did not consider the influence of site conditions. The authors did not recommend using their equation for hazard analysis purposes, since it was derived only for investigating the previous equations by Climent et al. (1994), which combined shallow crustal and subduction events. Arango et al. (2011a) compiled a regional database of ground motions for the Central America subduction zone from earthquakes occurred between 1976 and 2006 in Guatemala, El Salvador, Nicaragua, and Costa Rica. This database included 554 recordings from 80 subduction earthquakes, divided into 136 recordings from 22 interface events and 418 recordings from 58 intraslab events. The magnitude-distance distribution is shown in Figure 4.7. For interface earthquakes, the magnitude and distance ranges are **M**5.1-7.3 and R_{rup} 18-399 km, respectively. For intraslab earthquakes, the magnitude and distance ranges are **M**5.0-7.7 and R_{rup} 62-375 km, respectively.

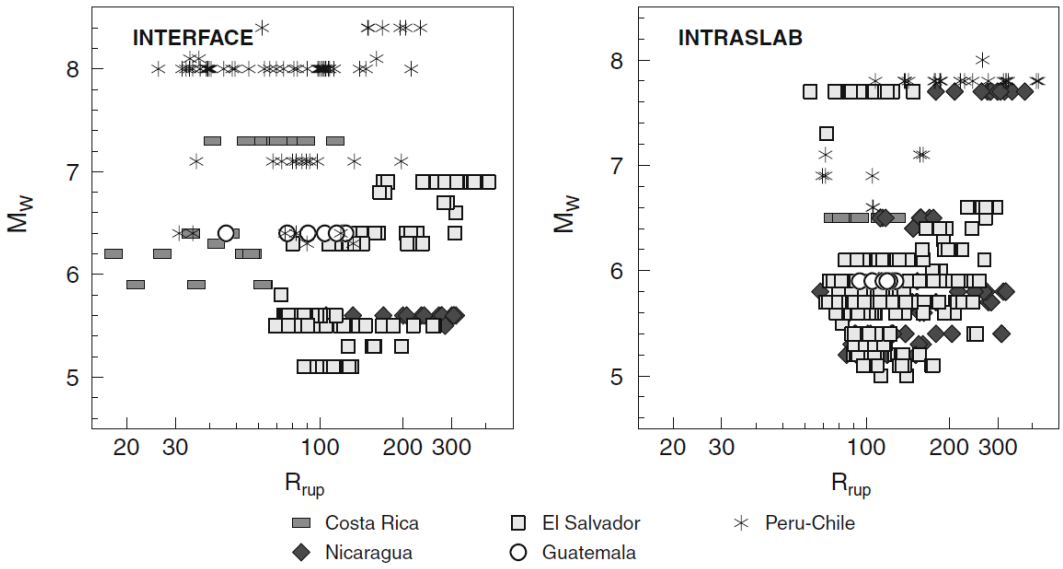

Figure 4.7 Magnitude-distance distribution of the Central America dataset compiled by Arango et al. (2011a). The distribution of the Chile-Peru dataset in Arango et al. (2011b) is also shown for reference.

Table 4.5 Ground motion datasets and GMMs for the Central America subduction zone.

Author	Region	Time frame	# Events	# Recordings	M range	R_{rup} or R_{hyp} range
Bommer et al. (1996) [1]	El Salvador, Nicaragua	Until 1993	20 subduction	36	3.7 – 7.0	62 – 260 km
Arango et al. (2011a)	Guatemala, El Salvador, Nicaragua, Costa Rica	1976-2006	22 interface 58 intraslab	136 418	5.1 – 7.3 5.0 – 7.7	18 - 399 km 62 - 375 km

[1] The authors did not recommend using this GMM for hazard analysis, since it was derived to investigate the previous model by Climent et al. (1994).

(b) Regional Databases and GMMs for South America

Arango et al. (2011b) compiled the first strong motion dataset for the South American subduction zone combining data for Chile and Peru. Information about the deployed strong motion networks and available ground motion recordings in Chile is provided in Section 4.3.2. In Peru, the first accelerograph was installed in Lima in 1944 after the 1940 Mw 8.2 earthquake (moment

magnitude reported in the ISC-Global Earthquake Model catalog, ISC-GEM; Storchak et al., 2013) that affected the city of Lima and the port of Callao (Knudson and Perez, 1976); the first recording was obtained in 1946 (Husid, 1973). Additional strong motion instruments were installed later in Lima by the Geophysical Institute of Peru (IGP), which recorded accelerograms during the 1966, 1970, 1971, and 1974 earthquakes occurred in the coast of Peru. Currently, strong motion networks in Peru are operated by the IGP, the South American Regional Seismological Center (CERESIS), the Japan–Peru Center for Seismic Research and Disaster Mitigation (CISMID), the Catholic University of Peru (PUCP), and the Peruvian state water company (SEDAPAL). The stations from these data operators have recorded significant events including the 2001 Arequipa (**M**8.4) and the 2007 Pisco (**M**8.0) earthquakes (Arango et al., 2011a).

The Arango et al. (2011b) dataset contained 98 recordings (67 from Chile and 31 from Peru) from 15 earthquakes between 1966 and 2007, with moment magnitudes ranging from 6.3 to 8.4, recorded at 55 different strong motion recording stations at distances of about R_{rup} 25-420 km. The magnitude-distance distribution for interface and intraslab events is shown in Figure 4.8. A later regional initiative was the South America Risk Assessment (SARA) project, which was implemented between 2013 and 2016 and was promoted by the Global Earthquake Model (GEM) foundation (Drouet et al., 2017). This project was developed as a community-based effort by the GEM team in collaboration with a group of scientists from South America. As part of the hazard component of the program, the SARA project also developed a South American ground motion database (Castillo et al., 2016; Drouet et al., 2017) consisting of 4110 recordings from Brazil (566), Chile (2197), Colombia (695), Ecuador (586), and Peru (66). In this dataset, the distance range is R_{rup} 20-1200 km approximately and the magnitude range is **M**2.0-8.8. The magnitude-distance

distribution of the SARA database for interface and intraslab events is shown in Figure 4.9. The SARA project flat file is available at https://sara.openquake.org/hazard_rt6.

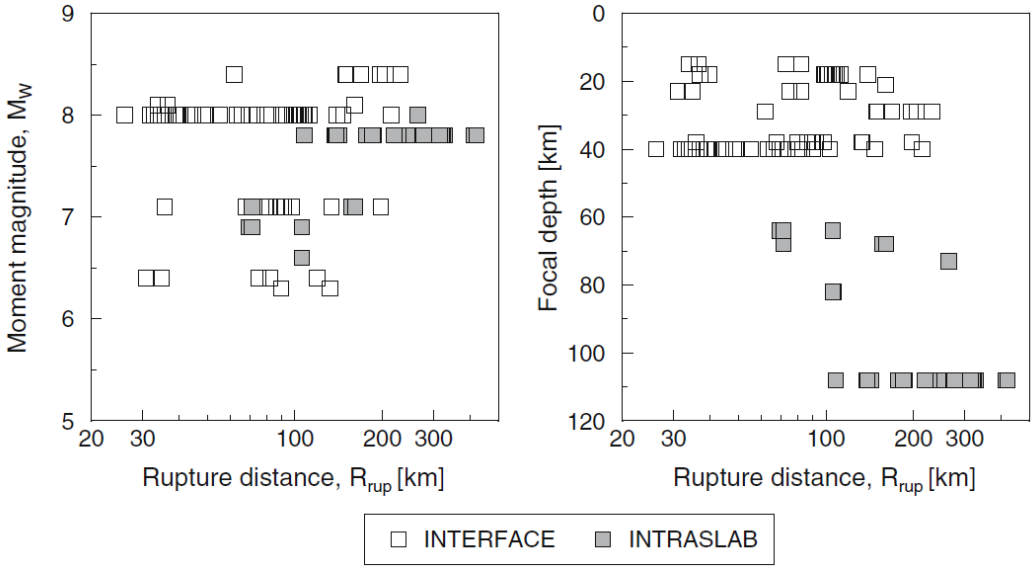

Figure 4.8 Magnitude-distance distribution of the Chile-Peru dataset compiled by Arango et al. (2011b).

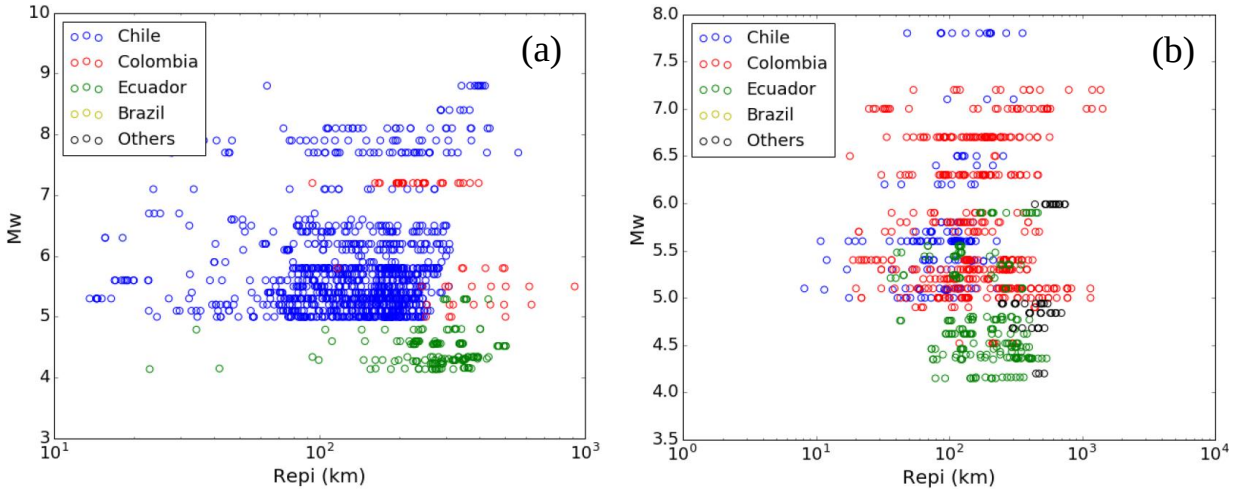

Figure 4.9 Magnitude-distance distribution of the SARA project database: (a) interface and (b) intraslab earthquakes. Repi = epicentral distance. Drouet et al. (2017).

In the case of the SARA project, Montalva et al. (2016, MEA2016) produced an adaptation of the Abrahamson et al. (2016) GMM calibrated to Chilean strong motion data included in the SARA project dataset.

Ground motions from subduction earthquakes in northern South America (northern Peru, Ecuador, and Colombia) have different characteristics and typically exhibit lower intensity than those recorded in the Chile-Peru subduction zone (Drouet et al., 2017). A recent local GMM for northern South America has been developed by Arteta et al. (2021; AEA2021) after regionalizing the global NGA-Sub GMM presented by Abrahamson and Gulerce (2020) for subduction events in South America. The AEA21 model estimates PSa values for periods between 0.01 and 10 seconds. It was developed utilizing 539 recordings from 60 subduction earthquakes that occurred in Colombia and Ecuador, including 222 recordings from 36 interface events and 317 recordings from 24 intraslab events. The model includes forearc and backarc effects and site classification is based on the natural period of the soil, which is estimated using the horizontal-to-vertical response spectral ratio (HVRSR) from low amplitude earthquake ground motions.

Table 4.6 Ground motion datasets and GMMs for the South America subduction zone.

Author	**Region**	**Time frame**	**# Events**	**# Recordings**	**M range**	**R_{rup} or R_{hyp} range**	**GMM**
Arango et al. (2011a)	Chile, Perú	1966-2007	10 interface 5 intraslab	66 32	6.3 – 8.4 6.6 – 7.8	26 – 231 km 54 – 420 km	-
SARA project, Castillo et al. (2016)	South America	1985-2015	286 interface 161 intraslab 126 other	2176 986 948	4.1 – 8.8 4.1 – 7.8 2.0 – 6.8	20 – 1200 km	MEA2016
Arteta et al. (2021)	Colombia, Ecuador	1995-2020	36 interface 24 intraslab	222 317	4.5 – 7.8 4.6 – 7.2	20 – 350 km	AEA2021

4.3.5 Local Databases for Individual Countries outside Latin America

In this subsection, previous efforts to compile strong motion datasets and develop GMMs for individual countries outside Latin America, are described. Table 4.7 shows a summary of such studies for different subduction zone regions. For cases in which a region has multiple generations of databases, only the most recent is shown in Table 4.7. The majority of the models were developed for Japan, probably facilitated by the availability of ground motion data due to both the high seismicity and the seismic network coverage in the country. Several of the GMMs listed in Table 4.7 combine subduction events (interface and intraslab) with shallow crustal earthquakes in both the database and the regression procedure (e.g., Zhao et al., 2006), although the event types are distinguished in the analysis and explicitly defined as input parameters in the formulation of these models. A comprehensive summary of GMMs (not only including subduction zones) can be found in Douglas (2021).

Table 4.7 Summary of recent local subduction models and databases for individual countries outside Latin America.

Reference	Region	M range	Event type	R_{rup} or R_{hyp} range (km)	# events	# recs
Zhao et al. (2006) [1]	Japan	5.0-8.3	Interface Intraslab	0-300	<269	4726
McVerry et al. (2006) [1]	New Zealand	5.08-7.09	Interface Intraslab	6-400	49	435
Sakamoto et al. (2006) [1]	Taiwan	5.5-8.3	Interface Intraslab	1-300	52	3198
Uchiyama and Midorikawa (2006) [1]	Japan	5.5-8.3	Interface Intraslab	Unspecified	52	3198
Dhakal et al. (2008)	Northern Japan	5.1-7.3	Interface Intraslab	70-300	30	2521
Kataoka et al. (2008) [1]	Japan	5.8-8.2	Interface Intraslab	0-900	25	4254

Table 4.7 Summary of recent local subduction models and databases for individual countries outside Latin America.

Reference	Region	M range	Event type	R_{rup} or R_{hyp} range (km)	# events	# recs
Lin and Lee (2008)	Taiwan	4.1-8.1	Interface Intraslab	15-630	54	4383
Goda and Atkinson (2009) [1]	Japan	5.5-7.9	Interface Intraslab	1.5-300	155	8557
Morikawa and Fujiwara (2013) [1]	Japan	5.5-9.0	Interface Intraslab	1-200	333	21681
Skarlatoudis et al. (2013)	Greece	4.4-6.7	Interface Intraslab	65-850	≤21	≤743
Ghofrani and Atkinson (2014)	Japan	7.0-9.0	Interface	30-1000	6	>1000
Vacareanu et al. (2014, 2015) [2]	Vrancea, Romania	5.1-8.0	Intraslab	2-399	38	704
Zhao et al. (2016a)	Japan	5.0-9.0	Interface	20-300	76	3574
Zhao et al. (2016b)	Japan	5.0-8.25	Intraslab	25-300	136	4710
Shoushtari et al. (2016)	Malaysia, Japan & Iran	5.0-7.7	Distant intraslab	120-1400	13	531
Shoushtari et al. (2018)	Japan & Malay Peninsula	5.0-9.1	Distant interface	120-1300	25	728
Chao et al. (2020) [1]	Taiwan	3.5-7.6	Interface Intraslab	0-437	≤316	≤40892
Hu et al. (2020) [1]	Sagami Bay, Japan	4.0-6.8	Interface Intraslab	5-300	456	4513
Phung et al. (2020)	Taiwan & Japan	4.5-9.1	Interface Intraslab	1-345	76	6690

[1] These studies also included records from non-subduction events (crustal earthquakes) to constrain the model features.

[2] The Vrancea zone is usually interpreted as the final stages of oceanic subduction; however, intermediate depth seismicity may result from other processes (Knapp et al., 2001). This study utilized epicentral distances.

4.3.6 Consistency and Documentation of Pre-NGA-Sub Local and Regional Databases

If we look at the regional and local databases as a whole, focusing on the most recent study for regions with several generations, there are several differences between these prior studies and

NGA-Sub with regard to data compilation and development procedures. Notable differences include:

- Lack of consistent approaches for ground motion data processing: Regional and local compilations often contain both raw and processed recordings. Among the processed records, different processing techniques are applied. Frequently the ground motion time series are not disseminated and only IM values are compiled (e.g., Arango et al., 2011a database for Central America; Abrahamson et al., 2016 global GMM). Additionally, most of these studies do not provide a clear indication of maximum usable period and the documentation explaining details about processing is very limited.
- Lack of clear protocols for site parameters assignments. In several cases, V_{S30} values are not provided and generic classifications such as "rock", "firm soil", or "soft soil" are utilized (e.g., for Mexico Jaimes and García, 2020 consider that all sites are NEHRP class B).
- Lack of clear protocols for development of source metadata, such as assignment of seismic moment, hypocenter, representation of finite fault geometry, and event type classification as interface or intraslab. For most of the studies listed in this Chapter, source metadata documentation is limited. For instance, in the case of the database developed by Bastías and Montalva (2016) for Chile, there is some discussion about event type assignments that explains briefly the protocols, but this discussion is more limited than NGA-Sub documentation.
- Databases are not always publicly accessible, and in several cases, the datasets utilized to develop GMMs are not provided (e.g., Jaimes and García-Soto, 2020 for Mexico; Zhao et

al., 2016a-b for Japan). On the other hand, a fair number of the studies listed in this Chapter provide flat files containing IM values (e.g., PGA, PGV, and PSa at specific periods) along with supporting metadata (e.g., Montalva et al., 2017 and Idini et al., 2017 for Chile). None of the listed studies provide the processed ground motions.

5 EXTENSION OF NGA-SUB DATABASE FOR CENTRAL AMERICA AND MEXICO

5.1 INTRODUCTION

Ongoing work is extending and improving the NGA-Sub database in Latin America, including the Mexico and South America regions. There are two reasons that events that are considered in the extended database were not used in the original database (Chapter 2). The first is that the events occurred too late to be considered, which mainly applies to Mexico, where two large intraslab events (**M**7.18 and **M**8.27) occurred in September 2017 and one interface earthquake (**M**7.2) occurred in February 2018. These earthquakes occurred after the 2016 cutoff applied in the project, as mentioned in Section 2.6. The second reason for events having not been included is that they fall below the magnitude threshold of 6, which was applied in the original database effort to control workload.

The additional data is anticipated to enhance ground motion characterization in the following respects:

a) Adding large magnitude events is important because they provide data within the parameter space that has a direct impact on the hazard levels that tend to control seismic design. Particularly, the 2017 **M**8.27 Mexico earthquake has a larger magnitude than the magnitude break parameter considered in this region for intraslab events (**M**7.4; Ji and Archuleta, 2018). As such, it can be considered in estimating the slope of the magnitude

scaling function beyond the break magnitude, which is useful both for the subject region and globally.

b) By adding more recordings, including those from large magnitude events, it is possible to improve the path characterization in this region. Specifically, additional recorded ground motions at both forearc and backarc sites could help to identify regional trends associated with backarc effects.

c) Adding new ground motions increases the number of recordings at selected sites (e.g., more than 10 recordings at the same site), which enables the evaluation of non-ergodic (site-specific) site response effects at those stations.

This chapter describes the status of the NGA-Subduction (NGA-Sub) database in the Central America and Mexico (CAM) region and identifies areas where the database has been extended and improved to support ground motion characterization research in Latin America. The areas of improvement (described in the following sections), are:

1. Development of source and path metadata for events already included in the NGA-Sub database but for which critical event type classifications (interface, intraslab, shallow crustal, or outer-rise) were not made. Absent those classifications, these events were not used for model-building in NGA-Sub. This applies to events with magnitudes below **M**6 in the Central America and Mexico region as described in Section 5.2.

2. Addition of new data that were not available at the time ground motion recordings were compiled for NGA-Sub or from events that occurred too late to be considered. This task involves ground motion data processing and development of source, path, and site metadata

as well, as described in Sections 5.3-5.5. This applies mainly to the two large-magnitude intraslab events that occurred in Mexico in September 2017 and one interface earthquake that occurred in February 2018.

The extension of NGA-Sub database for Mexico to support ground motion research in Latin America has been carried out in collaboration with the research group of Prof. Juan Mayoral at the Institute of Engineering of the National Autonomous University of Mexico (UNAM) and Prof. Xyoli Perez-Campos at the Institute of Geophysics at UNAM. Dr. Perez-Campos also serves as the head of the National Seismological Service (SSN) in Mexico since 2014. This collaboration has facilitated the access and interpretation of ground motion data and associated source, path, and site metadata.

5.2 ADDITION OF METADATA FOR EVENTS IN THE NGA-SUB DATABASE

There are a significant number of earthquakes included in the NGA-Sub database for which classifications of event-type (interface, intraslab, shallow crustal, or outer-rise) were not performed as part of the NGA-Sub project. As a result of these missing classifications, the data from these events could not be used during NGA-Sub model development. Moreover, the source/path metadata developed for these events did not go through quality assurance (QA) procedures applied to events with event-type classifications, and therefore their source parameters may be less reliable and certain information may be missing.

Figure 5.1 shows the region of Central America and Mexico, with the locations of both classified (colored circles) and unclassified (white circles) events. There are 181 unclassified events that have relatively small magnitudes (**M** 3.4-6) and that are in the same general locations as larger events that are included in the NGA-Sub database.

For the 181 unclassified events, a subset of 59 events has been selected to develop source and path metadata. These 59 events were selected because they were recorded at five or more stations, and as such, these data have the potential for greater contributions to the path and site response characterization. The source and path metadata have been developed in a way that is consistent with the work described earlier for NGA-Sub (Chapters 2-3). Considering that these are mid-size and small earthquakes (**M** 3.4-6), the methodology utilized to characterize events without an available FFM from literature has been applied. This methodology includes:

i. Identify seismic moment, moment magnitude, focal mechanism, and hypocenter location from earthquake catalogs (EHB, ISC, CMT) following the procedure presented in Sections 2.3.2(a)-(b).
ii. Assign fault type based on the rake angle as shown in Section 2.3.2(c).
iii. Classify sources as interface, intraslab, outer-rise, or shallow crustal following the procedure described in Section 2.3.2(d).
iv. Estimate dimensions, location, and orientation of the rupture surface using the simulation procedure presented in Section 2.5.2.
v. Compute the distance metrics as defined in Section 3.2.1.

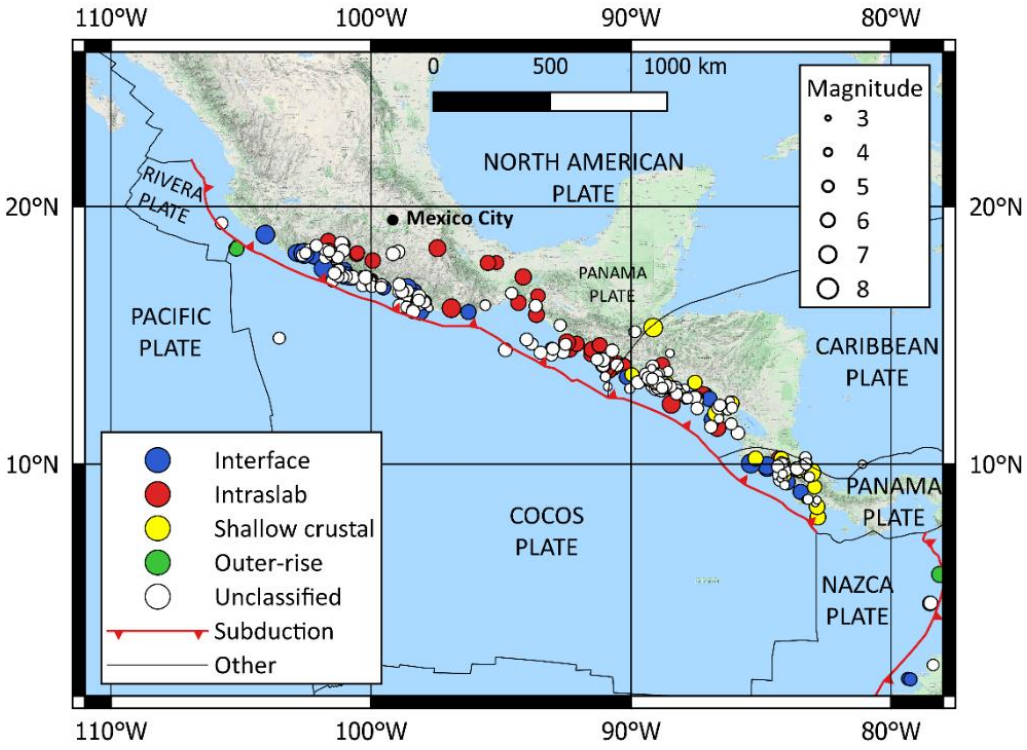

Figure 5.1. Locations of events in Central America and Mexico showing classified and unclassified earthquakes by event-type.

Figure 5.2 shows the locations of both classified (colored circles) and unclassified (white circles) events in CAM after addition of the 59 events, which include 34 interface events, 18 intraslab events, five shallow crustal events, and two outer-rise events. Figure 5.3 shows the magnitude-distance distribution of the NGA-Sub database in CAM including the data utilized by ground-motion modelers (April 2019 release, blue squares with $\mathbf{M} \geq 6$) and the updates described here (red circles with $\mathbf{M} < 6$). The updated data add 774 recordings from the 59 earthquakes. Figure 5.4 shows the magnitude-distance distribution in CAM for the updated database with differentiation by event-type. The additional number of recordings for subduction earthquakes is 704, including 418 recordings from interface events (blue squares with $\mathbf{M} < 6$) and 286 from intraslab events (red circles with $\mathbf{M} < 6$).

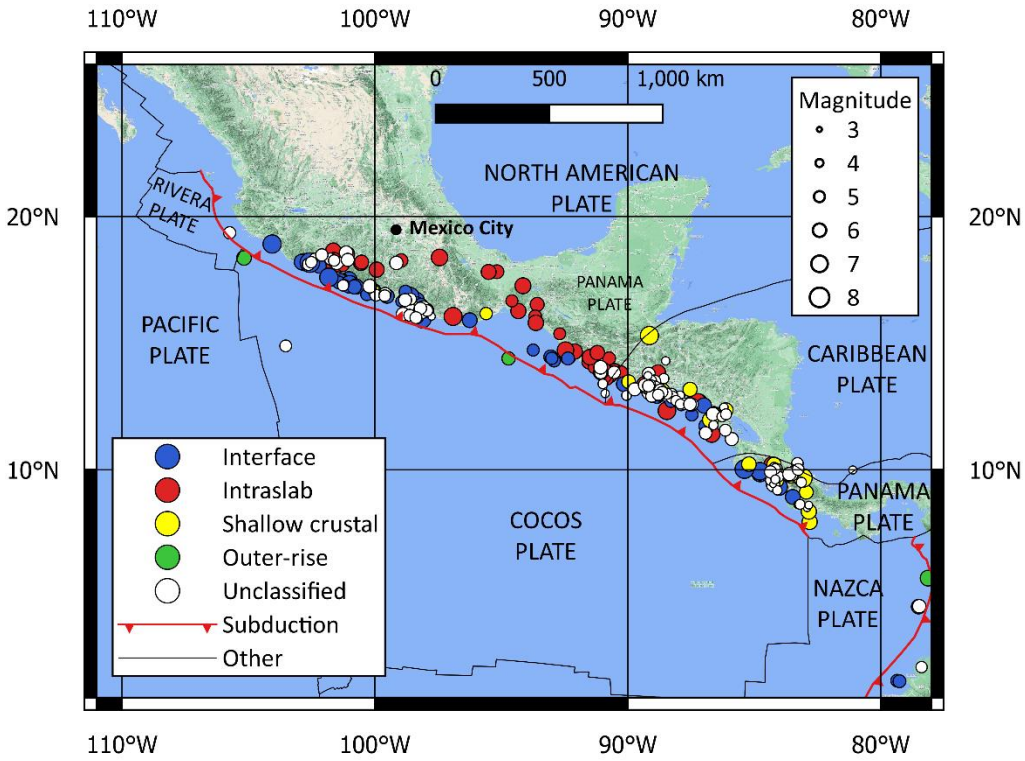

Figure 5.2. Locations of events in Central America and Mexico showing classified and unclassified earthquakes by event-type, after the addition of 59 previously-unclassified events.

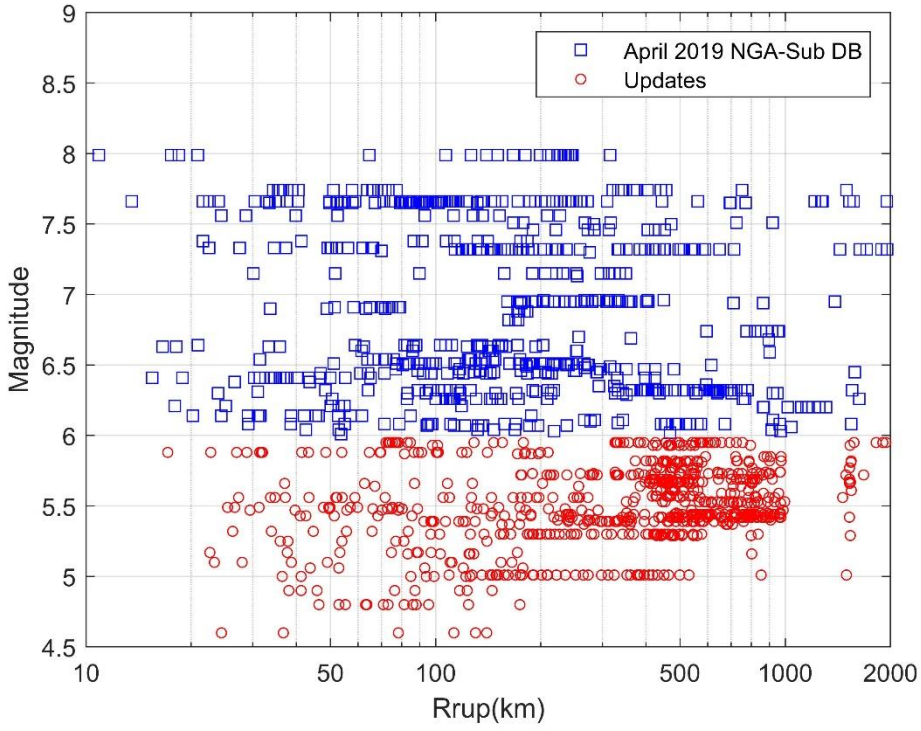

Figure 5.3. Magnitude-distance distribution of the NGA-Sub database in CAM following updates.

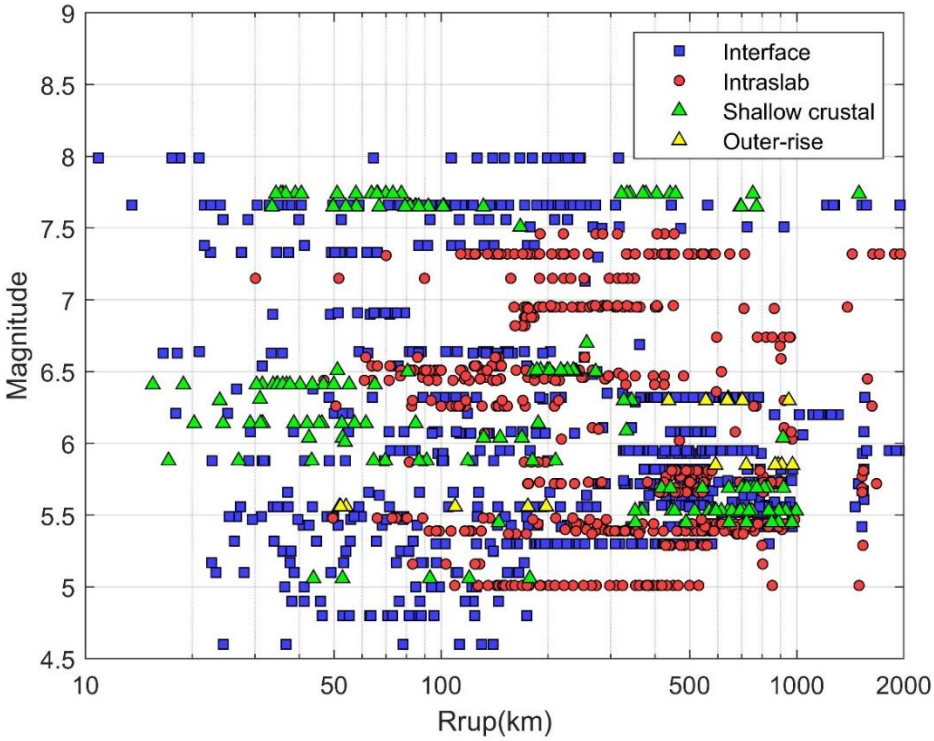

Figure 5.4. Magnitude-distance distribution of the NGA-Sub database in CAM including updates and differentiating by event-type.

Figure 5.5 shows the cumulative number of earthquakes over time in CAM for the updated database with differentiation by event-type. Also shown on the right side of the plot is the total number of events by event-type as used in NGA-Sub (i.e., prior to the present updates). The total number of interface earthquakes in the database more than doubled, whereas the total number of intraslab events increased by approximately 50%.

Figure 5.6a and Figure 5.6b show the cumulative number of recordings over time in CAM from interface and intraslab earthquakes, respectively. The number of recordings after the updates from interface events is approximately 2.3 times the number of recordings provided in the April 2019 NGA-Sub database release that was utilized by the ground-motion modelers. In the case of intraslab events, the number of recordings doubled.

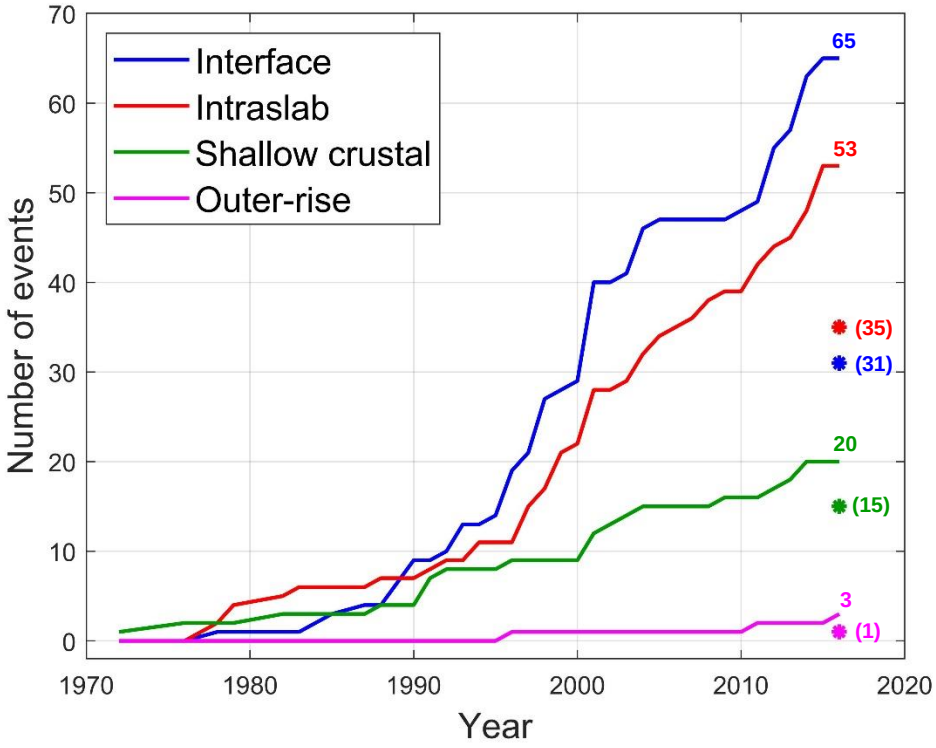

Figure 5.5. Cumulative number of earthquakes over time in CAM including updates and differentiating by event-type. Color dots indicate the total number of events before the updates, which is shown in parenthesis.

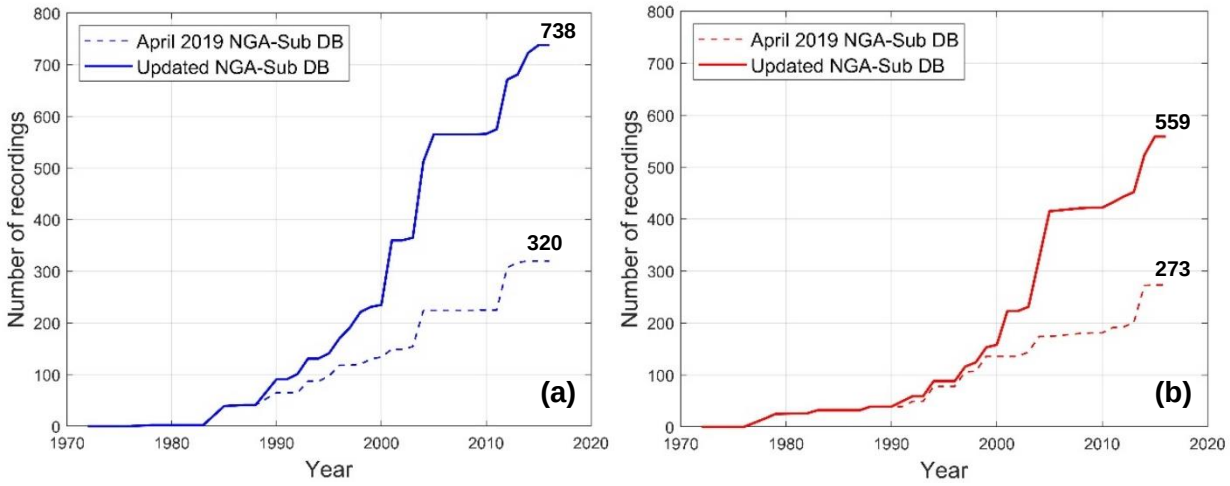

Figure 5.6. Cumulative number of recordings over time in CAM for (a) interface and (b) intraslab earthquakes.

5.3 POST-NGA-SUB LARGE MAGNITUDE EVENTS

Two large intraslab events occurred in Mexico in September 2017: the September 8, 2017, **M**8.27 offshore Chiapas earthquake and the September 19, 2017, **M**7.18 Puebla earthquake. As explained previously, these earthquakes were not included in the NGA-Sub database mainly because of the 2016 cutoff applied in the project. Each event produced substantial numbers of recordings which are now included in the updated database. Additionally, ground motion recordings from the February 16, 2018 **M**7.2 Oaxaca earthquake (an interface event) are also included in these updates. Figure 5.7 (Cruz-Atienza et al., 2021) shows the locations of epicenters and focal mechanisms ("beachballs") of these three earthquakes, along with the aftershock sequence of each event (orange dots). Figure 5.7 also shows rupture zones of historic interface earthquakes (white shaded areas), 1 cm aseismic slip contours (orange shaded areas), regional instrumentation (GPS stations and strong motion stations, indicated as green triangles and orange circles, respectively), and iso-depths of the plate interface (gray contours).

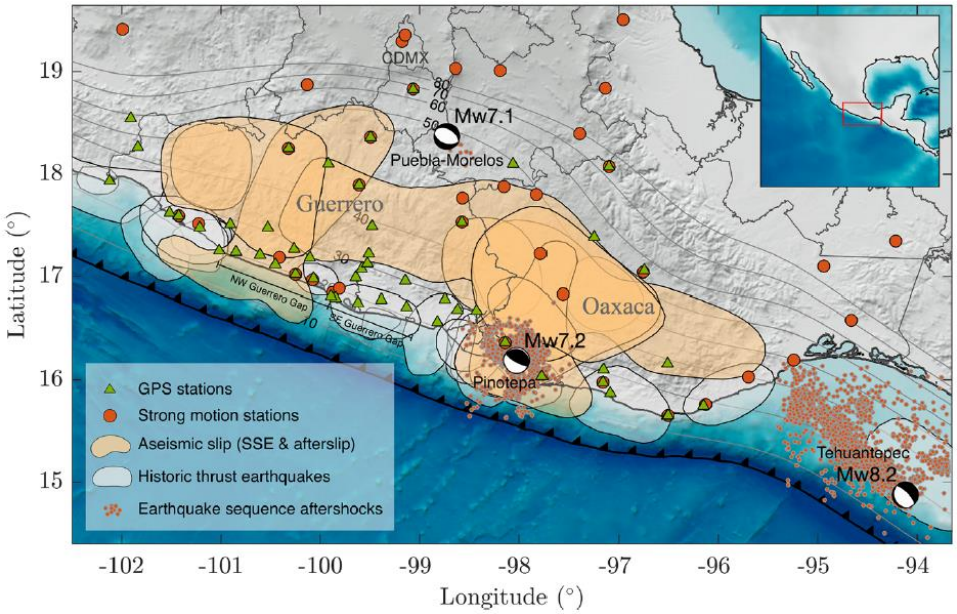

Figure 5.7. 2017 **M**8.27 offshore Chiapas, 2017 **M**7.18 Puebla, and 2018 **M**7.2 Oaxaca earthquake sequence. SSE=Slow Slip Events; CDMX=Mexico City. (Cruz-Atienza et al., 2021).

5.3.1 September 8, 2017 M8.27 Offshore Chiapas Earthquake

(a) Source description

The 2017 **M**8.27 offshore Chiapas earthquake occurred at 04:49 am (universal time, UTC) on September 8, 2017, in the Gulf of Tehuantepec off the southern coast of Mexico, near state of Chiapas. To establish the source parameters of this large earthquake, eight different finite fault models from literature were compiled, which are summarized in Table 5.1. For each of these models, the table lists the data sources utilized in the model, seismic moment M_0 (when available), moment magnitude **M**, and hypocentral depth. All the listed models have appeared in peer-reviewed journal papers, and they have been developed from different data sources: (1) Okuwaki and Yagi (2017) used 34 globally observed teleseismic P wave forms (vertical components only); (2) Ye et al. (2017) inverted global long-period W phase data (182 channels from 71 stations) and then refined their model using deepwater tsunami recordings and a preliminary data set of coseismic displacements from GPS records; (3) Melgar et al. (2018a) utilized 10 strong motion recordings, 11 static GPS, 55 high-rate GPS, four tsunami tide gauges sensors, and one ocean-bottom pressure (DART) sensor in the region; (4) Chen et al. (2018) used 11 high-rate GPS, 70 static GPS, InSAR measurements, and teleseismic displacement waveforms at 36 stations, then validated their model by tsunami observations at two DART sensors and three coastal tide gauges; (5) Heidarzadeh et al. (2018) used 14 tsunami tide gauge records, four DART records, and 76 teleseismic body-wave records (64 P and 12 SH); (6) Gusman et al. (2018) utilized tsunami waveforms recorded at 12 coastal tide gauges and four DART buoys; (7) Adriano et al. (2018) used six coastal tide stations and three nearby DART pressure gauge stations; (8) Guo et al. (2019) utilized 60 teleseismic body-wave records (36 P and 24 SH) and nine continuous GPS.

Table 5.1 Alternate finite-fault models for 2017 **M**8.27 offshore Chiapas earthquake.

Model	Data Sources	M_0 (N·m)	M	Hypocentral depth (km)
Okuwaki & Yagi (2017)	Teleseismic	1.85×10^{21}	8.14	18.0
Ye et al. (2017)	Teleseismic; tsunami; crustal displacement	2.57×10^{21}	8.24	50.5
Melgar et al. (2018a)*	**Local seismic data; crustal displacement; tsunami**	**-**	**8.2**	**45.9**
Chen et al. (2018)	Teleseismic; tsunami; crustal displacement	1.84×10^{21}	8.14	58.0
Heidarzadeh et al. (2018)	Teleseismic; tsunami	1.91×10^{21}	8.15	47.4
Gusman et al. (2018)	Tsunami	1.95×10^{21}	8.16	58.0
Adriano et al. (2018)	Tsunami	2.9×10^{21}	8.27	58.0
Guo et al. (2019)	Teleseismic; crustal displacement	2.61×10^{21}	8.24	50.5

***** The preferred model is indicated in bold font.

The model by Melgar et al. (2018a) is selected because it considered multiple data sources, including nearby strong motion data, crustal displacement measurements, and tsunami recordings, which is in accordance with NGA-Sub procedures (Section 2.4.2). The models by Ye et al. (2017) and Chen et al. (2018) have similar attributes but lack local seismic data. Figure 5.8(a) shows the fault slip distribution of the selected model and the applied trimming (purple line). The trimming was applied according with the criteria described in Section 2.4.3, i.e., trimming the fault regions with slip values lower than 15% of the maximum slip. Figure 5.8(b) shows the fault rupture location relative to the subducting slab geometry.

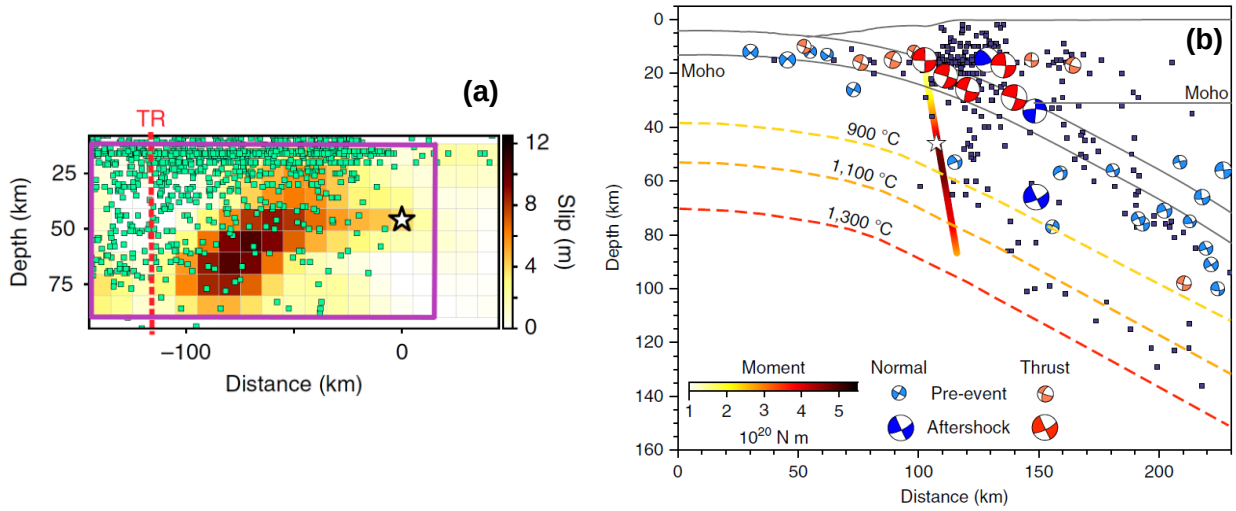

Figure 5.8. Selected FFM modified from Melgar et al. (2018a). The white star is the event hypocenter. **(a)** Slip distribution. The purple line represents the applied trimming. Green squares are the aftershocks within a distance of 10 km. The orange line labelled TR is the intersection of the fault plane with the projection of the Tehuantepec Ridge. **(b)** Subvertical fault rupture. Dark blue squares are aftershock locations. Black lines indicate the oceanic and continental crusts. Geotherms are indicated as dashed lines.

Figure 5.9 shows a map of Mexico with the epicenter and rupture area of the **M**8.27 offshore Chiapas earthquake, along with the ground motion stations where the event was recorded. The stations are from the IG, UV, and VM networks operated by the SSN; the RAII-UNAM network operated by the Institute of Engineering at UNAM; and the RACM network operated by the Instrumentation and Seismic Recording Center (CIRES). More information about these networks is provided in Section 5.4. As shown in Figure 5.9, most of the ground motion stations are located to the northwest of the rupture area, with rupture distances ranging from approximately 70 to 2900 km.

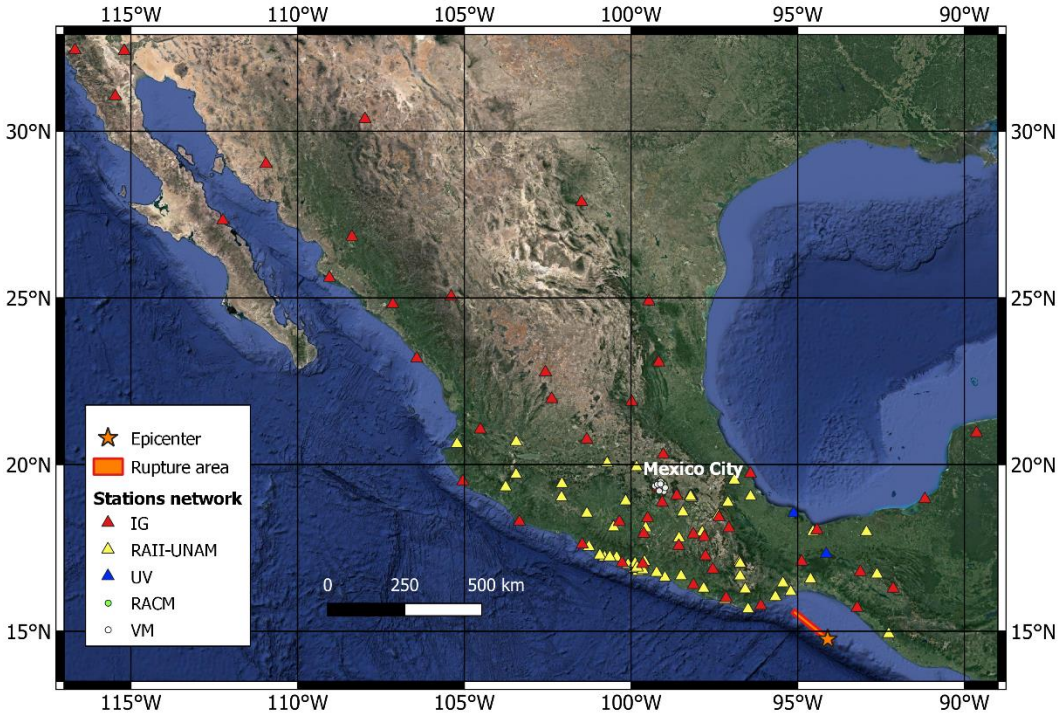

Figure 5.9. Epicenter location and rupture area of the **M**8.27 offshore Chiapas earthquake. All ground motion stations from different networks are shown.

Figure 5.10 shows a more detailed view of the epicentral area, including limits of the trimmed finite fault model, and relatively near-field stations that recorded the **M**8.27 offshore Chiapas earthquake. The hypocenter utilized in the finite fault model is located at 94.103° W longitude, 14.761° N latitude, and 45.9 km depth. This hypocenter location differs from results reported by the USGS due to errors in teleseismic-based hypocenter locations attributable to differences in local crustal velocities relative to that considered in global models. For earthquake locations in Mexico, global teleseismic models generate systematic biases that are on average 26 km northeast of those developed by local agencies in Mexico such as SSN (Hjörleifsdóttir et al., 2016). This event has a normal mechanism (rake angle is -93° from CMT catalog). The preferred moment tensor fault plane, selected to conform with the finite fault model, has a strike of 310° and a dip of 79°. Ground motion stations that are closest to the earthquake are on the coast of Chiapas

north of the rupture area. Additionally, there are clusters of sites that recorded this event in specific areas (indicated in Figure 5.10): 10 stations in the Oaxaca City area, seven stations in the Puebla City area, and 72 stations in the Mexico City area; at about 230 km, 500 km, and 570 km away from the earthquake rupture surface, respectively.

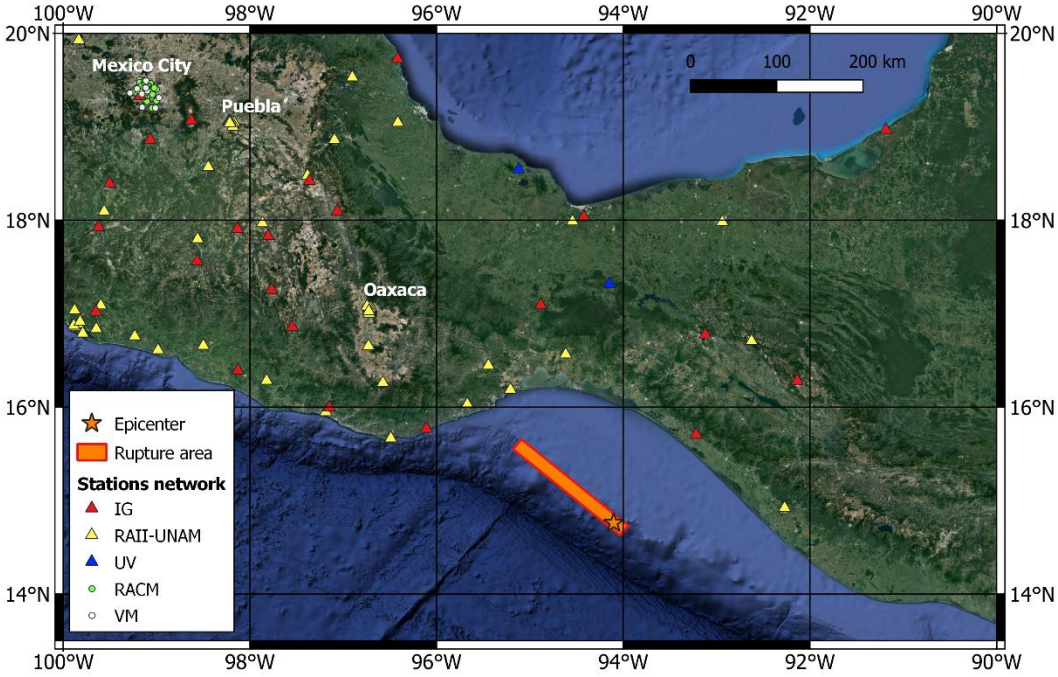

Figure 5.10. Epicenter location and rupture area of the **M**8.27 offshore Chiapas earthquake. Ground motion stations from different networks which are relatively close to the event source are shown.

The assigned moment magnitude **M** = 8.27 was computed using the seismic moment $M_0 = 2.82 \times 10^{21}$ N·m, which was taken from the CMT catalog following the procedures for magnitude assignments used in NGA-Sub (Section 2.3.2a). The CMT seismic moment differs from the value provided by the USGS, which is $M_0 = 2.16 \times 10^{21}$ N·m (**M** = 8.19). These differences in seismic moment (or moment magnitude) highlight the issue of uncertainty in these critical parameters as derived from modern moment tensor inversions. These issues are explored further in the following subsection.

(b) Moment tensor and seismic moment uncertainty

There are two general sources of uncertainty in moment tensor solutions that appear in seismic catalogs:

1. Variations from alternate inversions, which largely result from the use of different data sources, different inversion procedures, and different crustal velocity models (e.g., from different publications or catalogs). These variations reflect epistemic uncertainty in seismic moment (Kagan, 2003; Rösler et al., 2021).

2. Uncertainty in seismic moment from a particular inversion, which is caused by data scatter and limited data. These variations reflect random errors related to the limited ability of the utilized data to fully constrain the source model.

Most prior studies that have investigated moment magnitude uncertainty consider only the first type (Kagan, 2003; Rösler et al., 2021). The lack of consideration of inversion-related uncertainty causes overall seismic moment uncertainty to be underestimated (Scognamiglio et al., 2016; Valentine and Trampert, 2012). Although the second type of uncertainty is not often considered, moment tensor catalogs (e.g., CMT) provide standard errors on the terms in the moment tensor matrix,

$$\underline{M} \equiv M_0 \begin{pmatrix} M_{rr} & M_{r\theta} & M_{r\varphi} \\ M_{\theta r} & M_{\theta\theta} & M_{\theta\varphi} \\ M_{\varphi r} & M_{\varphi\theta} & M_{\varphi\varphi} \end{pmatrix} \tag{5.1}$$

The right side of Equation (5.1) includes the seismic moment scalar M_0 and a normalized tensor in a standard spherical coordinate system. The standard errors provided by CMT apply to each of the six unique elements of the moment tensor and are denoted E_{ij}, where i and j are the three

indices (r, θ, and φ). In the reporting of moment tensor uncertainty, the seismic moment uncertainty is not provided. For instance, for the **M**8.27 offshore Chiapas earthquake, the CMT catalog reported a seismic moment scalar $M_0 = 2.82 \times 10^{21}$ N·m (with unknown uncertainty), and the following moment tensor elements along with their standard errors (Ekström et al., 2012):

M_{rr} = -1.090 ± 0.004, $M_{\theta\theta}$ = 0.358 ± 0.003, $M_{\varphi\varphi}$ = 0.734 ± 0.003, $M_{r\theta}$ = 1.750 ± 0.023,

$M_{r\varphi}$ = -1.890 ± 0.024, $M_{\theta\varphi}$ = -0.652 ± 0.002.

Kagan (2002) studied random errors of shallow earthquakes (depth limit 0-70 km) reported in the Harvard catalog (currently CMT catalog) using a relative error ε, which is defined as the ratio of the Frobenius norms of the error tensor and the moment tensor, i.e.,

$$\varepsilon \equiv \sqrt{\sum_{i,j} E_{ij}^2 \Big/ \sum_{i,j} M_{ij}^2} \tag{5.2}$$

where E_{ij} and M_{ij} are standard error and moment tensor components, respectively. This relative error ε is apparently only a part of the total seismic moment error (1/3 to 1/2 of the total, as reported by Kagan 2000 and Kagan 2002). Considering the seismic moment tensor solution and the uncertainty reported for each tensor element of the 2017 offshore Chiapas earthquake, the relative error estimate for this event is $\varepsilon = 0.012$. Figure 5.11(a) shows the distribution of ε with moment magnitude in the Harvard catalog (1982/1/1–1999/12/31) for the shallow earthquakes studied by Kagan (2002); the red circle indicates the estimate for the **M**8.27 offshore Chiapas earthquake ($\log_{10}(\varepsilon)$ ~ -1.925), which is within the expected range according to the shown data.

To estimate the total random errors in CMT solutions, and their effect on magnitude uncertainty, Kagan (2002) utilized the dimensionless Γ index (Kagan, 2000) as a proxy. Although

the relation between the magnitude standard error ($\sigma_{\boldsymbol{M}}$) and the standard error of Γ (σ_Γ) is not one-to-one (because it varies depending on the focal mechanisms), it can be approximated based on results of simulations (Kagan, 2002), as follows:

$$\sigma_{\boldsymbol{M}} = \frac{\sigma_{M_0}}{1.5\ M_0\ ln(10)} \approx \frac{\sigma_\Gamma}{3.75\ ln(10)} \tag{5.3}$$

Figure 5.11(b) presents an example of how σ_Γ varies with moment magnitude, including a linear regression curve that approximates the decreasing trend. Using this relationship in the case of the **M**8.27 Chiapas event, the mean standard error of the Γ index can be estimated as σ_Γ ~ 0.183, which results in a magnitude uncertainty of $\sigma_{\boldsymbol{M}}$ ~ 0.021. If a mean + one standard error estimate of σ_Γ is taken (~ 0.234), the resulting magnitude uncertainty is $\sigma_{\boldsymbol{M}}$ ~ 0.027. As highlighted using the gray rectangle in Figure 5.11(b), for large earthquakes (**M**7-8) the variation of σ_Γ is high, and this standard error might take values in the range from 0.1 to 0.4, which leads to a magnitude uncertainty range $\sigma_{\boldsymbol{M}}$ ~ 0.012-0.046.

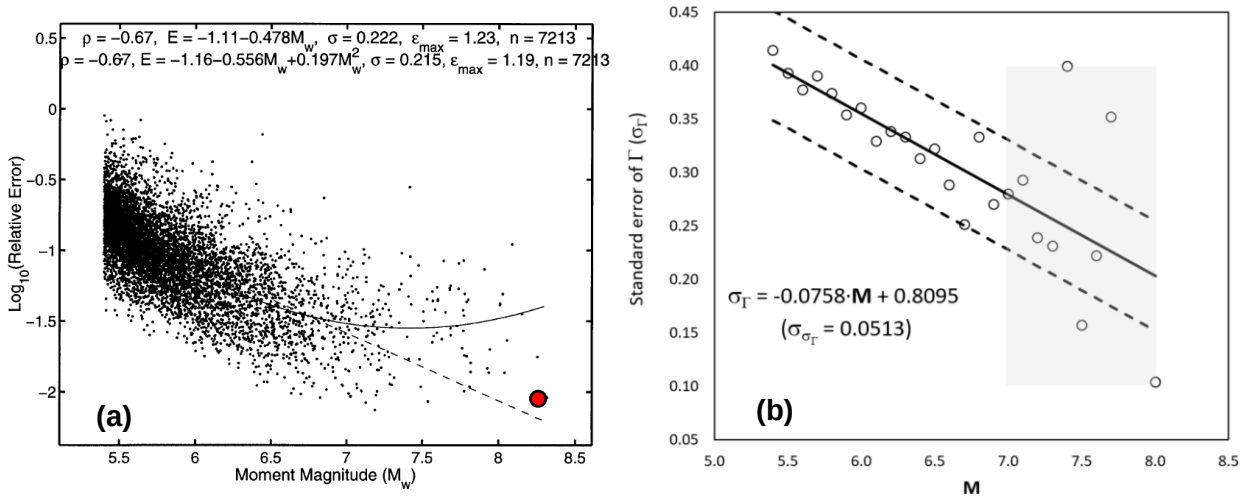

Figure 5.11. (a) Relative error $\boldsymbol{\varepsilon}$ (in $\log_{10}$-scale) versus moment magnitude for shallow earthquakes (depth limit 0-70 km) in the Harvard catalog (1982/1/1–1999/12/31). The curves show linear and quadratic fits; the red point is the **M**8.27 offshore Chiapas event. **(b)** Dependence of the standard error of **Γ** index ($\boldsymbol{\sigma_\Gamma}$) on moment magnitude for shallow earthquakes (depth limit 0-70 km). Linear regression curve ± one standard deviation is shown. Both plots were modified from Kagan (2002).

Several alternative methods have been used to estimate magnitude uncertainty in literature, which have not been applied to the subject events, but are described here for completeness. Stähler and Sigloch (2014) developed a framework for probabilistic seismic inversion using Bayesian inference to account for uncertainties related to inverted parameters (e.g., source depth), in the development of moment tensor solutions. The proposed method is essentially identifying the mean values and uncertainties of a series of source parameters, including earthquake depth, moment tensor (M_0 and M_{ij} quantities in Eq. 5.1), and a source time function based on previous non-Bayesian inversions. As an example, they applied this framework to a M_W 5.7 earthquake that occurred in central Virginia on 23 August 2011, reporting a 90% credible interval (1st to 9th decile) for M_W of 5.57-5.74.

Tape and Tape (2016) describe an alternative approach in which moment tensor uncertainties are represented using a "confidence curve" $\boldsymbol{P}$, which is the probability that the true moment tensor lies within a certain neighborhood of $\underline{M}$. This function is estimated from the misfit between the observed and the synthetic waveforms generated from a series of inversions. The area under the confidence curve ($\boldsymbol{P_{AV}}$) provides a single, abbreviated "confidence parameter" for $\underline{M}$. This approach was applied to 17 nuclear explosions and 12 earthquakes at the Nevada Test Site, 63 small (Mw<2.5) events at Uturuncu volcano in Bolivia, and 21 moderate (Mw>4) earthquakes in the southern Alaska subduction zone (Alvizuri et al., 2018). In the case of the 21 earthquakes in Alaska, $\boldsymbol{P_{AV}}$ ranges from 0.78 to 0.97 for the selected inversions, i.e., the inversions with the lowest misfit for each event. The disadvantage of this methodology is that it requires the production of multiple inversions for each event.

The uncertainties that are provided by both of these alternative methods (Stähler and Sigloch, 2014; Tape and Tape, 2016) evaluate the second type of uncertainty identified above (uncertainty in the inversion process given a certain data set). The approach proposed by Stähler and Sigloch (2014) provides uncertainty estimates for moment tensor elements and moment magnitude, whereas the approach of Tape and Tape (2016) does not expand the treatment of uncertainties beyond the probability given by the confidence curve, i.e., magnitude uncertainties are not estimated.

The first type of uncertainty (differences between catalogs) was investigated by Rösler et al. (2021), who evaluated differences in scalar moments reported by the USGS (M_0^{USGS}) and CMT (M_0^{CMT}) catalogs for 5,000 earthquakes. Specifically, they considered the normalized scalar moment difference defined in Equation 5.4.

$$\frac{\Delta M_0}{\overline{M_0}} \equiv \frac{M_0^{USGS} - M_0^{CMT}}{\frac{1}{2}(M_0^{USGS} + M_0^{CMT})} \tag{5.4}$$

Their study shows that taking into account all 5,000 earthquakes, these differences have a negative mean ($\mu = -12.1\%$ in Figure 5.12a), which implies that the scalar moment from the CMT catalog is generally larger than the value reported in the USGS catalog. In the case of the 2017 offshore Chiapas earthquake, the normalized scalar moment difference is -26% (also shown in Figure 5.12a), which is close to the total standard deviation of all observations ($\sigma = 26.7\%$). Rösler et al. (2021) also showed that these normalized differences decrease with seismic moment (or magnitude), as presented in Figure 5.12b. The differences for the magnitude bin 7.5-8.5 (N=22 events) have a negative mean $\mu = -0.5\%$ and a deviation $\sigma = 9.6\%$. Despite its large magnitude,

the 2017 offshore Chiapas earthquake has a relatively high normalized difference (-26%) when compared to similar size events.

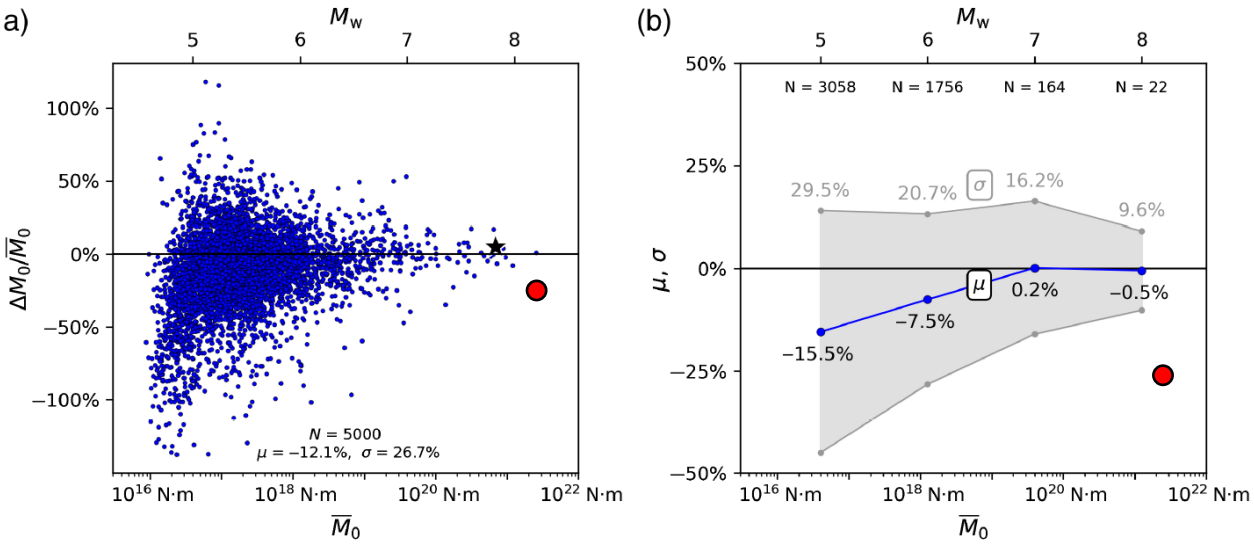

Figure 5.12. Differences in normalized scalar moment between USGS and CMT catalogs for the same earthquakes; modified from Rösler et al. (2021). The red circle marks the 2017 offshore Chiapas earthquake. **(a)** Differences for all N=5,000 events. The star marks the 2016 Kaikōura earthquake. **(b)** Differences by magnitude unit bins, for example, 4.5–5.5.

(c) Moment uncertainty of offshore Chiapas earthquake

Per the discussion in the previous section, estimates of seismic moment are subject to epistemic uncertainty (Type 1 above) and aleatory variability (Type 2). The Type 1 (epistemic) uncertainty is estimated from alternate solutions. Considering the eight FFMs reported in Table 5.1, the epistemic uncertainty of the seismic moment was estimated by calculating the standard deviation of the listed M_0 values, resulting in $\sigma_{M_0} \sim 0.41 \times 10^{21}$ N·m, which corresponds to a Type 1 uncertainty of moment magnitude of $\sigma_{\boldsymbol{M1}} \sim 0.052$. Normalizing σ_{M_0} by the mean scalar moment from USGS and CMT catalogs ($\overline{M_0}$), the estimated epistemic uncertainty is $\sigma_{M_0}/\overline{M_0}$ = 16.6%, which is also relatively high compared to the distribution of the magnitude bin 7.5-8.5.

As described in the previous section, the Type 2 (aleatory) variability is derived from the mean standard error of the Γ index using the relation in Figure 5.11(b). This results in an estimate of $\sigma_{\Gamma} \sim 0.183$, which results in a Type 2 variability of $\sigma_{\boldsymbol{M2}} \sim 0.021$. Assuming that the epistemic uncertainty and aleatory variability are independent, the combined uncertainty in moment magnitude can be estimated as:

$$\sigma_{\mathbf{M}} = \sqrt{{\sigma_{\boldsymbol{M1}}}^2 + {\sigma_{\boldsymbol{M2}}}^2} = \sqrt{0.052^2 + 0.021^2} = 0.056 \tag{5.5}$$

where $\sigma_{\mathbf{M}}$ is the total standard deviation of the moment magnitude **M**.

5.3.2 September 19, 2017 M7.18 Puebla Earthquake

The 2017 **M**7.18 Puebla earthquake occurred at 06:14 pm (universal time) on September 19, 2017, in the state of Puebla; its epicenter was approximately 90 km southwest of the city of Puebla. Casualties and structural damage were reported in the affected region, including the states of Puebla, Morelos, Guerrero, as well as Mexico City, located approximately at 120 km from the epicenter. During this earthquake, at least 46 structures collapsed in Mexico City alone and there were 246 casualties (Mayoral et al., 2017). To establish the source parameters of this earthquake, three different finite fault models from literature were compiled, which are summarized in Table 5.2. For each of these models, the table lists the data sources utilized in the model, seismic moment M_0 (when available), moment magnitude **M**, and hypocentral depth. All the listed models have appeared in peer-reviewed journal papers, and they have been developed from different data sources: (1) Melgar et al. (2018b) utilized 16 strong motion recordings and six static GPS records; (2) Mirwald et al. (2019) employed six strong motion recordings; (3) Atzori et al. (2019) used InSaR measurements and GPS data from six nearby stations.

The model by Melgar et al. (2018b) is selected because it considered multiple data sources, including nearby strong motion data and crustal displacement measurements, which is in accordance with NGA-Sub procedures (Section 2.4.2). The model by Mirwald et al. (2019) also considered local seismic data but Melgar et al. (2018b) included more ground motion stations in addition to crustal displacement data. Figure 5.13(a) shows the fault slip distribution of the selected model and the trimming (purple line) applied according with the criteria described in Section 2.4.3. The rupture area is modeled by two rectangles with the same dip (δ=44°) but different lengths, in a similar manner than that presented in Section 2.4.4 for other multi-rectangle rupture models in Japan and South America. Figure 5.13(b) shows the fault rupture location relative to the subducting slab geometry.

Table 5.2 Alternate finite-fault models for 2017 **M**7.18 Puebla earthquake.

Model	Data Sources	M_0 (N·m)	M	Hypocentral depth (km)
Melgar et al. (2018b)*	**Local seismic data; crustal displacement**	**-**	**7.1**	**57.5**
Mirwald et al. (2019)	Local seismic data	1.05×10^{20}	7.31	57.0
Atzori et al. (2019)	Crustal displacement	2.5×10^{19}	6.9	44.0

***** The preferred model is indicated in bold font.

Figure 5.14 shows a map of Mexico with the epicenter and rupture area of the **M**7.18 Puebla earthquake, along with the ground motion stations where the event was recorded. The stations are from the IG, UV, and VM networks operated by the SSN; the RAII-UNAM network operated by the Institute of Engineering at UNAM; and the RACM network operated by CIRES. More information about these networks is provided in Section 5.4. As shown in Figure 5.14,

ground motion stations are well distributed around the rupture area, with rupture distances ranging from approximately 60 to 2400 km.

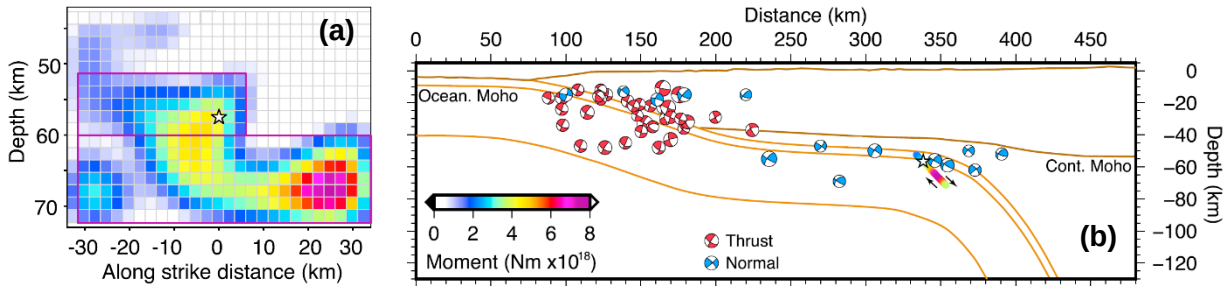

Figure 5.13. Selected FFM modified from Melgar et al. (2018b). The white star is the event hypocenter. **(a)** Slip distribution. The purple line represents the applied trimming. **(b)** Cross section showing the fault rupture with respect to the geometry of the subducting slab. Moment tensors from the global CMT database are shown. Slab model is from Ferrari et al. (2012). Oceanic crust thickness and continental Moho are from Pérez-Campos et al. (2008).

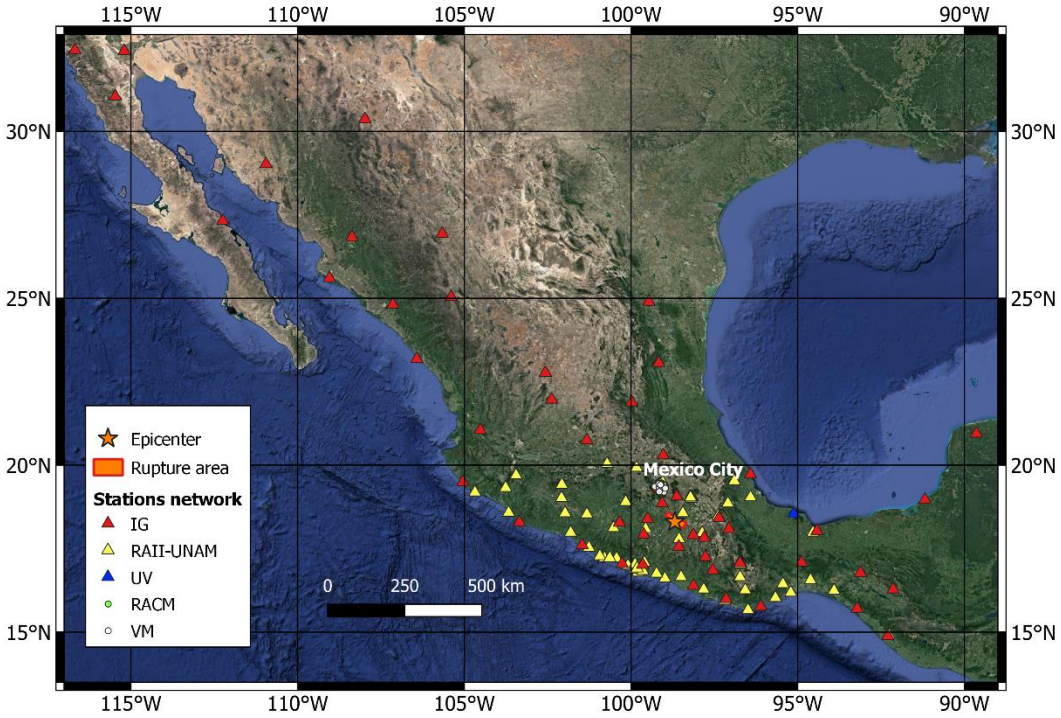

Figure 5.14. Epicenter location and rupture area of the **M**7.18 Puebla earthquake. All ground motion stations from different networks are shown.

Figure 5.15 shows a more detailed view of the epicentral area, including limits of the trimmed finite fault model, and relatively near-field stations that recorded the **M**7.18 Puebla earthquake. The hypocenter utilized in the finite fault model is located at 98.6878° W longitude, 18.3044° N latitude, and 57.5 km depth. This hypocenter location differs from results reported by the USGS (about 30 km) due to errors in teleseismic-based hypocenter locations explained previously. This event has a normal mechanism (rake angle is -83° from CMT catalog). The preferred moment tensor fault plane, selected to conform with the finite fault model, has a strike of 299° and a dip of 44°. Ground motion stations that are closest to the earthquake are in the states of Puebla, Morelos, Guerrero, and Oaxaca. Additionally, there are clusters of sites that recorded this event in specific areas (indicated in Figure 5.15): 11 stations in the Oaxaca City area, seven stations in the Puebla City area, and 75 stations in the Mexico City area; at about 210 km, 90 km, and 100 km away from the earthquake rupture, respectively.

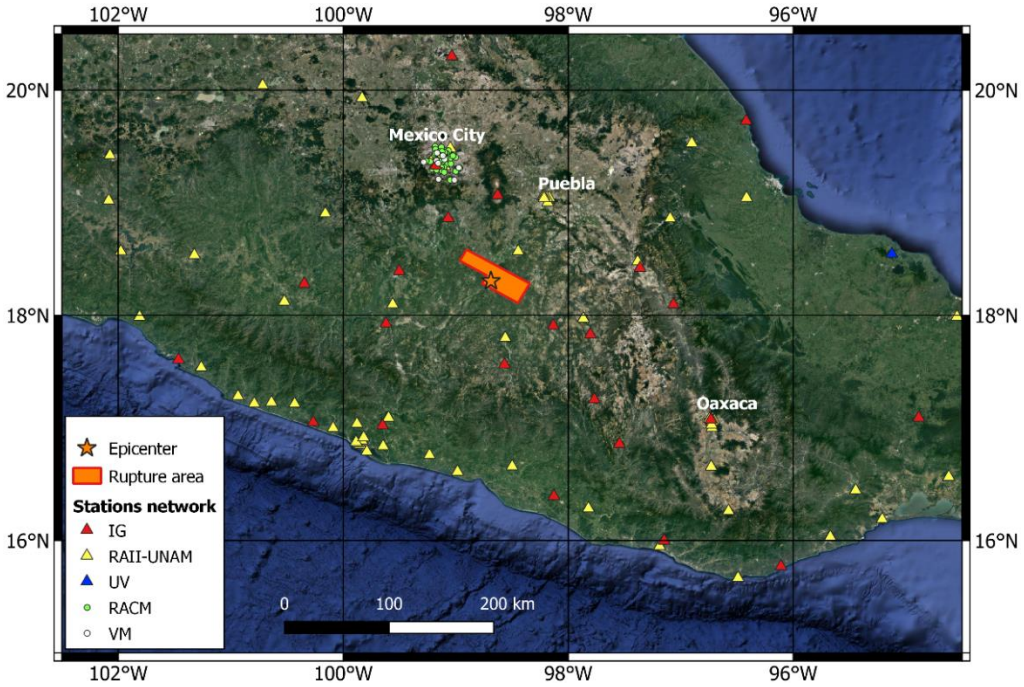

Figure 5.15. Epicenter location and rupture area of the **M**7.18 Puebla earthquake. Ground motion stations from different networks which are relatively close to the event source are shown.

The assigned moment magnitude **M** = 7.18 was computed using the seismic moment M_0 = 6.51×10^{19} N·m, which was taken from the CMT catalog following the procedures for magnitude assignments used in NGA-Sub (Section 2.3.2a). The CMT seismic moment is very similar to the value provided by the USGS, which is $M_0 = 6.381 \times 10^{19}$ N·m (**M** = 7.17).

Following procedures from the previous section, the Type 1 and Type 2 magnitude uncertainties are $\sigma_{M1} \sim 0.174$ and $\sigma_{M2} \sim 0.031$, respectively, leading to a combined uncertainty of $\sigma_M \sim 0.177$. Considering the limited number of finite-fault models found in literature that reported seismic moment for this earthquake (two models shown in Table 5.2), the moment magnitudes provided by the CMT and USGS catalogs were also used in the calculations of σ_{M1}.

5.3.3 February 16, 2018 M7.2 Oaxaca Earthquake

The 2018 **M**7.2 Oaxaca earthquake occurred at 11:39 pm (universal time) on February 16, 2018, in the state of Oaxaca; its epicenter was approximately 10 km southwest of the city of Pinotepa Nacional. To establish the source parameters of this earthquake, five different finite fault models from literature were compiled, which are summarized in Table 5.3. For each of these models, the table lists the data sources utilized in the model, seismic moment M_0 (when available), moment magnitude **M**, and hypocentral depth. All the listed models have appeared in peer-reviewed journal papers, and they have been developed from different data sources: (1) Tung et al. (2019) utilized InSaR measurements; (2) Atzori et al. (2019) used InSaR measurements and GPS data from four nearby stations; (3) Li et al. (2020) utilized InSaR measurements in addition to GPS data from seven nearby stations; (4) Mendoza and Martínez-López (2022) analyzed globally observed teleseismic data (24 P and 12 SH wave forms); (5) Yu et al. (2021) used InSAR measurements.

Table 5.3 Alternate finite-fault models for 2018 **M**7.2 Oaxaca earthquake.

Model	Data Sources	M_0 (N·m)	M	Hypocentral depth (km)
Tung et al. (2019)	Crustal displacement	-	7.2	22.0
Atzori et al. (2019)	Crustal displacement	4.2×10^{19}	7.05	13.0
Li et al. (2020)	**Crustal displacement**	**7.65×10^{19}**	**7.22**	**21.9**
Mendoza & Martínez-López (2022)	Teleseismic	-	7.2	16.2
Yu et al. (2021)	Crustal displacement	-	7.2	25.0

***** The preferred model is indicated in bold font.

The model by Li et al. (2020) is selected because, in addition to the InSAR measurements, it considered local data from seven nearby GPS stations, which is in accordance with NGA-Sub procedures (Section 2.4.2). The model by Atzori et al. (2019) also considered local GPS data but Li et al. (2020) included more GPS stations. Figure 5.16(a) shows the fault slip distribution of the selected model and the trimming (purple line) applied according with the criteria described in Section 2.4.3., i.e., trimming the fault regions with slip values lower than 15% of the maximum slip. The rupture area is modeled by two rectangles with the same dip (δ=14°) but different lengths, in a similar manner than that presented in Section 2.4.4 for other multi-rectangle rupture models in Japan and South America. Figure 5.16(b) shows southern Mexico including the epicenters of the three studied earthquakes (red stars), associated aftershocks (white and gray circles), and depth contours of the subducting slab (Hayes et al., 2012). The box in the upper right of Figure 5.16(b) shows the fault rupture location relative to the subducting slab geometry.

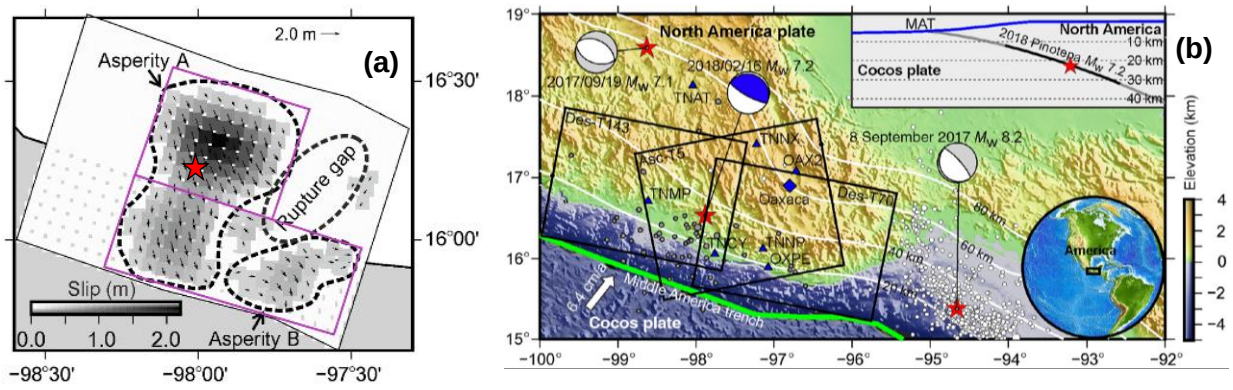

Figure 5.16. Selected FFM modified from Li et al. (2020). **(a)** Slip distribution. The red star is the event hypocenter, and the purple line represents the applied trimming. **(b)** Seismotectonic setting of southern Mexico. Aftershocks of the 2017 **M**8.27 and the 2018 **M**7.2 earthquakes are shown with white and gray circles, respectively. White lines represent the slab depth (Hayes et al., 2012). The box in the upper right presents a cross section showing the fault rupture with respect to the geometry of the subducting slab.

Figure 5.17 shows a map of Mexico with the epicenter and rupture area of the **M**7.2 Oaxaca earthquake, along with the ground motion stations where the event was recorded. The stations are from the IG, UV, and VM networks operated by the SSN; the RAII-UNAM network operated by the Institute of Engineering at UNAM; and the RACM network operated by CIRES. More information about these networks is provided in Section 5.4. As shown in Figure 5.17, most of the ground motion stations are located to the northwest of the rupture area, with rupture distances ranging from approximately 25 to 2600 km.

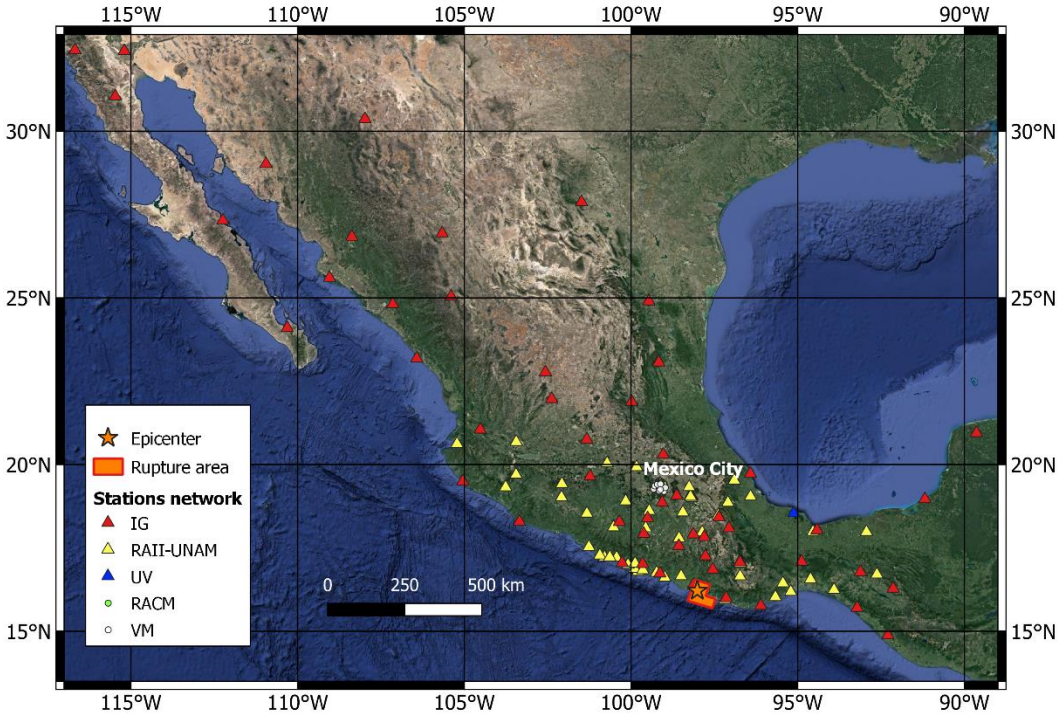

Figure 5.17. Epicenter location and rupture area of the **M**7.2 Oaxaca earthquake. All ground motion stations from different networks are shown.

Figure 5.18 shows a more detailed view of the epicenter, limits of the trimmed finite fault model, and relatively near-field stations that recorded the **M**7.2 Oaxaca earthquake. The hypocenter reported by the SSN is located at 98.0135° W longitude, 16.218° N latitude, and 16 km depth. This hypocenter location differs from results reported by the USGS (about 20 km) due to errors in teleseismic-based hypocenter locations explained previously. This event has a reverse mechanism (rake angle is 71° from Li et al., 2020). The preferred moment tensor fault plane, selected to conform with the finite fault model, has a strike of 288° and a dip of 14°. Ground motion stations that are closest to the earthquake are in the states of Oaxaca and Guerrero. Additionally, there are clusters of sites that recorded this event in specific areas (indicated in Figure 5.18): 10 stations in the Oaxaca City area, seven stations in the Puebla City area, and 75 stations

in the Mexico City area; at about 150 km, 330 km, and 400 km away from the earthquake rupture surface, respectively.

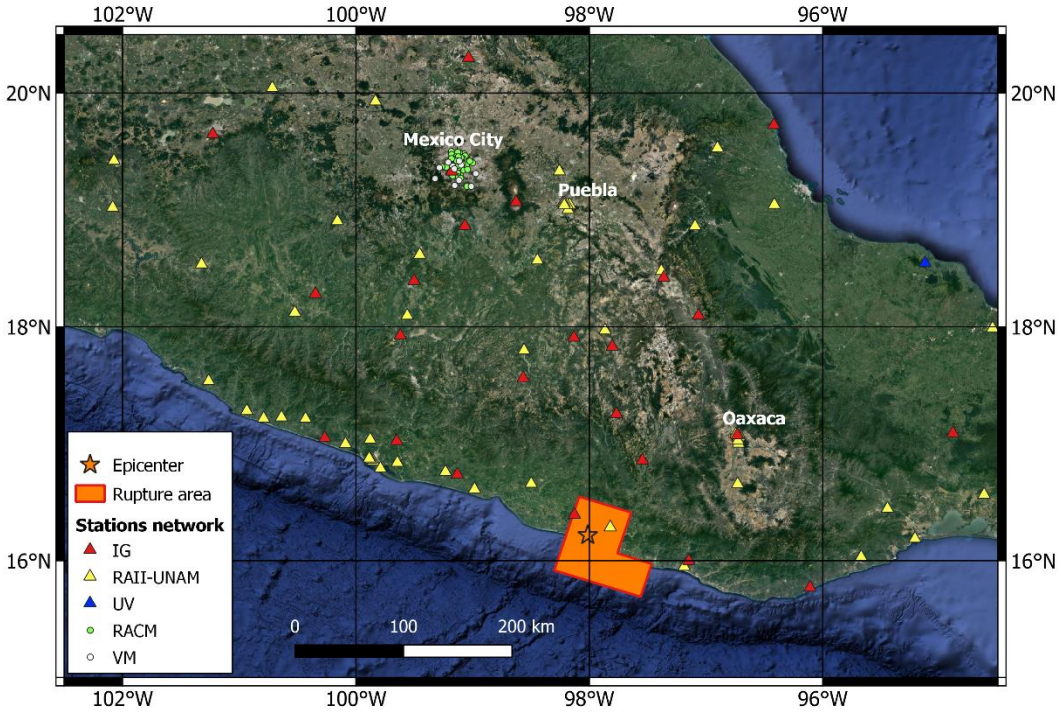

Figure 5.18. Epicenter location and rupture area of the **M**7.2 Oaxaca earthquake. Ground motion stations from different networks which are relatively close to the event source are shown.

The assigned moment magnitude **M** = 7.2 was computed using the seismic moment M_0 = 6.98×10^{19} N·m, which was taken from the CMT catalog following the procedures for magnitude assignments used in NGA-Sub (Section 2.3.2a). The CMT seismic moment is lower than the value provided by the USGS, which is $M_0 = 7.996 \times 10^{19}$ N·m (**M** = 7.24).

Following procedures from the previous section, the Type 1 and Type 2 magnitude uncertainties are $\sigma_{M1} \sim 0.086$ and $\sigma_{M2} \sim 0.031$, respectively, leading to a combined uncertainty of $\sigma_M \sim 0.091$. Considering the limited number of finite-fault models found in literature that reported

seismic moment for this earthquake (two models shown in Table 5.3), the moment magnitudes provided by the CMT and USGS catalogs were also used in the calculations of σ_{M1}.

5.4 GROUND MOTIONS FROM POST-NGA-SUB EVENTS

5.4.1 Ground Motion Networks and Recordings

Earthquake ground motions in Mexico from the three large-magnitude events characterized in Section 5.3, were obtained from three sources:

a) The Institute of Engineering at UNAM manages the RAII-UNAM network, which is deployed broadly across the southern part of Mexico at the locations shown in Figure 5.19. Currently, it has approximately 100 operative ground motion recording stations. The ground motion data are accessible through the RAII-UNAM network website: http://aplicaciones.iingen.unam.mx/AcelerogramasRSM/Inicio.aspx (last accessed April 2022). Acceleration time series were provided as *Standard Acceleration* files (ASA ver2.0, https://aplicaciones.iingen.unam.mx/AcelerogramasRSM/DscArcStd.aspx) in engineering units (cm/s^2). These ground motions already have instrument corrections applied.

Figure 5.19. Location of the ground motion recording stations of the RAII-UNAM network in Mexico.

b) The CIRES (Instrumentation and Seismic Recording Center) manages the RACM network (Accelerographic Network of Mexico City) deployed in Mexico City, which comprises 80 stations at the locations shown in Figure 5.20. The ground motion data can be requested from the CIRES website: http://www.cires.org.mx/racm_historico_es.php (last accessed April 2022). Once the request is approved, the data are delivered via email. Acceleration time series were provided as *Standard Acceleration* files (ASA ver2.0, https://aplicaciones.iingen.unam.mx/AcelerogramasRSM/DscArcStd.aspx) in engineering units (cm/s^2). These ground motions already have instrument corrections applied.

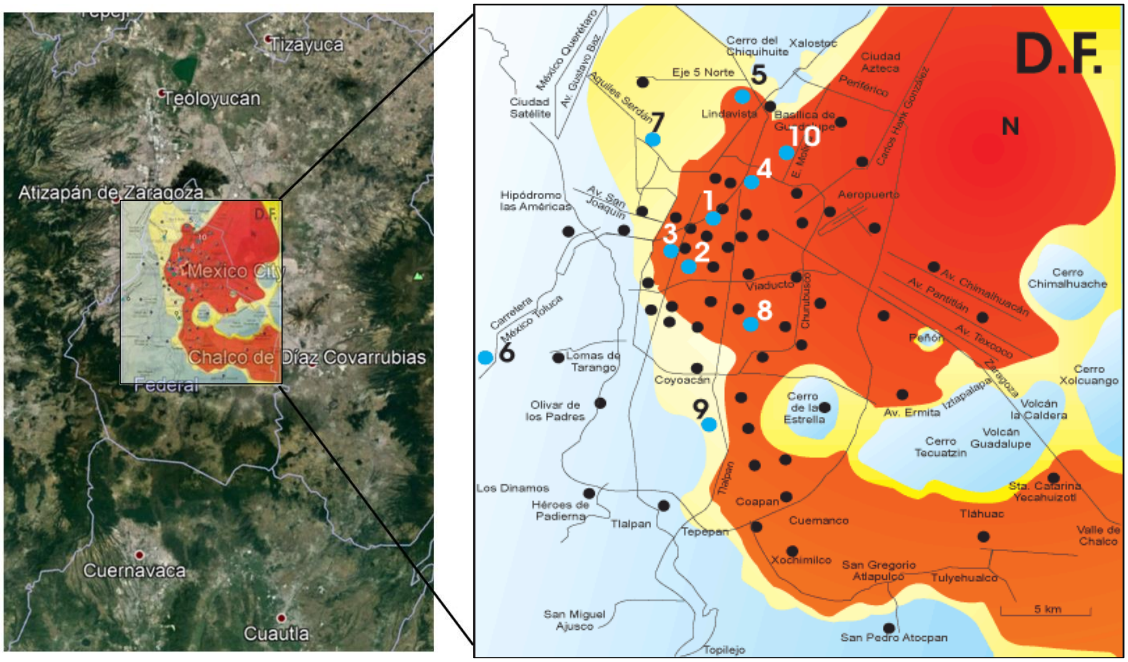

Figure 5.20. Location of the ground motion recording stations (black and blue circles) of the RACM network in Mexico City. The colors denote the microzonation of the city: red = lake zone, yellow = transition zone, light blue = hills zone.

c) The National Seismological Service of Mexico (SSN) distributes ground motion data from several seismic networks with national, regional, and local coverage. The ground motion data are accessible through a client called SSNstp and are provided upon request. Each of

the SSN network stations have both a broadband seismometer and accelerometer. The recordings utilized in this dissertation are from the following networks:

- The broadband seismic network, IG (Institute of Geophysics at UNAM), which is deployed broadly across the country at the locations shown in Figure 5.21. Currently, IG has 61 operative stations.

- The Valley of Mexico seismic network, VM, which is deployed mainly within the basin of Mexico City at the locations shown in Figure 5.22. Currently, VM has 30 operative ground motion recording stations.

- The Veracruz seismic network, UV, which is deployed in the State of Veracruz in East Mexico, at the locations shown in Figure 5.23. Currently, UV has six stations.

Figure 5.21. Location of the ground motion recording stations of the IG network in Mexico. Source: http://www.ssn.unam.mx/acerca-de/estaciones/

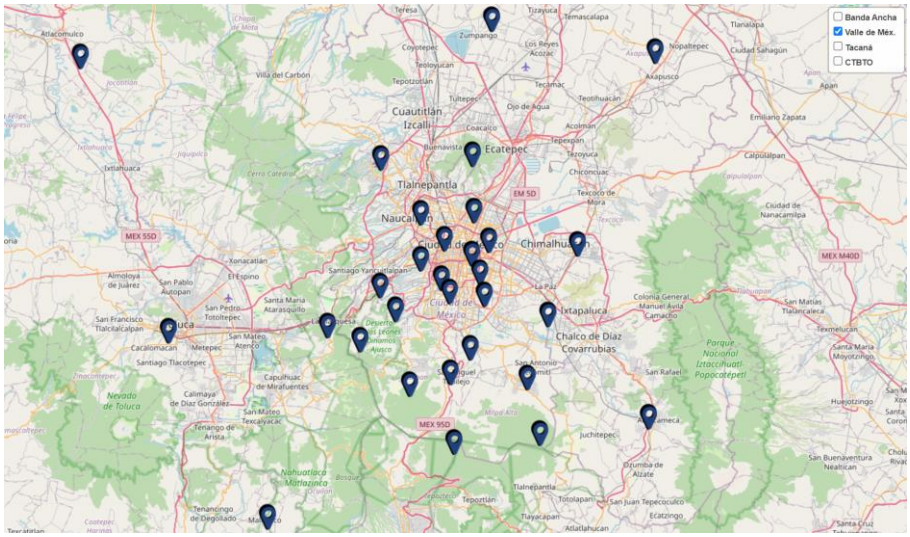

Figure 5.22. Location of the ground motion recording stations of the VM network in Mexico City. Source: http://www.ssn.unam.mx/acerca-de/estaciones/

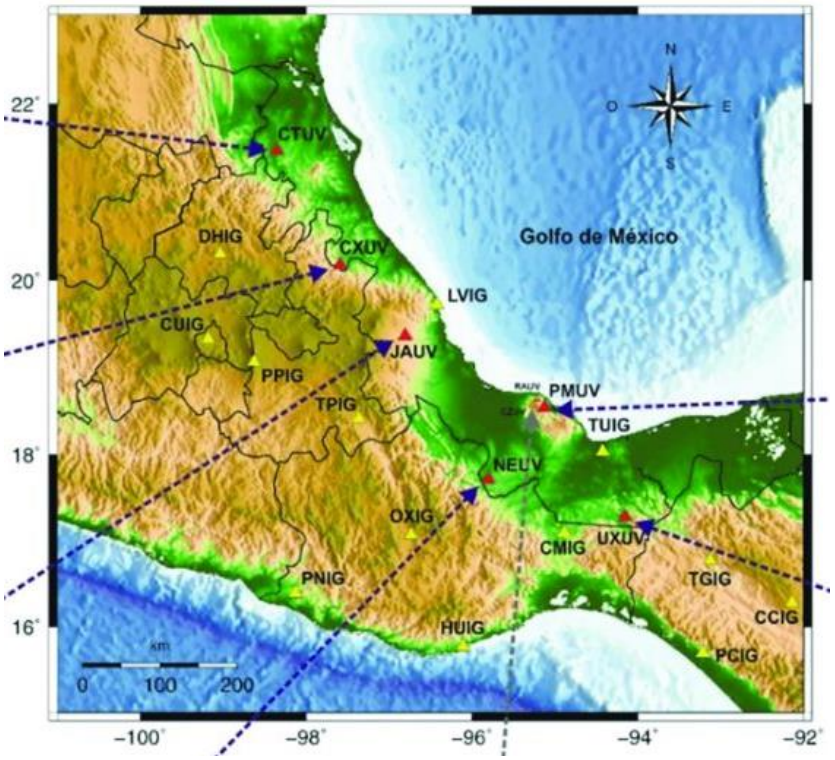

Figure 5.23. Location of the ground motion recording stations of the UV network in Mexico (red triangles). Source: https://www.uv.mx/cienciauv/blog/laredsismicade-veracruz/

The ground motion stations considered from the listed networks are free-field sites, except for one of the RAII-UNAM stations (code RFPP) which is located in a structure.

The acceleration time series from the SSN (IG, VM, and UV networks) were provided as *SAC* files (http://www.adc1.iris.edu/files/sac-manual/manual/file_format.html) in both engineering units (cm/s^2) and as raw data (counts). Additionally, the metadata containing the instrument response of the recordings from the IG and VM networks were provided as *dataless SEED* files (https://ds.iris.edu/ds/nodes/dmc/data/formats/dataless-seed/). For networks IG and VM, whenever raw files and instrument responses were available, the Python Toolbox for Seismology, Obspy (Beyreuther et al., 2010) was used to apply the instrument correction that changes both amplitude and frequency content of the time series and converts the data to engineering units (m/s^2). The main step in this instrument correction is the modification of the signal utilizing a transfer function $H(s)$, which is based on the Laplace Transform, and can be expressed in the zero-pole-gain format as the following rational transfer function:

$$H(s) = G\frac{(s-z_1)\cdot(s-z_2)\cdots(s-z_{n-1})\cdot(s-z_n)}{(s-p_1)\cdot(s-p_2)\cdots(s-p_{m-1})\cdot(s-p_m)}$$

where $s = \sigma + i\omega$ is a variable in the complex frequency domain (σ and ω are real), G is a scalar gain, $z_1, z_2,\ldots, z_n$ are n complex-valued zeros, and $p_1, p_2,\ldots, p_m$ are m complex-valued poles.

Figure 5.24 shows an example of the instrument correction applied to the ground motion recorded during the 2017 **M**8.27 offshore Chiapas earthquake at the station ARIG (Channel HLN, R_{rup} = 627.8 km) located in the state of Guerrero. The instrument is a Kinemetrics FBA-23 accelerometer with nominal natural frequency of 50 Hz and nominal damping ratio of 70%. The left column presents the Fourier Amplitude Spectrum (FAS) and the right column the ground motion time series. The first row shows the raw data before any correction, the second row shows the raw data after time domain pre-processing (basically offset removal, no pre-filtering is

applied), and the third row shows the corrected data after removal of the instrument response. The red lines shown in the FAS plots are the transfer functions of the pre-filtering (equal to 1 in the first row because no pre-filtering is applied), the instrument response (second row) and the inverse of the instrument response (third row). In this case, the instrument correction affects the signal about 45 Hz and beyond, very close to the Nyquist frequency. The resultant ground motions shown in the third row have acceleration units (m/s^2).

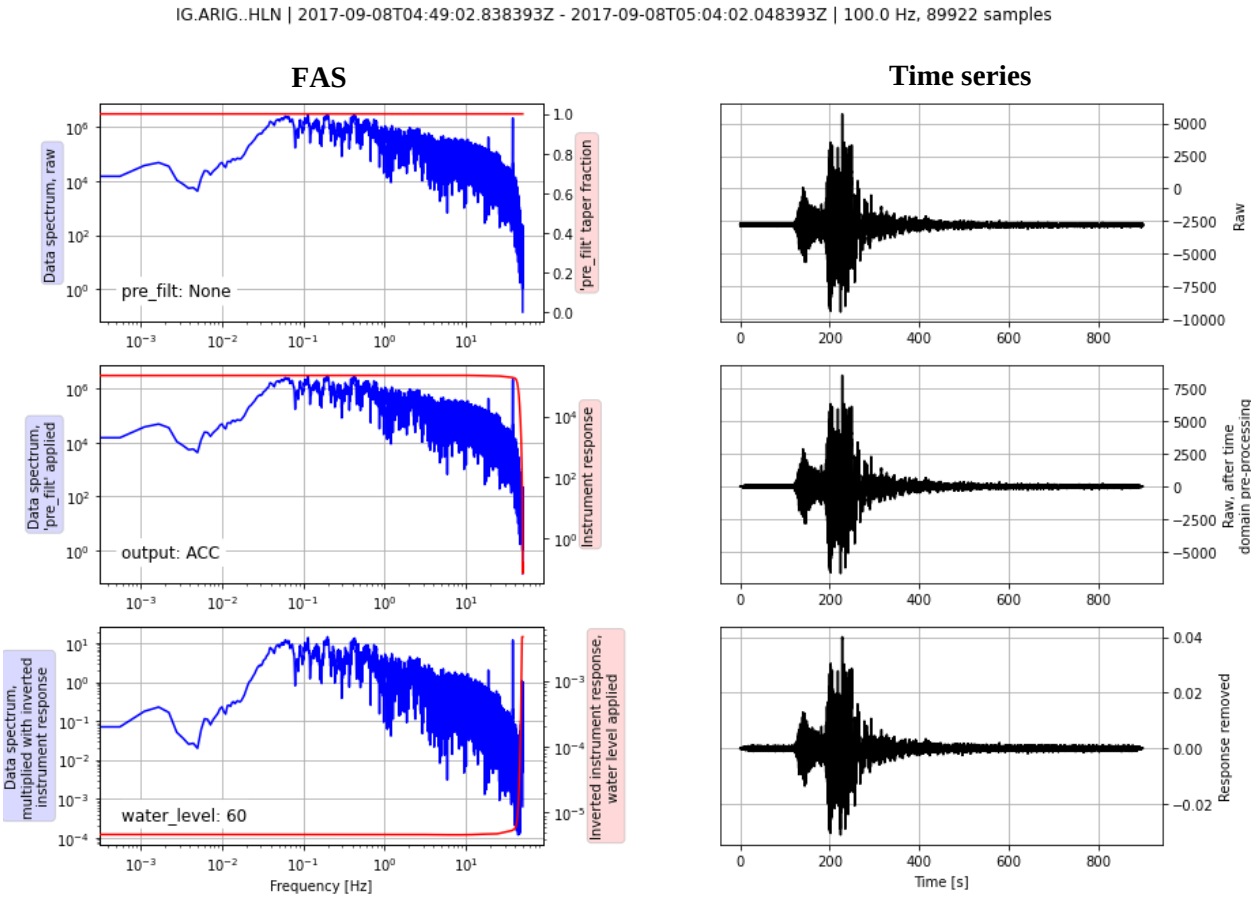

Figure 5.24. Instrument correction of the ground motion recording obtained at the ARIG station during the 2017 **M**8.27 offshore Chiapas earthquake (Channel HLN, R_{rup} = 627.8 km). The instrument is a Kinemetrics FBA-23 accelerometer with nominal natural frequency of 50 Hz and nominal damping ratio of 70%. Red lines represent the transfer functions of the pre-filtering (first row), the instrument response (second row), and the inverse of the instrument response (third row). The resultant ground motion (third row) has acceleration units (m/s^2).

Table 5.4 shows a summary of the number of ground motion recordings that were collected from the different networks presented previously. In total, 585 three-components acceleration recordings from 219 ground motion stations were compiled. In terms of number of recordings, 94% of the data (551 recordings) are from the RAII-UNAM, RACM, and IG networks, whereas the VM and UV networks contribute the remaining 6% (only 34 recordings). Approximately 40% of the stations are located in Mexico City, mainly from the RACM and VM networks, which produces clusters of the collected data within a narrow range of rupture distances.

Table 5.4 Number of ground motion stations and recordings by network.

Network (Operator)	# stations	# recordings
RAII (UNAM)	83	215
RACM (CIRES)	66	182
IG (SSN)	55	154
VM (SSN)	13	30
UV (SSN)	2	4
Total	**219**	**585**

Table 5.5 presents a summary of the number of recordings by earthquake and network. More than 190 recordings are available for each of the studied events and these recordings are similarly distributed among the different networks.

Table 5.5 Number of ground motion recordings by earthquake and network.

Earthquake	Date	M	RAII	RACM	IG	VM	UV	Total
Chiapas	9/8/2017	8.27	71	61	49	10	2	**193**
Puebla	9/19/2017	7.18	76	61	51	9	1	**198**
Oaxaca	2/16/2018	7.2	68	60	54	11	1	**194**
Total			**215**	**182**	**154**	**30**	**4**	**585**

5.4.2 Data processing

Data processing and computation of intensity measures (IMs) follows the methodology applied to the ground motions utilized in the NGA-Sub project. The procedure is described in Kishida et al. (2020) and the main steps, combined with any deviations applied in the present work, are the following:

1. Unprocessed time series (acceleration versus time as-is without filters or any other modifications) are plotted based on the sample rate of the recording (i.e., time step). The quality of the ground motion is evaluated visually, and the recording is accepted or rejected for processing based on the resolution of the data compared to the noise and the presence of other clear issues in the signal (e.g., incomplete recording, spurious spikes, offsets in the baseline by section). After screening the time series and accepting the recording, a time window that contains the ground motion to be processed is selected. This portion of the NGA procedure was applied without modification.

2. Six time windows are defined for each time series: (i) the entire signal based on the time window selected in step 1, (ii) the pre-event noise before P-wave arrival, and sections of the signal dominated by (iii) the P-waves, (iv) S- waves, (v) coda waves, and (vi) P-waves and S-waves together. In the present application, the processing uses the entire signal window and the pre-event noise window to compute signal-to-noise ratio (SNR).

3. Mean removal and cosine tapers are applied to the entire signal and to the noise time windows that are utilized in the procedure. The cosine tapers are applied at the beginning and at the end of these signals and their length is 1% of the total length for the entire signal and 0.5 seconds for the noise signal.

4. Zero-padding is applied at the end of the time series to increase the number of datapoints to a power of 2, expanding the duration of the recording to approximately 40-50 minutes depending on the sampling frequency. For instance, if the sampling frequency is 100 Hz the recording is increased to 2^{18} datapoints; if the sampling frequency is 200 Hz the recording is increased to 2^{19} datapoints.

5. Fourier Amplitude Spectrum (FAS) and Fourier Phase Spectrum (FPS) are computed for each time series. The results are smoothed utilizing a log-scale rectangular window with a size d = 0.05 in log scale (i.e., 5% of a log cycle in frequency), which smooths within a range of 6% of each window's central frequency. The shape of the FAS at low frequencies is compared to the theoretical acceleration decay according to the f^2 model (Brune, 1970; Boore and Bommer, 2005), along with the signal-to-noise ratio (SNR) computed as the ratio of the entire signal FAS and the noise (or pre-event) window FAS. These comparisons are used to facilitate the selection of the high-pass corner frequency utilized in the next step. A SNR = 3 is considered the acceptable threshold.

6. High-pass (low cut) and low-pass (high cut) Butterworth filters are applied to the entire signal in the frequency domain. Both causal and acausal filters are considered, in which 5 and 4 poles are utilized for high-pass and low-pass filters, respectively.

7. After filtering of the signal, zero pads described in step 4 are removed to obtain pad-stripped time series. A cosine taper is applied to this pad-stripped signal in the same manner described in step 3. The acceleration time series is then integrated to obtain velocity and displacement time series. The integration is performed in the time domain utilizing the

linear acceleration method (Nigam and Jennings, 1969) and assuming that the initial velocity and displacement are zero.

8. A base line correction procedure is applied to remove any baseline drift in the displacements. A 6^{th} order polynomial (with the zeroth and first order terms equal to zero) is fitted to the displacement time series, and its second derivative is subtracted from the filtered acceleration time series. This filtered and baseline corrected signal is integrated to obtain velocity and displacement time series.

9. IMs that are computed are PGA, PGV, and PGD values, along with 5% damped PSa values at 101 periods between 0.01s and 20 s. Two types of IMs are computed: (i) as-recorded values for each component of the time series, (ii) RotD50 values from the two horizontal components of the time series (Boore, 2010). Time series obtained using acausal filters are preferred to compute IMs, because acausal filters do not introduce a shift in the phase and therefore pseudo-spectral accelerations are not affected. The "R" package *RCTC* (Wang et al., 2017) is used to compute the response spectra. This software utilizes *Sinc* interpolation of the time series, which is useful to avoid underestimation of PSa values near the anti-aliasing corner frequency and to avoid spurious energy at high frequency from linear interpolation.

The procedures described above are incorporated into a computer code that was used to process the ground motions in the NGA-Sub project (Bozorgnia et al., 2022). This code is not available for public distribution, as it is unpublished. As such, I was unable to fully access the code for the present work and instead developed an equivalent code in MATLAB. An example application of the procedure utilizing the MATLAB code is presented for a recording obtained

during the 2017 **M**7.18 Puebla earthquake at the LI33 station, located in Mexico City (R_{rup} = 108.6 km). Figure 5.25 shows the acceleration time series of the two horizontal components (N00E, N90W) and the vertical component (+V) for this recording after selecting the time window that is considered for processing in step 1 (labeled as "windowed"). The vertical segmented lines in red identify the beginning of the earthquake ground motion (P-waves arrival) and define the end of the pre-event noise window described in step 2. The acceleration time series that result after mean removal and application of the cosine tapers in step 3, are shown in blue (labeled as "corrected"). No important changes are observed in the time series after this initial correction, which is typical for the ground motions utilized in this analysis.

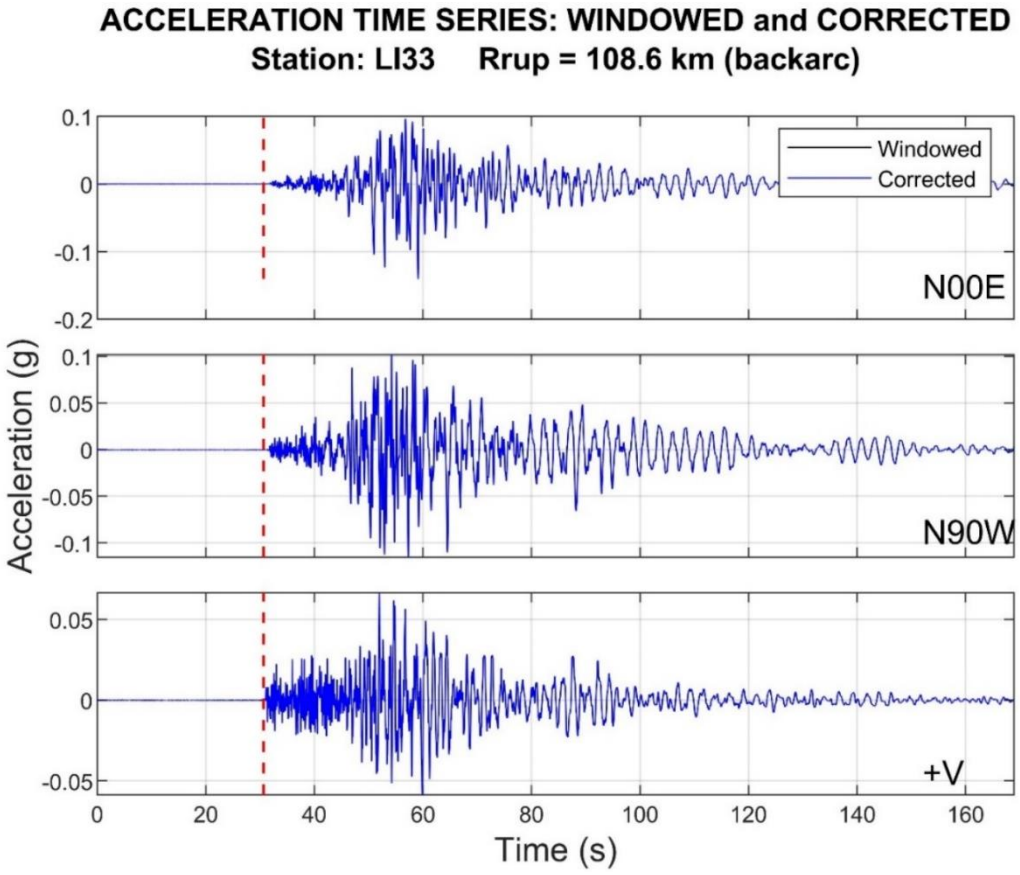

Figure 5.25. Acceleration time series of the recording obtained at LI33 station (Mexico City) during the 2017 **M**7.18 Puebla earthquake. The vertical segmented lines in red identify the P-waves arrival time that is used to define the pre-event noise window.

As explained in step 4, zero-pads were applied to the acceleration time series before computing the FAS and the FPS. To illustrate steps 5 and 6, Figure 5.26 shows the smoothed FAS of one of the horizontal components (N00E), for the entire signal (blue line) and for the pre-event noise (purple line). Additionally, the signal-to-noise ratio (SNR) along with the acceptable threshold (SNR=3) are shown in green. Both low-pass and high-pass corner frequencies are selected through a manual process for each recording. In this case, the low-pass frequency (f_{max} = 29.42 Hz) was selected based on the SNR threshold. On the other hand, the high-pass frequency (f_{min} = 0.06183 Hz) was selected in such a way that the filtered and baseline corrected displacement time series (i.e., after application of steps 7 and 8) do not present a baseline drift and have a "reasonable" shape (see Figure 5.27 and Figure 5.28).

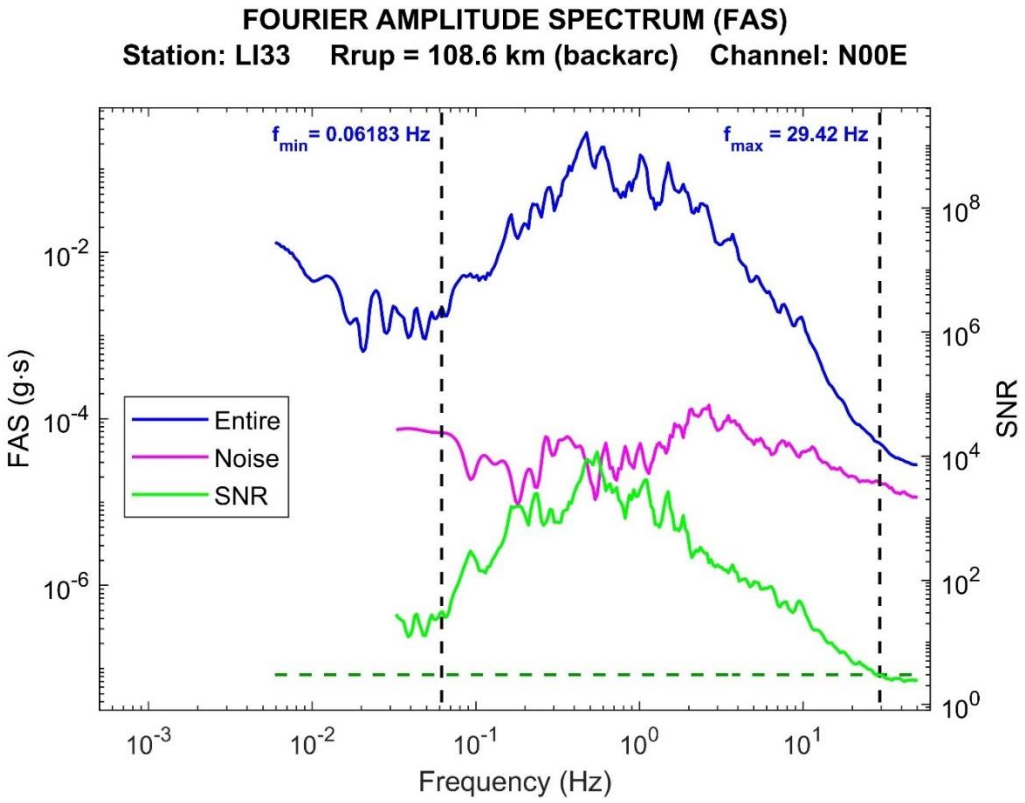

Figure 5.26. FAS of one of the horizontal components of the recording obtained at LI33 station (Mexico City) during the 2017 **M**7.18 Puebla earthquake. The vertical segmented lines are the cutoff frequencies utilized in the filtering of the signal.

Figure 5.27 and Figure 5.28 show the acceleration, velocity, and displacement time series that result after applying the causal and acausal Butterworth filters, respectively. The effect of the baseline correction is presented in these two figures as well.

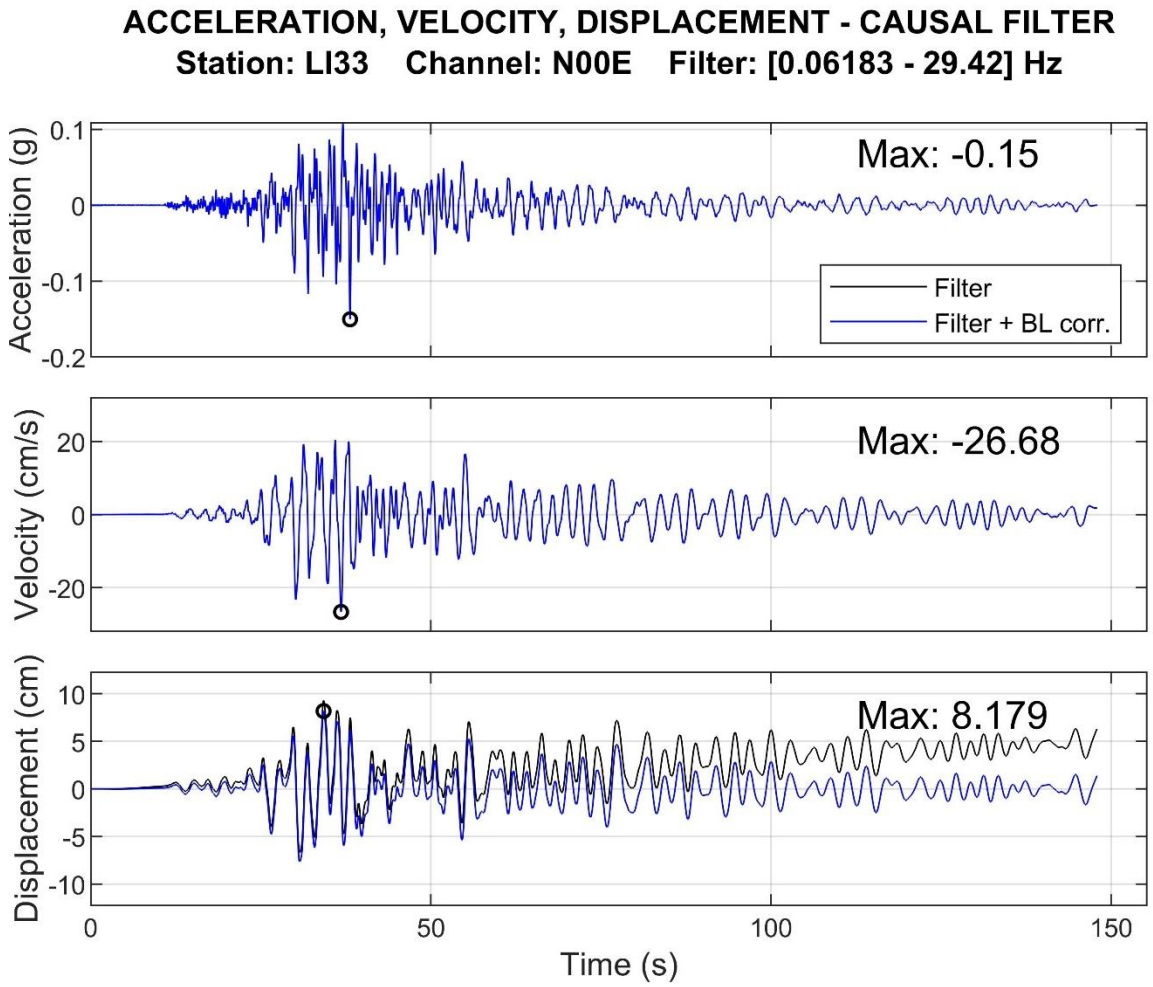

Figure 5.27. Acceleration, velocity, and displacement time series of one of the horizontal components of the recording obtained at LI33 station (Mexico City) during the 2017 **M**7.18 Puebla earthquake. Causal filter.

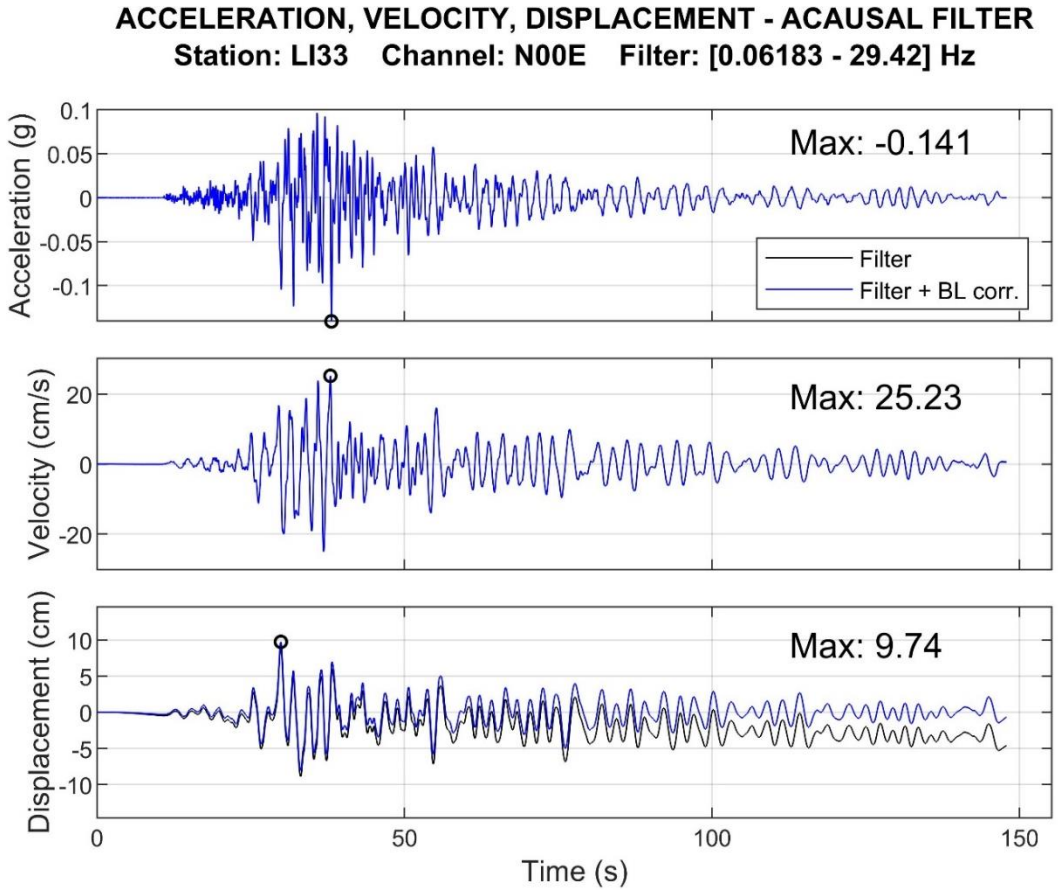

Figure 5.28. Acceleration, velocity, and displacement time series of one of the horizontal components of the recording obtained at LI33 station (Mexico City) during the 2017 **M**7.18 Puebla earthquake. Acausal filter.

Considering the same recording (station LI33, Channel N00E), Figure 5.29a shows the as-recorded pseudo-acceleration response spectra for the unprocessed time series (labeled as "Raw") and for the processed time series, i.e., filtered and baseline corrected (labeled as "Causal" and "Acausal", depending on the type of filter applied in each case). The usable period range is indicated with the vertical segmented lines in blue and is computed using the standard practice in NGA projects ($T_{min} = 1.25 \cdot f_{max}$ and $T_{max} = 0.8 \cdot f_{min}$). The response spectra of about 120 recordings that were processed using both the MATLAB code and the PEER-NGA code, were examined by eye to compare their results, finding no important differences. Figure 5.29b shows a representative example presenting a comparison between the pseudo-acceleration response spectra

obtained from the recording processed using the MATLAB code (black line) and the recording processed using the PEER-NGA code (red line), considering the acausal filter. The ratio between these two spectra (PSa ratio indicated with the green line) is close to 1.0 and the maximum difference does not exceed 3%.

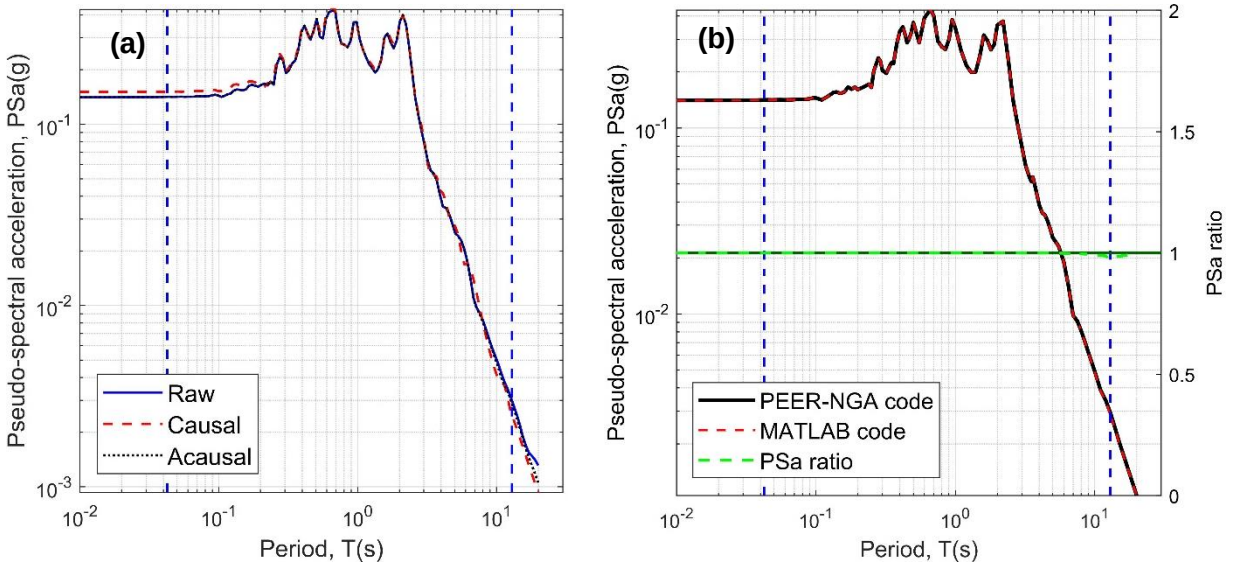

Figure 5.29. Pseudo-spectral acceleration of one of the horizontal components (Channel N00E) of the recording obtained at LI33 station (Mexico City) during the 2017 **M**7.18 Puebla earthquake: **(a)** Results obtained using the MATLAB code developed in this study. **(b)** Comparison between the results obtained with the code developed in this study and the PEER-NGA code for the acausal filter. The vertical blue lines represent the usable period range (between 0.0425 s and 12.939 s).

In total, 585 three-components time series were processed using the procedure previously described. Out of those 585 recordings, 410 were of relatively good quality and the pattern and features were similar to those presented in the previous figures associated with the chosen example (station LI33, Channel N00E). 187 recordings did not require the application of a low pass filter after evaluating the SNR at high frequencies. For those recordings where a low pass filter was required, in most cases its use did not affect the spectral acceleration at short periods. Figure 5.30 presents an example where one of the horizontal channels (N90E) required a low pass filter ($f_{max} = 50\ Hz$) due to a low SNR at high frequencies. However, as shown in Figure 5.30d, the

spectral accelerations are not affected at short periods. All the recordings that presented patterns like this were considered in the analysis presented in the next chapter.

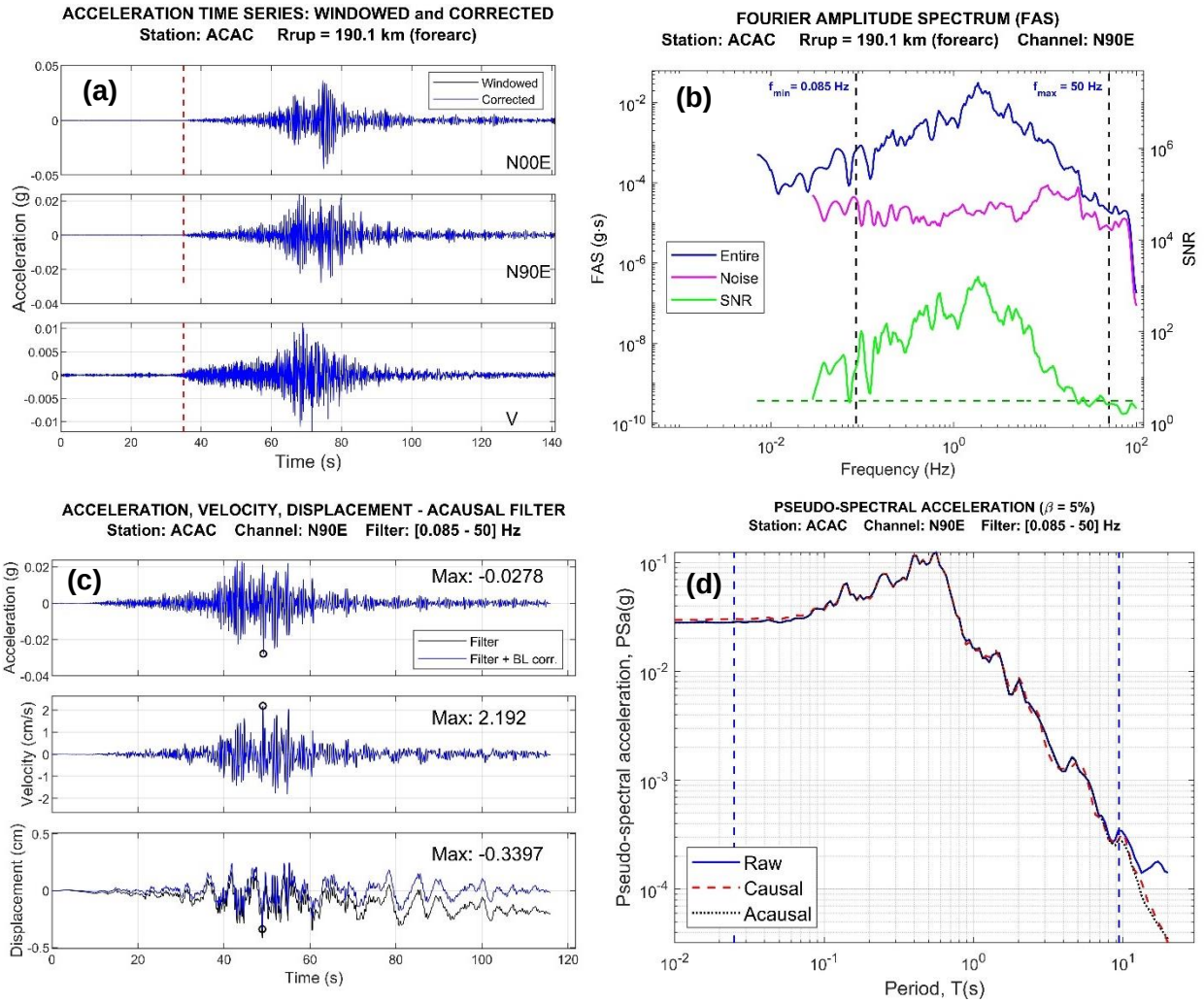

Figure 5.30. Example of application of a low pass filter to one of the horizontal components (N90E) of the recording obtained at ACAC station during the 2018 **M**7.2 Oaxaca earthquake: **(a)** Acceleration time series for the three components. **(b)** FAS and cutoff frequencies applied. **(c)** Filtered and baseline corrected acceleration, velocity, and displacement time series. **(d)** Pseudo-acceleration spectra. The vertical blue lines represent the usable period range (between 0.025 s and 9.412 s).

Some of the recordings (175) were more challenging and required special attention. The typical issues that were encountered and the manner in which they were addressed are as follows:

- 11 recordings presented a high level of noise across the entire signal, which is observable in the pre-event noise window and in the FAS. For many of these recordings, the SNR was too low beyond a certain frequency and, therefore, a low pass filter was required. Figure 5.31 presents an example where one of the horizontal channels (HLE) has a high level of noise.

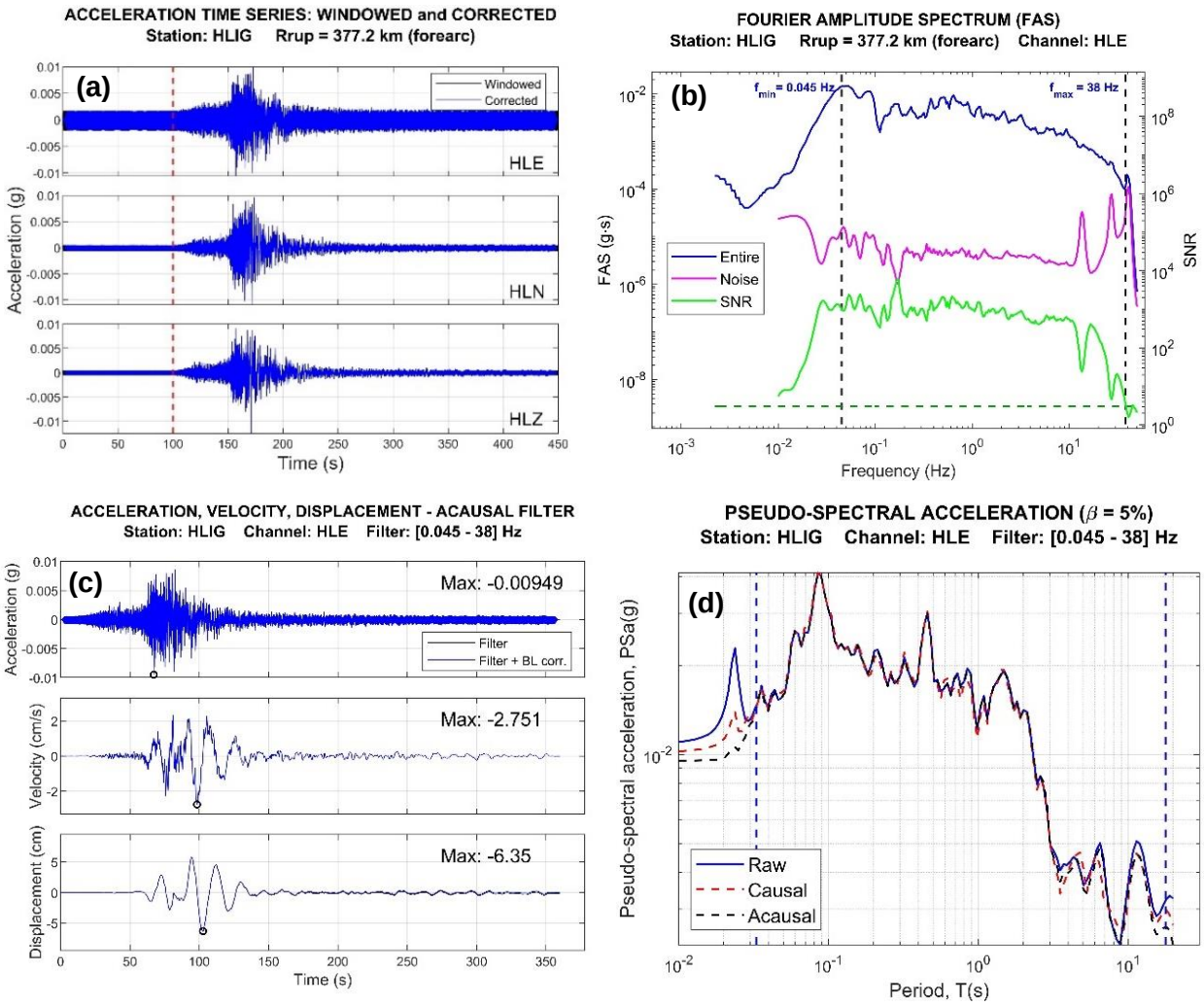

Figure 5.31. Example of application of a low pass filter to one of the horizontal components (HLE) of the recording obtained at HLIG station during the 2017 **M**8.27 offshore Chiapas earthquake: **(a)** Acceleration time series for the three components. **(b)** FAS and cutoff frequencies applied. **(c)** Filtered and baseline corrected acceleration, velocity, and displacement time series. **(d)** Pseudo-acceleration spectra. The vertical blue lines represent the usable period range (between 0.0329 s and 17.778 s).

In the example presented in Figure 5.31, a low pass filter (f_{max} = 38 Hz) was applied, which removed the energy related to the noise from the signal, as shown in Figure 5.31d (see the peak in the raw spectrum between T = 0.02s and 0.03s which is removed in the processed signal). All the recordings that presented a pattern like this were considered in the analysis presented in the next chapter, judging that the low pass filter effect is necessary.

- 13 recordings present a high level of noise and therefore the SNR was too low for a broad range of frequencies. These recordings were flagged as unreliable and were not used in the ground motion analyses.

- For seven recordings, application of the filter criteria necessitates use of a low-pass filter that affects the PSa to a visually appreciable extent. It was decided to not use these records in ground motion analyses.

- For 12 recordings, the instrument appeared to trigger during the p-wave and as a consequence, there is no pre-event noise window. In these cases, the FAS were examined to identify regions at low and high frequencies where the FAS flattens or increases in amplitude towards the frequency limits. The corner frequencies were then selected by eye at the upper end of the low-frequency flat region (high-pass frequency) or at the lower end of the high-frequency flat region (low-pass frequency).

- For six recordings, the processing procedure was applied in the standard manner and due to displacement “wobble”, the high-pass corner frequency was increased relative to that required to meet SNR criteria to a sufficient degree that key features of the recording were

removed, including potential site resonances. Figure 5.32 shows an example. These recordings were not used in subsequent analyses.

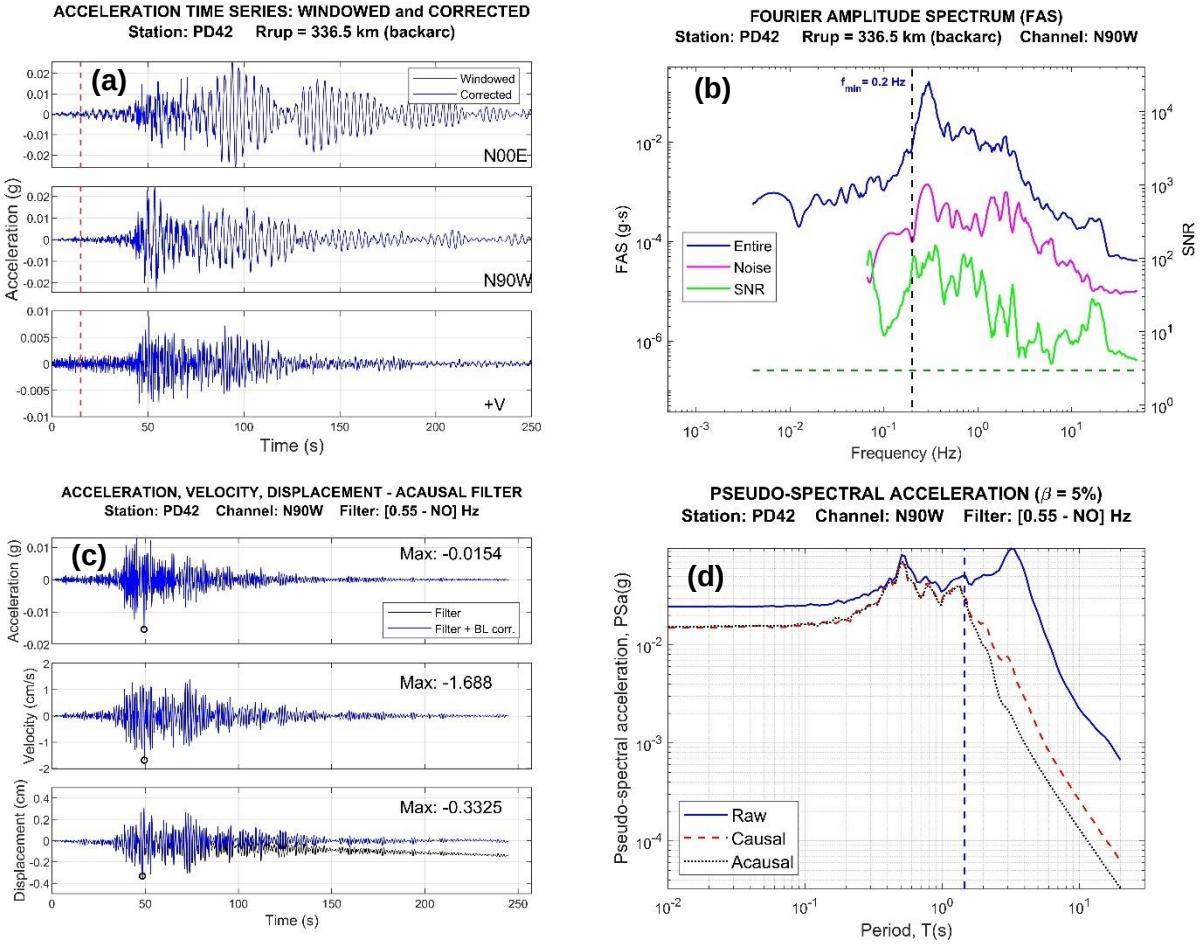

Figure 5.32. Example of application of a high- pass filter to one of the horizontal components (N90W) of the recording obtained at PD42 station during the 2018 **M**7.2 Oaxaca earthquake: **(a)** Acceleration time series for the three components. **(b)** FAS and cutoff frequencies required to meet SNR criteria. **(c)** Filtered and baseline corrected acceleration, velocity, and displacement time series. A high-pass cutoff frequency of f_{min} = 0.55 Hz was required to obtain a reasonable displacement trace. **(d)** Pseudo-acceleration spectra, which is highly modified due to the aggressive filter. The vertical blue line represents the usable period range (T <1.45 s).

- Additional issues encountered during data processing that required some records to be excluded include visually troublesome features (e.g., baseline offset, multiple events).

5.4.3 Ground motion attributes

Figure 5.33, Figure 5.34, and Figure 5.35 show the RotD50 PGA values versus rupture distance for the 2017 **M**8.27 offshore Chiapas, 2017 **M**7.18 Puebla, and the 2018 **M**7.2 Oaxaca earthquakes, respectively. In these figures, the data from different networks are highlighted. The rupture distances used in these calculations utilized the finite fault models described in Section 5.3 and the distance calculation procedures described in Section 5.5. The aim of this section is to describe data attributes that are of interest for ground motion modeling.

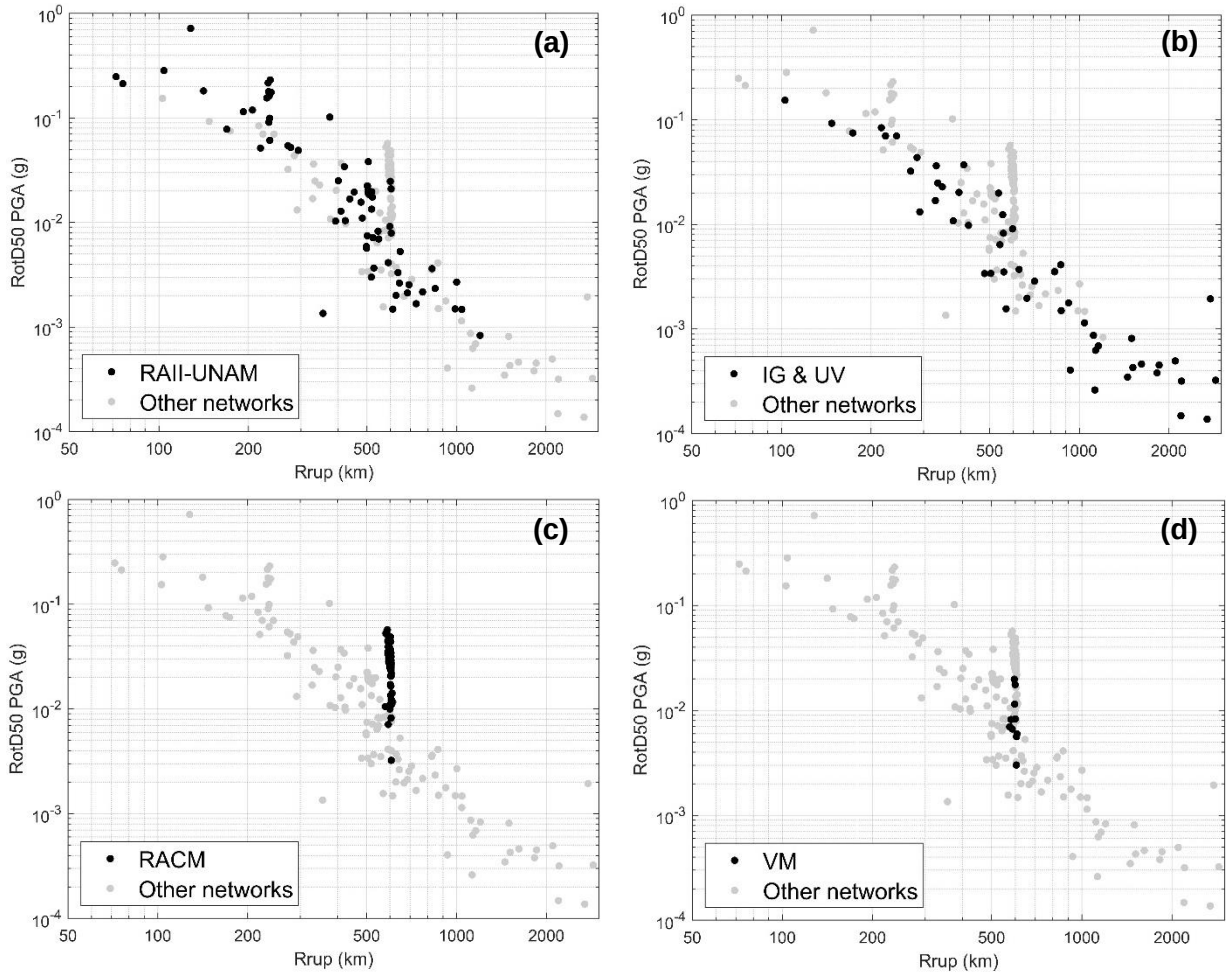

Figure 5.33. Recorded PGA values for the 2017 **M**8.27 offshore Chiapas earthquake from different networks: (a) RAII-UNAM, (b) IG and UV, (c) RACM, (d) VM. RACM and VM consist of stations in Mexico City only.

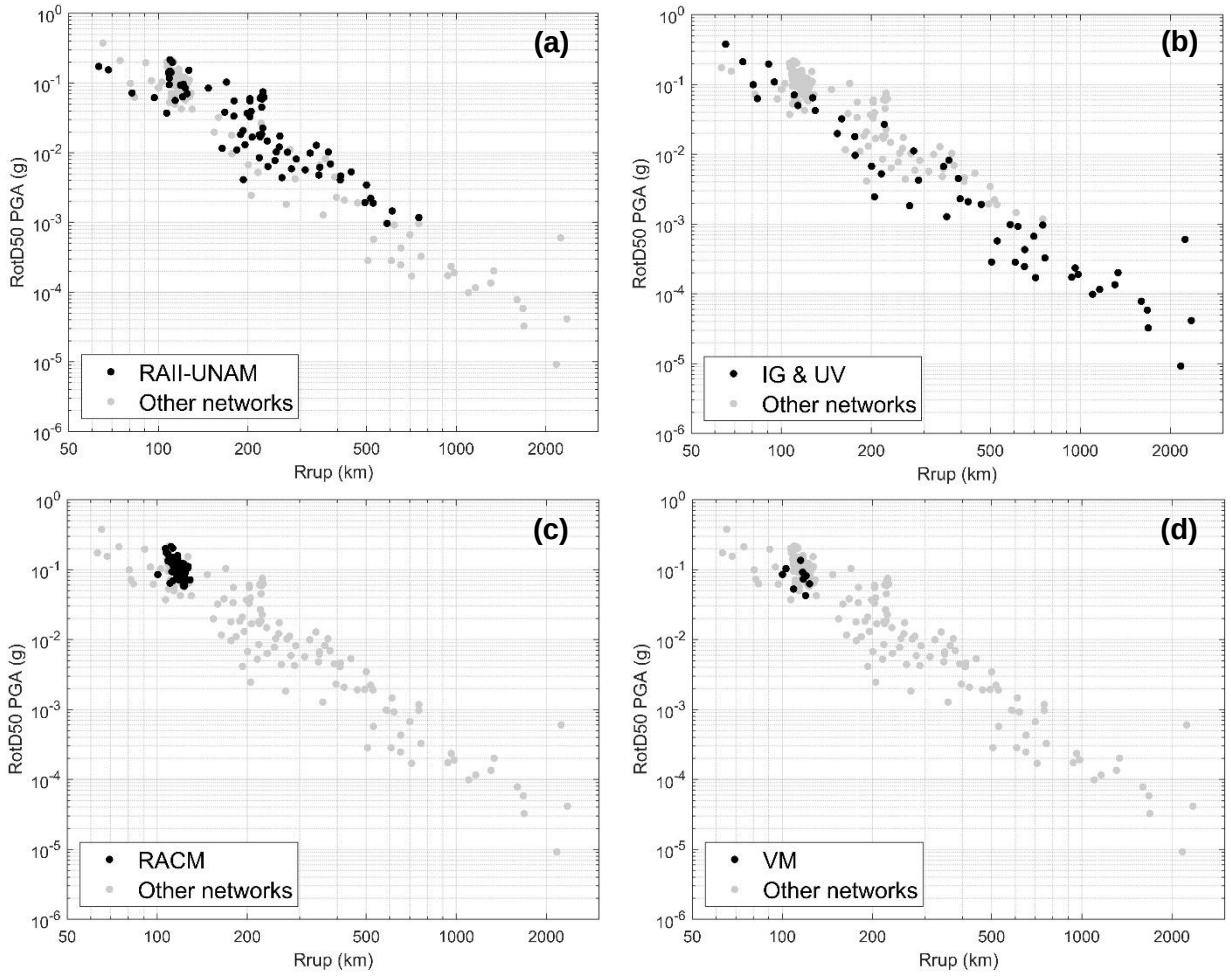

Figure 5.34. Recorded PGA values for the 2017 **M**7.18 Puebla earthquake from different networks: (a) RAII-UNAM, (b) IG and UV, (c) RACM, (d) VM. RACM and VM consist of stations in Mexico City only.

Several important ground motion features can be seen in these plots. Near-source saturation is evident in the Chiapas and Oaxaca data by flattening of the PGA trend for R_{rup} < ~150 km. These effects are thought to be caused by finite fault effects – namely, the closest distance to the fault may not produce the slip that controls the ground motion amplitude (e.g., Atkinson et al., 2016). Such features would be expected to vary from event-to-event, and indeed are not evident in the Puebla data.

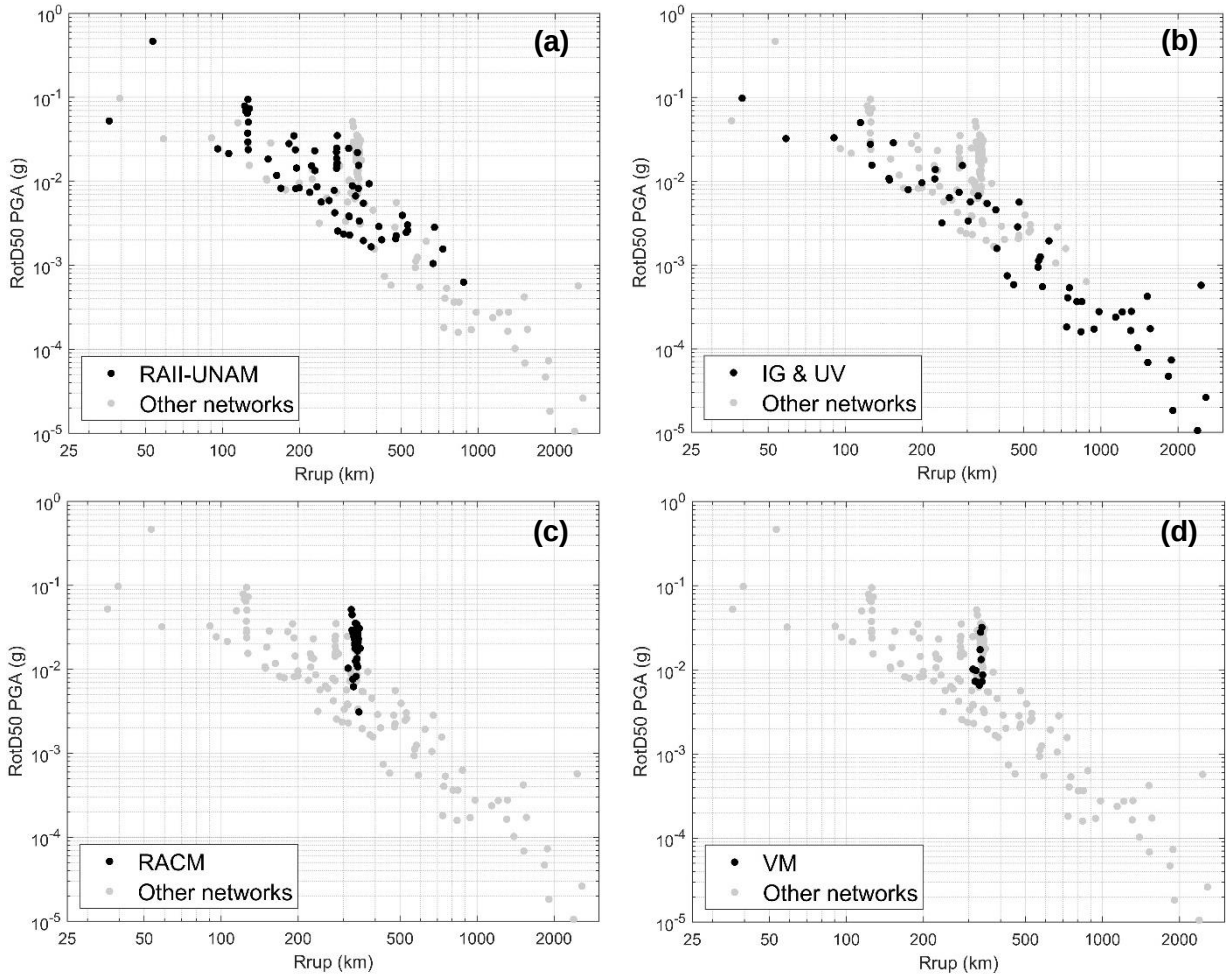

Figure 5.35. Recorded PGA values for the 2018 **M**7.2 Oaxaca earthquake from different networks: (a) RAII-UNAM, (b) IG and UV, (c) RACM, (d) VM. RACM and VM consist of stations in Mexico City only.

Starting at about 150 km distance and extending to approximately 400 km, PGA decays nearly linearly in log-log space, as expected from geometric spreading. At distances > 400 km, PGA decays more rapidly with distance (for the Chiapas and Oaxaca events), which is a well-known effect of anelastic attenuation (e.g., Boore 2003). Finally, at relatively great distances beginning at about 1000-1200 km, the PGA-distance trend flattens. While it is possible this represents a change in the predominant wave type (surface waves are known to attenuate more gradually than body waves; Boore 2003), given the very low amplitude of these motions (<

$\sim 3 \times 10^{-4} g$), it is likely that this flattening is affected by biased sampling of the possible ground motions. This issue is examined further in Section 5.5.3.

An additional feature of the data that is unique to Mexico is the extraordinary impact of site response in Mexico City. This appears in the plots as tall "stripes" of data within a narrow distance range, centered on approximately 600 km for Chiapas, 120 km for Puebla, and 320 km for Oaxaca. This occurs both because of the high variable site response within the city and the large numbers of recordings that are made, sampling a wide array of geotechnical conditions.

The cumulative data set for Mexico includes the NGA-Sub data that was considered in model development (**M** > 6 and pre-2016 events), data processed in NGA-Sub for which event metadata has been added in this study (**M** < 6 and pre-2016), and data from the three large events described in Section 5.3. For this cumulative data set, Figure 5.36 shows the distribution of recordings in magnitude-distance space, with different symbols for the three data subsets. The data covers a magnitude range of about 5-8.3 and a distance range of about 20-2000 km. Figure 5.37 shows the same data in magnitude-distance space, but with the symbols now indicating different event types (interface, intraslab, shallow-crustal). Subduction data is dominant in the data set. Figure 5.38 shows the number of available recordings as a function of period. Only records that were accepted after passing through the processing steps (Section 5.4.2) are tallied. The fall-off of numbers of records for periods > 1-3 sec occurs because these periods exceed the maximum usable period for some records (where the maximum usable period depends on the high-pass corner filter).

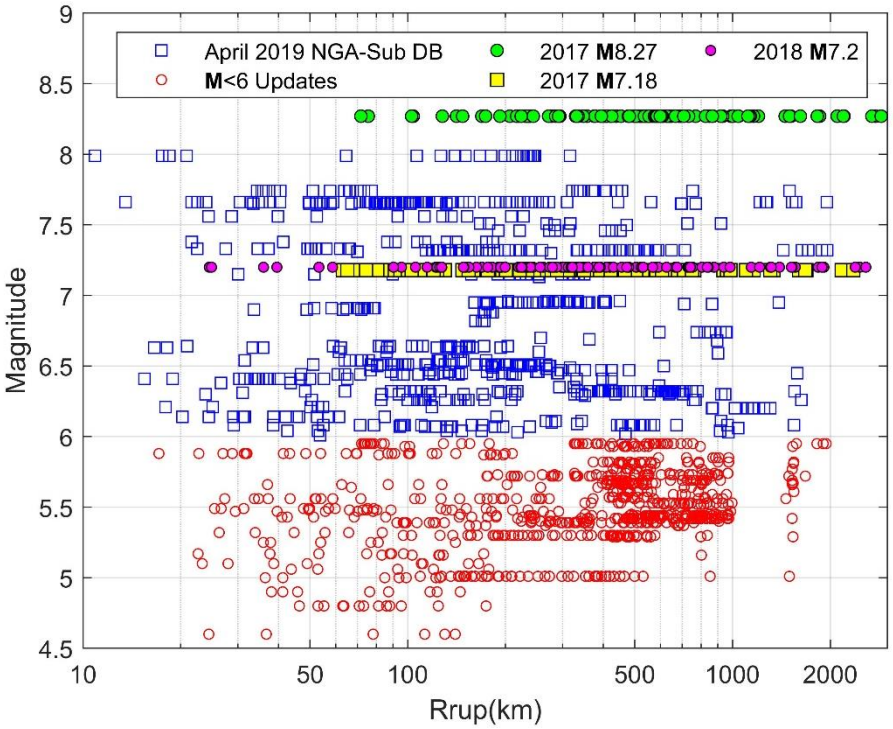

Figure 5.36. Magnitude-distance distribution of the NGA-Sub database in CAM following updates of events with **M**<6 and the addition of the three large-magnitude earthquakes occurred in 2017 and 2018.

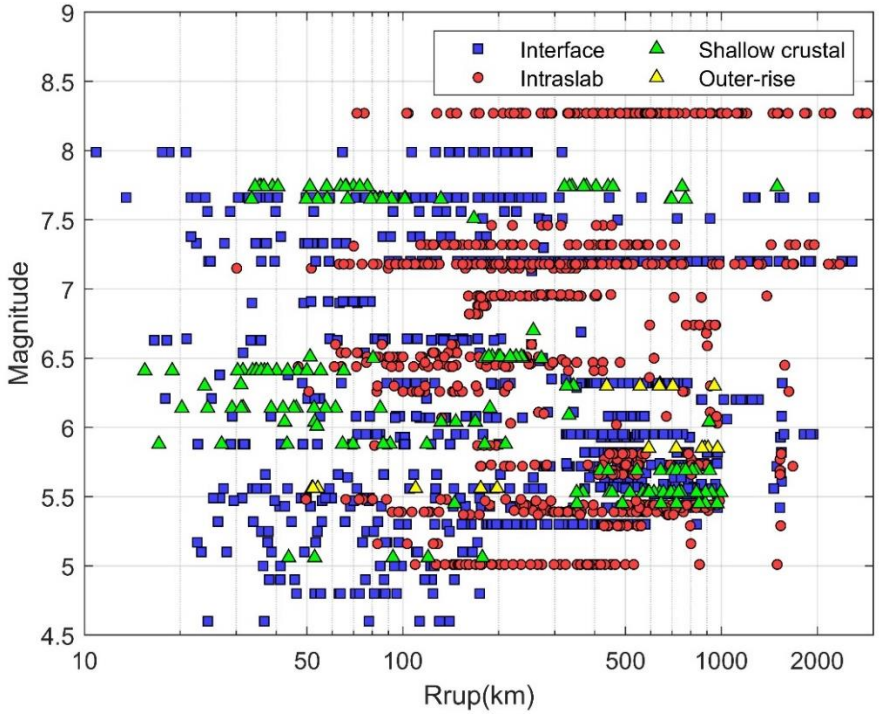

Figure 5.37. Magnitude-distance distribution of the NGA-Sub database in CAM including updates (events with **M**<6 and the new earthquakes in 2017 and 2018) and differentiating by event-type.

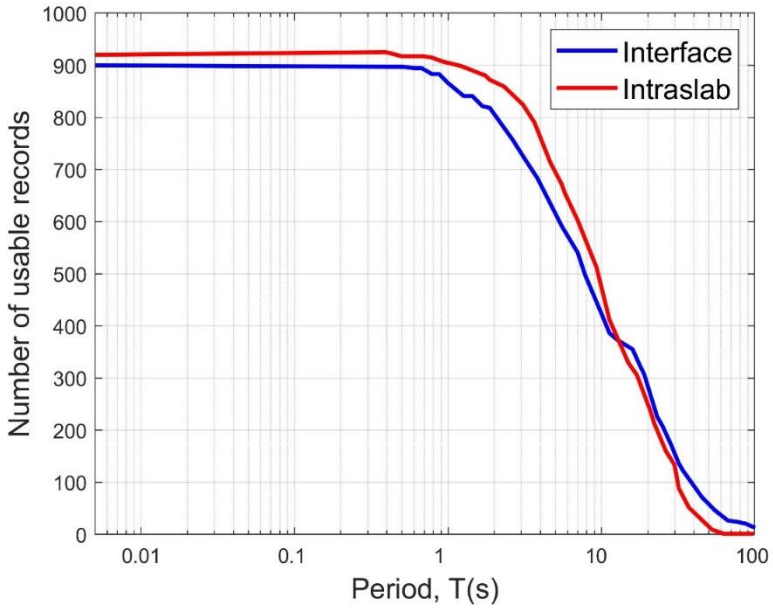

Figure 5.38. Number of recordings in composite database as function of oscillator period.

5.5 PATH PARAMETERS

Path parameters are essential metadata for ground motion analysis. The path parameters considered are rupture distance (R_{rup}), percentage of path through the forearc and backarc, which is defined by a volcanic arc boundary, and the maximum usable distance for a given array and earthquake (R_{max}). The development of these parameters for the NGA-Sub database was described in Section 3.2. These same procedures were applied for Mexico, with some revisions as described here.

5.5.1 Volcanic Arc Boundary

As with other subduction zone plate boundaries, Mexico has a volcanic arc caused by melting of the down-going oceanic slab that produces plumes of magma that rise to form volcanoes on the surface of the overriding slabs. As described in Section 3.3, in NGA-Sub volcanic arc locations were delineated by drawing (by hand) lines connecting volcanoes as provided by the Smithsonian Institute's Global Volcanism Program (2013). These lines were used to categorize the forearc

(trench-side) and backarc of each subduction zone region. Figure 5.39 (red line) shows this line in central Mexico.

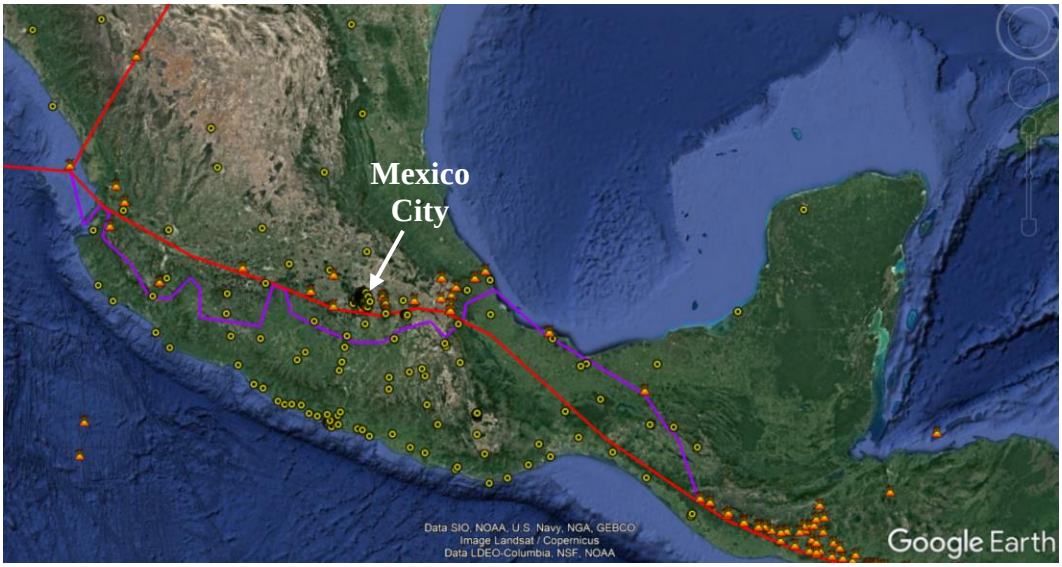

Figure 5.39. Map showing NGA-Sub (red line) and relocated volcanic front (purple line). Orange symbols are volcanoes with eruptions during the Holocene period and yellow symbols are ground motion stations.

Ferrari et al. (2012) provided a detailed description of the trans-Mexican volcanic belt, including its geologic history and current composition. Based on this study, the volcanic front has a complex geometry corresponding to the boundary of a volcanic sector located immediately north of crustal blocks inboard of the offshore plate boundary. This relatively complex representation of the volcanic front is shown in Figure 5.39 with the purple line and was used for the present study to define forearc and backarc regions. This relocation of the volcanic front places 16 ground motion stations in the backarc that had been classified in the forearc previously. For instance, there are seven stations located in the city of Puebla now classified as backarc that had been forearc. On the other hand, six ground motion stations now located in the forearc were previously classified as backarc. With both the current and previous boundaries, Mexico City is located in the backarc region as shown in Figure 5.39. Of the 121 subduction events considered in the combined database,

98% are in the forearc and the remainder are backarc (based on hypocenter location). Of the 612 recording stations, 51% are in the forearc, 46% are in the backarc, and the remainder are outside of the volcanic-arc zone. Figure 5.40 shows the relocated volcanic front along with stations considered in this study and the hypocenters of the three large events described in Section 5.3. Each of these events is in the forearc.

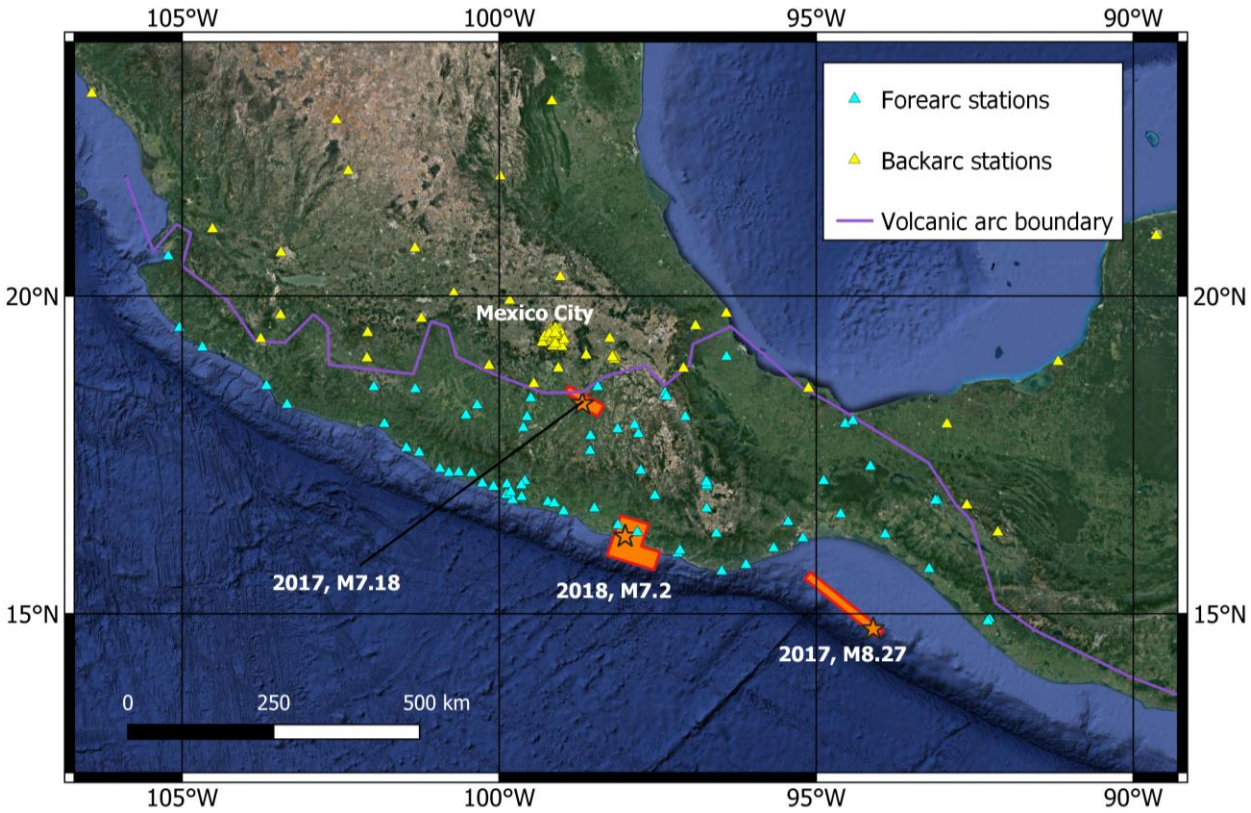

Figure 5.40. Map of central Mexico showing adopted volcanic front, ground motion stations considered in this region of Mexico, and hypocenters of the three large events described in Section 5.3.

5.5.2 Distance Calculations

Distance parameters (e.g., R_{rup}, R_{JB}) were computed using station locations and finite fault models from literature (for the three large events described in Section 5.3) or from simulations (for the **M** < 6 events described in Section 5.2). For each source-to-site path, the percentage of the direct-line

path in forearc and backarc was computing using the volcanic front boundary in Figure 5.40. Based on these calculations, 55.0% of paths are forearc-only, 42.2% originate in the forearc and end (at the station) in backarc, 2.1% originate in the forearc and end outside the volcanic-arc region, 0.4% originate in backarc and end in forearc, and 0.3% are backarc-only. Given these diverse path attributes, the Mexico dataset is well suited to studies of variable attenuation rates in forearc and backarc regions. Path data is assembled in a record table (*PathVolArc* table).

5.5.3 Network-specific maximum usable distance

Earthquake ground motion databases can contain sampling biases for conditions with low-amplitude shaking near the trigger threshold for triggered instruments or the noise threshold for continuously-streamed instruments. The problem is not that no records are obtained for such conditions, but that the recorded ground motions may be biased towards larger values. The bias occurs because weaker motions that do not exceed trigger thresholds or that fall near the noise are not recorded. In NGA-Sub, this problem was addressed in the development of GMMs by not using data beyond a limiting distance (R_{max}) (Contreras et al., 2022).

A key step in the estimation of R_{max} for a given network is the evaluation of the network truncation level. For well recorded events, truncation level can be evaluated from PGA vs. distance plots by identifying the PGA level where the data trend flattens. Contreras et al. (2022) describe methods that can be applied when the available data does not allow for a visual assessment of truncation level, or where procedures are desired that do not require the application of judgment. For the present case using the events described in Section 5.3, the truncation level was visually assessed as $3 \times 10^{-4} g$, which applies for the networks listed in Section 5.4.1.

Once truncation level is established for a network, R_{max} is estimated for a specific event by finding the distance where the median minus 2.5 within-event standard deviation (ϕ) ground motion matches the truncation level. This is done for the three large events by plotting the Parker et al. 2022 GMM through the data for each event. The model is adjusted up or down to pass through the center of the data, and once that median trend is set, the median minus 2.5ϕ PGA level is computed. Stations located on the Mexico City basin were not considered to adjust the median model, due to the amplification effects that these data exhibit. Examples for the three large events from Section 5.3 are shown in Figure 5.41, Figure 5.42, and Figure 5.43. R_{max} values for all other events were developed in the manner described presented by Contreras et al. (2022) and were retrieved from the NGA-Sub database (Mazzoni et al., 2022).

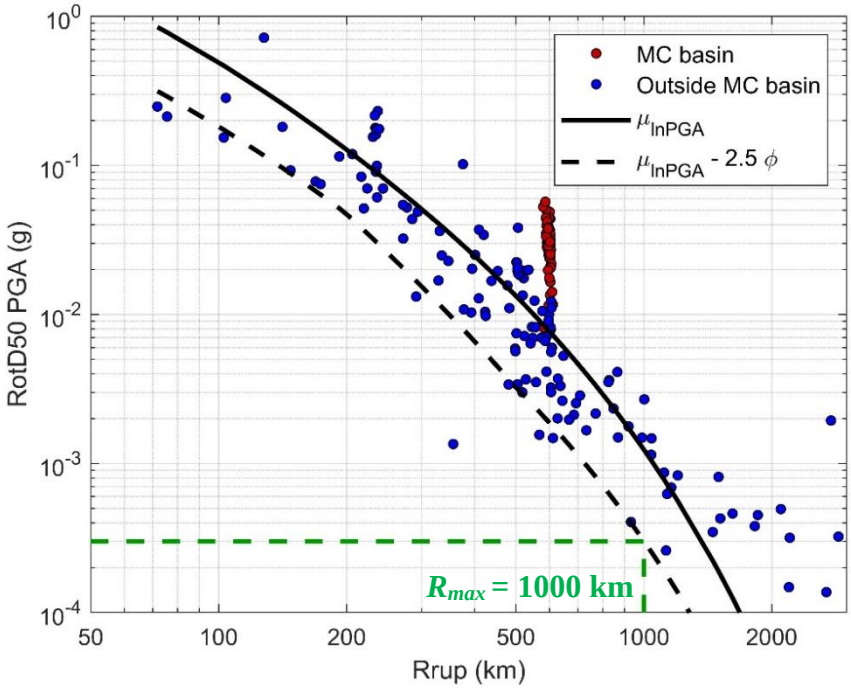

Figure 5.41. R_{max} evaluation for the 2017 **M**8.27 offshore Chiapas event. Records from all the networks are plotted with the truncation level evaluated in the text, along with R_{max} value. Stations located on the Mexico City (MC) basin are highlighted in red.

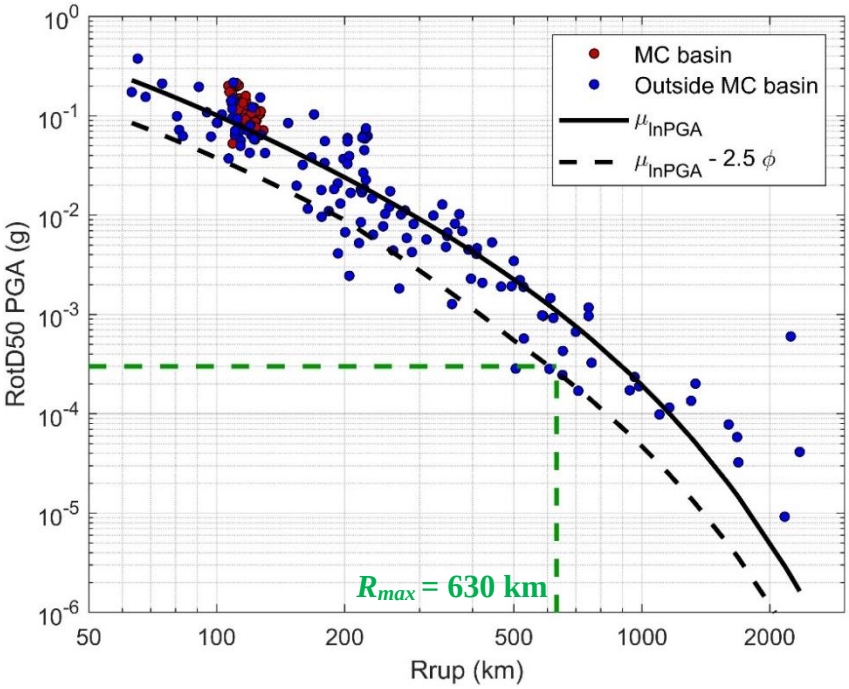

Figure 5.42. R_{max} evaluation for the 2017 **M**7.18 Puebla event. Records from all the networks are plotted with the truncation level evaluated in the text, along with R_{max} value. Stations located on the Mexico City (MC) basin are highlighted in red.

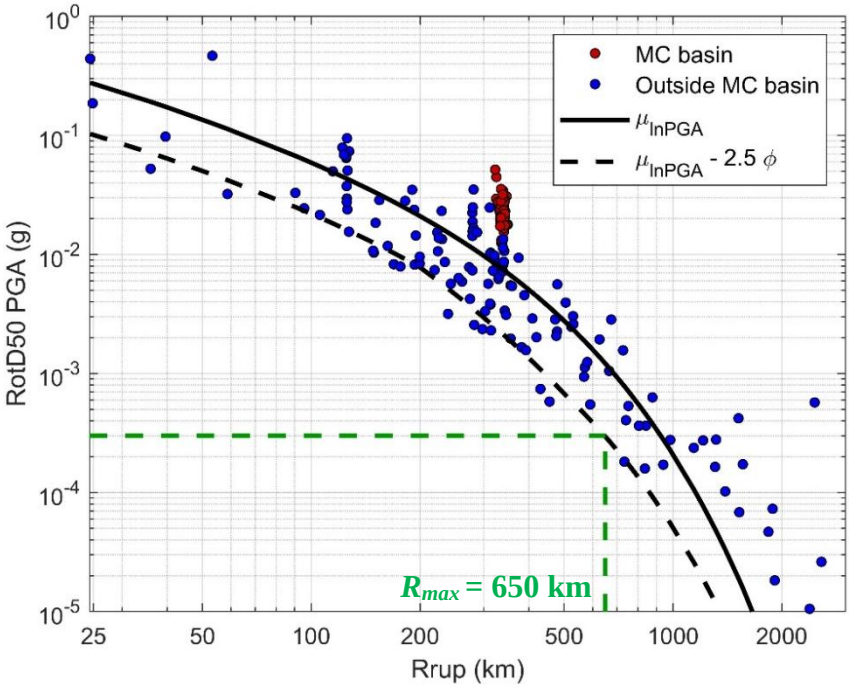

Figure 5.43. R_{max} evaluation for the 2018 **M**7.2 Oaxaca event. Records from all the networks are plotted with the truncation level evaluated in the text, along with R_{max} value. Stations located on the Mexico City (MC) basin are highlighted in red.

5.6 SITE PARAMETERS

Site parameters for the locations of ground motion recording stations have been developed for each of the 219 stations that recorded the three large magnitude earthquakes (Table 5.4). When applicable, these new data have been used to update site information of stations located in Mexico that were already included in the NGA-Sub database. The procedures used to assign site parameters are conceptually the same as those used in NGA-Sub (Ahdi et al., 2022), but more information on site conditions has been collected, particularly for Mexico City. Because Mexico City has a high concentration of instruments, and information on geotechnical conditions is much more available than in other parts of Mexico, the development of site parameters is discussed separately for Mexico City and the remainder of Mexico in the subsections that follow.

5.6.1 Mexico City Site Conditions

(a) Geologic Conditions

Mexico City is located within the eastern sector of the Trans-Mexican Volcanic Belt, north of the volcanic front as shown in Figure 5.40. As such it is surrounded by volcanos, including Iztaccíhuatl, Popocatépetl, La Malinche, Ajusco, and Nevado de Toluca. The oldest rocks in the region are Cretaceous limestones that are overlain by Oligocene and Miocene volcanic sequences, followed by Pliocene-Pleistocene to recent volcanic rocks (Arce et al., 2019). Surficial materials are lacustrine sediments as old as 1 Ma (1 million years) and with very recent sediments near the surface in some areas. These lacustrine sediments are remnants of Lake Texcoco within the Valley of Mexico. The lake occupied the entire Valley of Mexico between the Pleistocene epoch and the last glacial period (about 11,000 years ago). A series of four smaller lakes existed as recently as 1245 (upon arrival of the Aztecs), after which the lakes were impacted by human activity (Alcocer

and Williams, 1996). Figure 5.44 shows a general geologic map of the Mexico City area (Flores-Estrella et al., 2007).

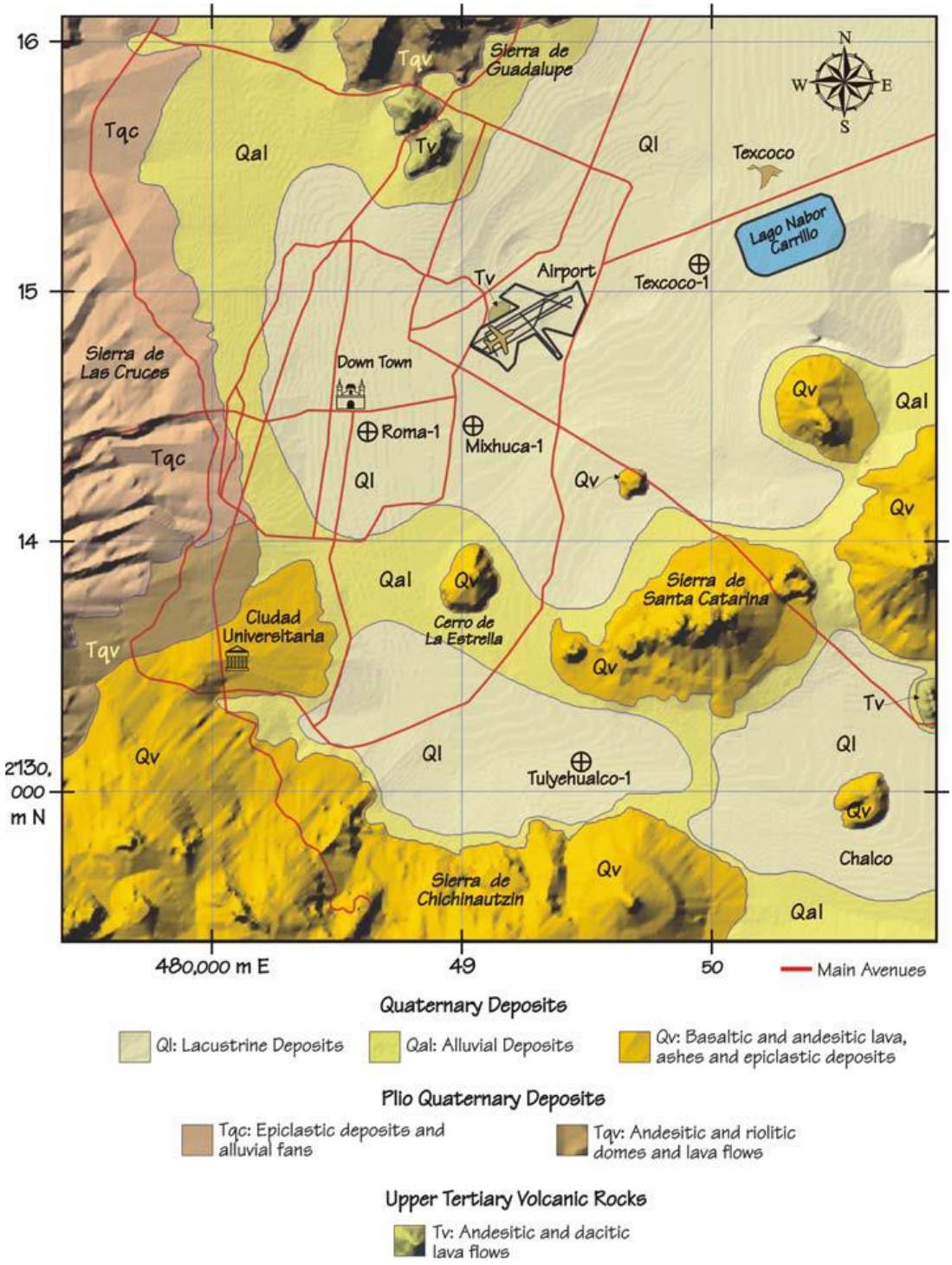

Figure 5.44. Surface geology of Mexico City region (Flores-Estrella et al., 2007).

As shown in Figure 5.45, the geotechnical conditions in Mexico City have commonly been defined in terms of a hill zone, transition zone, and lake zone (Marsal and Mazari, 1969; Romo et al., 1988). The lake zone includes the Texcoco Lake (while this was once encompassing the entire Valley of Mexico, as used here it refers to a smaller lake in the post-Aztec era), Xochimilco Lake, and Chalco Lake (Romo et al., 1988). General characteristics of these zones are as follows (Romo et al., 1988):

- Hill Zones: In the western part of Mexico City, this zone consists of firm soils including silty sands with gravels and cemented tuffs. To the south, lava flows up to 20 m in thickness overlie these formations. These zones carry the Tqc and Tv surface geologic descriptions from Figure 5.44.
- Transition Zones: Located between the hill and lake zones, the transition zone has variable sequences of firm soils, sands, silty sands, and soft clays. These zones are mapped as Qal in Figure 5.44.
- Lake Zones: The Texcoco Lake has a surface layer of desiccated alluvial deposits overlying thick soft lacustrine clay interbedded with thin seams of sands, silty sands, volcanic glass, and fossils, which is locally known as the Upper Clay formation. Underlying this formation are hard deposits of silty, weakly cemented sands, a deeper clay stratum known as the Lower Clay formation, and compact lacustrine cemented silty sands and gravels. The Xochimilco-Chalco Lake consists of a clay deposit (somewhat stiffer than the Upper Clay formation in Texcoco) with interbedded seams of silty sands, silts, and sands. This clayey deposit is underlain by a basalt layer (lava flow). Lake zones are indicated in Figure 5.44 as Ql.

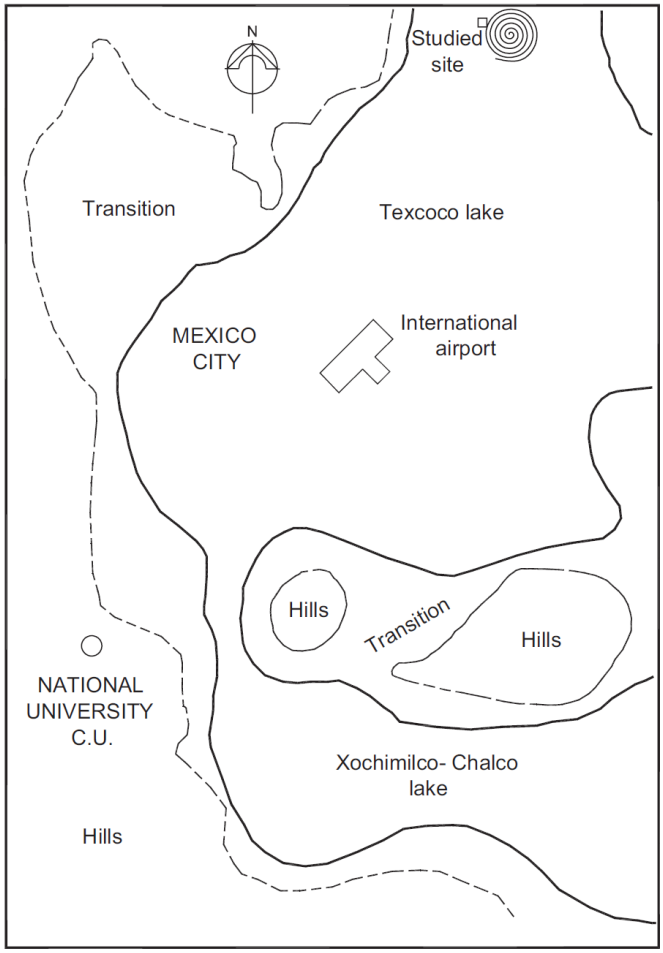

Figure 5.45. Schematic depiction of the hill, transition, and lake zones in Mexico City (Mayoral et al., 2008).

(b) Zonation in Mexico City Building Code

Seismic design in Mexico City uses response spectra that are derived by applying a procedure that takes into account the different ground conditions described above. In this procedure, Fourier amplitude spectra are derived for the Ciudad Universitaria (CU) site (Figure 5.45), which are then modified using transfer functions for different locations across the city.

Ground motions for the CU site are obtained using probabilistic seismic hazard analysis. Deaggregation results show that two sources are dominant: 7.5 intraslab event at a rupture distance

of 150 km and 7.8 interface event at a rupture distance of 265 km. These ground motions are developed using a Fourier amplitude spectra GMM (Ordaz et al., 1994) derived from 25 ground motion recordings.

Transfer functions are developed in a manner that depends on zones as defined in Figure 5.46 (hill, transition, lakebed; Reinoso and Ordaz 1999). Data from ground motion recording sites (numbered in Figure 5.46) are considered. In the case of hill sites, variations in ground motion by location are not considered and a single representative transfer function is given. For transition and lakebed sites, a smoothed empirical transfer function is provided conditional on site period. The site period-dependent representation of amplification is derived from recording sites with similar site periods using the reference site method (e.g., Borcherdt, 1994). The transfer function is multiplied by the reference site Fourier spectrum, and this site spectrum is converted to a response spectrum using Random Vibration Theory utilizing a suitable model for ground motion duration. As presented in Section 4.3.1, Jaimes et al. (2006) and Jaimes et al. (2015) revisited this procedure utilizing new recordings at the CU site and at sites located in the lake-bed zone (SCT and CAO) from interface and intraslab earthquakes, respectively. Jaimes et al. (2006) argue that a better method to compute the response spectra at sites across the city is to use transfer functions based on response spectra instead of Fourier amplitude spectra ratios. The use of Random Vibration Theory and estimation of ground motion duration in the latter method introduces significant uncertainties and errors. These studies by Jaimes et al. (2006, 2015) updated the GMM for the CU site from those developed by Ordaz et al. 1994, but the number of recordings remains small due to the fact that only a single station is used (21 interface event recordings by Jaimes et al. 2006, 22 intraslab event recordings by Jaimes et al. 2015; Table 4.2). The revisions to the CU GMM and site response models suggested by Jaimes et al. (2006, 2015) have not been implemented.

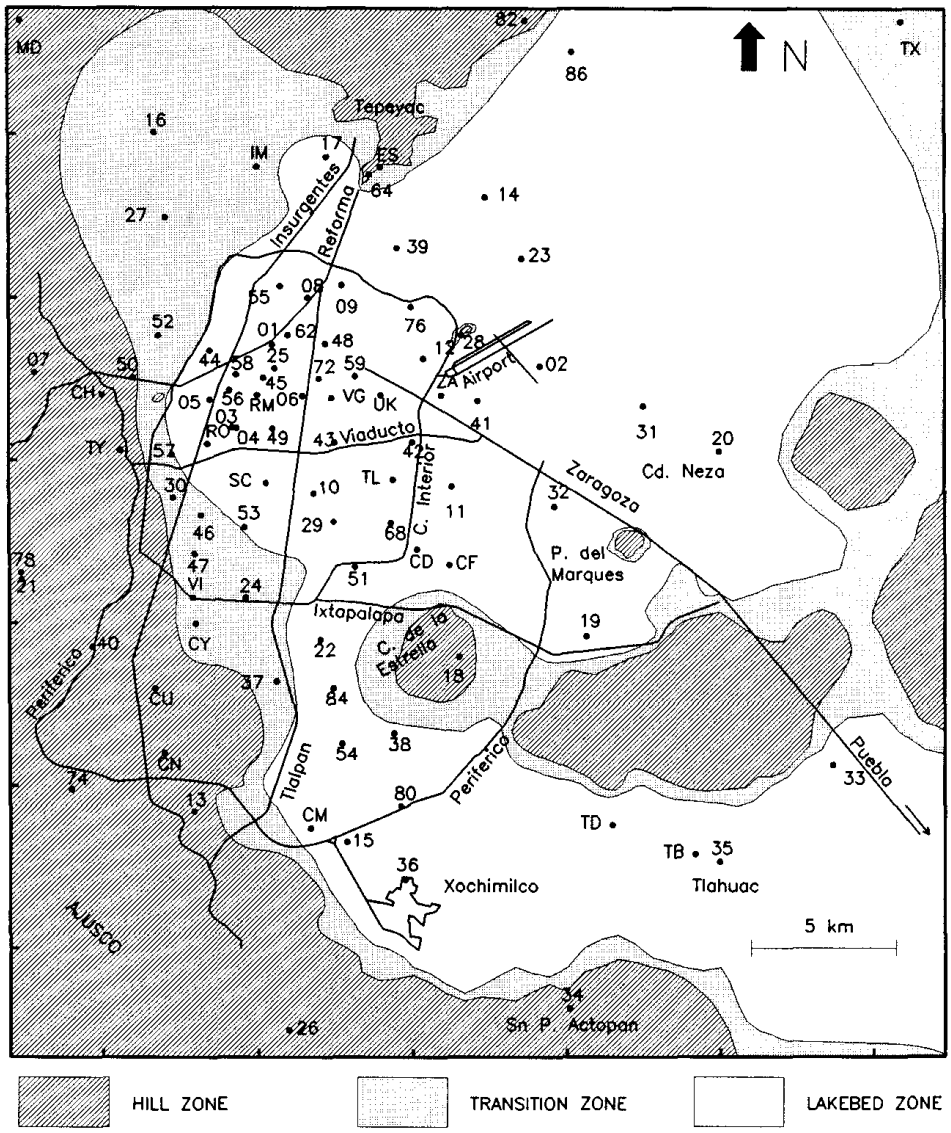

Figure 5.46. Zone map of Mexico City showing locations of recording sites used to derive transfer functions relative to the CU site (Reinoso and Ordaz, 1999).

For users, the key step in implementing this procedure is the selection of the site period. This can be obtained by looking up the site on a map such as Figure 5.47 (NTCS, 2004), in which Zone III was divided into four subzones:

- Zone II (transition): Ts = 0.5-1.0 sec
- Zone IIIa-d: Ts = 1.0-1.5, 1.5-2.5, 2.5-3.5, > 3.5 sec

In the current version of the seismic provisions (NTCS, 2020) the site-specific parameters are obtained through an online system called SASID (System of Seismic Actions for Design), that provides the seismic demand based on the geographical coordinates of the site (https://sasid.unam.mx/webNormasCDMX/, last accessed May 2022, registration is required). However, this procedure is simply an automated version of the procedure from NTCS (2003) and the underlying basis for the site response model (conditioned on Ts) is unchanged.

The zone map in Figure 5.47 is considered in the assignment of site parameters in this research, as described further in the next subsection. The impact of site period (zones) on response spectra is shown in Figure 5.48.

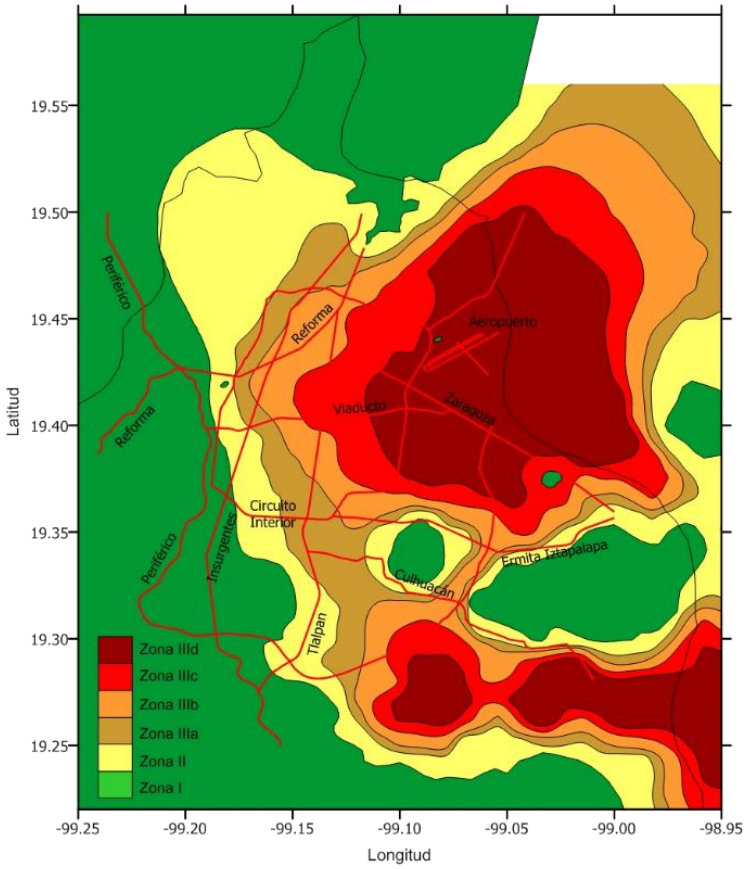

Figure 5.47. Zone map for Mexico City in which the lakebed zone is divided into four subzones that are used to predict site period based on location (NTCS, 2003).

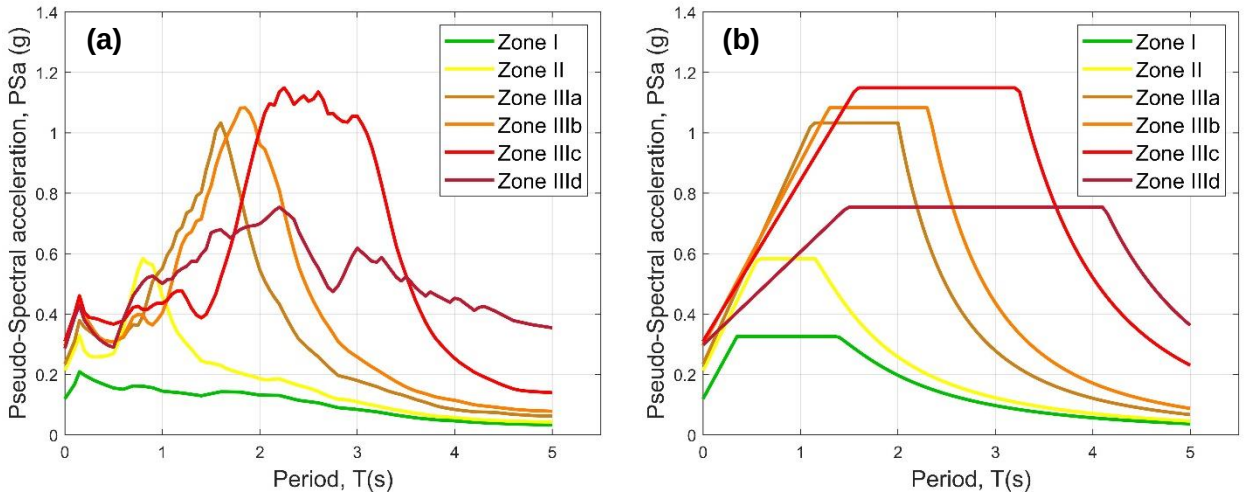

Figure 5.48. Example of zone-specific **(a)** uniform hazard spectra and **(b)** design response spectra derived using procedure from NTCS (2020). The following site periods were assigned by SASID: Ts = 0.5s, 0.8s, 1.4s, 1.8s, 2.9s, and 4.4s for the sites considered in the example at zones I, II, IIIa, IIIb, IIIc, and IIId, respectively.

(c) Velocity and Site Period Data

With the help of collaborators at UNAM and SSN, we have compiled available information on velocity profiles and site periods in the Valley of Mexico. The data are from technical reports, research papers, and student dissertations. Velocity data comes from invasive (downhole, crosshole, suspension logging, seismic cone penetration) and noninvasive methods (Multi-channel Analysis of Surface Waves – MASW, Microtremor Array Measurements – MAM, Modified microtremor seismic method using SPatial AutoCorrelation – MSPAC, seismic interferometry – SI, seismic refraction). Site period data are derived from microtremor-based measurements of Horizontal-to-Vertical Spectral Ratios (HVSR), the lowest peaks of which reveal the fundamental mode site period for soft soil conditions as encountered in Mexico City (Nogoshi and Igarashi,

1970; 1971; Field and Jacob 1993, 1995; Theodulidis et al. 1996; Bonilla et al. 1997, 2002; Satoh et al. 2001; Cadet et al. 2012). For sites with V_S profiles that reach a large impedance contrast (i.e., below the lower clay formation in Texcoco Lake, basalt layer in Xochimilco-Chalco Lake), site period was also derived from the V_S profile using procedures given in Urzúa et al. (2017).

Table 5.6 presents the compiled information, including the measurement locations, zones (from Figure 5.47), derived V_{S30} values, derived site periods, testing methods, and references. Two columns for site period are provided, one for results of HVSR testing and one for period derived from the V_S profile. Figure 5.6 shows the locations of these sites.

Table 5.6 Summary of site data from literature for Valley of Mexico stations.

ID	Site name	Latitude (deg)	Longitude (deg)	V_{S30} (m/s)	Measured site period (s)	Estimated site period (s)	Testing Methods (1)	Seismic zone	Reference
1	SCT	19.394694	-99.148678	61	–	1.96	DH, P-S SL	IIIb	Seed et al. (1987)
2	CAO	19.3738	-99.0971	46	–	3.26	DH, P-S SL	IIIc	
3	CAF	19.366	-99.086	60	–	2.35	DH, P-S SL	IIIb-IIIc	
4	TLB	19.279	-99.008	51	–	–	P-S SL	IIId	
5	TLD	19.293	-99.035	74	–	2.42	DH	IIIa-IIIb	
6	CUPJ	19.413	-99.158	62	–	2.01	DH	IIIb	
7	UNAM	19.33	-99.183	295	–	0.26	UKN	I	
8	Urban overpass	19.54634	-99.21104	193	–	0.23	CH	I	Mayoral et al. (2011)
9	Impulsora bridge	19.47627	-99.03488	48	–	3.08	P-S SL	IIId	
10	TXS0	19.58031	-99.01954	140	–	0.84	P-S SL	IIIa	Mayoral et al. (2016)
11	TXS1	19.49578	-98.97609	70	–	1.71	P-S SL	IIIb	
12	TXS2	19.49017	-98.97984	69	–	1.65	P-S SL	IIIb	
13	B-1 Texcoco Lake area	19.51126	-98.99731	47	–	2.01	P-S SL	IIIb	Mayoral et al. (2017)
14	Northwestern hills	19.35454	-99.27043	404	–	0.22	P-S SL	I	Mayoral et al. (2019)
15	Parque España	19.41546	-99.17138	92	1.35	1.17	MASW, MAM, HVSR	IIIa	Wood et al. (2019)
16	Escocia	19.38744	-99.16342	136	0.93	–	MASW, MAM, HVSR	IIIa	

Table 5.6 Summary of site data from literature for Valley of Mexico stations.

ID	Site name	Latitude (deg)	Longitude (deg)	V_{S30} (m/s)	Measured site period (s)	Estimated site period (s)	Testing Methods [(1)]	Seismic zone	Reference
17	La Morena	19.39861	-99.15873	93	1.28	1.21	MASW, MAM, HVSR	IIIa	Wood et al. (2019)
18	Hospital Gral Tlahuac	19.28735	-99.05354	88	2	1.81	MASW, MAM, HVSR	IIIb	
19	Parque Floresta Coyoacán	19.303931	-99.129369	145	0.89	0.63	MASW, MAM, HVSR	IIIa	Woodfield (2020)
20	Park on Hacienda de La Huerta	19.294529	-99.133217	158	0.95	0.62	MASW, MAM, HVSR	IIIa	
21	Parque Campestre Coyoacán	19.309202	-99.116568	90	1.26	1.11	MASW, MAM, HVSR	IIIa	
22	Park on Ejido Culhuacan	19.330913	-99.126851	111	1.25	–	MASW, MAM, HVSR	IIIa	
23	Park on Copa de Oro	19.333584	-99.142989	151	0.92	0.82	MASW, MAM, HVSR	II-IIIa	
24	Park on Cerro Cubilete	19.341828	-99.134183	115	1.09	0.82	MASW, MAM, HVSR	IIIa	
25	Parque Masayoshi Ohira	19.352357	-99.142272	97	0.99	0.94	MASW, MAM, HVSR	IIIa	
26	Kiosko	19.302363	-99.105545	67	2.07	1.56	MASW, MAM, HVSR	IIIb	
27	Parque el Triangulo	19.314396	-99.109342	99	1.6	–	MASW, MAM, HVSR	IIIa-IIIb	
28	Jardin Fraccionamiento Los Sauces	19.305735	-99.116391	95	1.3	0.94	MASW, MAM, HVSR	IIIa	
29	Park on Ejido de los Reyes	19.336769	-99.126444	93	1.33	0.99	MASW, MAM, HVSR	IIIa	
30	Parque Naciones Unidas	19.343699	-99.124395	102	1.32	1.56	MASW, MAM, HVSR	IIIa	
31	Sports Field on Cafetales	19.331476	-99.112617	110	0.99	0.91	MASW, MAM, HVSR	II	
32	Parque Italia	19.314019	-99.126533	96	1.09	0.93	MASW, MAM, HVSR	IIIa	
33	Parque Hacienda de San Juan	19.289901	-99.142843	159	0.78	0.64	MASW, MAM, HVSR	II	

Table 5.6 Summary of site data from literature for Valley of Mexico stations.

ID	Site name	Latitude (deg)	Longitude (deg)	V_{S30} (m/s)	Measured site period (s)	Estimated site period (s)	Testing Methods (1)	Seismic zone	Reference
34	Parque Ecologico Huayamilpas	19.323619	-99.15115	305	0.73	0.7	MASW, MAM, HVSR	I	Woodfield (2020)
35	Parque Tagle	19.348499	-99.182919	319	NA	0.36	MASW, MAM, HVSR	I-II	
36	Parque Xicotencatl	19.356837	-99.150813	134	1	0.85	MASW, MAM, HVSR	II-IIIa	
37	Plaza de La Conchita	19.346991	-99.159394	138	0.65	0.65	MASW, MAM, HVSR	II	
38	Parque de los Venados	19.373266	-99.155449	124	1.09	0.97	MASW, MAM, HVSR	II-IIIa	
39	Parque Jose Refugio Menez	19.39133	-99.143364	84	1.54	1.25	MASW, MAM, HVSR	IIIb	
40	Parque Hundido	19.378554	-99.179385	338	NA	0.35	MASW, MAM, HVSR	II	
41	Garden Squarel Balbuena	19.408969	-99.108158	51	3.38	2.58	MASW, MAM, HVSR	IIId	
42	Parque Alfonso Esparza Oteo	19.38952	-99.17751	236	0.55	0.52	MASW, MAM, HVSR	II	
43	Plaza de las Naciones Unidas	19.400533	-99.149236	74	1.88	1.55	MASW, MAM, HVSR	IIIb	
44	Santa Catarina	19.33442	-98.997269	427	–	0.15	MASW	I	Luna (2012)
45	3era Sección del Bosque de Chapultepec	19.408824	-99.217339	460	–	0.18	SI	I	Cárdenas-Soto et al. (2015)
46	ESIA-CT.	19.508343	-99.13319	150	–	0.91	MASW	II	Luna (2012)
47	Conjunto Urbano Tlalpan	19.338567	-99.141874	**498 (*)**	–	–	SR	IIIa	Pérez (2017)
48	Parque Ramón López Velarde	19.409682	-99.157285	80	–	–	CH	IIIb	Díaz-Rodríguez (2003)
49	Nuevo Aeropuerto en Texcoco	19.517739	-99.001427	55	–	–	P-S SL	IIIb	Chamorro (2016)
50	Lago de Texcoco	19.496256	-98.972533	41	–	2.98	SCP	IIIb	Stephenson and Lomnitz (2005)
51	Cuemanco	19.300109	-99.096779	96	–	–	MASW	IIIc	Luna (2012)

Table 5.6 Summary of site data from literature for Valley of Mexico stations.

ID	Site name	Latitude (deg)	Longitude (deg)	V_{S30} (m/s)	Measured site period (s)	Estimated site period (s)	Testing Methods (1)	Seismic zone	Reference
52	Lago de Texcoco	19.491359	-99.020753	47	–	–	SCP	IIIc	Flores-Guzmán et al. (2014)
53	Chalco	19.25299	-98.971323	48	5.8	5.62	MSPAC, HVSR	IIIc	Vergara-Huerta & Aguirre (2020)
54	Zona Nororiente de la CDMX	19.456157	-99.040635	53	–	–	CH	IIId	De La Rosa et al. (2013)
55	Zona Nororiente de la CDMX	19.419678	-99.011745	53	–	3.25	CH	IIId	De La Rosa et al. (2013)
56	Nonoalco	19.474934	-99.01586	68	–	–	P-S SL	IIId	Romo and Garcia (2003)
57	Noreste de la CDMX, Lago de Texcoco	19.460643	-99.041256	40	–	2.89	SIM	IIId	Ramos-Martínez et al. (1997)

(1) Testing methods:

DH = Downhole
P-S SL = P-S Suspension Logging
CH = Crosshole
MASW = Multi-channel Analysis of Surface Waves
MAM = Microtremor Array Measurements
HVSR = Horizontal-to-Vertical Spectral Ratio
SI = Seismic Interferometry
SR = Seismic Refraction
SCP = Seismic Cone Penetration
MSPAC = Modified microtremor seismic method using SPatial AutoCorrelation
SIM = Stochastic Inversion Method
UKN = Unknown

(*) This measurement (ID = 47, seismic refraction) was considered an outlier and it was not used in the analysis.

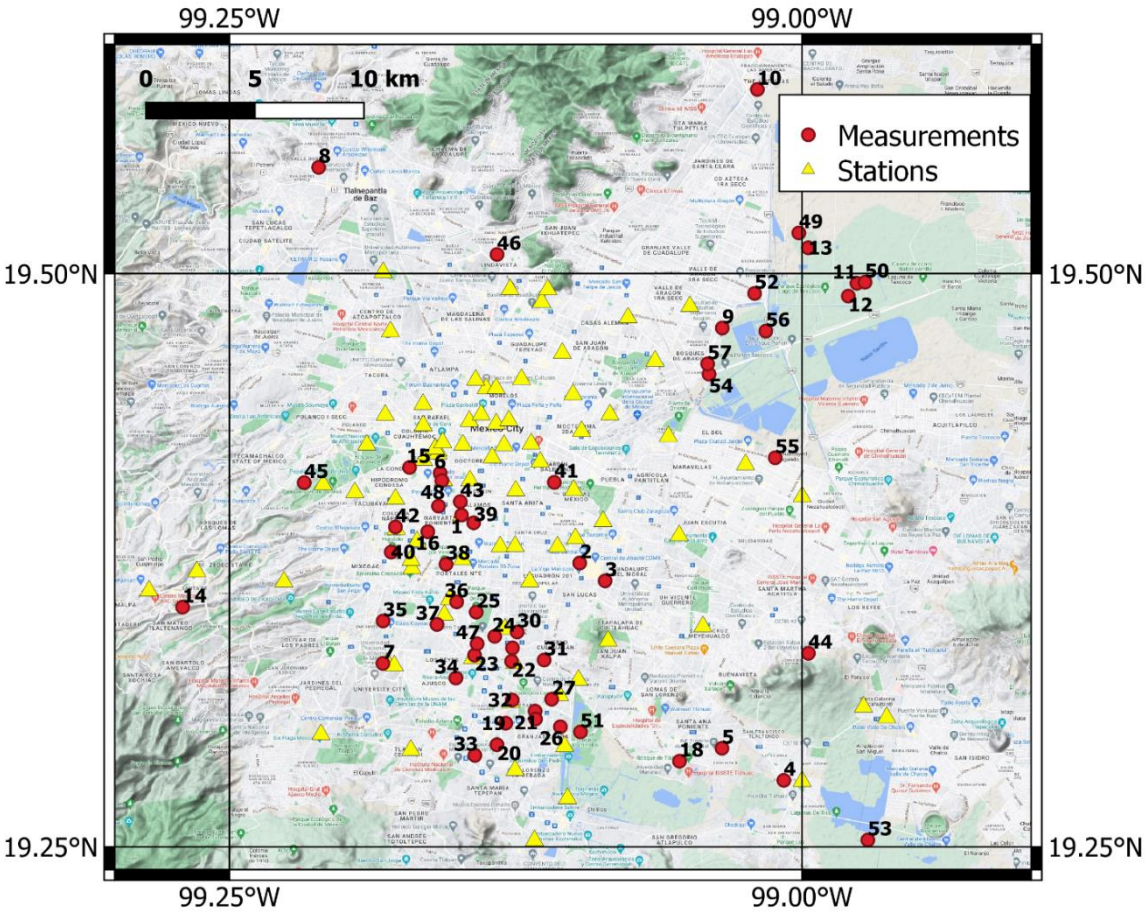

Figure 5.49. Locations of sites from Table 5.6. Numbers next to sites are the ID numbers from Table 5.6.

Figure 5.50 shows box and whisker plots of V_{S30} and site period by zone. Both data types for site period are used; for sites with both types of site period, only the HVSR result was used. Median values of V_{S30} and site period are indicated by the red lines in the figures. The lower and upper quartile are indicated by the box and the extremes are indicated by the whiskers (extreme horizontal lines). Results in Figure 5.50 show that, on average, the three main zones (i.e., Zone I-Hills, Zone II-Transition, and Zone III-Lake) segregate relatively well. V_{S30} values and the differences are statistically significant. The subdivision of Zone III shows significant differences between V_{S30} values in Zone III-a and in the other zones (III-b, c, d); however, the differences

between these latter zones are lower and not necessarily significant. In the case of site periods, the Zones segregate well, and the differences are statistically significant. An exception is Zones IIIc-d, which present a similar median. In addition, Zone IIIc shows a large variability in comparison with the other zones.

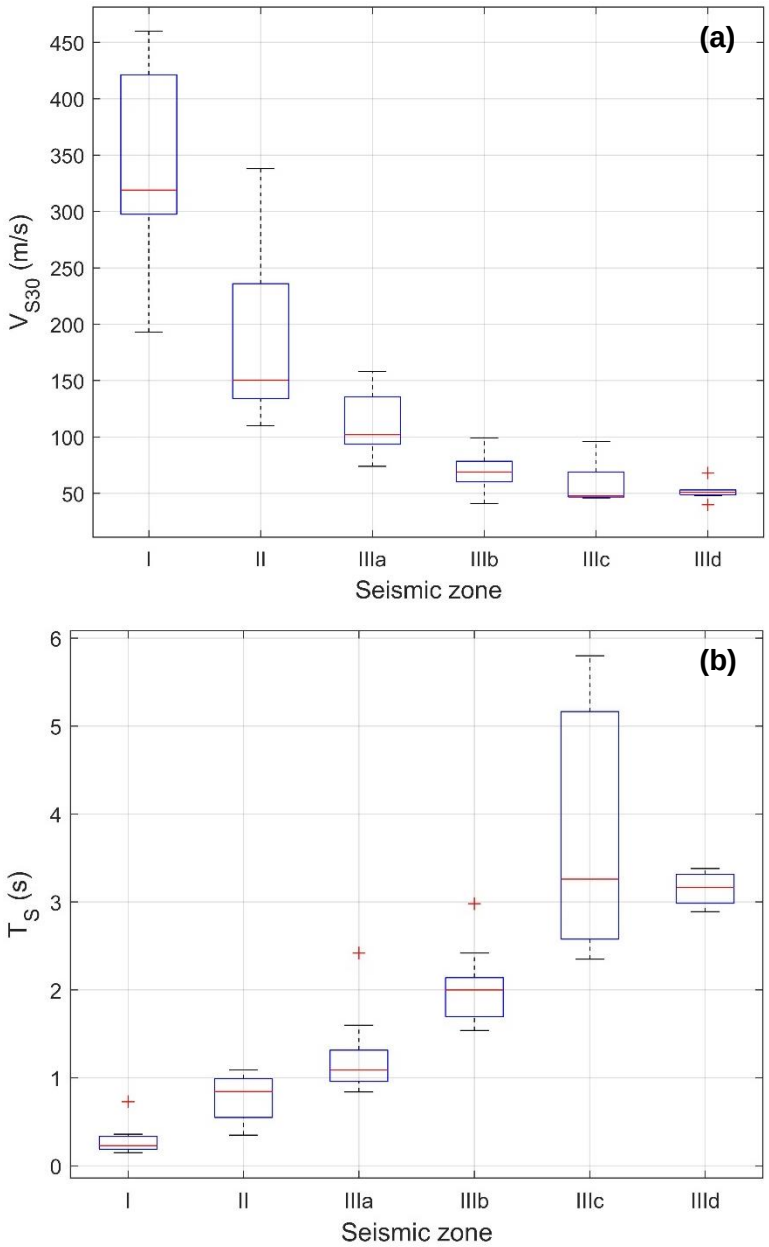

Figure 5.50. Box and whisker plots of **(a)** V_{S30} and **(b)** site period (T_S) for characterized sites in the Valley of Mexico (using data from Table 5.6).

Figure 5.51 shows the relationship between V_{S30} and site period. The negative correlation is strong, with short-period sites having high V_{S30}, and V_{S30} decreasing with increasing T_S. This result was expected given that about 57% of the data showed in Figure 5.51 are from measured V_S profiles that were constrained using the measured HVSR site periods.

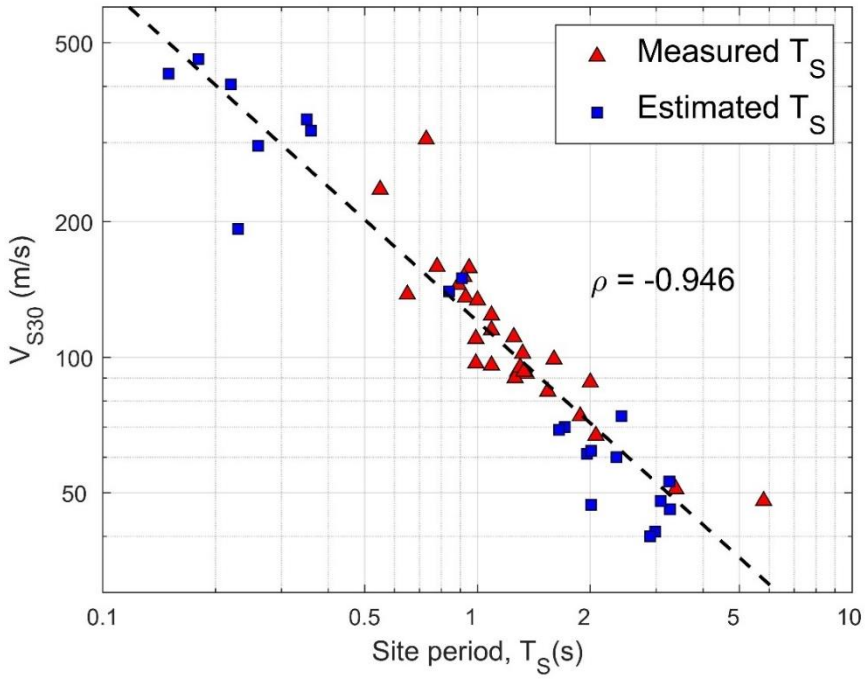

Figure 5.51. Correlation between V_{S30} and site period (T_S) for sites in the Valley of Mexico (using data from Table 5.6). The correlation coefficient between log(V_{S30}) and log(T_S) is shown.

(d) Velocity and Site Period Assignments for Ground Motion Stations

Ahdi et al. (2022) provide protocols for characterizing V_{S30} for ground motion sites, which were applied here. That study also classifies different methods of V_{S30} prediction for use at sites without seismic velocity measurements. The data compilation described previously in this section was not available at the time the NGA-Sub database was assembled. Hence, while the general approach is the same as given by Ahdi et al. (2022), the assigned site parameters are different for sites that were already in the database, and many new sites have been added to the database.

The database contains 97 ground motion sites in the Valley of Mexico. Of these 17 are Code 0 sites per Ahdi et al. 2022 (their Table 5), meaning that V_{S30} was computed from a V_S profile, which is taken as the median (μ_{lnV}), and the natural log standard deviation (σ_{lnV}) is taken as 0.1. Separation distances up to 300 m were considered in assigning a V_S profile to a ground motion site.

For the 80 sites without a V_S profile, we assigned μ_{lnV} based on the zone the site is located in. This is an example of a region-specific prediction model, which is indicated as Code 2MC (Code 2 is as given in Table 5 of Ahdi et al. 2022; the letters "MC" are added for this Mexico City specific model, which was not available when the NGA-Sub database was developed). The natural log standard deviation is computed from the data for each zone as follows: Zone I (0.296), Zone II (0.394), Zone IIIa (0.214), Zone IIIb (0.234), Zone IIIc (0.311), Zone IIId (0.157). Table 5.7 presents a summary of the natural log means and standard deviations for each zone, along with the corresponding V_{S30} values adopted in the analysis.

Table 5.7 Summary of V_{S30} parameters developed for Valley of Mexico stations without a V_S profile.

Zone	**# sites**	μ_{lnV} **(m/s)**	σ_{lnV}
I	7	331.3	0.296
II	10	172.3	0.394
IIIa	19	110.5	0.214
IIIb	15	67.1	0.234
IIIc	5	56.9	0.311
IIId	7	51.5	0.157

The site table for Mexico only lists site periods when they are measured at the site or estimated from measured V_S profiles. We do not use proxy relationship to estimate site period in the absence of a measurement.

5.6.2 Non-Valley of Mexico Sites

As part of this research, we searched for V_S profile data for sites outside of the Valley of Mexico from literature, dissertations, and consulting reports (from firms familiar to colleagues at UNAM and SSN). This effort was unsuccessful. No V_S profiles outside of the Valley of Mexico have been identified, even from Oaxaca and Puebla, which have sites located on relatively soft deposits that produce similar ground motion amplification (although in a much smaller scale) than those in Mexico City. Based on available geologic maps (1:50,000 scale map for Puebla and 1:250,000 map for Oaxaca by INEGI (1985, 1994)), these soft deposits in Oaxaca are mainly sands and silts classified as Holocene alluvium (Qhoal), whereas in the case of Puebla there is a mix of aeolic deposits with volcanic origin, lacustrine deposits, and alluvial deposits.

Given the lack of V_S data, for sites outside of the Valley of Mexico, we apply proxy models for V_{S30} prediction that were developed for California. The procedure involved looking up site surface geology, relating the mapped geology to geologic categories used in California (Wills et al., 2015), and then assigning the California-based μ_{lnV} and σ_{lnV}. The Mexico geology maps used in this process were 1:250,000 scale maps by Convenio INEGI-SGM, 1995, 2005. For sites that were used in NGA-Sub, a similar procedure was used, but geomorphic terrain (Iwahashi and Pike 2007) was used instead of surface geology, and the proxy model is that of Yong (2016). Some of these assignments were updated in the present work, but most were not and remain as terrain-based estimates. This use of proxy relationship derived for one region and applied in another region

without local validation is termed Approach III in Ahdi et al. (2022). Approach III carries with it epistemic uncertainty in the mean estimates, which is taken as σ_{ep}=0.2 (Ahdi et al., 2022). These epistemic uncertainties are included in the site table for site where Approach III was applied. Per Ahdi et al. (2022) (their Table 5), the code that is assigned to these sites is Code 4C-M, where "C" indicates California as the source region for the proxy models, and "M" indicates Mexico as the target region.

An exception to the above was applied for three sites on lacustrine deposits in Puebla. Given the relatively small size (and presumably limited depth) of these lake deposits, we use Zone IIIa values of μ_{lnV} and σ_{lnV}. Given the large uncertainties, σ_{ep}= 0.2 is assigned.

6 ADAPTATION OF NGA-SUB GROUND MOTION MODEL FOR MEXICO

6.1 INTRODUCTION

The NGA-Sub project developed ground motion models (GMMs) for subduction zone regions (Bozorgnia et al., 2022) using the project database (Mazzoni et al., 2022). These models were either developed for a specific region, namely Japan (Si et al., 2022), or were developed for global regions with regional adjustment factors (Abrahamson et al., 2020; Kuehn et al., 2020; Parker et al., 2022). For the global models, the regional adjustment factors pertain to the constant terms, the anelastic attenuation coefficients, the magnitude-scaling break point (separating strong scaling below the break and weaker scaling above the break), and coefficients for site response (V_{S30}-scaling). The degree to which these regional adjustment factors are well resolved depends on the amount and quality of data for the region. Where the data is limited in quantity and quality, some of these regional factors are not well resolved. In this case, they are set at the global average.

In the case of Mexico, data quantity is limited due to the relatively small number of recordings per event (average of 9), although not in the number of events (82 events). Data quality is also relatively poor, with highly uncertain site parameters and most events lacking finite fault models. For these reasons, Mexico components of an NGA-Sub model (Parker et al., 2022) apply global coefficients for site response and constant terms (slab events), whereas regional coefficients were derived for anelastic attenuation and constant terms (interface events).

The data developed in this study, particularly the three large events described in Section 5.3, have significantly expanded the size and quality of the Mexico data set. In this chapter, we use a combination of the original (NGA-Sub) data (Mazzoni et al., 2022) and new data (Chapter 5) to examine the performance of the Parker et al. (2022) GMM in Mexico. My specific objectives are to evaluate whether regional coefficients require adjustment to fit the data, to evaluate whether differences between backarc and forearc anelastic attenuation are evident from the data, and to investigate regional site response characteristics.

The site response topic is of particular interest in Mexico City, which has typically been evaluated in past work using reference site approaches that have well-known drawbacks (the most significant of which is that the results are dependent on the attributes of the reference sites, which in Mexico City is the single CU site; Figure 5.45). Here we derive site response using non-reference site approaches (adapted from Field and Jacob, 1995) in a manner than ensures consistency with the GMMs. Such approaches have been successfully applied elsewhere to derive regional (e.g., Parker and Stewart, 2022) and local (Wang et al., 2022) site response models.

The approach utilized in this investigation differs significantly from prior ground motion studies for Mexico. Most prior work, including the studies that produce ground motion models currently in use for the national PSHA, use solely ground motion data from Mexico (Sections 4.3.1 and 5.6). In contrast, the approach in the NGA-Sub project is to use the far larger global database to constrain model components that are unlikely to have significant regional variations (magnitude scaling, source depth scaling, geometric spreading, between- and within-event aleatory variability, nonlinear components of site response) and then adjust other aforementioned components to fit

regional data. By performing the regional analysis for Mexico using the enhanced database from Chapter 5, in this study I am able to better assess the regional components.

Subsequent sections describe the analysis approach (Sec 6.2), evaluate regional bias and magnitude scaling (Sec 6.3), evaluate path misfit (Sec 6.4), evaluate regional site response for Mexico (outside of Mexico City) and local site response in Mexico City (Sec 6.5), and evaluate the impact of the database enhancements on epistemic uncertainty (Sec 6.6). The result of these analyses is an adjusted version of the Parker et al. (2022) model that can be used with greater confidence for seismic hazard studies in Mexico.

6.2 APPROACH

Two key aspects of the approach are data selection and residuals analysis. These are described in the subsections below.

6.2.1 Data Selection Criteria

The combined database for Mexico has three components: (1) the NGA-Sub database for Central America and Mexico (CAM), which contains only $\mathbf{M} \geq 6$ events for this region prior to 2016 with reviewed event type flags; (2) NGA-Sub data with $\mathbf{M} < 6$ for which event type flags are now provided (Section 5.2); and (3) three large and well-recorded events since 2016 (Section 5.3). This combined database contains 2071 three-component time series from 144 earthquakes in Mexico and neighboring central American nations. The magnitude-distance distribution of the combined data set is shown in Figure 6.1. The combined database was assembled into a project flatfile to facilitate the analyses performed in this chapter.

Records from the project flatfile were selected for use in ground motion analyses in manner consistent with that of Parker et al. (2022), as follows:

1. Metadata necessary for model development are available in the NGA-Sub database (Mazzoni et al., 2022) such as **M**, rupture distance (R_{rup}), hypocentral depth (Z_{hyp}), and V_{S30};

2. Earthquake classified with high confidence as being interface or intraslab;

3. Earthquake is a mainshock (Class 1; *C1*) rather than an aftershock (Class 2; *C2*) according to the Wooddell (2018) method 2 using an 80-km cutoff distance;

4. $R_{rup} \leq R_{max}$, where R_{max} is a maximum distance limit set based on seismic network and event properties (Section 5.5.3).

5. Sensor depth ≤ 2m;

6. Interface events with hypocentral depths (Z_{hyp}) ≤ 55 km and intraslab events with Z_{hyp} ≤ 200 km;

7. Pseudo-spectral acceleration at oscillator periods $T \leq T_{LU}$, where T_{LU} refers to the longest usable period based on the corner frequencies used to process the record;

8. Earthquakes without multiple event flags; these are events for which the recordings do not indicate that more than one seismic source affected the ground motions;

9. Earthquakes with source review flags = 0, 1, 2 or 4, which indicate earthquakes that underwent quality control checks and meet metadata quality standards;

10. Records that capture the start of the P-wave (i.e. those without a late P-wave trigger flag);

11. After applying criteria 1–10, we only used records from events having at least three recordings.

A criterion from Parker et al. (2022) that is not applied is to require that the earthquake epicenter and stations are both located in the forearc region. This criterion was not applied to allow for analyses of potential differences in anelastic attenuation between the two regions as part of the present study.

The numbers of events and recordings used for model development vary as a function of period due to Criterion 7, with a range of 329–758 records for combined data from both event types. Figure 6.2 shows 369 usable interface records in the screened database at rupture distances of 14-1270 km from events with **M** 5.3-8.0. Of the 369 records, 204 were in the NGA-Sub database presented by Mazzoni et al. (2022). For intraslab events, there are 460 records following screening from events with **M** 5.3-8.3 and rupture distances of 47-1430 km; 109 of these records were in the Mazzoni et al. (2022) data set.

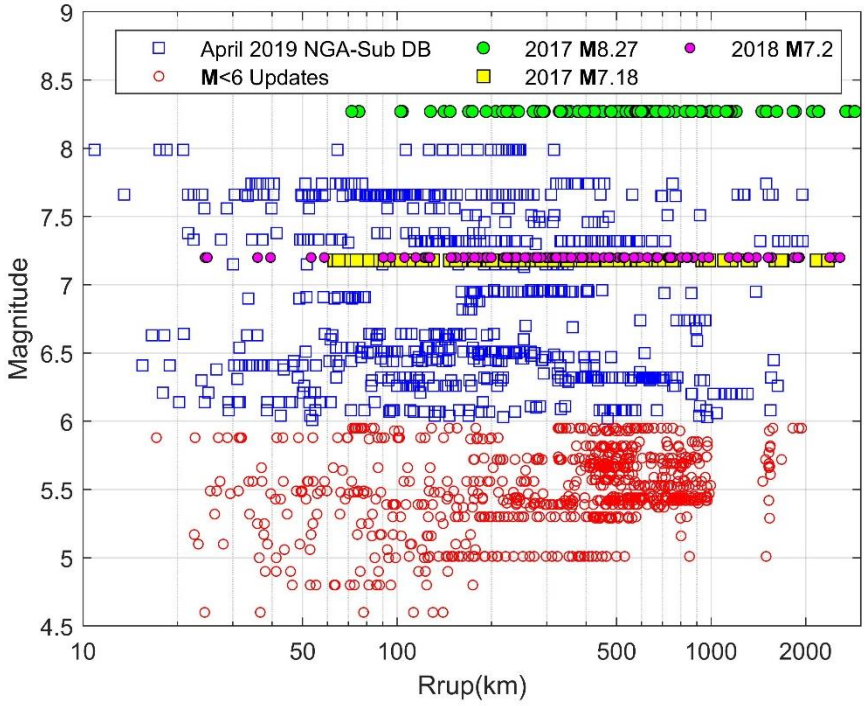

Figure 6.1. Magnitude-distance distribution of the NGA-Sub database in CAM following updates and addition of large-magnitude Mexico events since 2016.

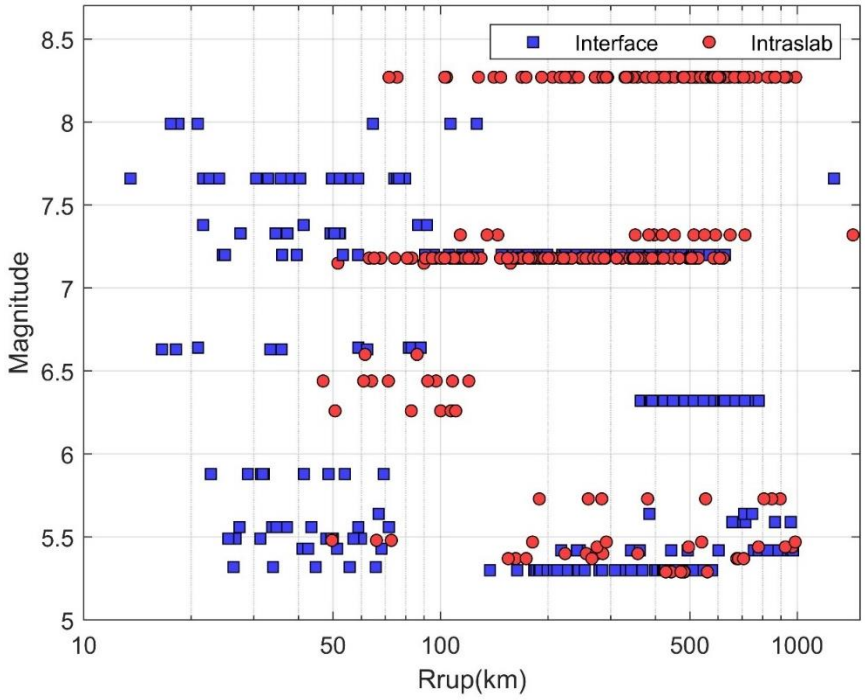

Figure 6.2. Magnitude-distance distribution of the screened NGA-Sub database in CAM.

6.2.2 Residuals Analysis Procedures

Using the screened data from Section 6.2.1, residuals analyses are performed to examine various attributes of the Mexico ground motions, including:

1. Constant term: Allows for an assessment of the degree to which the data are systematically higher or lower than those for a global NGA-Sub model. The constant term is a regionalized attribute in NGA-Sub models.

2. Source parameter scaling: Check of whether the Mexico data are consistent with magnitude- and source depth-scaling relations in an NGA-Sub model. These source scaling relations are not regionalized in NGA-Sub models.

3. Distance attenuation: GMMs have terms for geometric spreading and anelastic attenuation, the latter of which is regionalized in NGA-Sub models. We seek to investigate Mexico-specific regional attributes of anelastic attenuation, both in the forearc and backarc, and for interface and slab events.

4. Site response: The scaling of site response with V_{S30} is a regionalized feature in NGA-Sub models. At the time the models were developed, regional V_{S30} scaling terms different from those of the global model were not considered to be justified by the data, although the data were limited. This is re-examined with the larger data set, and site response in Mexico City is examined as a special case.

Consider an earthquake event i that produces ground motion j. Ground motion intensity measures (e.g., peak acceleration, peak velocity, pseudo-spectral accelerations for a range of

oscillator periods *T*) can be computed for each ground motion, which are denoted Y_{ij} in arithmetic units.

We compute the total residual, R^v, as the difference between the ground motion intensity measure (Y_{ij}) and a model prediction:

$$R_{ij}^{v} = ln\left(Y_{ij}\right) - \left[\mu_{ln,ij}^{r}\left(\mathbf{M}_i, F_S, (R_{rup})_{ij}\right) + F_{V,j}\right] \tag{6.1}$$

where $\mu_{ln,ij}^{r}$ is the mean ground motion prediction for reference rock site conditions in natural log units from a GMM. We use the Parker et al. (2022) (Pea22) GMM with the arguments of moment magnitude (**M**), event-type parameter (F_S), and rupture distance R_{rup}. F_V is a site amplification model conditioned on V_{S30}:

$$F_V = F_{lin} + F_{nl} \tag{6.2}$$

where F_{lin} and F_{nl} are linear and nonlinear site-amplification terms initially take from the global model of Parker and Stewart (2022). The use of superscript *v* on the residual in Eq. (6.1) is to indicate that a V_{S30}-based site amplification model is considered in their derivation.

To quantify systematic event and site misfits from the ergodic model (referred to as *event terms* and *site terms*, respectively), we partition total residuals from Eq. (6.1) using mixed effects analyses (Gelman et al., 2014):

$$R_{ij}^{v} = c_0 + \eta_{E,i} + \delta W_{ij}^{v} \tag{6.3}$$

where c_0 is an overall model bias, η_E is the event term, and δW_{ij}^{v} is the within-event residual. The within-event residual contains information on misfit of path and site parameters, and for many applications it is useful to separate these by further partitioning the within-event residual as,

$$\delta W_{ij}^{v} = c_1 + \eta_{S,j}^{v} + \varepsilon_{ij} \tag{6.4}$$

where η_S^v is the site term and ε_{ij} is the remaining residual. The mixed-effects analyses are performed in *Matlab* using the *fitlme* command (documentation available at https://www.mathworks.com/help/stats/linear-mixed-effects-models.html).

The need for a non-zero regional constant in Mexico can be judged from the statistical significance of c_0 as different from zero. The checks of source-scaling relations requires an evaluation of whether η_E values for intraslab or interface events have trends with source parameters (magnitude and hypocentral depth). Distance attenuation features of the data are evaluated using remaining residual ε_{ij}, which should not contain "contaminating" influence from source or site response misfits. Trends of ε_{ij} with distance, particularly for the distance range strongly influenced by anelastic attenuation (> ~ 100 km) allow assessments of regional bias, potential differences between forearc and backarc attenuation, and potential differences between anelastic attenuation by event type.

If it is found that non-zero constant terms or adjusted path coefficients are needed to fit the data, these modifications will be made and the GMM updated accordingly. This requires re-computation of residuals, event-terms, and site-terms, to confirm that misfits are removed. In this way, the residuals analyses are iterative with the steps to regionalize the model.

Site response can be examined by computing site terms relative to the reference condition in the adjusted GMM:

$$\eta_{S,j}^{r} = c_1 + \eta_{S,j}^{v} + (F_V)_{ij} \tag{6.5}$$

Superscript *r* indicates the term is for the reference-rock velocity condition of 760 m/sec. Reference rock site terms η_S^r are not expected to average to zero because they represent the difference between data for site *j* and model predictions for a reference-rock condition. In aggregate, these residuals estimate site response per the non-reference site approach (Field and Jacob, 1995). Plots of η_S^r with V_{S30} illustrate V_{S30}-scaling, which can be checked against Parker and Stewart (2022). For sites in Mexico City, η_S^r can be examined within zones or as a function of V_{S30} or site period to evaluate the relative effectiveness of different site parameters for predicting site response.

Once site response models are developed, the linear portion of the F_V model used in Eq. (6.1) is updated, and all subsequent analyses repeated to ensure that the modified model components are compatible.

6.3 REGIONAL BIAS AND SOURCE PARAMETER SCALING

6.3.1 Initial Analyses

The Parker et al. (2022) GMMs have different sets of coefficients for interface and intraslab events. The respective models were used with the data that meet screening criteria (Figure 6.2) to compute residuals using Eq. (6.1). The subset of residuals for sites located outside of the Valley of Mexico (Mexico City) were partitioned using mixed effects analysis to evaluate constant terms (c_0) and event terms using Eq. (6.3). The Valley of Mexico (VM) sites were removed because of strong

site effects (Section 6.5). Path-related biases in the backarc are not corrected for in these calculations (i.e., the Parker et al. model is used as-published).

Figure 6.3 shows the two sets of constant terms, which provide a preliminary indication of model bias. The results for interface events indicate positive bias (indicating under-prediction) for PGA and short periods < 0.15 sec. Longer periods and PGV have negative bias. The results for intraslab events show negative bias (indicating over-prediction) of up to 0.3 for PGA and periods up to 0.5 sec and positive bias for PGV and long periods. The standard errors of these model biases, as derived from the mixed-effects analyses, are sufficiently large that the 95% confidence interval includes zero for most intensity measures, the only exception being 0.3-2.5 sec for interface events. Hence, arguably the bias that is shown is generally not statistically significant. These biases are considered preliminary because the data set used in their derivation does not include VM sites and the GMM has not been adjusted for backarc-related path biases.

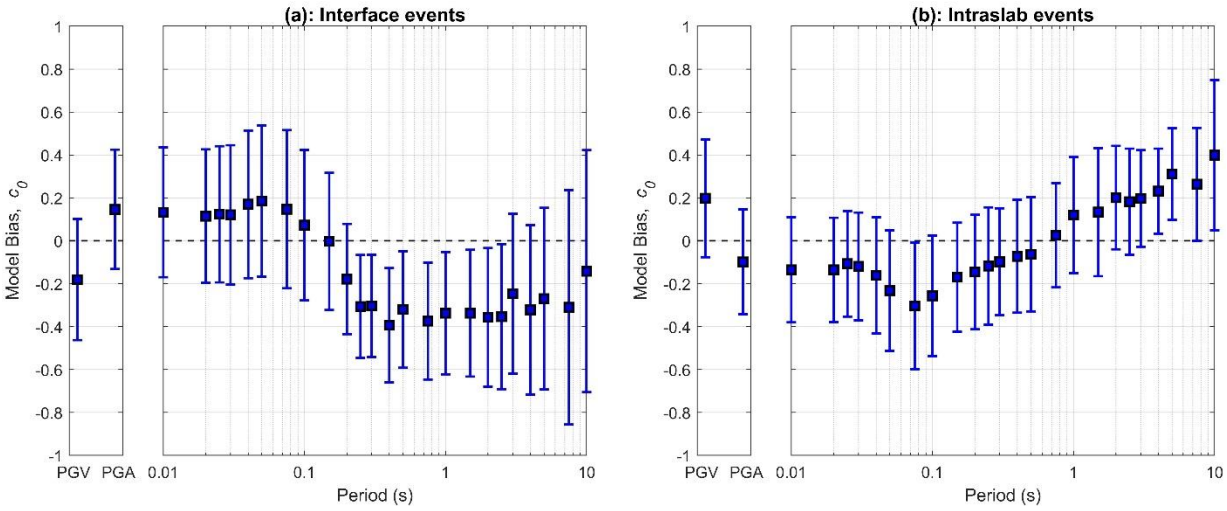

Figure 6.3. Model bias for peak acceleration, peak velocity, and Sa for a range of periods: (a) interface events, (b) instraslab events. Range indicates 95% confidence interval of the mean bias.

Figures 6.4 and 6.5 show the variation of event terms (η_E) with magnitude for the intensity measures of PGA, PGV, 0.3 sec Sa and 3.0 sec Sa for interface and intraslab events. For both event types, the event terms do not exhibit any appreciable overall trend up to **M** 7.5, which is near the break magnitude m_c. For both the interface and intraslab results, the lack of bias for **M** < 6 events is notable because data in that **M** range from Central America and Mexico was not considered in the development of the Parker et al. (2022) model. For larger magnitudes, no trend is evident for interface events, but positive bias is seen for the **M** 8.27 Chiapas event, which is the largest intraslab event in the NGA-Sub database. This could indicate that a steeper slope is needed for some intensity measures for $\mathbf{M} > m_c$, although we defer such decisions to future work where other large **M** events that have occurred globally subsequent to 2016 can be considered.

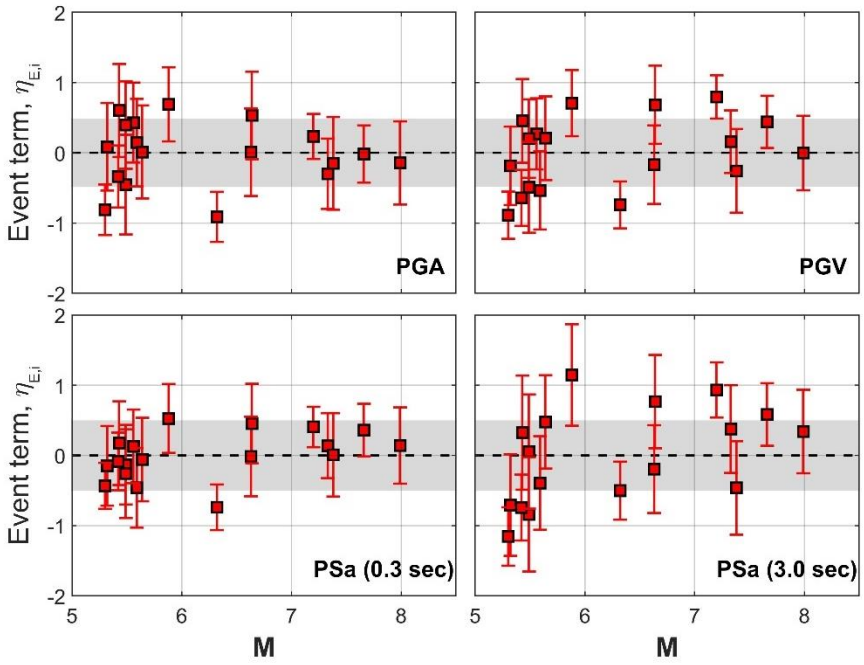

Figure 6.4. Trend of event terms for PGA, PGV, 0.3 sec Sa and 3.0 sec Sa with magnitude for interface events. Error bars are 95% confidence intervals.

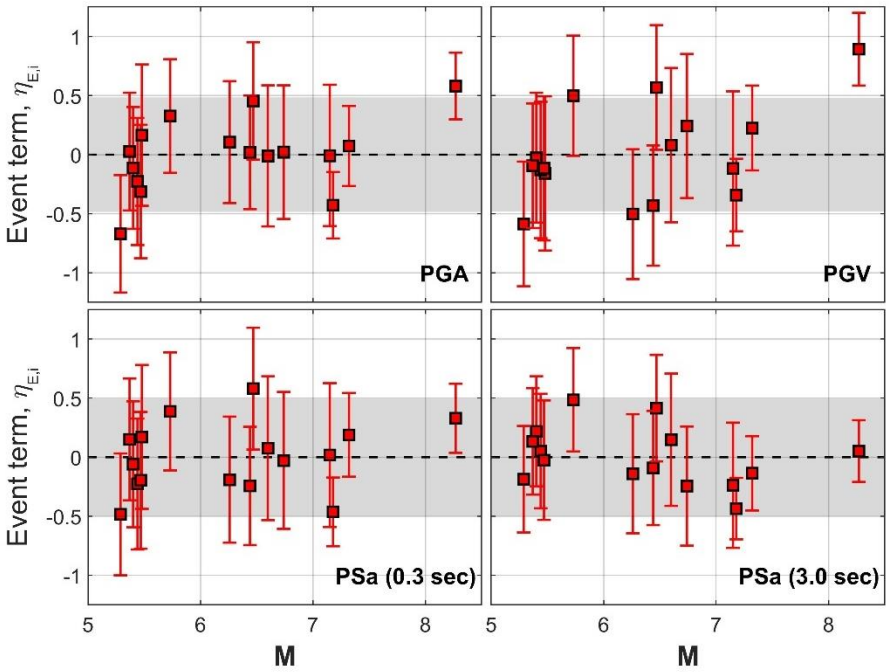

Figure 6.5. Trend of event terms for PGA, PGV, 0.3 sec Sa and 3.0 sec Sa with magnitude for intraslab events. Error bars are 95% confidence intervals.

Figures 6.6 and 6.7 show the variation of event terms (η_E) with hypocentral depth (Z_{hyp}) for the intensity measures of PGA, PGV, 0.3 sec Sa and 3.0 sec Sa for interface and intraslab events. In the case of interface, no trend is observed for the depth range of ~15-40 km where most of the data occur. This is consistent with the data for global events – no depth dependence is considered in the GMM. The interface event with Z_{hyp}=50 km is NGAsubEQID 3000137 with **M** 5.3. The event's hypocenter plots within the interface zone (Figure 6.8), which is why it is classified as such, but with the depth uncertainty that typically accompanies such events, it could be below the interface in the slab. Hence its event type classification carries additional uncertainty. In the case of intraslab, again no trend with depth is observed, although in this case the model includes depth effects. Hence, the lack of trend in the results indicates that the intraslab depth model applies for Mexico.

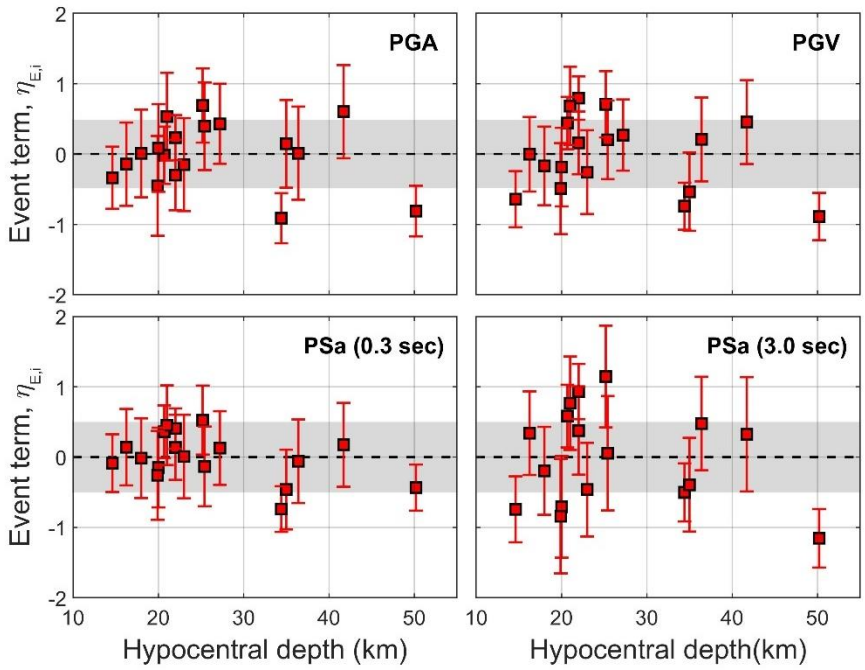

Figure 6.6. Trend of event terms for PGA, PGV, 0.3 sec Sa and 3.0 sec Sa with Z_{hyp} for interface events. Error bars are 95% confidence intervals.

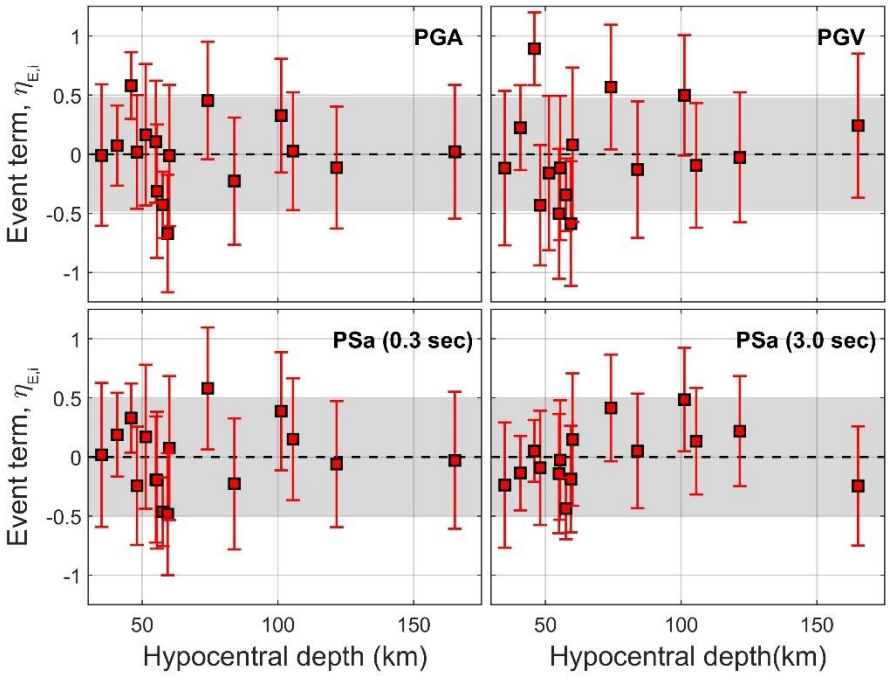

Figure 6.7. Trend of event terms for PGA, PGV, 0.3 sec Sa and 3.0 sec Sa with Z_{hyp} for intraslab events. Error bars are 95% confidence intervals.

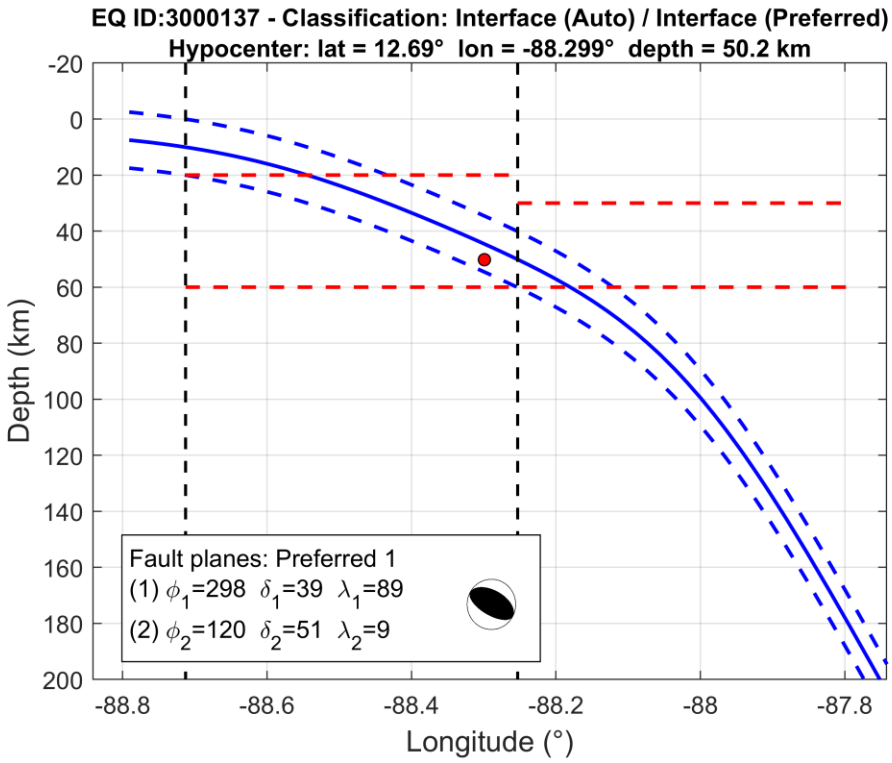

Figure 6.8. Event-type classification for NGAsubEQID 3000137 based on hypocenter location relative to the top of the surface of the subducting plate. The event is defined as interface.

6.3.2 Results from Recommended Model

Section 6.4 describes adjustments made to the backarc path anelastic attenuation models for interface and intraslab events. Section 6.5 describes the development of a local VM site response model that can be used to replace the Parker and Stewart (2022) site term for this region. These model adjustments were applied with the Parker et al. (2022) GMM and residuals analyses were repeated. For interface, short period bias has increased slightly, while long period bias is reduced relative to the results in Figure 6.3. For intraslab, bias is reduced at short periods and no appreciable change occurs at long periods relative to the results in Figure 6.3. The changes at short period are due to the anelastic attenuation model. Figures 6.10-6.11 show the resulting event terms, which have the same general pattern as observed in the original model.

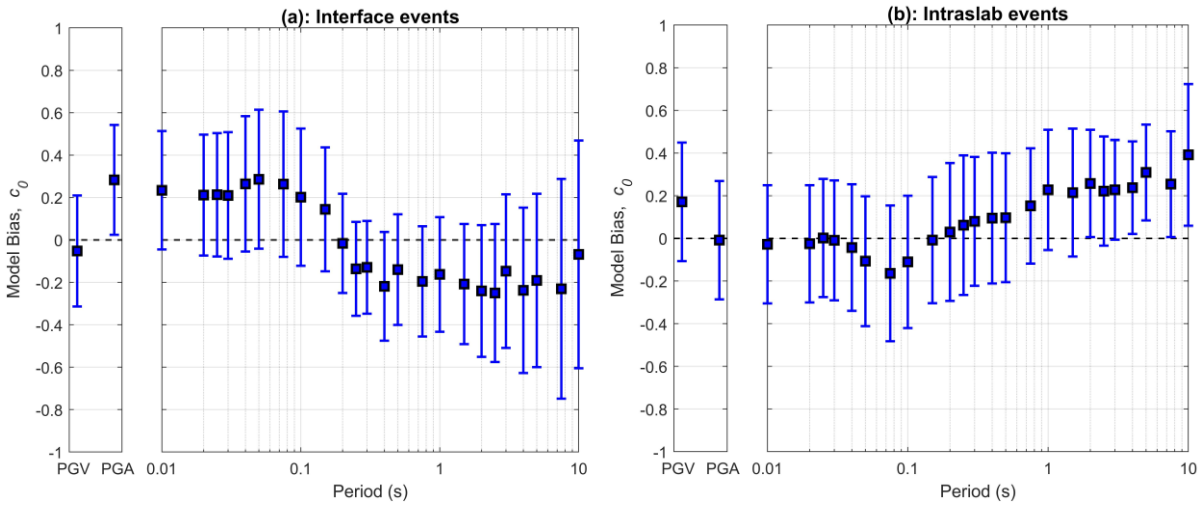

Figure 6.9. Model bias for peak acceleration, peak velocity, and Sa for a range of periods using Pea22 GMM adjusted for backarc attenuation and VM site response effects: (a) interface events, (b) instraslab events. Range indicates 95% confidence interval of the mean bias.

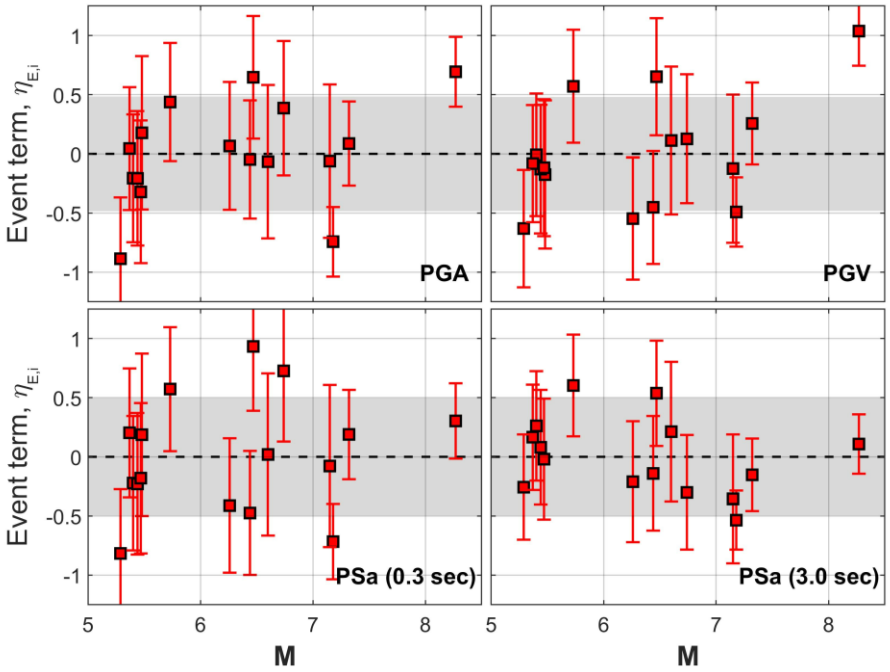

Figure 6.10. Trend of event terms for PGA, PGV, 0.3 sec Sa and 3.0 sec Sa with magnitude for interface events using revised Pea22 GMM. Error bars are 95% confidence intervals.

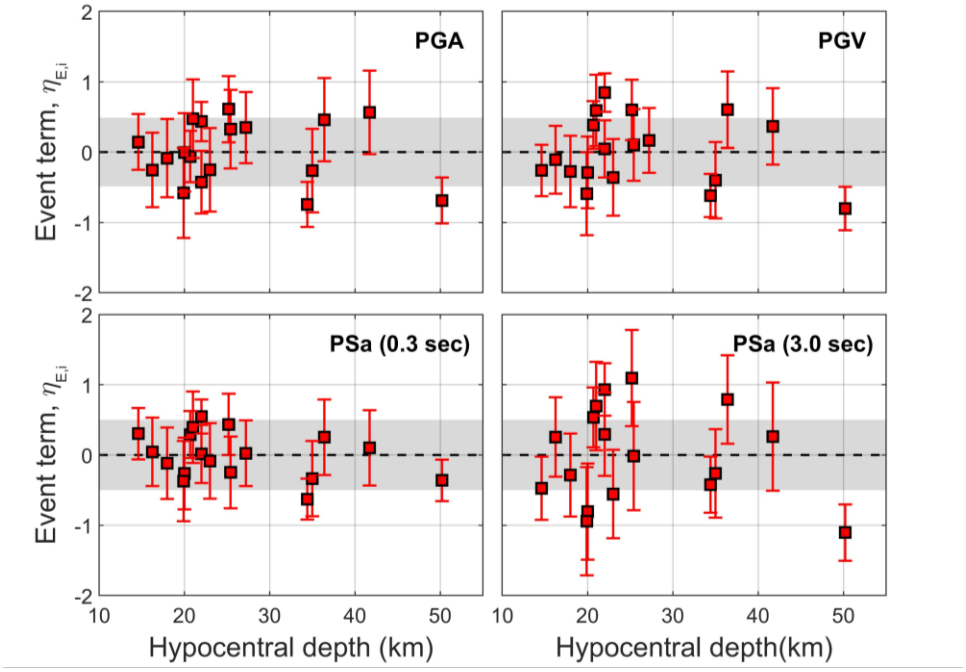

Figure 6.11. Trend of event terms for PGA, PGV, 0.3 sec Sa and 3.0 sec Sa with magnitude for intraslab events using revised Pea22 GMM. Error bars are 95% confidence intervals.

6.4 REGIONAL BIAS AND SOURCE PARAMETER SCALING

6.4.1 Initial Analyses

The Parker et al. (2022) GMMs describe the effects on ground motion of the wave propagation path using the following equations:

$$F_P = c_1 lnR + b_4 \mathbf{M} ln(R/R_{ref}) + a_0 R \tag{6.6}$$

$$R = \sqrt{R_{rup}^2 + h^2} \tag{6.7}$$

The F_P term is in natural log units and takes on negative values. It is additive with source and site response terms in the GMM. In Eq. (6.6), the lnR terms model geometric spreading and are region-independent. The $a_0 R$ term models anelastic attenuation, with the strength of this attenuation increasing as a_0 decreases (becomes more negative). The anelastic term (a_0) is

regionalized for forearc regions (values are not provided for the backarc), with region-specific values provided by Parker et al. (2022) for Central America and Mexico. The use of R (Eq. 6.7) in place of R_{rup} is to handle near-source saturation effects, which are not addressed here. We investigate whether the Parker et al. (2022) path models are able to capture data trends with distance for interface and intraslab events. We also apply the models to backarc data to investigate potentially faster anelastic attenuation relative to the forearc.

Preliminary analyses of path model performance examine the trends of δW_{ij}^{v} (Eq. 6.3) against R_{rup} (these analyses are preliminary because VM sites are excluded and the Parker et al. 2022 model is applied without modification to backarc sites). Beginning with forearc sites, Figures 6.12-6.13 show within-event residuals and their binned means for interface and intraslab earthquakes, respectively. In both cases, no appreciably slope is evident, indicating that the Parker et al. (2022) model is capturing the data trends. Note that VM data is in the backarc and therefore does not affect these plots.

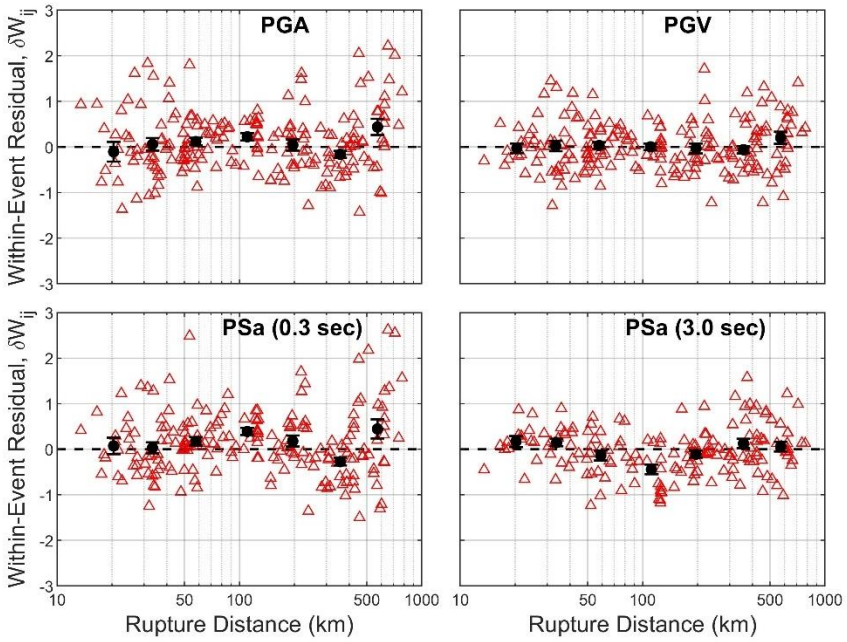

Figure 6.12. Trend of within-event residuals for PGA, PGV, 0.3 sec Sa and 3.0 sec Sa with R_{rup} for interface events and forearc sites using Pea22 GMM.

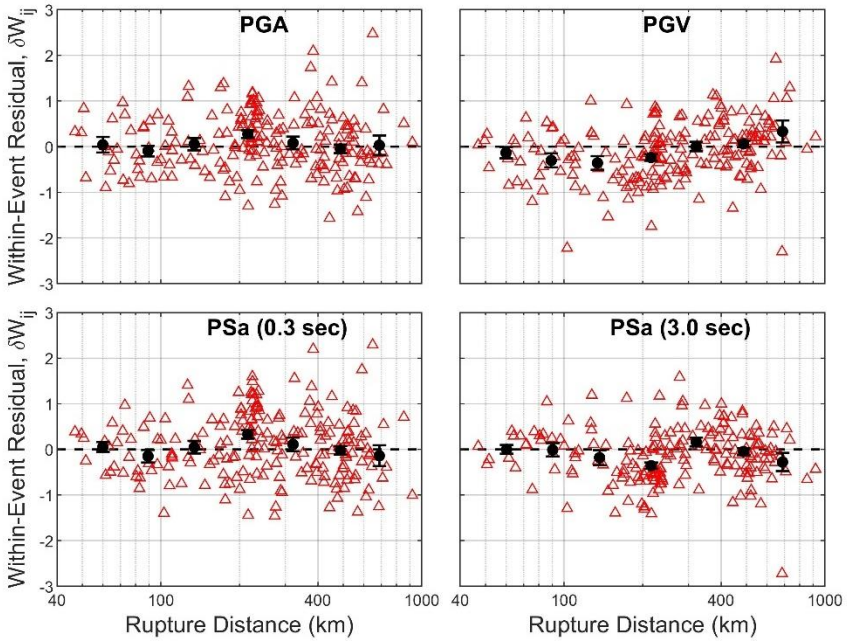

Figure 6.13. Trend of within-event residuals for PGA, PGV, 0.3 sec Sa and 3.0 sec Sa with R_{rup} for intraslab events and forearc sites using Pea22 GMM.

We anticipate that backarc regions of Mexico may have different rates of anelastic attenuation based on findings elsewhere, mainly Japan (e.g., Ghofrani and Atkinson 2011). Beginning with the null hypothesis that the forearc attenuation rate applies in the backarc, we plot in Figures 6.14-6.15 δW_{ij}^{v} vs. the backarc portion of the rupture distance ($R_{rup,b}$), which is defined as,

$$R_{rup,b} = F_b R_{rup} \tag{6.8}$$

where F_b is the fraction of the rupture distance in the backarc. Because the anelastic attenuation effect operates on R and not lnR (Eq. 6.6), in the figures a linear distance scale is used for $R_{rup,b}$. The results indicate for high-frequency IMs an approximately linear decay of within-event residuals with backarc distance. This suggests that a lower (more negative) anelastic coefficient is needed for Mexico's backarc regions. This is developed in the next subsection.

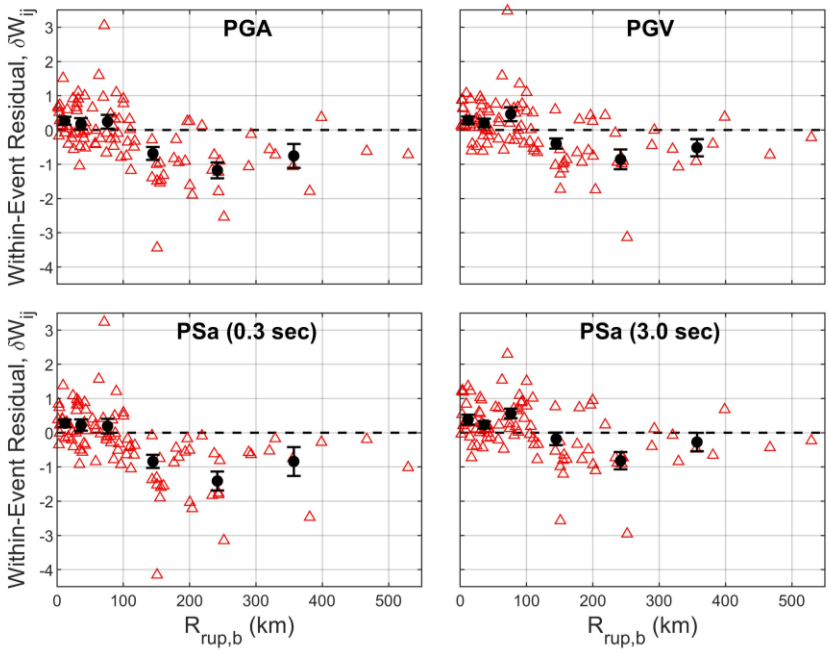

Figure 6.14. Trend of within-event residuals for PGA, PGV, 0.3 sec Sa and 3.0 sec Sa with $R_{rup,b}$ for interface events and backarc sites using Pea22 GMM.

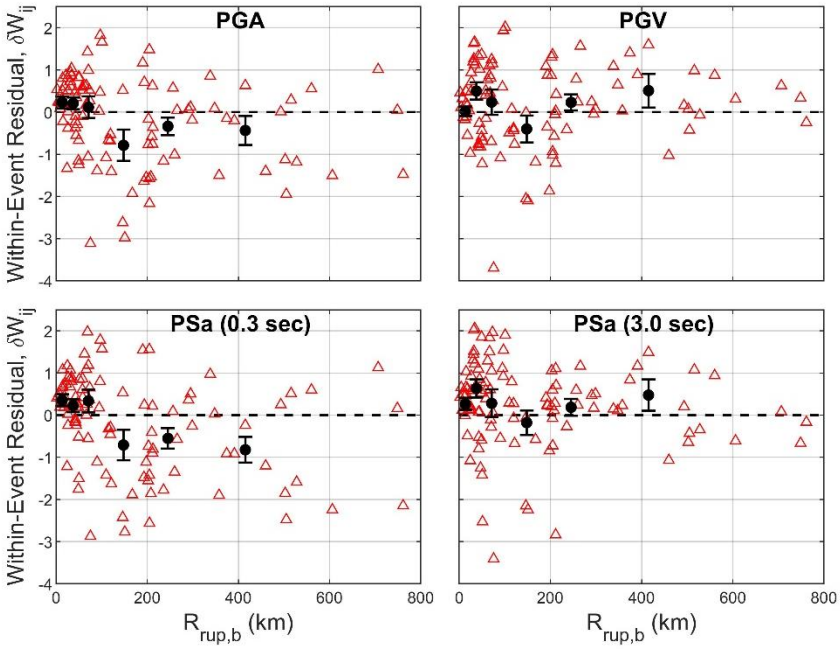

Figure 6.15. Trend of within-event residuals for PGA, PGV, 0.3 sec Sa and 3.0 sec Sa with $R_{rup,b}$ for intraslab events and backarc sites using Pea22 GMM.

6.4.2 Regional Model for Mexico Backarc Anelastic Attenuation

To remove the faster backarc anelastic attenuation trend that is evident in Figures 6.14-6.15, we fit a linear trend line as follows:

$$\delta W_{ij}^{v} = a + a_{0b} R_{rup,b} \tag{6.9}$$

where a_{0b} is the additional anelastic attenuation required in the backarc. When used with the predictive model, $a_{0b}c$ would appear as an additive term,

$$F_P = c_1 lnR + b_4 \mathbf{M} ln(R/R_{ref}) + a_0 R + a_{0b} R_{rup,b} \tag{6.10}$$

Note that by using $R_{rup,b}$ instead of rupture distance combined with finite fault parameter h as in Eq. 6.7, an assumption is being made that $R_{rup} \gg h$, which is generally valid for backarc

sites when the earthquake is located in the forearc. The intercept parameter a is not used for forward modeling, and is generally small.

Example fits of Eq. (6.9) to the data are shown in Figures 6.16-6.17. Figure 6.18 plots a_{0b} for different spectral periods (along with PGA and PGV) for interface and intraslab events. The results show faster attenuation for interface than intraslab events. For both event types, the faster backarc scaling reduces at long-periods. The faster scaling disappears for periods > 3 sec for intraslab events.

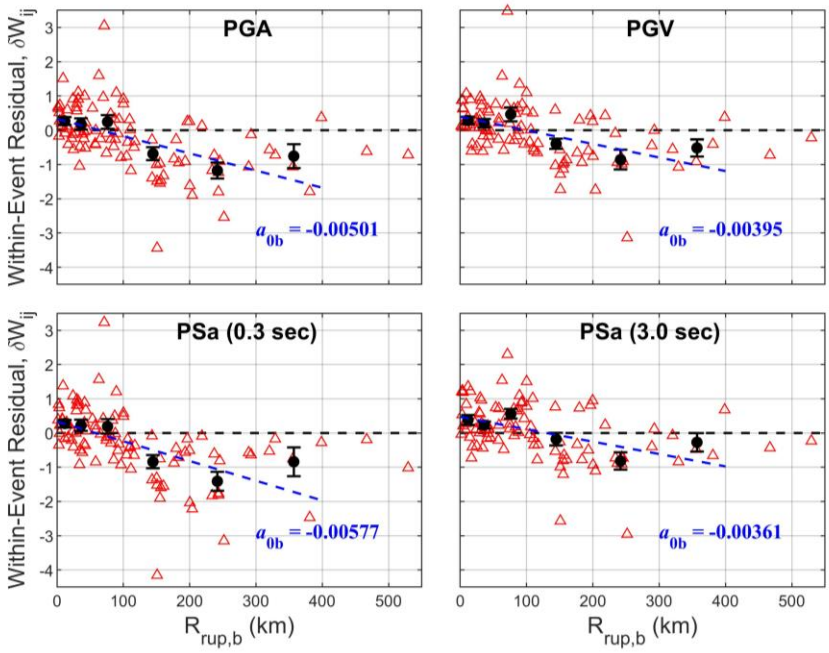

Figure 6.16. Fit of backarc model (Eq. 6.9) to within-event residuals for PGA, PGV, 0.3 sec Sa and 3.0 sec Sa from interface events.

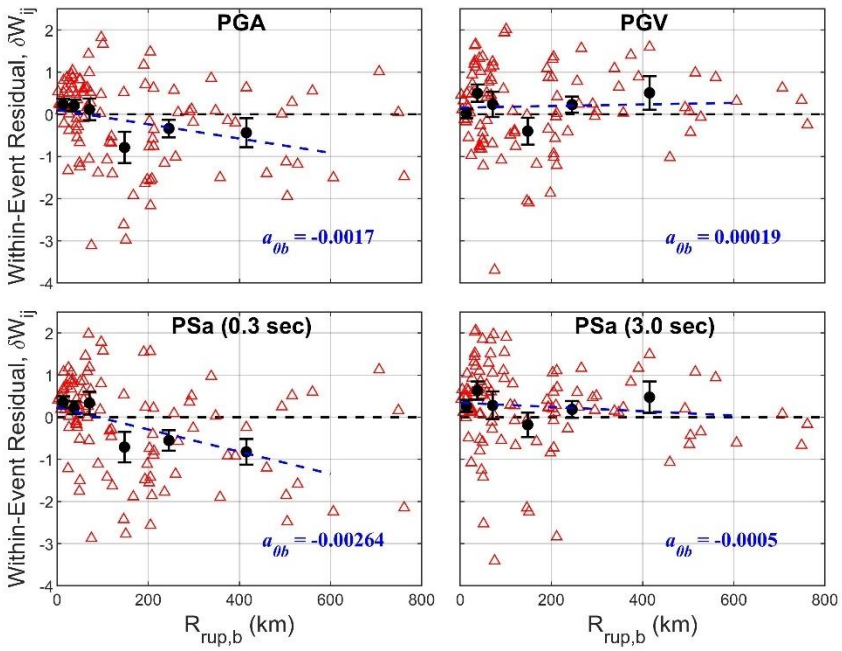

Figure 6.17. Fit of backarc model (Eq. 6.9) to within-event residuals for PGA, PGV, 0.3 sec Sa and 3.0 sec Sa from intraslab events.

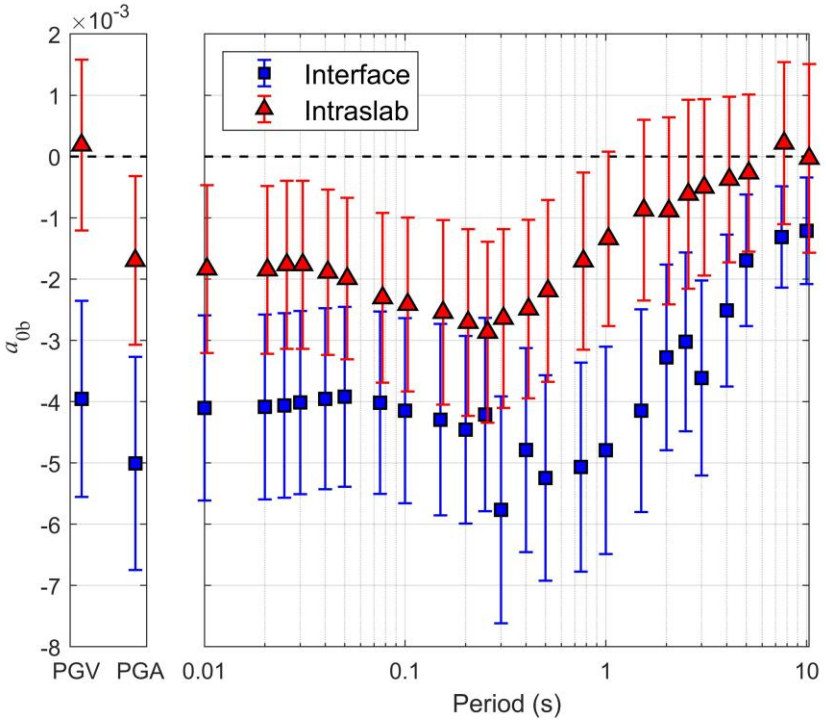

Figure 6.18. Backarc additional anelastic attenuation coefficient a_{0b} for interface and intraslab events. Range indicates ± one standard error of the mean estimate.

6.5 REGIONAL SITE RESPONSE FOR MEXICO

Site response calculations are performed using residuals analyses as described in Section 6.2.2. Because of backarc path effects, the Parker et al. (2022) GMM was revised to include additional anelastic attenuation (Eq. 6.10 with coefficients in Fig 6.17) for the residuals calculations using Eq. 6.1. Those residuals were used to calculate updated constant terms and event terms (Section 6.3.2). They were also used to calculate site terms η_S^v as given in Eq. 6.4 and site terms referenced to 760 m/s (η_S^r) as given in Eq. 6.5.

Because the global site response model of Parker and Stewart (2022) was recommended by Pea22 for application in Central America and Mexico (CAM), I evaluate the performance of the global model relative to the Mexico data. Data exclusive of Valley of Mexico (VM) sites are considered first (Section 6.5.1) and then VM site responses are evaluated using a non-reference site approach.

6.5.1 Site Response Exclusive of Valley of Mexico Sites

Model performance is evaluated from residuals analyses using site terms η_S^v. To compute these site terms, within-event residuals δW_{ij}^v (Eq. 6.3) are first computed using the revised Pea22 interface and intraslab models as described above. Because site response is independent of event type (Parker and Stewart 2022), δW_{ij}^v values from interface and intraslab events are combined, which increases the data quantity (i.e., number of recorded events) for most sites. For example, at sites in Oaxaca, there are 2 and 1 recordings from slab and interface events, respectively.

Using the combined data set exclusive of VM sites (i.e. 266 sites at the locations in Figure 5.39), Eq. 6.4 is used to partition δW_{ij}^{v} into site terms η_S^v and remaining residuals ε_{ij}. Constant term c_1 is also computed and is expected to be nearly zero because the mean of δW_{ij}^{v} is necessarily zero. Figure 6.19 shows the period-dependence of constant term c_1 – while the values are non-zero, their confidence intervals include zero and hence the constant can be considered to be practically null. Figure 6.20 shows the V_{S30}-dependence of site terms η_S^v for PGA, PGV, Sa(0.3 s), and Sa(3.0 s), with Puebla and Oaxaca sites highlighted. Binned means for the full data set have no appreciable trend with V_{S30}. As a result, our conclusion is that the global V_{S30}-scaling model of Parker and Stewart (2022) is suitable for modeling ergodic site response for sites outside of VM.

As described in Section 5.6.2, Puebla and Oaxaca have soft soil deposits where strong site response effects may be anticipated. These sites occupy V_{S30} ranges of 250-700 m/s, as derived from California proxy relationships. As shown in Figure 6.20, the soft sites in Puebla and Oaxaca (V_{S30} < 300 m/s) have site responses that depart substantially from the global ergodic model, including larger low-period amplification (PGA and Sa(0.3 s)) and smaller long-period amplification (Sa(3.0 s)). These patterns of amplification are expected for soft soil deposits of modest depth, although the depth conditions in these two cities are currently unknown.

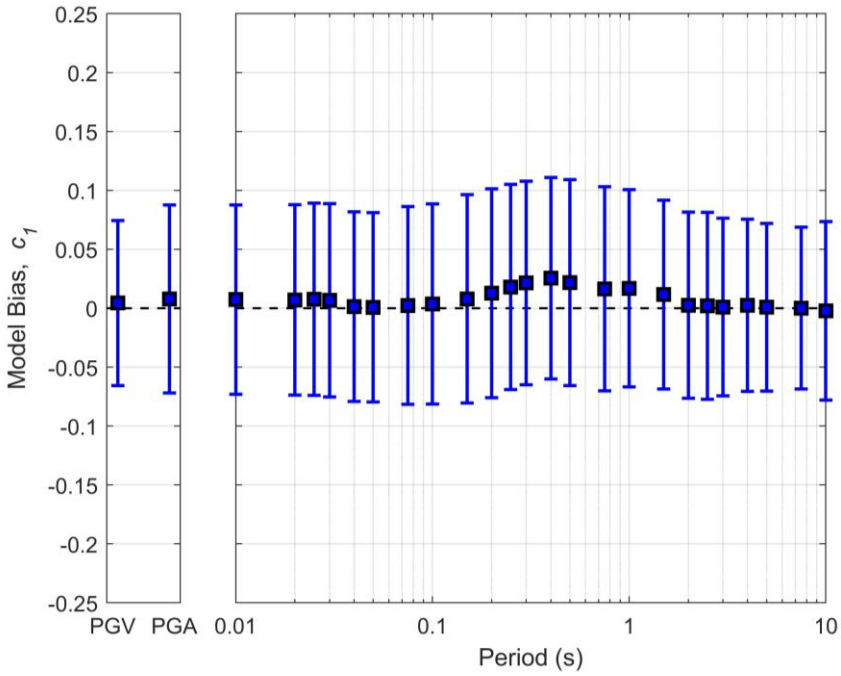

Figure 6.19. Site response model bias c_1 for peak acceleration, peak velocity, and Sa for a range of periods. Range indicates ± one standard error of the mean bias.

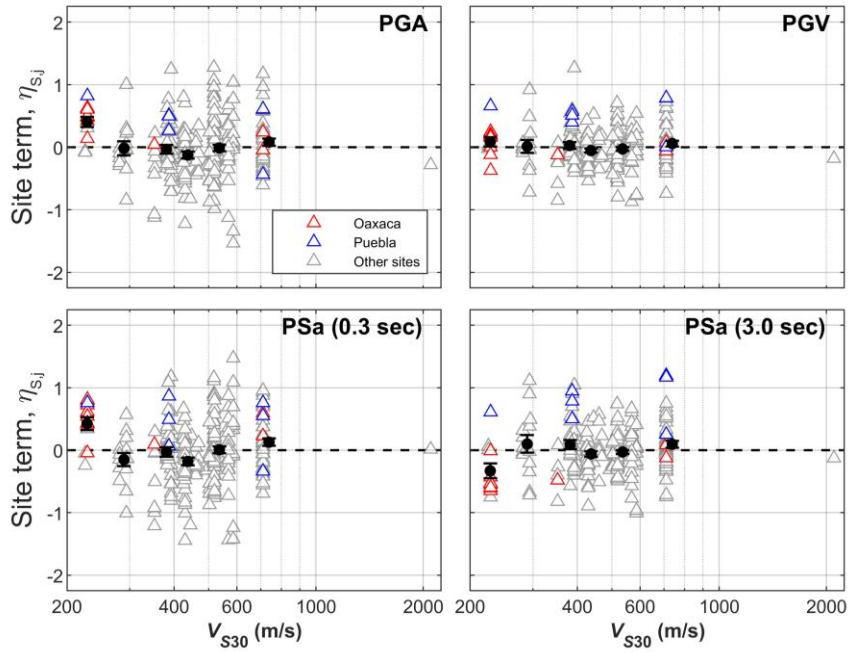

Figure 6.20. Trend of site terms for PGA, PGV, 0.3 sec Sa and 3.0 sec Sa with V_{S30} for Mexico sites exclusive of VM locations. Site terms for Puebla and Oaxaca are highlighted because there are concentrations of stations in these locations and portions of these regions have soft soils where strong site response might be anticipated.

6.5.2 Valley of Mexico Site Response

Site response in the VM is evaluated with a non-reference site approach using site terms referenced to a site condition of V_{S30} = 760 m/s, which are denoted η_S^r. The procedure used to calculate these site terms is similar to that used for sites outside of the VM. First, site terms are derived from within-event residuals as described in Section 6.5.1. In accordance with the results in Figure 6.19, the constant term c_1 in Eq. 6.4 is taken as zero, which forces all of the site response bias into the η_S^v term. This analysis includes the use of the Parker and Stewart (2022) ergodic model, which for many VM sites requires extrapolation of the model to low V_{S30} values below its operable range (< 150 m/s). However, the ergodic model prediction is then added (Eq. 6.5) to compute reference rock site term η_S^r. Accordingly, these site terms are independent of the ergodic model. The physical meaning of η_S^r is the mean difference between ground motions for a given site and what would be expected for the site if its site condition was V_{S30} = 760 m/s. Subsequently, η_S^r is referred to as the "site response."

In the calculations of both types of site terms (η_S^v and η_S^r) for VM sites, we "turn of" the nonlinear component of the Parker and Stewart (2022) model by setting $F_{nl} = 0$. The reasons for this are (1) to avoid the mixing of linear and nonlinear responses in the analysis of the site terms and (2) to allow the resulting model for VM site response to be linear in the first pass, with potential nonlinear effects judged subsequently from analysis of within-event variability trends against reference site shaking intensity. This nonlinear check is not completed in this thesis, but is identified in Chapter 7 as needed future work.

Typical characteristics of VM site response is illustrated with example results for six sites from different zones in the city, the locations of which are shown in Figure 6.21. The site responses for these six sites are shown in Figure 6.22. The Zone I site (CUP5) has appreciable amplification, ranging from 1.1 to 1.6, with the maximum amplification being essentially constant for T = 1.5-5 sec. The Zone II site (ES57) has higher amplification of PGA and for T > 0.3 sec, with a peaked response at 0.8 sec that is much stronger than for CUP5 (~ 2.2), which then decays sharply for T > 1 sec. The Zone III sites (IIIa, IB22; IIIb, SCT2; IIIc, XP06; IIId, AE02) also have larger amplification than CUP5 for PGA and T > 0.3 sec. At the longer periods, the site responses are peaked at amplitudes ranging from 3.0-3.7 (factors of 20 to 40) at periods of 1.5 sec for IIIa, 1.5-2 sec for IIIb, 2.5 sec for IIIc, and 4-5 sec for IIId. Interestingly, for periods of 0.04 to 0.25, the site responses for all six sites are nearly identical (the differences in site response occur for periods below and above that range). These patterns of site response between Zones and across periods are broadly consistent with the code-based spectra shown in Figure 5.48, although the present site responses are significantly larger due to the different reference site condition.

Results in Figure 6.22 for the CUP5 site are particularly notable, because it has been widely used as a reference site in prior studies of VM site response (e.g., Reinoso and Ordaz, 1999). The V_{S30} for this site is 295 m/s (Table 5.6, see ID#7), and the site response is appreciable. Reference sites used in other regions have generally corresponded to much stiffer geologic conditions (e.g., 750-1000 m/s; Borcherdt 1994, 2002). The implications of taking CU as a reference site are discussed further in Section 6.5.3.

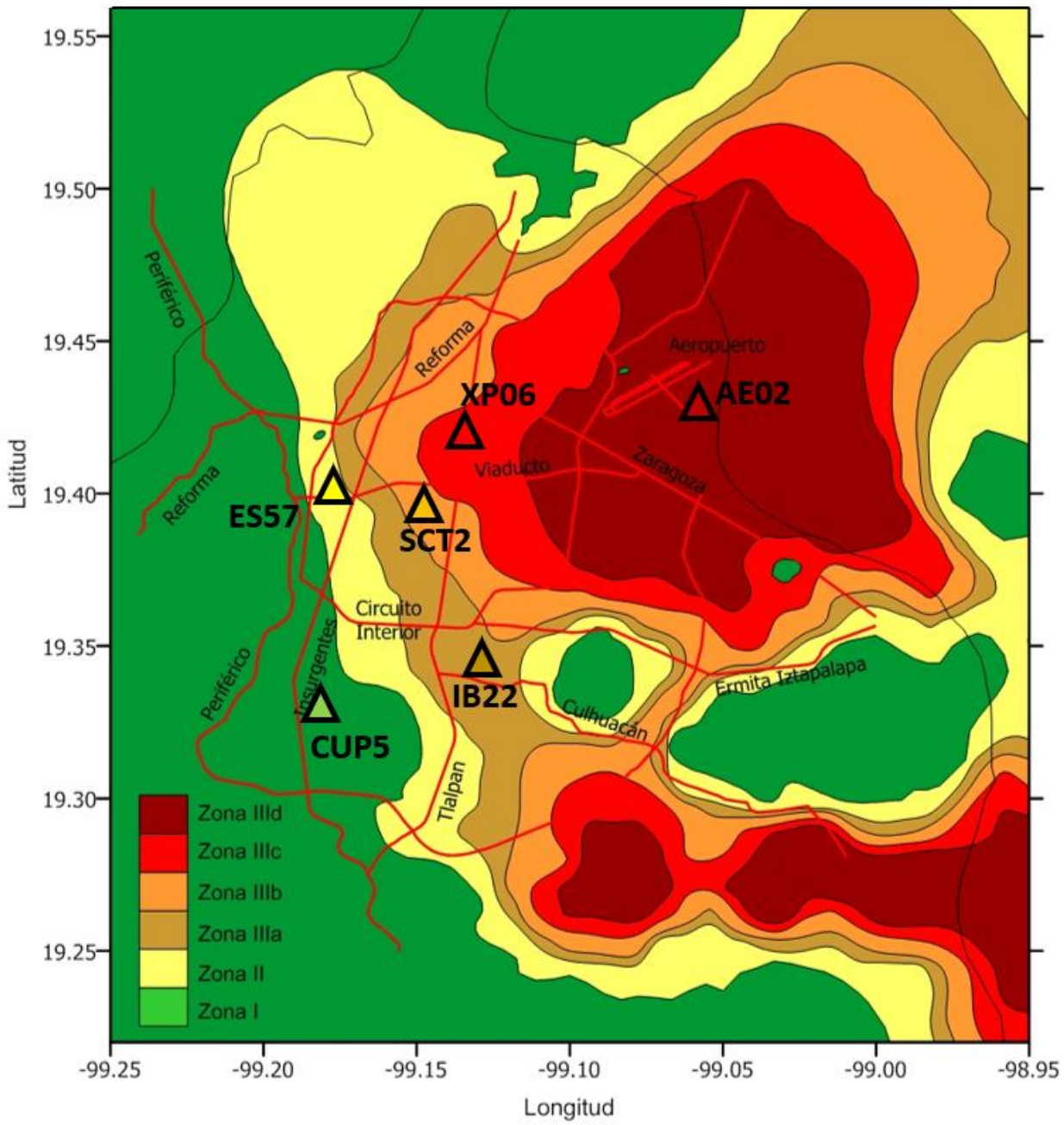

Figure 6.21. Locations of six example sites – CUP5 (Zone I), ES57 (Zone II), IB22 (Zone IIIa), SCT2 (Zone IIIb), XP06 (Zone IIIc), and AE02 (Zone IIId). Base map is from Figure 5.47.

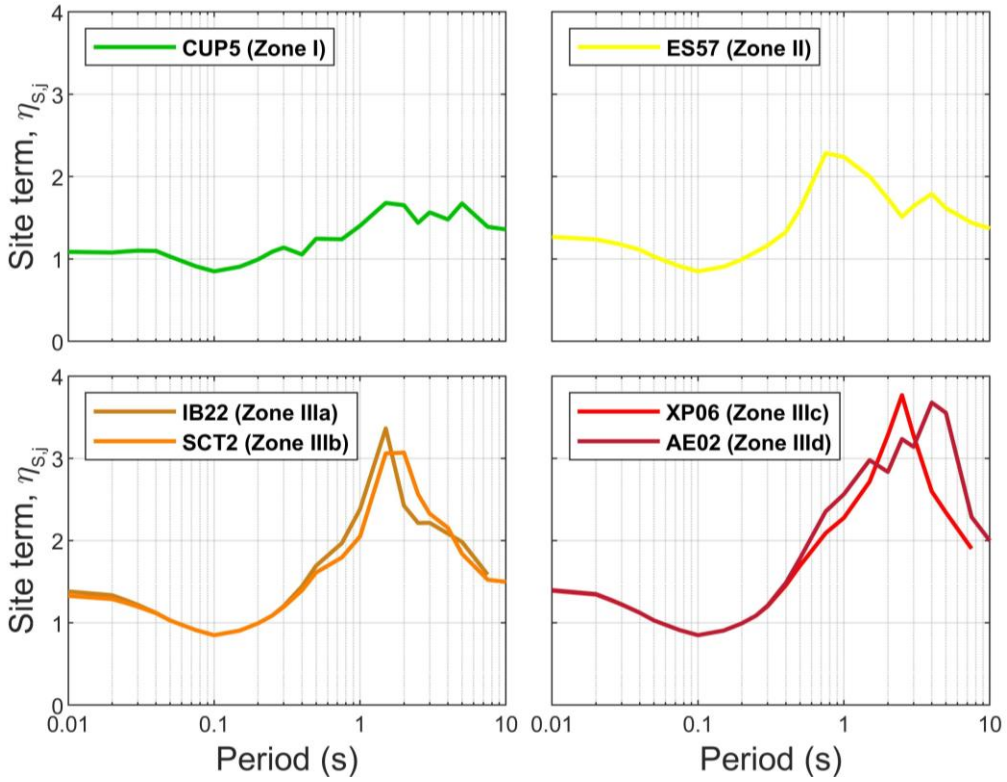

Figure 6.22. Period-dependent site response as derived from non-reference site approach for six sites in Mexico City (locations in Figure 6.21).

Figure 6.23a shows site response for all VM sites as a function of V_{S30} for the intensity measures of PGA, PGV, Sa(0.3 s), and Sa(3.0 s). At short periods (e.g., PGA), the site response increases as V_{S30} decreases from about 400 to 150 m/s. For softer sites, the site response does not scale with V_{S30}. This general pattern is retained up to a period of 2.0 s, but for longer periods the saturation at low V_{S30} gradually disappears, instead continuing to increase as V_{S30} decreases to its minimum values of 50 m/s. Figure 6.23b shows the same data with the Parker and Stewart (2022) ergodic model (the portion of the model below 150 m/s is an extrapolation beyond the recommended application range). The VM data for PGA and short periods have a much weaker trend with V_{S30} and stronger amplification that predicted by the global model. For PGV and long

periods, the trends with V_{S30} are similar to the global model, but amplification levels are higher, essentially being shifted up in amplification space relative to the model prediction.

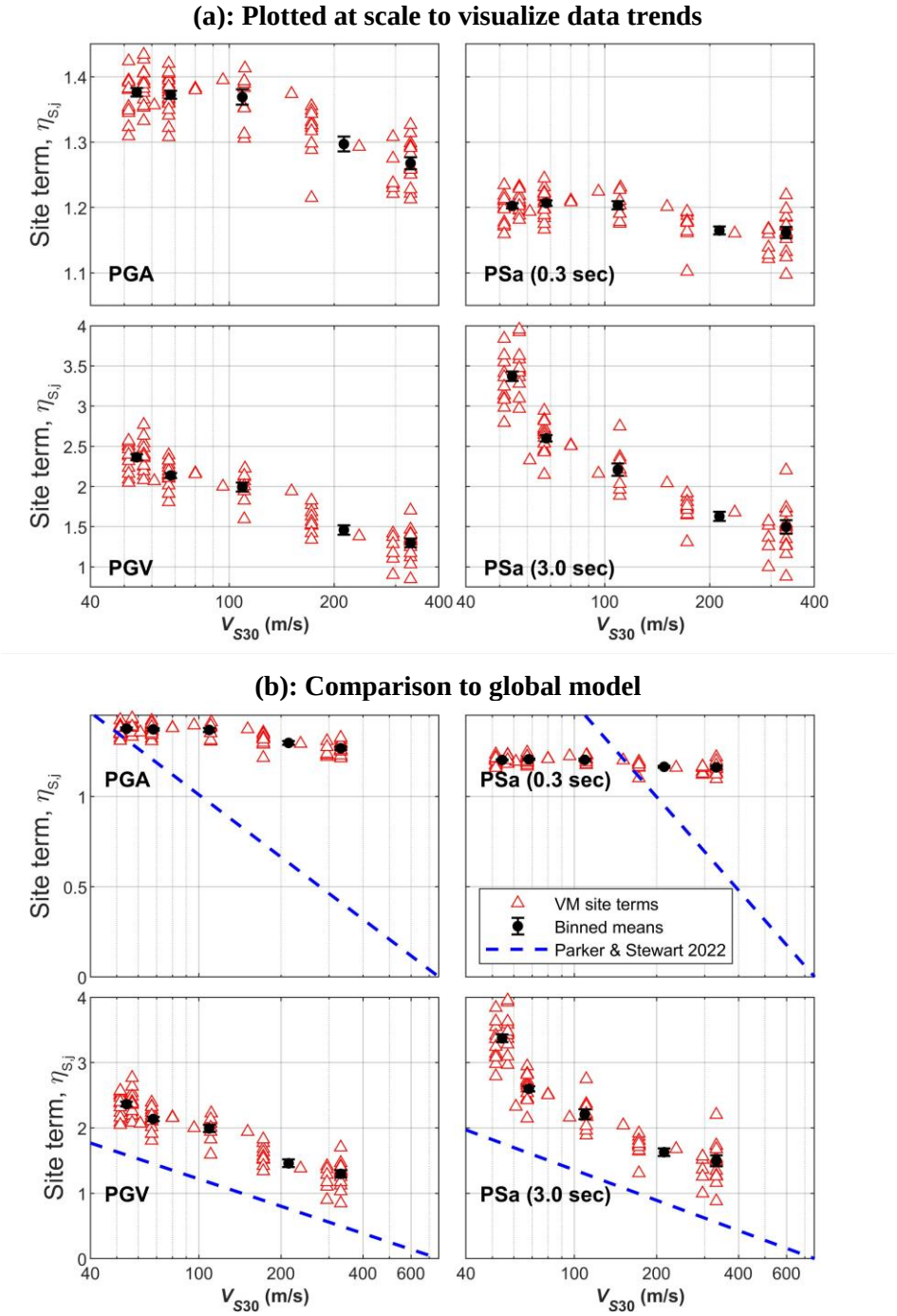

Figure 6.23. Variation of site amplification with V_{S30} for peak acceleration, peak velocity, Sa(0.3 s), and Sa(3.0 s): **(a)** Data plotted at a scale on y-axis that allows the trends with V_{S30} to be visualized, **(b)** Data plotted at scale that facilitates comparison with the global model of Parker and Stewart (2022).

The Parker and Stewart (2022) model does a reasonably good job of capturing the site response features at short periods, but for longer periods it significantly underpredicts site response for all sites (even the Zone I sites). To capture the regional response, the following model is proposed:

$$F_{lin}^{VM} = \begin{cases} s_1 ln\left(\frac{V_{S30}}{V_1}\right) + s_2 ln\left(\frac{V_1}{V_{ref}}\right) + f_{VM} & V_{S30} \leq V_1 \\ s_2 ln\left(\frac{V_{S30}}{V_{ref}}\right) + f_{VM} & V_1 < V_{S30} < V_{ref} \end{cases} \quad (6.11)$$

where the VM superscript indicates it is a Valley of Mexico model, V_{ref} = 760 m/s, V_1 is a break velocity (model parameter), s_1 is the V_{S30}-scaling for $V_{S30} < V_1$, and s_2 is the V_{S30}-scaling for $V_{S30} > V_1$. This model is similar to that used by Parker and Stewart (2022), with the following changes: (1) site response is only modelled for $V_{S30} < V_{ref}$ (higher velocities are not applicable in VM); and (2) an amplification shift parameter f_{VM} is introduced that allows for higher site response across all V_{S30}, which is needed across the full period range. Figure 6.24 shows the fit of the model in Eq. 6.11 to the data, with model coefficients indicated in the figure. The selected function is seen to fit the data well.

Figure 6.25 shows the period-variations of model coefficients. Slope parameters are null for the period range of 0.3-0.25 sec, but generally negative elsewhere. An exception is positive slopes s_1 for 0.5-2.0 sec, indicating a decrease of amplification as V_{S30} softens in this range. The strongest negative slopes are at long periods (>2.0 sec for s_1, > 0.7 sec for s_2), which are needed to model the large long-period amplification. Break velocity V_1 ranges from 150 m/s at short periods to 70 m/s for T > 2 s.

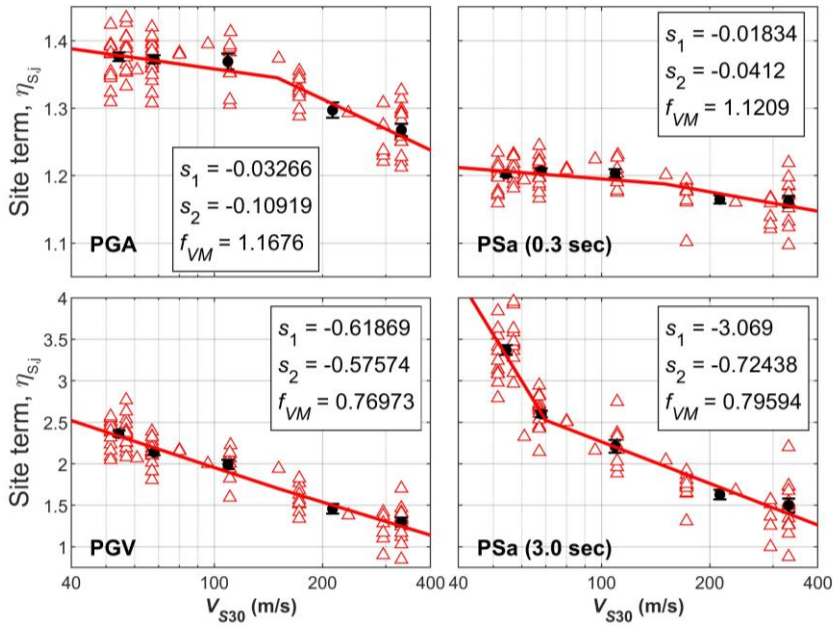

Figure 6.24. Fit of VM model to site amplification data for peak acceleration, peak velocity, Sa(0.3 s), and Sa(3.0 s). Model coefficients are marked in the figure.

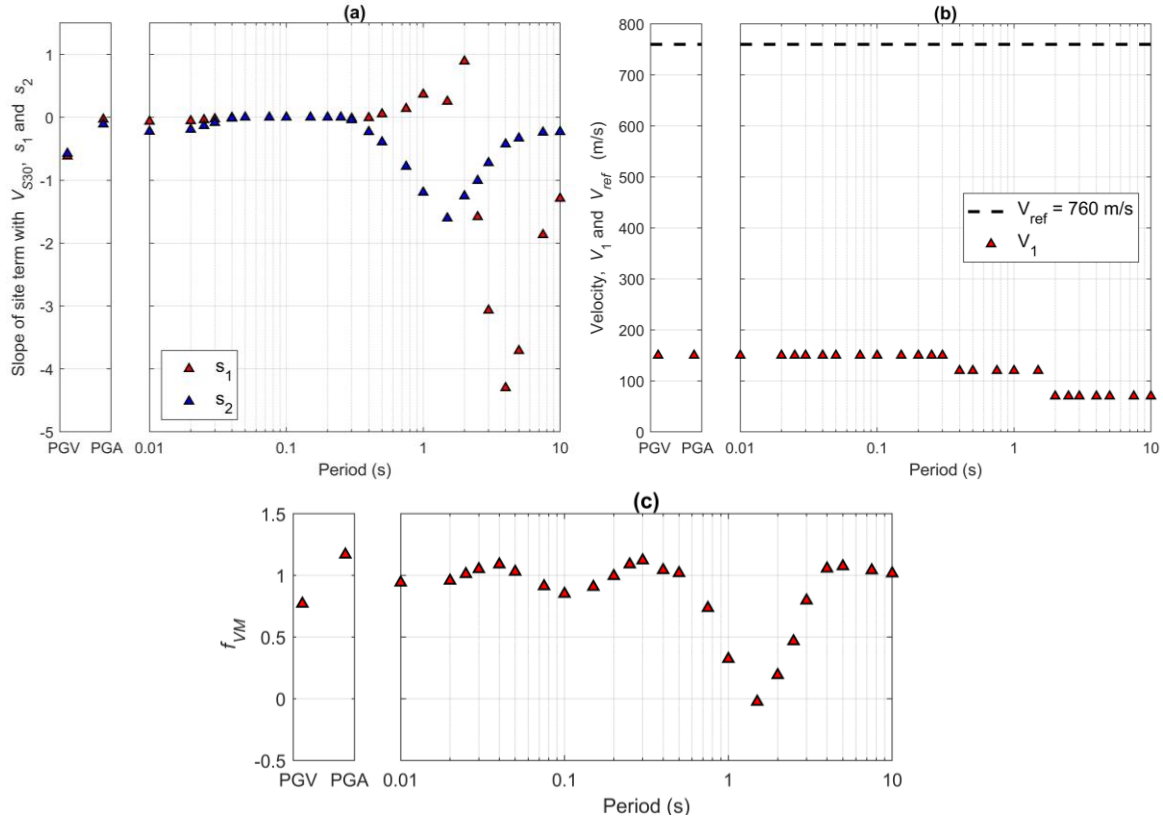

Figure 6.25. Period-dependence of coefficients for VM-specific site response model in Eq. 6.11: (a) V_{S30}-scaling gradients, (b) reference velocity V_{ref} and corner velocity V_1, and (c) amplification shift parameter f_{VM}.

6.5.3 Discussion

As described in Section 4.3.1 and 5.6.1, previous site response studies in Mexico have largely been limited to Mexico City (VM sites) and have utilized reference site approaches in which ground motions within the lakebed are normalized relative to those at the Zone 1 CU site. As shown in Figure 6.22, the CUP5 site has an appreciable level of site response across a broad period range – it only appears to be small in the present context because of the highly unusual (from a global perspective) and substantial site response elsewhere in the lakebed. These are not ideal conditions for a reference site.

In consideration of the body of prior site response work in Mexico, the present findings are original and significant in several respects:

1. By looking broadly across Mexico, we see that on average its site response matches global models. This is useful because it provides a basis for site response estimation across the region, but with "carve outs" for special areas like the VM where region-specific models should be used.
2. The soft sediments in Oaxaca and Puebla produce different site responses than those provided by the global model. Our ability to study these site response features in detail is limited by a lack of velocity profile data. However, empirical site responses clearly indicate strong amplification levels in the soft sediments, particularly at short periods.
3. In Mexico City, the results of the present work are broadly similar to previous findings with regard to relative amplification levels between zones and the period ranges where these amplifications are maximized. However, amplification levels are notably higher due

to the referencing of amplification to V_{ref} = 760 m/s in the present work and the use of data from multiple events in the derivation of site amplifications. The use of the non-reference site approach for the derivation of amplifications is particularly significant from a ground motion modeling perspective, because it removes the need to derive single-station reference GMMs for the CU site. Doing so increases dramatically the level of rigor with which the reference site GMM can be defined.

6.6 EPISTEMIC UNCERTAINTY

Parker et al. (2022) estimated the epistemic uncertainty in their GMM using the uncertainty in the constant terms. For regional models, these uncertainties scale with the inverse of the square root of the number of observations (recordings). Since the number of recordings has increased significantly from 103 in the Parker et al. (2022) model development (after data selection criteria were applied) to 821 from the present work, a reduction of epistemic uncertainty is expected.

Figure 6.26 shows the epistemic uncertainty in the Parker et al. (2022) constant terms (c_0) for Central America and Mexico. This epistemic uncertainty is denoted σ_ε and can be used with a scaled-backbone approach for modeling epistemic uncertainty in PSHA (Atkinson et al. 2014). The epistemic uncertainty of the Mexico model as derived in the present work is the standard error of the constant terms given in Figure 6.9, which has been lowered by approximately 30-50%. As such, this is an example of how investing in the improvement and the expansion of databases can reduce modeling uncertainty.

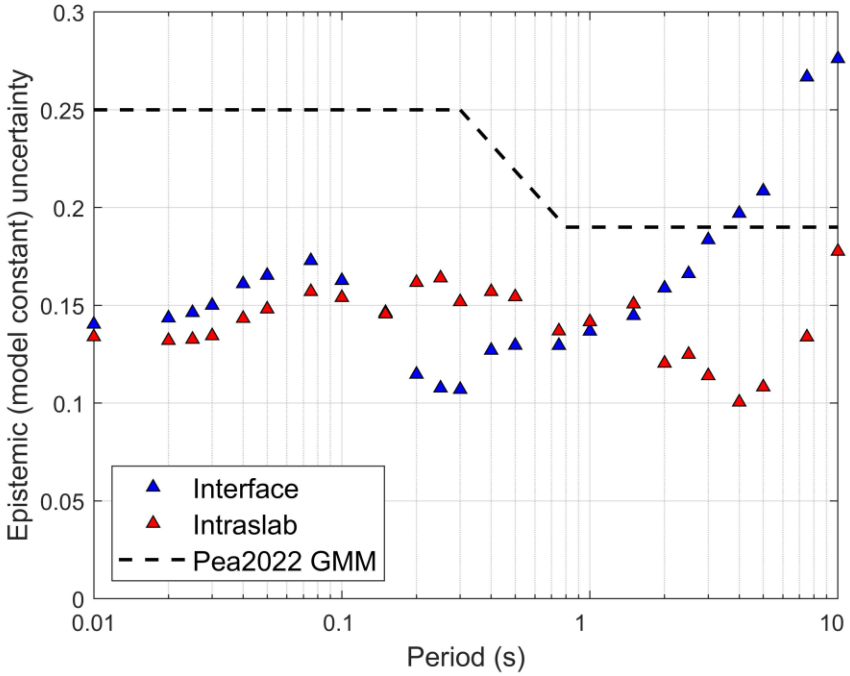

Figure 6.26. Epistemic uncertainty σ_ε for Central America and Mexico from Parker et al. (2022) as derived using NGA-Sub database and as found from the present analysis using the expanded database. The Parker et al. (2022) epistemic uncertainties are identical for intraslab and interface events.

7 SUMMARY AND CONCLUSIONS

7.1 SCOPE OF RESEARCH

The scope of the research presented in this dissertation has two principal elements. The first element occurred during the NGA-Sub project (Bozorgnia et al. 2022) and contributed to the development of the NGA-Sub database. I was part of a team of researchers at UCLA and elsewhere that developed the relational database structures (published as Mazzoni et al. 2022), metadata related to site conditions from locations globally that have recorded subduction earthquakes (Ahdi et al. 2022), and metadata related to the source and path components of the database. The portion of that broader effort that I had the largest role in was the source and path database components. My work on these topics is presented in Chapter 2-3 of this dissertation.

The relational database contains nine tables related to source parameters and two tables related to path parameters. Source parameters include earthquake information (event name, date, and time), moment-tensor parameters (hypocenter location, seismic moment, and the strike, dip, and rake angles of nodal planes), rupture surface geometry parameters (along-strike length, down-dip width, and depth to top-of-rupture for one or more rectangles), categorizations of event type (e.g., interface, intraslab), and sequence classification [mainshock (Class 1), aftershock (Class 2)]. Path parameters include rupture distance, partitioning of distance into forearc and backarc components, and various other distance metrics that are available in the database but have not been used directly in the current GMMs. The source and path tables were used to generate the NGA-Sub flatfile (Mazzoni et al. 2021). These data resources should also be useful for future regional ground motion studies and as a template for future ground motion database work.

The second element of this research was a detailed examination of ground motions from subduction earthquakes in Mexico. I reviewed an extensive body of literature on prior ground motion databases and ground motion models used in Mexico (Chapter 4). I have summarized in Section 5.6.1 how those models are used in practice for the design of structures in Mexico City. As described in Chapter 5, I significantly extended the amount of information for Mexico in the database relative to what was used in NGA-Sub. The added information was from a **M**8.3 instraslab event in 2017, a **M**7.1 intraslab event in 2017, a **M**7.2 interface event in 2018, and many **M** < 6 events that had been considered in NGA-Sub but lacked adequate metadata to be used in model development. Metadata was added for each of these events and ground motions were processed for the three large events in 2017-18 following NGA protocols. The three events produced 585 usable recordings.

The expanded database for Mexico was then used to evaluate regional features of ground motion models (GMMs) for Mexico, which is presented in Chapter 6. Among the factors considered in these analyses were overall ground motion levels (represented by the GMM constant term), magnitude-scaling, source depth-scaling, path effects in forearc and backarc regions, site response generally across Mexico, and site response in the Valley of Mexico (Texcoco Lake).

7.2 RESEARCH FINDINGS AND SIGNIFICANCE

The source and path database that was developed for NGA-Sub contains 991 earthquakes between 1937 and 2016 that meet quality assurance standards and have assigned event types (mostly interface or intraslab). Data curation emphasized large magnitudes: 73% of events have **M** > 5 and 13 events have **M** > 8. Improvements relative to prior NGA projects include: (1) more complete documentation of earthquake catalogs for moment tensors; (2) development of consistent criteria

for selecting and trimming finite-fault models from literature; (3) updates to, and more complete documentation of, simulation procedures used to estimate rupture surface geometry when models from literature are unavailable; and (4) formalized quality assurance procedures. New database elements specific to subduction earthquakes include event-type classification, forearc and backarc assignments to hypocenters and sites, and subduction-specific rupture dimension models.

The procedures for event-type assignments developed in NGA-Sub have practical significance, because separate GMMs are provided for interface and intraslab events. Although a review of seismic source characterization models used in global subduction regions was beyond the scope of the NGA-Sub project, it would be appropriate for such models to define event types in a similar manner to that used here for compatibility with the GMMs.

Analysis of the ground motion data from Mexico produces several important findings, most of which are related to the degree to which the data now available for Mexico supports or requires modifications to NGA-Sub models. I found that the constant terms for an NGA-Sub GMM (Parker et al. 2022) did not require adjustment and that the scaling of the models with source parameters (magnitude and source depth) is sufficient. However, it is notable that the 2017 **M** 8.3 intraslab event from Mexico is now the largest slab event in the global database, and the event term for this event is positive. While this apparent bias could be removed with the use of steeper magnitude-scaling at large magnitudes, we are not yet confident in making such a recommendation based principally on results from one event.

I found that the forearc distance-scaling in the Parker et al. (2022) model for this region is unbiased with respect to the new data. However, faster attenuation occurs in the backarc for both instraslab and interface events. I proposed a modification to the path model to account for these

effects (Eq. 6.10) and regressed the coefficients (Fig 6.18). The faster backarc attenuation is significant at short periods (< 2 sec) and is more pronounced for interface than for intraslab events. A number of significant findings were obtained from the site response analyses, which have been summarized and commented on in Section 6.5.3. The database expansion and model refinements for Mexico have significantly reduced epistemic uncertainties for ground motion modeling in this region (Section 6.6).

7.3 RECOMMENDATIONS FOR FUTURE RESEARCH

When the NGA-Sub project was underway, it was necessary to apply a cutoff date for data collection and metadata development, which was 2016. Future work will likely extend and improve the source and path tables by (1) adding information for major events in Alaska, South America since 2016; (2) adding event types for the 889 events for which such classifications were not made in NGA-Sub; and (3) considering finite fault uncertainties, whether from published models or simulations, which would produce distance uncertainties that are currently not provided. One of the major future work items identified in the NGA-Sub project was data synthesis and analysis of the recent Mexico events, which was completed in the second part of this work.

An interesting topic of future research, whether for subduction zones or other tectonic domains, is the impact of finite fault model uncertainties on the uncertainty of ground motion predictions, particularly for near-fault ground motions. Such work would demonstrate the value of rigorous standards for finite fault definition, as investigated and developed in this study (Section 2.4).

Chile is a region that would be an excellent candidate for a detailed study similar to what was completed here for Mexico. Like Mexico, there is a substantial amount of data from **M** < 6

events that was not considered in the NGA-Sub project. Moreover, there have been important large-magnitude events that could be considered in such a study, including the 2016 **M**7.6 Melinka earthquake (located in the area of the **M**9.5 Valdivia earthquake).

The study of Mexico ground motions produced important results, but a number of details should be attended to before papers are submitted for review in journals, including:

1. Some V_{S30} assignments for sites outside of Mexico City are inconsistent in the database for events < 2016 and ≥ 2016 which should be reconciled.
2. Smoothing of model coefficients is needed and spectral shapes should be checked for reasonableness and consistency.
3. Comparisons of the site response model for VM sites from the present work and from prior work should be made. As discussed in Section 6.5.3, the current model provides higher levels of amplification.
4. Comparisons of the reference rock model from Parker et al. (2022) with previously models for Mexico.
5. Investigation of potential refinement of the V_{S30}-based VM site response model based on site period information.
6. Investigation of potential nonlinearity in the VM site responses.
7. Aleatory variability of ground motions in Mexico should be quantified (between-event, within-event, site-to-site, single-station).
8. A second NGA-Sub GMM should be used in residuals analyses to check the period-dependence and magnitude of constant terms, the magnitude-dependence of event terms,

and the distance dependence of within-event residuals. We plan to use Kuehn et al. (2020) for this work.

Longer-term future work could examine, among other topics, the spatial correlation of site responses in Mexico City and local site responses in Puebla and Oaxaca (once site data becomes available). Models for nonlinear site response based on simulations are also needed.

REFERENCES

Abe K. (1975). Static and dynamic fault parameters of the Saitama earthquake of July 1, 1968, *Tectonophysics*, 27, 223-238.

Abrahamson, NA, Gulerce, Z (2020) Regionalized ground-motion models for subduction earthquakes based on the NGA-SUB database. PEER report no. 2020/25. Berkeley, CA: Pacific Earthquake Engineering Research Center (PEER), December 2020, University of California, Berkeley.

Abrahamson N.A., Gregor N., Addo K. (2016). BC Hydro Ground motion prediction equations for subduction earthquakes. *Earthquake Spectra*, 32(1), 23-44.

Adriano, B., Fujii, Y., Koshimura, S., Mas, E., Ruiz-Angulo, A., & Estrada, M. (2018). Tsunami source inversion using tide gauge and DART tsunami waveforms of the 2017 M_w 8. 2 Mexico earthquake. *Pure and Applied Geophysics, 175*, 33–48.

Ahdi, SK, Kwak, DY, Ancheta, TD, Contreras, V, Kishida, T, Kwok, AOL, Mazzoni, S, Ruz, F, Stewart, JP (2022). Site parameters applied in NGA-Sub database. *Earthquake Spectra*, 38(1): 494–520.

Aki K. and Richards P.G. (1980). Quantitative Seismology, 2nd Edition, W.H. Freeman, San Francisco, CA.

Alcocer J., Williams WD (1996). Historical and recent changes in Lake Texcoco, a saline lake in Mexico, *Int. Journal of Salt Lake Research*, 5:45-61.

Alfaro CS, Kiremidjian AS, White RA (1990). Seismic zoning and ground motion parameters for El Salvador, Report No. 93, The John Blume Earthquake Engineering Center, Stanford University

Algermissen ST, Hansen SL, Thenhaus PC (1988). Seismic hazard evaluation for El Salvador, Report for the US Agency for International Development, 21 pg.

Alvizuri, C., Silwal, V., Krischer, L., Tape, C. (2018). Estimation of full moment tensors, including uncertainties, for nuclear explosions, volcanic events, and earthquakes. *Journal of Geophysical Research: Solid Earth*, 123, 5099–5119.

Ammon C. J., Kanamori H., and Lay T. (2008). A great earthquake doublet and seismic stress transfer cycle in the central Kuril islands, *Nature*, 451(31), 561-565.

Ancheta T.D., Darragh R.B., Stewart J.P., Seyhan E., Silva W.J., Chiou B.S.J., Woodell K.E., Graves R.W., Kottke A.R., Boore D.M., Kishida T., and Donahue J.L. (2013). PEER NGA-West 2 database, *PEER Report 2013/03*, Pacific Earthquake Engineering Research Center, Berkeley, CA.

Anderson JG (1997) Nonparametric description of peak acceleration above a subduction thrust. *Seism Res Lett* 68(1):86–93

Anderson JG, Lei Y (1994) Nonparametric description of peak acceleration as a function of magnitude, distance, and site in Guerrero, Mexico. *Bull Seism Soc Am* 84(4):1003–1017

Anderson JG, Quaas R (1988) The Mexico earthquake of September 19, 1985—effect of magnitude on the character of strong ground motion: an example from the Guerrero,Mexico, strong motion network. *Earthq Spectra* 4(3):635–646

Anderson J. G., Kawase H., Biasi G. P., Brune J. N., and Aoi S. (2013). Ground Motions in the Fukushima Hamadori, Japan, Normal-Faulting Earthquake, *Bull. Seismol. Soc. Am.*, 103(3), 1935-1951.

Arango MC, F. Strasser, J. Bommer, D. Hernández, J. Cepeda. (2011a). A strong-motion database from the Central American subduction zone. *Journal of Seismology* 15:261–294

Arango M. C., Strasser F. O., Bommer J. J., Boroscheck R., Comte D., and Tavera H. (2011b). A strong-motion database from the Peru-Chile subduction zone, *Journal of Seismology*, 15, 19–41.

Arce JL, Layer PW, Macías JL, Morales-Casique E, García-Palomo A, Jiménez-Domínguez FJ, Benowitz J, Vásquez-Serrano A (2019). Geology and stratigraphy of the Mexico Basin (Mexico City), central Trans-Mexican Volcanic Belt, *Journal of Maps*, 15:2, 320-332.

Arroyo, D. García, D. Ordaz, M. Mora M.A., Krishna Singh S. (2010). Strong ground-motion relations for Mexican interplate earthquakes, *J. Seismol*, 14: 769-785.

Arteta CA, Pajaro CA, Mercado V, Montejo J, Arcila M, Abrahamson NA. Ground-motion model for subduction earthquakes in northern South America. *Earthquake Spectra*. 2021;37(4):2419-2452.

Atkinson, G. M. and Boore D. M. (2003). Empirical ground-motion relations for subduction-zone earthquakes and their application to Cascadia and other regions, *Bull. Seismol. Soc. Am*. 93, 1703-1729.

Atkinson G. M. and Macias M. (2009). Predicted Ground Motions for Great Interface Earthquakes in the Cascadia Subduction Zone, *Bull. Seismol. Soc. Am.*, 99(3), 1552–1578.

Atkinson G.M., Bommer J.J. and Abrahamson N.A. (2014), Alternative approaches to modeling epistemic uncertainty in ground motions in probabilistic seismic-hazard analysis. *Seismological Research Letters* 85: 1141–1144.

Atkinson G.M., Yenier E., Sharma N., Convertito V. (2016). Constraints on the near-distance saturation of ground-motion amplitudes for small-to-moderate induced earthquakes, *Bull. Seismol. Soc. Am.*, 106: 2104–2111.

Atzori S., Antonioli A., Tolomei C., De Novellis V., De Luca C., & Monterroso F. (2019). InSAR full-resolution analysis of the 2017–2018 M> 6 earthquakes in Mexico. *Remote Sensing of Environment*, *234*, 111461.

Bai L., Luna L.M., Hetland E.A., Ritsema J. (2014). Focal depths and mechanisms of Tohoku-Oki aftershocks from teleseismic P wave modeling, *Earthquake Science*, 27, 1–13.

Bastías N. and Montalva G. A. (2016). Chile strong ground motion flatfile, *Earthquake Spectra*, 32(4), 2549–2566.

Beyreuther M., Barsch R., Krischer L., Megies T., Behr Y., & Wassermann J. (2010). ObsPy: A Python toolbox for seismology. *Seismological Research Letters*, *81*(3), 530-533.

Bilek, S.L., and Lay, T. (2018). Subduction zone megathrust earthquakes: Geosphere, v. 14, no. 4, p. 1468–1500, *https://doi.org/10.1130/GES01608.1*.

Bird, P. (2003). An updated digital model of plate boundaries, *Geochemistry, Geophysics, Geosystems*, 4(3), 1-52.

Bommer J., Hernandez D., Navarrete J.A., Salazar, W. (1996). Seismic hazard assessments for El Salvador. *Geofisica Internacional*. 35. 227-244.

Bonilla, L. F., J. H. Steidl, G. T. Lindley, A. G. Tumarkin, and R. J. Archuleta (1997). Site amplification in the San Fernando Valley, California: Variability of site-effect estimation using the S-wave, coda, and H/V methods, *Bull. Seismol. Soc. Am.* **87**, 710–730.

Bonilla, L.F., J. H. Steidl, J.-C. Gariel, and R.J. Archuleta (2002). Borehole response studies at the Garner Valley downhole array, Southern California, *Bull. Seismol. Soc. Am.* **92**, 3165–3179.

Boore DM (2003). Simulation of ground motion using the stochastic method, *Pure and Applied Geophysics*, **160**, 635-675.

Boore D.M. (2010). Orientation-independent, non geometric-mean measures of seismic intensity from two horizontal components of motion, *Bull. Seismol. Soc. Am.* **100**, 1830–1835.

Boore DM and JJ Bommer, 2005. Processing of strong-motion accelerograms: needs, options and consequences, *Soil Dyn. Eqk. Eng.*, **25**, 93-115.

Borcherdt, 1994. Estimates of site-dependent response spectra for design (methodology and justification). *Earthquake Spectra*, **10**, 617-653.

Boroschek R., Giuliano A., Garcia H., Schmidt V., Climent A., Singaucho JC, Viracucha C, Torres R., Alcantara L., Talavera E., Tavera H., Lazares F., Rendón H., Rocabado V., Schmitz M. (2017). Site Characterization for Strong Motion Stations in Latin American Countries, *16th World Conf. Eqk. Eng*., Santiago Chile,

Bozorgnia Y., Abrahamson N. A., Al Atik L., Ancheta T. D., Atkinson G. M., Baker J. W., Baltay A., Boore D. M., Campbell K. W., Chiou B. S.-J., Darragh R., Day S., Donahue J., Graves R. W., Gregor N., Hanks T., Idriss I. M., Kamai R., Kishida T., Kottke A., Mahin S. A., Rezaeian S., Rowshandel B., Seyhan E., Shahi S., Shantz T., Silva W., Spudich P., Stewart J. P., Watson-Lamprey J., Wooddell K., and Youngs R. (2014). NGA-West2 Research Project, *Earthquake Spectra*, 30(3), 973-987.

Bozorgnia Y, Abrahamson NA, Ahdi SK, Ancheta TD, Al Atik L, Archuleta RJ, Atkinson GM, Boore DM, Campbell KW, Chiou BSJ, Contreras V, Darragh RB, Derakhshan S, Donahue JL, Gregor N, Gulerce Z, Idriss IM, Ji C, Kishida T, Kottke AR, Kuehn N, Kwak DY, Kwok AOL, Lin P, Mazzoni S, Midorikawa S, Muin S, Parker GA, Rezaeian S, Si H, Silva WJ, Stewart JP, Walling M, Wooddell K, Youngs RR (2022). NGA-Subduction research program, *Earthquake Spectra*, 38(2): 783–798.

Brune J. N. (1970). Tectonic stress and the spectra of seismic shear waves from earthquakes, *J. Geophys. Res.* **75**, 4997–5009.

Cadet, H., P.-Y. Bard, A.-M. Duval, and E. Bertrand (2012). Site effect assessment using KiK-net data: Part 2—Site amplification prediction equation based on f0 and Vsz, *Bull. Earthq. Eng*. **10**, 451–489.

Campbell K.W. (2020). Proposed methodology for estimating the magnitude at which subduction megathrust ground motions and source dimensions exhibit a break in magnitude scaling: Example for 79 global subduction zones, *Earthq. Spectra*, 36: 1271-1297.

Castillo L. F., Dimaté C., Drouet S., Fernandez G. A., Montalva G., Bastias N., Morales C., Pirchiner M., Singaucho J. C., and Weatherill G. (2016). A South American Strong Motion Database and Selection of ground motion prediction equations (GMPEs) for seismic hazard analysis in South America,

Research topic 6 (RT6), wiki of the SARA project (GEM), available at *https://sara.openquake.org/hazard_rt6* (last accessed May 2017).

Castro, R., Singh, S.K. & Mena, E., 1988. An empirical model to predict Fourier amplitude spcctra of horizontal ground motion, *Earthq. Spectra*, 4, 675-686.

Cepeda, J.M., Benito M.B., Burgos E.A. (2004). Strong-motion characteristics of January and February 2001 earthquakes in El Salvador, Geological Society of America, Special Paper 375.

Chao S.-H., B. Chiou, C.-C. Hsu, and P.-S. Lin (2020). A horizontal ground-motion model for crustal and subduction earthquakes in Taiwan. *Earthquake Spectra*, 36(2):463-506.

Chemenda A.I., Yang R.K., Hsieh C.-H., Groholsky A.L. (1997). Evolutionary model for the Taiwan collision based on physical modeling, *Tectonophysics*, 274, 253-274.

Climent A.W., Taylor M., Ciudad Real M., Strauch W., Villagram M., Dahle A., Bungum H., (1994). Spectral strong-motion attenuation in Central America, NORSAR Technical Report No. 2-17, 46 pg.

Chamorro C (2016). Medición de los valores de velocidad de onda cortante (Vs) en suelos provenientes del ex lago Texcoco. M.S. Thesis, Institute of Engineering, National Autonomous University of Mexico (UNAM), Mexico (In Spanish).

Chen K., Feng W., Liu Z., and Song Y.T. (2018). 2017 M w 8.1 Tehuantepec Earthquake: Deep Slip and Rupture Directivity Enhance Ground Shaking but Weaken the Tsunami, *Seismological Research Letters*, 89:1314-1322.

Chiou B. S.-J. and Youngs R. R. (2008). NGA Model for Average Horizontal Component of Peak Ground Motion and Response Spectra, *PEER report 2008/09*, Pacific Earthquake Engineering Research Center, Berkeley, CA.

Contreras, V. (2009). *Curvas de atenuación para sismos chilenos*, Thesis, Department of Civil Engineering, University of Chile, Santiago, Chile. (In Spanish).

Contreras V. and Boroschek R. (2012). Strong ground motion attenuation relations for Chilean subduction zone interface earthquakes, *Proceedings of the 15th World Conference on Earthquake Engineering 15WCEE*, Lisboa, Portugal.

Contreras V. and Boroschek R. (2015). Response spectral attenuation relations for Chilean earthquakes, *Proceedings XI Congreso Chileno de Sismologia e Ingenieria Sismica ACHISINA 2015*, March 18-20, Santiago, Chile. (In Spanish).

Contreras, V, F Ruz, SK Ahdi, JP Stewart (2018). Vs profile database and proxy based model for Vs30 prediction in Chile for NGA-subduction, *11th National Conf. on Earthquake Engineering,*, June 25-29, 2018, Los Angeles, CA, Paper 1473.

Contreras V., Stewart J.P., Kishida T., Darragh R.B., Chiou B.S.J., Mazzoni S., Kuehn N., Ahdi S.K., Wooddell K., Youngs R.R., Bozorgnia Y., Boroschek R., Rojas F., Órdenes J. (2020). Chapter 4: Source and Path Metadata, in Data Resources for NGA-Subduction Project, *PEER Report 2020/02*, J.P. Stewart (editor), Pacific Earthquake Engineering Research Center, UC Berkeley (headquarters).

Contreras, V, Stewart, JP, Kishida, T, Darragh, RB, Chiou, BSJ, Mazzoni, S, Youngs, RR, Kuehn, NM, Ahdi, SK, Wooddell, K, Boroschek, R, Rojas, F, Ordenes, J (2022). NGA-Sub source and path database. *Earthquake Spectra*, 38 (2): 799–840.

Convenio INEGI-SGM (1995, 2005). Carta Geológica de la República Mexicana escala 1:250,000

Cramer CH, Jambo E (2020). Impact of a Larger Fore-Arc Region on Earthquake Ground Motions in South-Central Alaska Including the 2018 M 7.1 Anchorage Inslab Earthquake. *Seismological Research Letters* 91 (1): 174–182.

Crouse C. B. (1991). Ground-motion attenuation equation for earthquake on Cascadia subduction-zone earthquake, *Earthquake Spectra*, 7, 210–236.

Crouse C. B, Yogesh K. V., and Schell B. A. (1988). Ground motions from subduction zone earthquakes, *Bull. Seismol. Soc. Am*., 78, 1–25.

Cruz-Atienza, V.M., Tago, J., Villafuerte, C. *et al.* (2021). Short-term interaction between silent and devastating earthquakes in Mexico. *Nat Commun* **12,** 2171

CSN (2020). Chilean National Seismological Center, strong motion database available at *http://evtdb.csn.uchile.cl/* (last accessed March 2020).

Dahle A., Climent A., Taylor W., Bungum H., Santos P., Ciudad Real M., Lindhom C., Strauch W., Segura F. (1995). New spectral strong motion attenuation models for Central America, *Proc. 5th Int. Conf. Seismic Zonati*on, Nice, France, Vol. II, 1005-1012.

De La Rosa J., Flores F., and Guasch J. (2013). Caracterización geo-sísmica de una zona del ex-lago Texcoco para el diseño de un túnel de desagüe. XIX National Conference on Earthquake Engineering, Boca del Río, Veracruz, Mexico (In Spanish).

Delouis B., Nocquet J.-M., and Vallée M. (2010). Slip distribution of the February 27, 2010 Mw = 8.8 Maule Earthquake, central Chile, from static and high-rate GPS, InSAR, and broadband teleseismic data, *Geophys. Res. Lett*., 37, L17305.

Dhakal Y. P., N. Takai, and T. Sasatani (2008). Path effects on prediction equations of pseudo-velocity response spectra in northern Japan. In Proceedings of Fourteenth World Conference on Earthquake Engineering, 2008. Paper no. 03-02-0023.

Díaz-Rodríguez JA (2003). Characterization and engineering properties of Mexico City lacustrine soils. Characterisation and Engineering Properties of Natural Soils – Tan et al. (eds.) © 2003 Swets & Zeitlinger, Lisse, ISBN 90 5809 537 1.

Douglas, J. (2021). Ground motion prediction equations 1964–2021, Department of Civil and Environmental Engineering, University of Strathclyde

Drouet S. Montalva G., Dimate C., Castillo L., Fernandez G.A., Morales C., Bastias N., Pirchiner M., Singaucho J., Weatherill G., (2017). Building a ground-motion logic tree for South America within the GEM-SARA project framework. 16th World Conference on Earthquake Engineering.

Duputel Z., Rivera L., Kanamori H., Hayes G. (2012). W phase source inversion for moderate to large earthquakes (1990–2010), *Geophy. J. Int*., 189 (2), 1125–1147, *https://doi.org/10.1111/j.1365-246X.2012.05419.x*.

EIC (2003). 2003/10/31 Fukushima-oki (Mj6.8) Inversion analysis by farfield waveforms (preliminary) *EIC Seismology Note No.141*, Nov. 02, 03, *http://wwweic.eri.u-tokyo.ac.jp/sanchu/Seismo_Note/EIC_News/031031.html*.

Ekström G., Nettles M., and Dziewonski A. M. (2012). The global CMT project 2004-2010: Centroid-moment tensors for 13,017 earthquakes, *Phys. Earth Planet. Inter*., 200-201, 1-9.

Engdahl, E.R., R. van der Hilst, and R. Buland (1998). Global teleseismic earthquake relocation with improved travel times and procedures for depth determination, *Bull. Seism. Soc. Am*. 88, 722-743.

ERI (2009). 2009/08/09 Tokaido South-oki Earthquake: inversion process, Earthquake Research Institute, University of Tokyo, *http://www.eri.u-tokyo.ac.jp/topics/200908_Tokaido/#SourceInversion*.

Ferrari F, Orozco-Esquivel T, Manea V, Manea M (2012). The dynamic history of the Trans-Mexican Volcanic Belt and the Mexico subduction zone, *Tectonophysics*, Vol. 522–523, 122-149

Field, E. H., K.H. Jacob (1993). The theoretical response of sedimentary layers to ambient seismic noise, *Geophys. Res. Lett.* **20**, 2925–2928.

Field, E. H., K.H. Jacob (1995). A comparison and test of various site response estimation techniques, including three that are not reference site dependent, *Bull. Seismol. Soc. Am*., **85**, 1127–1143.

Flores-Estrella H., Yussim S, Lomnitz C (2007). Seismic response of the Mexico City Basin: A review of twenty years of research, *Nat. Hazards*, 40:357-372.

Flores-Guzmán M., Ovando-Shelley E., and Valle-Molina C (2014). Small-strain dynamic characterization of clayey soil from the Texcoco Lake, Mexico. *Soil Dynamics and Earthquake Engineering*, 63:1-7.

Fukuyama E., Irikura K. (1986). Rupture process of the 1983 Japan sea (Akita-Oki) earthquake using a waveform inversion method, *Bull. Seism. Soc. Am*., 76, 1623-1640.

Fukuyama E. (1991). Inversion for the Rupture Details of the 1987 East Chiba Earthquake, Japan, Using a Fault Model Based on the Distribution of Relocated Aftershocks, *J. Geophy. Res.*, 96(B5), 8205-8217.

García, D (2006) Estimación de parámetros del movimiento fuerte del suelo para terremotos interplaca e intraslab en México central. PhD Thesis, Facultad de Ciencias Físicas, Universidad Complutense de Madrid, Madrid (in Spanish).

Garcia D, Singh SK, Herra´ iz M, et al. (2005) Intraslab earthquakes of Central Mexico: Peak groundmotion parameters and response spectra. *Bulletin of the Seismological Society of America* 95(6): 2272–2282.

García D, Singh SK, Herraiz M, Ordaz M, Pacheco JF, Cruz-Jiménez H (2009) Influence of subduction zone structure on coastal and inland attenuation in Mexico. *Geophys J Int* 179(1):215–230

García-Soto, AD, Jaimes, MA (2017) Ground-Motion Prediction Model for Vertical Response Spectra from Mexican Interplate Earthquakes. Bulletin of the Seismological Society of America 107(2): 887–900.

Gardner J., Knopoff L. (1974). Is the Sequence of Earthquakes in Southern California, with Aftershocks Removed, Poissonian?, *Bull. Seism. Soc. Am.*, 64 (5), 1363-1367.

Gelman A., Carlin J.B., Stern H.S., Dunson D.B., Vehtari A., Rubin D.B., 2014. *Bayesian Data Analysis*, 3rd edition, CRC Press.

Ghofrani H. and G. M. Atkinson (2011). Forearc versus Backarc Attenuation of Earthquake Ground Motion. *Bulletin of the Seismological Society of America*, 101 (6): 3032–3045.

Ghofrani H. and G. M. Atkinson. (2014). Ground-motion prediction equations for interface earthquake of M7 to M9 based on empirical data from Japan. *Bulletin of Earthquake Engineering*, 12(2):549-571.

Goda, K. and G. M. Atkinson (2009). Probabilistic characterization of spatially correlated response spectra for earthquakes in Japan. *Bulletin of the Seismological Society of America*, 99(5): 3003-3020

Goulet C. A., Kishida T., Ancheta T. D., Cramer C. H., Darragh R. B., Silva W. J., Hashash Y. M. A., Harmon J., Stewart J. P., Wooddell K. E., Youngs R. R. (2014). PEER NGA-East Database, Pacific *Earthquake Engineering Research Reports, No. 2014/17*.

Guo R., Zheng Y., Xu J., Jiang Z. (2019). Seismic and Aseismic Fault Slip Associated with the 2017 *M*w 8.2 Chiapas, Mexico, Earthquake Sequence. *Seismological Research Letters* 90 (3): 1111–1120.

Gusman A.R., Mulia I.E., and Satake K. (2018). Optimum sea surface displacement and fault slip distribution of the 2017 Tehuantepec earthquake (Mw 8.2) in Mexico estimated from tsunami waveforms, Geophysical Research Letters, https://doi.org/10.1002/2017GL076070.

Haendel, A., Specht, S., Kuehn, N.M. *et al.* Mixtures of ground-motion prediction equations as backbone models for a logic tree: an application to the subduction zone in Northern Chile. *Bull Earthquake Eng* **13,** 483–501 (2015).

Hanks T.C. and Kanamori H. (1977). A moment magnitude scale, *J. Geophy. Res*., 84(B5), 2348-2350.

Hatanaka Y., Takeo M. (1989). Detailed rupture process of the 1975 Central Oita, Japan, earthquake inferred from near-field data, *J. Phys. Earth*, 37, 251-264.

Hayes G. (2010). Updated Result of the Feb 27, 2010 Mw 8.8 Maule, Chile Earthquake, NEIC, available at *http://earthquake.usgs.gov/earthquakes/eqinthenews/2010/us2010tfan/finite_fault.php* (last accessed August 19, 2013).

Hayes (2016). Preliminary Finite Fault Results for the Apr 16, 2016 Mw 7.8 28 km SSE of Muisne, Ecuador Earthquake (Version 1), *http://earthquake.usgs.gov/earthquakes/eventpage/us20005j32#finite-fault.*

Hayes G. (2017). Preliminary Finite Fault Results for the Feb 27, 2010 Mw 8.9 -36.2200, -73.1740 Earthquake (Version 1), NEIC, available at *https://earthquake.usgs.gov/earthquakes/eventpage/official20100227063411530_30#finite-fault* (last accessed May 2017).

Hayes G. P., Wald D. J., and Johnson R. L. (2012). Slab1.0: A three-dimensional model of global subduction zone geometries, *J. Geophys. Res*., 117, no. B01302.

Hayes GP, Moore GL, Portner DE, Hearne M, Flamme H, Furtney M and Smoczyk GM (2018) Slab2, a comprehensive subduction zone geometry model. Science 362(6410): 58–61.

Heidarzadeh M., Ishibe, T. & Harada, T. (2018). Constraining the Source of the Mw 8.1 Chiapas, Mexico Earthquake of 8 September 2017 Using Teleseismic and Tsunami Observations. *Pure Appl. Geophys.* 175, 1925–1938

HERP (2006). Evaluation of seismic activity in November 2004, Headquarters for Earthquake Research Promotion, *http://www.static.jishin.go.jp/resource/monthly/2004/2004_11.pdf*, in Japanese.

HERP (2011). Source model of 2011/04/12 Chiba East-oki Earthquake(M6.4) (preliminary), Headquarters for Earthquake Research Promotion, *http://www.jishin.go.jp/main/chousa/11may/p26.htm*, in Japanese.

Hjörleifsdóttir, V., Singh S.K., Husker A. (2016). Differences in Epicentral Location of Mexican Earthquakes between Local and Global Catalogs: An update, *Geofís. Intl* 55(1)

Ho C.S. (1986). A synthesis of the geologic evolution of Taiwan, *Tectonophysics*, 125, 1-16.

Hong, H.P., Pozos-Estrada, A., and Gomez, R. 2009. Orientation effect on ground motion measure for Mexican subduction earthquakes. Earthquake Engineering and Engineering Vibration, 8(1): 1-16. doi:10.1007/s11803-009-8155-z.

Hu J., J. Tan, and J. X. Zhao (2020). New GMPEs for the Sagami Bay region in Japan for moderate magnitude events with emphasis on differences on site amplifications at the sea floor and land seismic stations of K-NET. *Bulletin of the Seismological Society of America*, 110(5):2577-2597.

Husid R. (1973). Earthquakes: spectral analysis and characteristics of accelerograms as a basis of earthquake-resistant design, *Editorial Andrés Bello* [c1973], Santiago, Chile, 447 p.

Ichinose G. A. Thio H. K., and Somerville P. G. (2004), Rupture process and near-source shaking of the 1965 Seattle-Tacoma and 2001 Nisqually, intraslab earthquakes, *Geophy. Res. Lett*., 31, L10604, *https://doi:10.1029/2004GL019668*.

Ichinose G. A. Thio H. K., and Somerville P. G. (2006a), Ground motion studies of modern and historical Cascadia intraslab earthquakes using one and three-dimensional waveform modeling methods to generate ground shaking maps, *USGS Technical Report Award Number 04HQGR0050,* United States Geological Survey, Washington, D.C.

Ichinose G. A., Thio H. K., and Somerville P. G. (2006b). Moment tensor and rupture model for the 1949 Olympia, Washington, earthquake and scaling relations for Cascadia and global intraslab earthquakes, *Bull. Seismol. Soc. Am*., 96(3), 1029-1037.

Ide S. and Takeo M. (1996). The dynamic rupture process of the 1993 Kushiro-oki earthquake, *J. Geophys. Res.*, 101(B3), 5661-5675.

Idini B., Rojas F., Ruiz S., and Pastén C. (2017). Ground motion prediction equations for the Chilean subduction zone, *Bull. Earthquake Eng.,* 15:1853–1880.

International Seismological Centre (2019), On-line Bulletin, *https://doi.org/10.31905/D808B830*. ISC, Thatcham, United Kingdom (last accessed Dec 2019).

INEGI (1985, 1994). Geologic map of Puebla and Tlaxcala. Puebla E14B43, Scale 1:50,000, Instituto Nacional de Estadística, Geografía e Informática, Mexico (In Spanish).

IRIS (2020). Peru-Chile Subduction Zone: Earthquakes & Tectonics, Incorporated Res. Institutions for Seism., animation available at *https://www.iris.edu/hq/inclass/animation/peruchile_subduction_zone_earthquakes__tectonics* (last accessed March 2020).

Iwahashi J., Pike R.J. (2007). Automated classifications of topography from DEMs by an unsupervised nested-means algorithm and a three part geometric signature, *Geomorphology 86*, nos. 3/4, 409–440.

Jaimes MA, Reinoso E (2006) Comparacio´ n de comportamiento de edificios en el valle de Mexico ante sismos de subduccio´ n y de falla normal. *Revista de Ingenierı´a Sı´smica*. DOI:10.18867/ris.75.59 (in Spanish).

Jaimes MA, Reinoso E, Ordaz M (2006) Comparison of methods to predict response spectra at instrumented sites given the magnitude and distance of an earthquake, *J. Earthquake Engineering*, 10(6), 887-902.

Jaimes MA, García-Soto AD. (2020). Updated ground motion prediction model for Mexican intermediate-depth intraslab earthquakes including V/H ratios. *Earthquake Spectra*. 36(3):1298-1330.

Jaimes MA, García-Soto AD. (2021). Ground-Motion Duration Prediction Model from Recorded Mexican Interplate and Intermediate-Depth Intraslab Earthquakes. *Bull. Seismol. Soc. Am*. 111:258-273.

Jaimes MA, Ramirez-Gayta´n A and Reinoso E (2015) Ground-motion prediction model from intermediate-depth intraslab earthquakes at the hill and lake-bed zones of Mexico City. *Journal of Earthquake Engineering* 19(8): 1260–1278.

Ji C. and Archuleta R.J. (2018). Scaling of PGA and PGV deduced from numerical simulations of intraslab earthquakes, Department of Earth Science, University of California, Santa Barbara, in press.

JMA (2005). The earthquake that occurred off Sanriku on November 15, 2005. *http://cais.gsi.go.jp/KAIHOU/report/kaihou75/03_15.pdf* .

JMA (2008). Earthquake Prediction Information Division, Earthquake and Tsunami Observation Division, JMA, The M7.1 Earthquake off Tokachi District on September 11, 2008, *http://cais.gsi.go.jp/KAIHOU/report/kaihou81/02_02.pdf*.

JMA (2011a). 2011/03/11 Ibaraki-oki Earthquake - Inversion analysis by nearfield waveforms (preliminary)

JMA (2011b). 2011/03/11 Iwate-oki Earthquake - Inversion analysis by nearfield waveforms (preliminary)

JMA (2011c). 2011/03/09 Sanriku-oki Earthquake - Inversion analysis by nearfield waveforms (preliminary)

JMA (2011d). 2011/04/07 Miyagi-oki Earthquake - Inversion analysis by farfield waveforms (preliminary)

JMA (2011e). 2011/07/10 Sanriku-oki Earthquake - Inversion analysis by farfield waveforms (preliminary)

JMA (2011f). 2011/06/23 Iwate-oki Earthquake - Inversion analysis by nearfield waveforms (preliminary)

JMA (2011g).2011/09/17 Iwate-oki Earthquake - Inversion analysis by farfield nearforms (preliminary)

JMA (2011h). 2011/07/31 Fukushima Earthquake - Inversion analysis by nearfield waveforms (preliminary)

JMA (2011i). 2011/07/23 Miyagi-oki Earthquake - Inversion analysis by nearfield waveforms (preliminary)

JMA (2011j). 2011/07/25 Fukushima-oki Earthquake - Inversion analysis by nearfield waveforms (preliminary)

JMA (2011k). 2011/08/19 Fukushima-oki Earthquake - Inversion analysis by nearfield nearforms (preliminary)

JMA (2011l). 2011/11/24 Urakawa-off earthquakes- inversion analysis by nearfield waveforms

JMA (2011m). 2011/03/15 East Shizuoka Earthquake - Inversion analysis by nearfield waveforms (preliminary)

JMA (2011n). 2011/08/01 Surugawan Earthquake - Inversion analysis by nearfield waveforms (preliminary)

JMA (2011o). 2011/04/12 Fukushima Nakadori Earthquake - Inversion analysis by nearfield waveforms (preliminary)

JMA (2011p). 2011/03/19 North Ibaraki Earthquake - Inversion analysis by nearfield waveforms (preliminary)

JMA (2012a). 2012/12/07 Miyagi-oki Earthquake - Inversion analysis by farfield waveforms (preliminary)

JMA (2012b). 2012/03/14 Sanriku-oki Earthquake - Inversion analysis by farfield waveforms (preliminary)

JMA (2012c). 2012/01/01 Torishima Near Sea Earthquake - Inversion analysis by farfield waveforms (preliminary)

JMA (2015). 2015/05/30 Ogawawara west-off earthquakes- inversion analysis by farfield waveforms.

Kagan Y.Y (2000). Temporal correlations of earthquake focal mechanisms, *Geophys. J. Int*., 143:881-897.

Kagan Y.Y (2002). Seismic moment distribution revisited. I. Statistical results, *Geophys. J. Int.*, 148:520-541.

Kagan, Y. Y. (2003). Accuracy of modern global earthquake catalogs, *Phys. Earth Planet*. In. 135, nos. 2/3, 173–209.

Kakehi, Y. (2004). Analysis of the 2001 Geiyo, Japan, earthquake using high-density strong ground motion data: Detailed rupture process of a slab earthquake in a medium with a large velocity contrast. *J. Geophys. Res.*, 109 (B8), B08306, *https://doi:10.1029/2004JB002980*.

Kanamori H. (1971). Great earthquakes at island arcs and the lithosphere, *Tectonophysics*, 12(3), 187-198.

Kataoka S., S. Matsumoto, T. Kusakabe, and N. Toyama (2008). Attenuation relationships and amplifcation map for ground motion in rather-long period range. Doboku Gakkai Ronbunshuu A, 64(4):721_738, 2008. doi:10.2208/jsceja.64.721. In Japanese with English abstract.

Kikuchi M., Fukao, Y. (1987). Inversion of long-period P-waves from great earthquakes along subduction zones, *Tectonophysics*, 144(1-3), 231-247.

Kikuchi M., Yamanaka Y. (2001) Near Coast of Peru earthquake (Mw 8.2) on June 23, 2001 (Revised), *EIC Seismological Note: N°105*, University of Tokyo Earthquake Information Center, *http://wwweic.eri.utokyo.ac.jp/EIC/EIC_News/105E.html*.

Kishida T., Darragh R.B., Chiou B.S.-J., Bozorgnia Y., Mazzoni S., Contreras V., Boroschek R., Rojas F., Stewart J.P. (2020). Chapter 3: Ground Motions and Intensity Measures, in Data Resources for NGA Subduction Project, *PEER Report 2020/02*, J.P. Stewart (editor), Pacific Earthquake Engineering Research Center, University of California, Berkeley, California (headquarters).

Knudson, CF, (1978) Strong-Motion Networks for Latin America. Central American Conference on Earthquake Engineering, San Salvador, El Salvador, 1978.

Knapp J., Knapp C., Hauser F., Prodehl C., Raileanu V., Matenco L., Bala A., Keller R., Stephenson R., Mocanu V., Dinu C. (2001). The Vrancea Zone, Romania: Intermediate Depth Seismicity in Search of a Viable Subduction Zone. AGU Fall Meeting Abstracts.

Koketsu K., Hikima K., Miyazaki S., and Ide S. (2004). Joint inversion of strong motion and geodetic data for the source process of the 2003 Tokachi-oki, Hokkaido, earthquake, *Earth Planets Space*, 56, 329–334.

Kuehn N., Bozorgnia Y., Campbell K.W., Gregor N. (2020). Partially non-ergodic ground-motion model for subduction regions using NGA-Subduction database, *PEER Report 2020/03*, Pacific Earthquake Engineering Research Center, UC Berkeley (headquarters).

Kuge K., Kase Y., Urata Y., Campos J., and Perez A. (2010). Rupture characteristics of the 2005 Tarapaca, northern Chile, intermediate-depth earthquake: Evidence for heterogeneous fluid distribution across the subducting oceanic plate?, *J. Geophys. Res*., 115, B09305.

Lay T., Ammon C. J., Hutko A. R., and Kanamori H. (2010). Effects of kinematic constraints on teleseismic finite-source rupture inversions: Great Peruvian earthquakes of 23 June 2001 and 15 August 2007, *Bull. Seismol. Soc. Am*., 100, 969-994.

Lay T., Yue H., Brodsky E. E., and An C. (2014). The 1 April 2014 Iquique, Chile, Mw 8.1 earthquake rupture sequence, *Geophys. Res. Lett*., 41, 3818–3825.

Lee S.J., Liang W. T., Huang B. S. (2008). Source mechanisms and rupture processes of the 26 December 2006 Pingtung earthquake doublet as determined from the regional seismic records, *Terr. Atmos. Ocean. Sci.*, 19, 555-565, *https://doi:10.3319/TAO.2008.19.6.555(PT)*.

Lee S.J. (2019). Inversion of finite fault model for Taiwan earthquakes, Appendix B in *Development of the Hazard Input Document for Taiwan Using SSHAC Level 3 Methodology*, National Center for Research on Earthquake Engineering, Taiwan.

Lermo Samaniego, J. Jaimes, M., Sánchez-Sesma, F., Campuzano-Sánchez, C., Cruz-Jiménez, H., Campos Enriquez, J. (2020). Ground motion prediction model for southeastern México removing site effects using the Earthquake horizontal-to-vertical ratio (EHVSR). *Geofísica Internacional*. 59. 257-272. 10.22201/igeof.00167169p.2020.59.4.1894.

Leyton F., Ruiz S., and Sepúlveda S. A. (2009). Preliminary re-evaluation of probabilistic seismic hazard assessment in Chile: from Arica to Taitao Peninsula, *Advances in Geosciences*, 22, 147–153.

Li Y, Shan X, Zhu C, Qiao X, Zhao L, Qu C (2020). Geodetic Model of the 2018 *M*w 7.2 Pinotepa, Mexico, Earthquake Inferred from InSAR and GPS Data. *Bulletin of the Seismological Society of America*, 110 (3): 1115–1124.

Lin P.-S., Lee C.-T. (2008). Ground-motion attenuation relationships for subduction-zone earthquakes in Northeastern Taiwan, *Bull. Seismol. Soc. Am*., 98, 220–240.

Lorito S., Romano F., Atzori S., Tong X., Avallone A., McCloskey J., Cocco M., Boschi E., and Piatanesi A. (2011). Limited overlap between the seismic gap and coseismic slip of the great 2010 Chile earthquake, *Nature Geoscience*, 4, 173–177.

Luna B (2012). Análisis de movimiento sísmico en la porción sur de la ciudad de México, una evaluación de la amenaza sismológica. M.S. Thesis, School of Engineering and Architecture, National Polytechnic Institute of Mexico, Mexico (In Spanish).

Lundberg N., Reed D., Liu C.-S., Lieske J. (1997). Forearc-basin closure and arc accretion in the submarine suture zone south of Taiwan, *Tectonophysics*, 274, 5-23.

Luttrell K. M., Tong X., Sandwell D. T., Brooks B. A., and Bevis M. G. (2011). Estimates of stress drop and crustal tectonic stress from the 27 February 2010 Maule, Chile, earthquake: Implications for fault strength, *J. Geophys. Res.: Solid Earth*, 116(B11).

Mai P.M., Spudich P., Boatwright J. (2005). Hypocenter locations in finite-source rupture models, *Bull. Seismol. Soc. Am.*, 95, 965-980.

Mai P.M. and Thingbaijam K.K.S. (2014). SRCMOD: An online database of finite-fault rupture models, *Seismol. Res. Lett*., 85(6), 1348-1357.

Malavieille J., Lallemand S.E., Dominguez S., Deschamps A., Lu C.-Y., Liu C.-S., and Schnürle P. (2002). Arc-continent collision in Taiwan : New marine observations and tectonic evolution, in *Geology and Geophysics of an Arc-Continent collision*, T.B. Byrne and C.-S. Liu (eds.), Taiwan, Republic of China: Boulder, Colorado, Geological Society of America Special Paper 358, p. 189-213.

Marsal RJ, Mazari M (1969) El subsuelo de la Ciudad de Me´xico. Facultad de Ingenierı´a, UNAM, Mexico, p 614

Mayoral JM, Romo MP, Osorio L (2008). Seismic parameters characterization at Texcoco lake, Mexico, *Soil Dynamics and Earthquake Engineering*, 28(7):507-521

Mayoral JM, Flores FA, Romo MP (2011). Seismic response evaluation of an urban overpass, *Earthquake Engineering & Structural Dynamics*, 40: 827-845.

Mayoral JM, Castañon E, Alcantara L, Tepalcapa S (2016). Seismic response characterization of high plasticity clays, *Soil Dynamics and Earthquake Engineering*, 84, 174-189.

Mayoral JM, TC Hutchinson, KW Franke (2017). Geotechnical engineering reconnaissance of the 19 September 2017 Mw 7.1 Puebla-Mexico City earthquake, Geotechnical Extreme Events Reconnaissance Association, Report no. GEER-055A

Mayoral JM, De la Rosa D, Tepalcapa S (2019). Topographic effects during the September 19, 2017 Mexico city earthquake, *Soil Dynamics and Earthquake Engineering*, 125:105732.

Mazzoni S., Kishida T., Ahdi S.K., Contreras V., Darragh R.B., Chiou B.S.-J., Kuehn N., Bozorgnia Y., Stewart J.P. (2020). Chapter 2: Relational Database, in Data Resources for NGA-Subduction Project, *PEER Report No. 2020/02*, J.P. Stewart (editor), Pacific Earthquake Engineering Research Center, University of California, Berkeley, California (headquarters).

Mazzoni S., Kishida T., Ahdi S.K., Ancheta T.D., Contreras V., Darragh R.B., Kuehn N., Kwak D.Y., Kwok A.O., Chiou B.S.J., Silvia W.J., Bozorgnia Y., Stewart J.P. (2021). NGA-Sub Flatfile R211022, The B. John Garrick Institute for the Risk Sciences. Dataset. https://doi.org/10.34948/N3Z59T, October.

Mazzoni S, Kishida T, Stewart JP, Contreras V, Darragh RB, Ancheta TD, Chiou BS-J, Silva WJ and Bozorgnia Y (2022). Relational database used for ground-motion model development in the NGA-Sub project. *Earthquake Spectra*, 38(2): 1529–1548.

McCaffrey R. (2008). Global frequency of magnitude 9 earthquakes. *Geology*, 36 (3): 263–266, *https://doi.org/10.1130/G24402A.1*.

McVerry G. H., Zhao J. X., Abrahamson N. A., and Somerville P. G. (2006). New Zealand acceleration response spectrum attenuation relations for crustal and subduction zone earthquakes. *Bulletin of the New Zealand Society for Earthquake Engineering*, 39(4):1_58, Mar 2006

Melgar D., Fan W., Riquelme S., Geng J., Liang C., Fuentes M., Vargas G., Allen R. M., Shearer P. M., and Fielding E. J. (2016). Slip segmentation and slow rupture to the trench during the 2015, Mw8.3 Illapel, Chile earthquake, *Geophys. Res. Lett*., 43, 961‐966.

Melgar D, A Ruiz-Angulo, ES Garcia, M Manea, V Manea, X Xu, et al. (2018a). Deep embrittlement and complete rupture of the lithosphere during the Mw 8.2 Tehuantepec earthquake, *Nature Geoscience*, 11 (12), 955-960.

Melgar D, Pérez-Campos X, Ramirez-Guzman L, Spica Z, Espíndola VH, Hammond WC, Cabral-Cano E. (2018b). Bend Faulting at the Edge of a Flat Slab: The 2017 Mw7.1 Puebla-Morelos, Mexico Earthquake, *Geophys. Res. Lett*., 45, 2633-2641.

Mendoza C., Fukuyama E. (1996). The July 12, 1993, Hokkaido-Nansei-Oki, Japan, earthquake: Coseismic slip pattern from strong-motion and teleseismic recordings, *J. Geophys. Res*., 101, 791-801.

Mendoza C. (1993). Coseismic Slip of 2 Large Mexican Earthquakes from Teleseismic Body Wave-Forms - Implications for Asperity Interaction in the Michoacan Plate Boundary Segment, *J. Geophys. Res: Solid Earth*, 98 (B5), 8197-8210.

Mendoza C., Hartzell S.H. (1989). Slip Distribution of the 19 September 1985 Michoacan, Mexico, Earthquake - near-Source and Teleseismic Constraints, *Bull. Seismol. Soc. Am*., 79 (3), 655-669.

Mendoza C., Martínez-López M. (2022). Rapid finite-fault analysis of large Mexico earthquakes using teleseismic P waves. *Journal of Seismology*. 26. 10.1007/s10950-022-10083-y.

Mendoza C., Hartzell S., and Monfret T. (1994). Wide-Band Analysis of the 3 March 1985 Central Chile Earthquake - Overall Source Process and Rupture History, *Bull. Seismol. Soc. Am.*, 84 (2), 269-283.

Mirwald, A., Cruz-Atienza, V. M., Díaz-Mojica, J., Iglesias, A., Singh, S. K., Villafuerte, C., & Tago, J. (2019). The 19 September 2017 (Mw 7.1) intermediate-depth Mexican earthquake: A slow and energetically inefficient deadly shock. *Geophysical Research Letters*, *46*(4), 2054-2064.

Montalva et al. (2016). Unpublished, adaptation of the Abrahamson et al. (2016) BC Hydro GMPE, calibrated to Chilean strong motion data.

Montalva G. A., Bastías N. and Rodriguez-Marek A. (2017). Ground-Motion Prediction Equation for the Chilean Subduction Zone, *Bull. Seismol. Soc. Am.*, 107 (2): 901-911.

Montalva G., Bastias N., Leyton F. (2021). Strong Ground Motion Prediction Model for PGV and Spectral Velocity for the Chilean Subduction Zone. *Bulletin of the Seismological Society of America*. 10.1785/0120210037.

Morikawa N. and H. Fujiwara. A new ground motion prediction equation for Japan applicable up to M9 mega-earthquake. *Journal of Disaster Research*, 8(5):878_888, 2013.

Murotani S., Satake K., and Fujii Y. (2013). Scaling relations of seismic moment, rupture area, average slip, and asperity size for M∼ 9 subduction-zone earthquakes, *Geophys. Res. Lett.*, 40, 1–5.

Nagai R., Kikuchi M. and Yamanaka Y. (2001). Comparative Study on the Source Processes of Recurrent Large Earthquakes in Sanriku-oki Region: the 1968 Tokachi-oki Earthquake and the 1994 Sanriku-oki Earthquake, *Jishin*, 54: 267-280.

Nagumo H. (2012), Rupture process of northern Nagano Prefecture earthquake on March 12th, 2011 (Mj6.7), Annual Meeting of Japan Association for Earthquake Engineering, Japan Association for Earthquake Engineering.

Nakayama W., Takeo M.. (1997). Slip history of the 1994 Sanriku-Haruka-Oki, Japan, earthquake deduced from strong-motion data, *Bull. Seismol. Soc. Am.*, 87 (4), 918-931.

Namegaya Y., Tsuji Y. (2005). Delayed peaks of tsunami waveforms at Miyako from earthquakes east of Hokkaido, Earthquake Research Institute, University of Tokyo, Tokyo, Japan.

Nigam N.C., Jennings P.C. (1969). Calculation of response spectra from strong-motion earthquake records, *Bull. Seismol. Soc. Am.,* **59**, 909–922.

Nogoshi M, Igarashi T (1970) On the amplitude characteristics of ambient noise (part 1). *J. Atmos. Oceanic Technol.*, **24**: 282–308.

Nogoshi M, Igarashi T (1971) On the amplitude characteristics of ambient noise (part 2). *J. Atmos. Oceanic Technol.*, **24**:26–40

Nozu (2007). 1993 Kushiro-Oki earthquake finite fault model (2nd ver.) – with digital supplement, *http://www.pari.go.jp/bsh/jbn-kzo/jbn-si/taisin/research_jpn/research_jpn_2007/japanese_research_24.html*.

NTCS (2003). Normas Técnicas Complementarias para diseño por Sismo. Gaceta oficial del Distrito Federal (Ed.), México (In Spanish)

NTCS (2020). Normas Técnicas Complementarias para diseño por Sismo. Gaceta oficial del Distrito Federal (Ed.), México (In Spanish)

Okada T. and Hasegawa A. (2003). The M7.1 May 26, 2003 off-shore Miyagi Prefecture Earthquake in northeast Japan: Source process and aftershock distribution of an intra-slab event, *Earth Planets Space*, 55, 731–739.

Okuwaki, R., & Yagi, Y. (2017). Rupture process during the Mw 8.1 2017 Chiapas Mexico earthquake: shallow intraplate normal faulting by slab bending. *Geophysical Research Letters*, 44. *https://doi.org/10.1002/2017GL075956*.

Oppenheimer D., Eaton J., Jayko A., Lisowski M., Marshall G., Murray M., Simpson R., Stein R., Beroza G., Magee M., Carver G., Dengler L., McPherson R., Gee L., Romanowicz B., Gonzalez F., Li W. H., Satake K., Somerville P., Valentine D. (1993). The Cape Mendocino, California, Earthquakes of April 1992: Subduction at the Triple Junction, *Science*, 261 (5120), 433-438.

Ordaz M, Jara JM, Singh SK (1989) Riesgo sísmico y espectros de diseño en el estado de Guerrero, Report No 8782/9745, UNAM Instituto de Ingeniería (In Spanish)

Ordaz, M., Singh S.K., Archiniega, A. (1994). Bayesian attenuation regressions: an application to Mexico City, *Geophys. J. Int.*, 117, 335-344

Okuwaki R., Y. Yagi (2017). Rupture Process During the Mw 8.1 2017 Chiapas Mexico Earthquake: Shallow Intraplate Normal Faulting by Slab Bending, *Geophysical Research Letters*, 44(23): 11,816-11,823

Parker, GA, JP Stewart (2022). Ergodic site response model for subduction zone regions, Earthquake Spectra, 38(2), 841-864.

Parker, GA, JP Stewart, DM Boore, GM Atkinson, B Hassani (2022). NGA-subduction global ground motion models with regional adjustment factors, Earthquake Spectra, 38(1), 456-493.

Perea T. and Sordo E. (1988). Direct Response Spectrum Prediction Including Local Site Effects, *Proc. 11th European Conf. Eqk. Eng*., Paris, France.

Pérez O (2017). Estudio geofísico de refracción sísmica para la caracterización del terreno, en el conjunto urbano Tlalpan, ubicado en la delegación Coyoacán, CDMX. Technical report, AXDSCA Consultants.

Pérez-Campos X., Kim Y., Husker A., Davis P.M., Clayton R.W., Iglesias A., Pacheco J.F., Singh S.K., Manea V.C., Gurnis M. (2008). Horizontal subduction and truncation of the Cocos Plate beneath central Mexico. *Geophysical Research Letters*, 35, L18303

Phung V.-B., C. H. Loh, S. H. Chao, and N. A. Abrahamson (2020). Ground motion prediction equation for Taiwan subduction zone earthquakes. *Earthquake Spectra*, 36(3):1331-1358,

Pitarka A., Thio H. K., Somerville P. G. and Bonilla L. F. (2013), Broadband Ground-Motion Simulation of an Intraslab Earthquake and Nonlinear Site Response: 2010 Ferndale, California, Earthquake Case Study, *Seismol. Res. Lett*., 84(5), 785-795.

Poblete J.D. (2008). *Determinación experimental de la Intensidad de Mercalli Modificada para Chile*, Thesis, Department of Civil Engineering, University of Chile, Santiago, Chile. (In Spanish).

Pollitz F. F., Brooks B., Tong X., Bevis M. G., Foster J. H., Bürgmann R., Smalley R., Vigny C., Socquet A., Ruegg J. C., and Campos J. (2011). Coseismic slip distribution of the February 27, 2010 Mw 8.8 Maule, Chile earthquake, *Geophys. Res. Lett*., 38, L09309.

Power M., Chiou B., Abrahamson N., Bozorgnia Y., Shantz T., and Roblee C. (2008). An Overview of the NGA Project, *Earthquake Spectra*, 24(1), 3–21.

Ramos-Martínez J, Chávez-Garcia F, Romero-Jiménez E, Rodríguez-Zúñiga J, Gómez-González, J (1997). Site effects in Mexico City: Constraints from surface wave inversion of shallow refraction data. *Journal of Applied Geophysics*, 36: 157-165.

Reinoso E, Ordaz M (1999). Spectral ratios for Mexico City from free-field recordings, *Earthquake Spectra*, 15: 273-295.

Reyes, C. (1998). El estado límite de servicio en el diseño sísmico de edificios, Ph.D. Thesis, School of Engineering, National Autonomous University of Mexico (UNAM), Mexico (In Spanish).Rodriguez-Perez, Q. (2014). Ground-Motion Prediction Equations for Near-Trench Interplate and Normal-Faulting Inslab Subduction Zone Earthquakes in Mexico, Bulletin of the Seismological Society of America 104(1): 427-438.

Romo M. and García S. (2003). Neurofuzzy mapping of CPT values into soil dynamic properties. *Soil Dynamics and Earthquake Engineering*, 23: 473–482.

Romo MP, Jaime A, Resendiz D (1988). The Mexico earthquake of September 19 1985 – General soil conditions and clay properties in the Valley of Mexico, *Earthquake Spectra*, 4:731-752

Rösler, B., Stein, S., & Spencer, B.D. (2021). Uncertainties in Seismic Moment Tensors Inferred from Differences between Global Catalogs. *Seismological Research Letters*. 92 (6): 3698–3711

Rosenblueth E, Ordaz M, Sánchez-Sesma FJ, Singh SK (1989) The Mexico earthquake of September 19, 1985—design spectra for Mexico's Federal District. *Earthq Spectra* 5(1):273–291

Ruiz S. and Saragoni G. (2005). Attenuation equations for subduction-zone earthquakes in Chile considering two seismogenic mechanisms and site effects, *IX Jornadas Chilenas de Sismología e Ingeniería Antisísmica*, Concepción, Chile (*In Spanish*).

Sakamoto S., Y. Uchiyama, and S. Midorikawa (2006). Variance of response spectra in attenuation relationship. In Proceedings of the Eighth U.S. National Conference on Earthquake Engineering, Apr 2006. Paper no. 471.

Salichon J., Delouis B., Lundgren P., Giardini D., Costantini M., and Rosen P. (2003). Joint inversion of broadband teleseismic and interferometric synthetic aperture radar (InSAR) data for the slip history of the Mw = 7.7, Nazca ridge (Peru) earthquake of 12 November 1996, *J. Geophys. Res*, 108(B2), *https://doi:10.1029/2001JB000913*.

Satoh T., H. Kawase, S. Matsushima (2001). Differences between site characteristics obtained from microtremors, S-waves, P-waves, and codas, *Bull. Seismol. Soc. Am.*, **91**, 313–334.

Schmidt, V., Bungum, H., Dahle, A. (1997). Costa Rican spectral strong motion attenuation.- 45 págs. NORSAR, Norway [Reporte Técnico]

Schroeder K. D. (2016). “Subduction-en.svg” from Wikimedia Commons, CC-BY-SA 4.0, available at *https://commons.wikimedia.org/wiki/File:Subduction-en.svg* (last accessed March 2020).

Schurr B., Asch G., Rosenau M., Wang R., Oncken O., Barrientos S., Salazar P., and Vilotte J.-P. (2012). The 2007 M7.7 Tocopilla northern Chile earthquake sequence: Implications for along-strike and downdip rupture segmentation and megathrust frictional behavior, *J. Geophys. Res*., 117, B05305.

Scognamiglio L., Magnoni F., Tinti E., Casarotti E. (2016). Uncertainty estimations for moment tensor inversions: the issue of the 2012 May 20 Emilia earthquake, *Geophysical Journal International*, Volume 206, Issue 2, 792–806.

Seed HB, Romo MP, Sun JI, Jaime A, Lysmer J (1987). Relationships between soil conditions and earthquake ground motions Mexico City in the earthquake of September 19 1985, *Report UCB/EERC-87/15*, Earthquake Engineering Research Center, UC Berkeley.

SEVO (1996). Institute of Seismology and Volcanology, Faculty of Science, Kyushu University.

Shao G. and Ji C. (n.d.). Preliminary Result of the Jul 30, 1995 Mw 8.14 Antofagasta Earthquake, UCSB, available at *http://www.geol.ucsb.edu/faculty/ji/big_earthquakes/1995/07/chile.html* (last accessed May 2017).

Shao G., Li X., Liu, Q., Zhao, X., Yano, T., Ji, C. (2010). Preliminary slip model of the Feb 27, 2010 Mw 8.9 Maule, Chile Earthquake, UCSB, *http://ji.faculty.geol.ucsb.edu/big_earthquakes/2010/02/27/chile_2_27.html*.

Shiba Y. and Uetake T. (2011). Rupture Process of the 1964 MJMA 7.5 Niigata Earthquake Estimated from Regional Strong-Motion Records, *Bull. Seismol. Soc. Am*., 101, 1871–1884.

Shoushtari A. V., A. B. Adnan, and M. Zare. On the selection of ground-motion attenuation relations for seismic hazard assessment of the Peninsular Malaysia region due to distant Sumatran subduction intraslab earthquakes. *Soil Dynamics and Earthquake Engineering*, 82:123-137.

Shoushtari A. V., A. Z. Adnan, and M. Zare. Ground motion prediction equations for distant subduction interface earthquakes based on empirical data in the Malay Peninsula and Japan. *Soil Dynamics and Earthquake Engineering*, 109:339-353.

Si H, Midorikawa S, Kishida T. Development of NGA-Sub ground-motion prediction equation of 5%-damped pseudo-spectral acceleration based on database of subduction earthquakes in Japan. *Earthquake Spectra*. May 2022. doi:10.1177/87552930221090326

Singh SK, Mena E, Castro R, Carmona C (1987) Empirical prediction of ground motion in Mexico City from coastal earthquakes. *Bull Seism Soc Am* 87(6):1862–1867.

Singh SK, Gutierreez C, Arboleda J, Ordaz M (1993). Peligro sismico en El Salvador, Universidad Nacional Autonoma de Mexico, Mexico

Skarlatoudis AA, Papazachos C B (2012). Preliminary Study of the Strong Ground Motions of the Tohoku, Japan, Earthquake of 11 March 2011: Assessing the Influence of Anelastic Attenuation and Rupture Directivity. *Seismological Research Letters* 83 (1): 119–129

Skarlatoudis A. A., C. B. Papazachos, B. N. Margaris, C. Ventouzi, I. Kalogeras, and the EGELADOS Group. (2013). Ground-motion prediction equations of intermediate-depth earthquakes in the Hellenic Arc, southern Aegean subduction area. *Bulletin of the Seismological Society of America*, 103:1952-1968

Skarlatoudis A.A., Somerville P.G., Thio H.K. (2016). Source-Scaling Relations of Interface Subduction Earthquakes for Strong Ground Motion and Tsunami Simulation, *Bull. Seismol. Soc. Am.*, 106, 1652-1662.

Sladen A. (2007). Preliminary Result 11/14/2007 (Mw 7.7), Tocopilla Earthquake, Chile, Source Models of Large Earthquakes, Caltech, available at *http://www.tectonics.caltech.edu/slip_history/2007_tocopilla/tocopilla.html* (last accessed July 1, 2013).

Sladen A. (2010). Preliminary Result, 02/27/2010 (Mw 8.8), Chile, Source Models of Large Earthquakes, Caltech, available at *http://www.tectonics.caltech.edu/slip_history/2010_chile/index.html* (last accessed May 2017).

Smithsonian Institute's Global Volcanism Program (2013). *https://volcano.si.edu/*.

Stähler S., Sigloch K. (2014). Fully probabilistic seismic source inversion – Part 1: Efficient parameterisation. *Solid Earth*. 5. 1055-1069.

Stein, S., and Okal, E.A. (2007). Ultralong period seismic study of the December 2004 Indian Ocean earthquake and implications for regional tectonics and the subduction process, *Seismological Society of America Bulletin*, v. 97, p. S279–S295, https://doi:10.1785/0120050617.

Stephenson C and Lomnitz B (2005). Shear-wave velocity profile at the Texcoco strong-motion array site, Valley of Mexico. *Geofísica Internacional*, 44(1):3-10.

Storchak, D.A., D. Di Giacomo, I. Bondár, E.R. Engdahl, J. Harris, W.H.K. Lee, A. Villaseñor and P. Bormann (2013). Public Release of the ISC-GEM Global Instrumental Earthquake Catalogue (1900-2009). Seism. Res. Lett., 84, 5, 810-815, doi: 10.1785/0220130034

Strasser F. O., M.C. Arango, and J.J. Bommer (2010). Scaling of the source dimensions of interface and intraslab subduction-zone earthquakes with moment magnitude, *Seismol. Res. Lett*. 81, 941–950.

Suzuki W., Aoi S. and Sekiguchi H. (2009), Rupture Process of the 2008 Northern Iwate Intraslab Earthquake Derived from Strong-Motion Records, *Bull. Seismol. Soc. Am*. 99, 2825–2835.

Takahashi H., Hirata K. (2003). The 2000 Nemuro-Hanto-Oki earthquake, off eastern Hokkaido, Japan, and the high intraslab seismic activity in the southwestern Kuril Trench, *J. Geophys. Res*., 108 (B4), pp 2-1 - 2-9.

Takeo M. and Mikami N. (1990). Fault heterogeneity of inland earthquakes in Japan. *Bulletin of the Earthquake Research Institute*, University of Tokyo, 65 (2), 541-569.

Takiguchi M., Asano K., Iwata T. (2011). The comparison of source models of repeating subduction-zone earthquake estimated using broadband strong motion records - 1982 and 2008 Ibaraki-ken-oki M7 Earthquakes, *J. Seism. Soc. Japan*, 63, 223-242.

Tanioka Y., Ruff L., Satake K. (1995). The great Kurile earthquake of October 4, 1994 tore the slab, *Geophys. Res. Lett*., 22, 1661-1664.

Tape W., Tape C. (2016). A confidence parameter for seismic moment tensors *Geophysical Journal International* 205 (2), 938-953

Theodulidis N., Bard P.Y., Archuleta R., Bouchon M. (1996). Horizontal-to-vertical spectral ratio and geological conditions: The case of Garner Valley downhole array in southern California. *Bull. Seismol. Soc. Am.*, **86(2)**, 306–319.

Tichelaar B.W,, Ruff L.J. (1993). Depth of seismic coupling along subduction zones, *J. Geophys. Res.: Solid Earth*, 98 (B2), 2017-2037.

Tsuchida H., Inatomi T., Ueda H. (1983). The Damage to Port Facilities by the 1982 Urakawa-oki Earthquake, *Technical Note No.472*, Port and Harbour Research Institute Ministry of Transport, Japan.

Tung S., Fielding E. J., Bekaert D. P. S., Masterlark T. (2019). Rapid geodetic analysis of subduction zone earthquakes leveraging a 3-D elastic Green's function library. *Geophysical Research Letters*, 46. https://doi.org/10.1029/2018GL080578

Uchiyama Y. and S. Midorikawa (2006). Attenuation relationship for response spectra on engineering bed rock considering effects of focal depth. *Journal of Structural and Construction Engineering, Architectural Institute of Japan*, 606:81-88.

Urzúa A, Dobry R, Christian JT (2017). Is Harmonic Averaging of Shear Wave Velocity or the Simplified Rayleigh Method Appropriate to Estimate the Period of a Soil Profile? *Earthquake Spectra*, 33:895-915.

USGS (1996). This Dynamic Earth: the Story of Plate Tectonics by W. Jacquelyne Kious and Robert I. Tilling, U.S. Geological Survey, illustrations available at https://doi.org/10.3133/7000097 (last accessed March 2020).

USGS (2003). M7.8 Rat Islands, Alaska earthquake of 17 November 2003, *ftp://hazards.cr.usgs.gov/maps/sigeqs/20031117/20031117.pdf*.

USGS (2014). Preliminary finite fault results for the Jun 23, 2014 Mw 7.9 51.7968, 178.7591 earthquake (Version 1), *http://earthquake.usgs.gov/earthquakes/eventpage/usc000rki5#finite-fault*.

USGS (2016). Preliminary finite fault results for the Jan 24, 2016 Mw 7.1 83 km E of Old Iliamna, Alaska earthquake (Version 1), *http://earthquake.usgs.gov/earthquakes/eventpage/us10004gqp#finite-fault*.

Vacareanu R., S. Demetriu, D. Lungu, F. Pavel, C. Arion, M. Iancovici, A. Aldea, and C. Neagu (2014). Empirical ground motion model for Vrancea intermediate-depth seismic source. Earthquakes and Structures, 6(2):141-161.

Vacareanu R., M. Radulian, M. Iancovici, F. Pavel, and C. Neagu (2015). Fore-arc and back-arc ground motion prediction model for Vrancea intermediate depth seismic source. *Journal of Earthquake Engineering*, 19(3):535-562

Valentine A.P. Trampert J. (2012) Assessing the uncertainties on seismic source parameters: towards realistic error estimates for centroid-moment-tensor determinations, *Phys. Earth planet. Inter.*, Vol. 210–211, 36-49.

Van Houtte C., Bannister S., Holden C., Bourguignon S., McVerry G. (2017). The New Zealand strong motion database, *Bull. New Zealand Soc. Eqk. Eng.*, 50(1), 1-20, *https://doi.org/10.5459/bnzsee.50.1.1-20.*

Vergara-Huerta F., and Aguirre J. (2020). One-dimensional seismic velocity model of the sub-basin of Chalco, Mexico. *Physics of the Earth and Planetary Interiors*, 300:106426.

Wang, P., Stewart J.P., Bozorgnia Y., Boore D.M., Kishida T. (2017). "R" package for computation of earthquake ground-motion response spectra" *Report No. 2017/09*, Pacific Earthquake Engineering Research Center, UC Berkeley.

Wang P, P Zimmaro, TE Buckreis, T Gospe, SJ Brandenberg, SK Ahdi, A Yong, JP Stewart (2022). Relational database for Horizontal-to-Vertical Spectral Ratios, Seism. Research Letters, 93(2A), 1075-1088.

Wells R.E., Blakely R.J., Simpson R.W., Weaver C.S., Haugerud R., Wheeler K. (2000). Tectonic plate motions, crustal blocks, and shallow earthquakes in Cascadia, *Great Cascadia Earthquake Tricentennial Open House, 26 January 2000*, Burke Museum, University of Washington, Seattle, WA (poster).

Williams M. C., Tréhu A. M., and Braunmiller J. (2011). Seismicity at the Cascadia plate boundary beneath the Oregon continental shelf, *Bull. Seismol. Soc. Am*., 101, 940–950.

Wood CM, Deschenes M, Ledezma C, Meneses J, Montalva G, Morales-Velez AC (2019). Dynamic site characterization of areas affected by the 2017 Puebla-Mexico city earthquake, *Soil Dynamics and Earthquake Engineering*, 125:105704,

Wooddell K. (2018). New earthquake classification for the NGA-subduction project, *Proc. 11th National Conference on Earthquake Engineering*, Los Angeles, CA, Paper 1275.

Wooddell K., Abrahamson N.A. (2014). Classification of Mainshocks and Aftershocks in the NGA-West2 Database, *Earthquake Spectra*, 30, 1257-1267.

Woodfield, L (2020). Development of Vs Profiles and Site Periods in the Mexico City Basin, MS Thesis, University of Arkansas.

Wu F. T., Liang W.-T., Lee J.-C., Benz H., Villasenor A. (2009), A model for the termination of the Ryukyu subduction zone against Taiwan: A junction of collision, subduction/separation, and subduction boundaries, *J. Geophys. Res.*, 114, B07404, *https://doi:10.1029/2008JB005950*.

Wu YM, Cheng SN and Liu TY (2016) A foundation and basic analysis of earthquake catalog and historical earthquakes database. Final report, prepared for Taiwan SSHAC Level 3 PSHA Project (Appendix B of volume 2). National Center for Research in Earthquake Engineering, Taipei, Taiwan, 90 pp.

Yagi Y. (2004). 2004/09/05 Kii Peninshula SouthEast offshore Earthquake, *http://iisee.kenken.go.jp/staff/yagi/eq/Japan20040905/Japan20040905_1j.html*.

Yagi Y., Kikuchi M., Yoshida S., and Yamanaka Y. (1998). Source Process of the Hyuga-nada Earthquake of April 1, 1968 (Mjma 7.5), and its Relatonship to the Subsequent Seismicity, *J. Seismol. Soc. Japan*, 51, 139-148.

Yagi Y., Kikuchi M., Yoshida S., and Sagiya T. (1999). Comparison of the coseismic rupture with the aftershock distribution in the Hyuga-nada earthquakes of 1996, *Geophys. Res. Lett.*, 26 (20), 3161-3164.

Yamanaka Y., Kikuchi, M. (2004). Asperity map along the subduction zone in northeastern Japan inferred from regional seismic data, *J. Geophys. Res*., 109 (B7), B07307, *https://doi:10.1029/2003JB002683*.

Yamanaka Y. (2005). *EIC Semiology Note No.168*, *http://wwweic.eri.u-tokyo.ac.jp/sanchu/Seismo_Note/2005/EIC168a.html* (last access 01/17/2017).

Ye L., Lay T., Kanamori H., Koper K.D. (2013). Energy Release of the 2013 Mw 8.3 Sea of Okhotsk Earthquake and Deep Slab Stress Heterogeneity, *Science*, 341, 1380-1384.

Ye L., Lay T., Kanamori H., and Rivera L. (2016). Rupture characteristics of large (Mw ≥ 7) megathrust earthquakes from 1990-2015: I. Moment-Scaling Relationships, *J. Geophys. Res*., 121, 826-844.

Ye, L., Lay, T., Bai, Y., Cheung, K. F., & Kanamori, H. (2017). The 2017 Mw 8.2 Chiapas, Mexico, earthquake: Energetic slab detachment. *Geophysical Research Letters*, 44. *https://doi.org/10.1002/2017GL076085*.

Yokota Y., Koketsu K., Fujii Y., Satake K., Sakai S., Shinohara M., and Kanazawa T. (2011). Joint inversion of strong motion, teleseismic, geodetic, and tsunami data sets for the rupture process of the 2011 Tohoku earthquake, *Geophys. Res. Lett*., 38, L00G21, *https://doi:10.1029/2011GL050098*.

Yong A. (2016). Comparison of measured and proxy-based V_{S30} values in California, *Earthq. Spectra*, 32, no. 1, 171–192.

Yoshioka N. and Abe K. (1976). Focal mechanism of the Iwate-oki earthquake of June 12, 1968, *J. Phys. Earth*, 24, 251-262.

Youngs, R.R., S.M. Day, and J.P. Stevens (1988). Near field motions on rock for large subduction zone earthquakes, in *Earthquake Engineering and Soil Dynamics II Recent Advances in Ground Motion Evaluation,* ASCE Geotechnical Special Publication 20, 445-462.

Youngs R.R., Chiou B.S.J., Silva W.J., and Humphrey J. (1997). Strong ground motion attenuation relationships for subduction zone earthquakes, *Seismol. Res. Lett*., 68, 58–73.

Yu C., Li Z., Song C. (2021). Geodetic constraints on recent subduction earthquakes and future seismic hazards in the southwestern coast of Mexico. *Geophysical Research Letters, 48*(13), e2021GL094192.

Zhao J. X., Zhang J., Asano A., Ohno Y., Oouchi T., Takahashi T., Ogawa H., Irikura K., Thio H. K., Somerville P. G., Fukushima Y., and Fukushima Y. (2006). Attenuation relations of strong ground motion in Japan using site classification based on predominant period, *Bull. Seismol. Soc. Am*., 96, 898–913.

Zhao J. X., F. Jiang, P. Shi, H. Xing, H. Huang, R. Hou, Y. Zhang, P. Yu, X. Lan, D. A. Rhoades, P. G. Somerville, K. Irikura, and Y. Fukushima (2016a). Ground-motion prediction equations

for subduction slab earthquakes in Japan using site class and simple geometric attenuation functions. *Bulletin of the Seismological Society of America*, 106(4):1535-1551.

Zhao J. X., X. Liang, F. Jiang, H. Xing, M. Zhu, R. Hou, Y. Zhang, X. Lan, D. A. Rhoades, K. Irikura, Y. Fukushima, and P. G. Somerville (2016b). Ground-motion prediction equations for subduction interface earthquakes in Japan using site class and simple geometric attenuation functions. *Bulletin of the Seismological Society of America*, 106(4):1518-1534.